JULIUS-MAXIMILIANS-UNIVERSITÄT WÜRZBURG
Graduate School of Science and Technology
Sektion Molecular & Material Sciences

Dissertation zur Erlangung des naturwissenschaftlichen Doktorgrades
der Graduate School of Science and Technology,
Julius-Maximilians-Universität Würzburg

Structure-Dependent Ultrafast Relaxation Dynamics in Multichromophoric Systems

Strukturabhängigkeit ultraschneller Relaxationsdynamik in multichromophoren Systemen

vorgelegt von
Federico Juan Koch

aus
Erlangen

Würzburg, 2016

Eingereicht am: . . . .

Stempel des GSST Büro

Mitglieder des Promotionskomitees:

Vorsitzende/r: . . . .

1. Betreuer:	Prof. Dr. Tobias Brixner
2. Betreuer:	Prof. Dr. Frank Würthner
3. Betreuer:	Prof. Dr. Volker Engel

Tag des Promotionskolloquiums: . . . .

Doktorurkunde ausgehändigt am: . . . .

Kurzfassung

Zeitaufgelöste Spektroskopie ermöglicht die Untersuchung lichtinduzierter Energietransferprozesse und molekularer Wechselwirkungen. Derartige Ergebnisse bilden wiederum die Grundlage für die Entwicklung von Synthesestrategien für neuartige Materialien sowie für effizientere optoelektronische Anwendungen. Um die lichtinduzierte Dynamik komplexer molekularer Systeme aufzuklären, wurden die Techniken der transienten Absorption (TA) und der kohärenten zweidimensionalen (2D) Spektroskopie mit weiteren experimentellen Messungen sowie theoretischen Ansätzen und Simulationen kombiniert.

In Kooperation mit der Forschungsgruppe von Prof. Dr. Frank Würthner an der Universität Würzburg wurde eine molekulare Serie von Merocyaninen untersucht, die sich in der Anzahl der Chromophore und dem Substitutionsmuster an einem Benzolring unterscheiden. Eine globale Analyse der TA-Experimente für die verschiedenen Moleküle der Serie sowie weitere kohärente 2D-Spektroskopie-Experimente ermöglichten es, ein Relaxationsmodell zu ermitteln, das für alle untersuchten Merocyaninsysteme anwendbar ist. Dieses Relaxationsmodell basiert auf einem doppelten Minimum in der Potentialfläche des ersten angeregten Zustands. Eines dieser Minima wurde einem intramolekularen Ladungstransferzustand zugeordnet, welcher durch die Wechselwirkung benachbarter Chromophore stabilisiert wird und dadurch einen Anstieg der Lebensdauer des angeregten Zustands bewirkt. Zusätzliche elektrooptische Absorptionsmessungen in Kombination mit Ergebnissen der Dichtefunktionaltheorie offenbarten eine bevorzugte relative Chromophororientierung, die das Dipolmoment eines einzelnen Chromophors weitestgehend kompensiert. Basierend auf dieser Strukturbestimmung wurde eine strukturabhängige Exzitonenaufspaltungsenergie ermittelt und mit der Aufspaltung in den linearen Absorptionsspektren verglichen. Die linearen Absorptionsspektren der multichromophoren Merocyanine können durch eine Kombination von monomerischen und exzitonischen Beiträgen beschrieben werden, was eine gewisse strukturelle Flexibilität erfordert.

In einer weiteren Kooperation mit den Gruppen von Prof. Dr. Christoph Lambert und Prof. Dr. Roland Mitrić der Universität Würzburg wurde ein strukturell komplexer, polymerer Squarainfarbstoff untersucht. Dieses Polymer besteht aus einer Superposition von Zickzack- und Helixstrukturen, welche lösungsmittelabhängig ist. Rechnungen basierend auf neuesten Methoden der Dichtefunktionaltheorie bestätigten die vorherige Zuordnung, dass Zickzack- und Helixstrukturen als J- und H-Aggregate behandelt werden können. Mittels transienter Absorption konnte ermittelt werden, dass in Abhängigkeit des Lösungsmittels sowie der Anregungsenergie ultraschneller Energietransfer innerhalb des Squarain-Polymers entweder von zunächst angeregten Helix- zu Zickzacksegmenten stattfindet oder von Zickzack- zu Helixsegmenten. Zusätzlich konnte die Subpikosekundendynamik durch die kohärente 2D-Spektroskopie bestätigt werden. Im Gegensatz zu anderen konjugierten Polymeren wie MEH-PPV, welches im letzten Kapitel dieser Arbeit

behandelt wird, basiert der ultraschnelle Energietransfer in Squarainpolymeren auf dem energetischen Überlapp der Zustandsdichten von Donor- und Akzeptorsegmenten, welcher auf die geringe Reorganisationsenergie in cyaninähnlichen Farbstoffen beruht.

Abschließend wurde die lichtinduzierte Dynamik der aggregierten Phase des konjugierten Polymers MEH-PPV in Kooperation mit der Gruppe von Prof. Dr. Anna Köhler von der Universität Bayreuth untersucht. Unsere Kooperationspartner hatten zuvor die Aggregation von MEH-PPV bei Abkühlung durch die Formation von sogenannten HJ-Aggregaten, welche auf der Exzitonentheorie beruhen, beschrieben. Durch transiente Absorptionsmessungen und einer zugehörigen Bandenanalyse konnte zwischen Relaxationsprozessen im angeregten Zustand und zurück zum Grundzustand unterschieden werden. Die Anwendung der kohärenten 2D-Spektroskopie ermöglichte es, Energietransferprozesse zwischen konjugierten Segmenten des aggregierten Polymers aufzuklären. Die anfängliche Exzitonenrelaxation innerhalb der aggregierten Phase deutet auf eine geringe Mobilität der Exzitonen hin, welche im Gegensatz zu den anschließenden Energietransferprozessen zwischen unterschiedlichen Chromophoren innerhalb einiger Pikosekunden steht.

Diese Arbeit trägt durch eine systematische Untersuchung der strukturabhängigen Relaxationsdynamik zum grundlegenden Verständnis des Verhältnisses zwischen Struktur und Funktion von komplexen molekularen Systemen bei. Die untersuchten Molekülklassen weisen dabei ein hohes Potential auf, um durch gezielte Wahl der Morphologie zu einer Steigerung von Effizienzen in optoelektronischen Anwendungen, wie beispielsweise organischen Solarzellen, beizutragen.

Abstract

Time-resolved spectroscopy allows for analyzing light-induced energy conversion and chromophore–chromophore interactions in molecular systems, which is a prerequisite in the design of new materials and for improving the efficiency of opto-electronic devices. To elucidate photo-induced dynamics of complex molecular systems, transient absorption (TA) and coherent two-dimensional (2D) spectroscopy were employed and combined with additional experimental techniques, theoretical approaches, and simulation models in this work.

A systematic series of merocyanines, synthetically varied in the number of chromophores and subsitution pattern, attached to a benzene unit was investigated in cooperation with the group of Prof. Dr. Frank Würthner at the University of Würzburg. The global analysis of several TA experiments, and additional coherent 2D spectroscopy experiments, provided the basis to elaborate a relaxation scheme which was applicable for all merocyanine systems under investigation. This relaxation scheme is based on a double minimum on the excited-state potential energy surface. One of these minima is assigned to an intramolecular charge-transfer state which is stabilized in the bis- and tris-chromophoric dyes by chromphore–chromophore interactions, resulting in an increase in excited-state lifetime. Electro-optical absorption and density functional theory (DFT) calculations revealed a preferential chromophore orientation which compensates most of the dipole moment of the individual chromophores. Based on this structural assignment the conformation-dependent exciton energy splitting was calculated. The linear absorption spectra of the multi-chromophoric merocyanines could be described by a combination of monomeric and excitonic spectra.

Subsequently, a structurally complex polymeric squaraine dye was studied in collaboration with the research groups of Prof. Dr. Christoph Lambert and Prof. Dr. Roland Mitrić at the University of Würzburg. This polymer consists of a superposition of *zigzag* and *helix* structures depending on the solvent. High-level DFT calculations confirmed the previous assignment that *zigzag* and *helix* structures can be treated as J- and H-aggregates, respectively. TA experiments revealed that in dependence on the solvent as well as the excitation energy, ultrafast energy transfer within the squaraine polymer proceeds from initially excited *helix* segments to *zigzag* segments or vice versa. Additionally, 2D spectroscopy confirmed the observed sub-picosecond dynamics. In contrast to other conjugated polymers such as MEH-PPV, which is investigated in the last chapter, ultrafast energy transfer in squaraine polymers is based on the matching of the density of states between donor and acceptor segments due to the small reorganization energy in cyanine-like chromophores.

Finally, the photo-induced dynamics of the aggregated phase of the conjugated polymer MEH-PPV was investigated in cooperation with the group of Prof. Dr. Anna Köhler

at the University of Bayreuth. Our collaborators had previously described the aggregation of MEH-PPV upon cooling by the formation of so-called HJ-aggregates based on exciton theory. By TA measurements and by making use of an affiliated band analysis distinct relaxation processes in the excited state and to the ground state were discriminated. By employing 2D spectroscopy the energy transfer between different conjugated segments within the aggregated polymer was resolved. The initial exciton relaxation within the aggregated phase indicates a low exciton mobility, in contrast to the subsequent energy transfer between different chromophores within several picoseconds.

This work contributes by its systematic study of structure-dependent relaxation dynamics to the basic understanding of the structure-function relationship within complex molecular systems. The investigated molecular classes display a high potential to increase efficiencies of opto-electronic devices, e.g., organic solar cells, by the selective choice of the molecular morphology.

List of Publications

Parts of this thesis have been published in the following references:

Reference [1]:

F. Koch, A. Steinbacher, C. Consani, A. Zitzler-Kunkel, M. Stolte, F. Würthner, and T. Brixner,
The Role of the Dipolar Neighborhood on the Relaxation Dynamics of Multichromophoric Merocyanines,
submitted on April 12, 2016.

Reference [2]:

F. Koch, M. Stolte, D. Bialas, A. Zitzler-Kunkel, A. Steinbacher, T. Brixner, and F. Würthner,
Unraveling the Molecular Structure of Interacting Multichromophoric Merocyanines in Solution,
in preparation, status April 12, 2016.

Reference [3]:

C. Lambert, F. Koch, S. F. Völker, A. Schmiedel, M. Holzapfel, A. Humeniuk, M. I. S. Röhr, R. Mitric, and T. Brixner,
Energy Transfer Between Squaraine Polymer Sections: From Helix to Zigzag and All the Way Back,
J. Am. Chem. Soc. **137**, 7851–7861 (2015).

Reference [4]:

C. Consani, F. Koch, F. Panzer, T. Unger, A. Köhler and T. Brixner,
Relaxation dynamics and exciton energy transfer in the low-temperature phase of MEH-PPV,
J. Chem. Phys. **142**, 212429 (2015).

Further publications which are not related to this thesis:

Reference [5]:

F. Koch, M. Kullmann, U. Selig, P. Nuernberger, D. C. G. Götz, G. Bringmann, and T. Brixner,
Coherent two-dimensional electronic spectroscopy in the Soret band of a chiral porphyrin dimer,
New. J. Phys. **15**, 025006 (2013).

Reference [6]:

P.K. Verma, F. Koch, A. Steinbacher, P. Nuernberger, and T. Brixner,
Ultrafast UV-induced photoisomerization of intramolecularly H-bonded symmetric β-diketones,
J. Am. Chem. Soc. **136**, 14981–14989 (2014).

Reference [7]:

P.K. Verma, A. Steinbacher, F. Koch, P. Nuernberger, and T. Brixner,
Monitoring ultrafast intramolecular proton transfer processes in an unsymmetric β-diketones,
Phys. Chem. Chem. Phys. **17**, 8459–8466 (2015).

Reference [8]:

T. Unger, F. Panzer, C. Consani, F. Koch, T. Brixner, H. Bässler and A. Köhler,
Ultrafast Energy Transfer between Disordered and Highly Planarized Chains of Poly[2-methoxy-5-(2-ethylhexyloxy)-1,4-phenylenevinylene] (MEH-PPV),
ACS Marco Lett. **4**, 412–216 (2015).

The publications listed above have partly been used in this dissertation. The following table itemizes to what extent the different sections of the publications have been reused at which position in this work. The sources of adapted figures are additionally indicated at the end of the corresponding figure captions.

Publication	Usage	Dissertation
Ref. [1]		
p. 1	text partly reproduced and extended	p. 41
p. 2	text reproduced	pp. 43–44
	figure adapted, minor modifications	
pp. 3–9	text reproduced, minor modifications	pp. 51–62
(& S1 in SI)	figures adapted, minor modifications	
p. 10	text partly reproduced and extended	p. 66
Ref. [2]		
pp. 1–3	text reproduced, modified, and extended	pp. 41–42
p. 4	text reproduced, modified, and extended	p. 44
pp. 5–12	text reproduced, minor modifications	pp. 45–51
	figures adapted	
pp. 15–20	text reproduced, minor modifications	pp. 62–67
(& S10 in SI)	figures adapted	
Ref. [3]		
pp. 1–5	text modified, extended	pp. 69–77
	figures adapted, minor modifications	
pp. 5–8	text modified, extended	pp. 78–83
	figures adapted, minor modifications	
pp. 9–10	text reproduced, modified, and extended	pp. 83–85
pp. 5, 15–17	text modified, extended	pp. 77–78
(& S4–S6 in SI)	figures adapted, minor modifications	
Ref. [4]		
pp. 2–11	text modified, extended	pp. 87–101
	figures adapted, minor modifications	
p. 21	table adapted	pp. 92–93
(& S9 in SI)	figure adapted, minor modifications	
pp. 22–23	text modified, extended	pp. 95–96
(& S10–S11 in SI)	figure adapted	

Ref. [3] - Reproduced in part with permission from Journal of the American Chemical Society, 2015, **137**, pp. 7851–7861.

Ref. [4] - Reproduced in part with permission from The Journal of Chemical Physics, 2015, **142**, 212429.

Contents

List of Publications **VII**

1 Motivation **1**

2 Theoretical Background and Experimental Techniques **5**
2.1 Molecular Transitions 5
2.2 Molecular Interactions 8
2.2.1 Exciton Coupling 9
2.2.2 Energy Transfer 16
2.3 Experimental Setup 20
2.4 Femtosecond Pulse Generation 20
2.5 Frequency Conversion for Ultrafast Laser Spectroscopy 23
2.6 Femtosecond Laser Pulse Shaping 25
2.7 Laser Pulse Characterization 26
2.8 Transient Absorption (TA) Spectroscopy 27
2.9 Coherent Two-Dimensional (2D) Spectroscopy 31
2.9.1 Coherent 2D Spectroscopy in Pump–Probe Geometry 33
2.9.2 Coherent 2D Spectroscopy in Box-Geometry 35
2.9.3 Chirp in 2D Spectroscopy 35
2.9.4 Heterodyne Detection 36
2.9.5 Scattered Light 37
2.9.6 Phase Stability 38
2.9.7 Phasing of 2D Spectra 38
2.9.8 Coherent 2D Spectroscopy in TA vs. Box geometry 39

3 Multichromophoric Merocyanines **41**
3.1 Introduction 41
3.2 Unraveling the Molecular Structure 44
3.2.1 Electro-Optical Absorption 45
3.2.2 Density Functional Theory 49
3.3 Relaxation Dynamics of Multichromophoric Merocyanines 51
3.3.1 Relaxation Dynamics of the Mono-Merocyanine **1** 51
3.3.2 Relaxation Dynamics of **2p**, **2m**, and **3** 54
3.3.3 Influence of Excitation Wavelength 55
3.3.4 Coherent 2D Spectroscopy 57

3.3.5 Relaxation Model 59
3.4 Chromophore Interaction and Orientation 62
3.5 Conclusion 66

4 Energy Transfer Between Squaraine Polymer Sections 69
4.1 Introduction 69
4.2 Computations 71
4.3 Transient Absorption 74
4.3.1 Transient Absorption Experiments 74
4.3.2 Global Analysis 77
4.3.3 Target Analysis 78
4.4 Coherent 2D Spectroscopy 82
4.5 Summary and Conclusions 85

5 Relaxation Dynamics in the Low-Temperature Phase of MEH-PPV 87
5.1 Introduction 87
5.2 Results and Analysis 89
5.2.1 Transient Absorption 89
5.2.2 Coherent 2D Spectroscopy 94
5.3 Discussion 96
5.3.1 Population Dynamics 96
5.3.2 Energy Transport and Relaxation 98
5.4 Summary and Conclusions 100

6 Conclusion 103

Bibliography XIII

CHAPTER 1

Motivation

Improvements in polymer chemistry in combination with mass production in the 1950s led to a revolution of plastic materials in society, and paved the way for the so-called “plastic age”. Plastic materials brought along new colored shapes and applications which are indispensable in our everyday lives. The prerequisite for this evolution of plastics relied on the outstanding properties of polymers in comparison to other classes of molecules. Characteristics such as ductility, hardness, and stability combined with a high flexibility in manufacturing allow versatile applications, ranging from plastic bags and toys to affordable high-tech electronics. Additionally, polymer processing is highly efficient concerning resources, energy, cost, and eco-efficiency. The driving force for the continuous improvement of properties and applications based on polymers is provided by chemistry. In the last three decades, especially highly functionalized polymers revolutionized the focus of polymer science. In particular, scientists deal with the question how polymers can contribute to the world’s rising energy demand in a sustainable manner. Since this recent plastic revolution, the application of polymers for a resource-efficient solar-energy conversion is thoroughly investigated.

Polymer solar cells (PSCs), also called “plastic solar cells”, are devices based on semiconducting polymers that can be used to generate electrical power upon light illumination. The used term plastic solar cell already implies characteristics of polymers such as flexibility, transparency, and low weight. These properties motivate applications of solar cells in windows, walls, and flexible electronics, while providing an on-site energy source. Moreover, polymers bring along the customizability on the molecular level and a low-cost production. Therefore, PSCs are highly attractive to compete with solid-state solar cells, which are predominantly based on crystalline silicon. Silicon solar cells require highly purified silicon crystals and a rather complex and energy-intensive production process, which is reflected in their production costs. Hence, an alternative material for energy conversion is sought. Due to these beneficial properties, polymers might be the future choice in solar energy conversion. Nevertheless, the disadvantages of PSCs can not be disregarded. The state-of-the-art energy conversion efficiency of PSCs is approximately only about one third compared to solid-state solar cells [9]. Furthermore, PSCs suffer from photochemical degradation due to the lack of an effective protective coating [10]. The prospect of a flexible device which is inexpensive in production made the challenge to overcome these disadvantages of PSCs an extremely attractive research field throughout the last decades [11]. One of the recent results of intense research are tandem PSCs which achieve efficiencies greater than 10% [12]. Due to the low cost of PSCs, an economic viability could already be realized for PSCs with efficiencies between $10 - 15\%$ [13]. Therefore, further improvements have to be made, including the promotion of charge carrier diffusion and the control of order and morphology [14].

A first step towards systematically optimizing the efficiency of PSCs is to understand the structure-function relationship of polymers on a molecular level. These fundamental insights motivate the preparation of polymers with a specific morphology aiming for enhanced efficiencies.

Ultrafast spectroscopic techniques, such as femtosecond transient absorption (TA) and coherent two-dimensional (2D) spectroscopy, provide the tools to study photo-induced processes in molecular systems, e.g., energy transport, energy transfer, and relaxation dynamics. These observations allow to elucidate the applicability of a given structure, or vice versa, to determine the molecular structure by its properties. For that purpose, especially 2D spectroscopy is a powerful technique as it correlates the excitation energy with the emitted energy of a molecular system. Hence, it discloses the coupling and energy transfer between different energetic states of the system under investigation.

In order to create a basis for the performed experiments in this thesis, Chapter 2 provides a brief overview of basic concepts of the interaction of molecules with light and interactions between molecules themselves. Furthermore, the theoretical concepts and experimental realization of TA and 2D spectroscopy are discussed. Subsequently to this overview, the performed experiments on molecular systems with ascending structural complexity are presented. In this thesis different molecular structures have been studied by the variation of parameters, such as the connection and orientation of chromophores by synthesis, choice of solvent, and temperature.

In the first experiment in Chapter 3, the influence of the substitution pattern on chromophore orientation and relaxation dynamics as well as chromophore interaction is investigated. For this purpose, a systematic study of merocyanine dyes which are chemically linked via a benzene bridge was performed. The mono-, bis-, and tris- merocyanine dyes differ in the substitution position and in the number of chromophores attached to the benzene linker unit. Although not being a polymeric system, this study investigates how the substitution position influences the (relative) orientation of the merocyanine dyes, their relaxation dynamics, interaction, and energy transport between chromophores. These information are highly important as the variation on the molecular level determines optical properties and local superstructures in polymers.

In Chapter 4 squaraine polymers are investigated, which exhibit different local superstructures in solution, namely a *zigzag* and a *helix* structure. The ratio between *zigzag* and *helix* structures within the squaraine polymers is tunable by the choice of the solvent. This tunability allows to compare the influence of the superstructure on the response of polymers to light by studying the polymer in two different solvents, i.e., with primarily the *zigzag* or *helix* superstructure being present. Due to diluted conditions, the interactions and energy transfer within and between different superstructures was studied within single polymer strands, respectively.

The third experiment analyzes the effect of polymers strands which do not only interact with themselves but additionally with other polymers by supramolecular interactions. Hence, in Chapter 5, the polyphenyl vinylene polymer MEH-PPV is studied which tends to form planarized aggregates upon cooling. MEH-PPV has already been soundly investigated under different conditions and studied for applications within solar technology. However, the aggregated phase created within low-temperature conditions has not been studied yet. This experiment allows to analyze the effect of structural properties on photo-induced dynamics within planarized aggregated polymers which arise from highly disordered structures by changing the temperature.

Finally, in Chapter 6 the results and key observations of all performed experiments of this thesis are summarized.

CHAPTER 2

Theoretical Background and Experimental Techniques

This chapter aims at providing a theoretical basis and experimental realization for the ultrafast molecular spectroscopy experiments presented in this thesis. In Section 2.1 photoinduced molecular transitions and excited-energy relaxation processes are described. As this thesis strongly focuses on the effect of interactions between molecules on the relaxation dynamics, Section 2.2 deals with the concept of exciton theory (Subsection 2.2.1) for multichromophoric systems from dimers to polymers. In addition, Subsection 2.2.2 provides common mechanisms in the description of energy transfer between chromophores.

Having described the basic molecular background for this thesis, Sections 2.3–2.9 focus on the experimental realizations which were employed to study ultrafast molecular transitions and interactions. While fundamental physical background and concepts of the optical setups are pointed out, general basics of ultrashort laser pulses are required, which can be found in the literature (see, e.g., Refs. [15–20] for femtosecond pulses in general and Refs. [21–24] for ultrafast spectroscopy). For details of the experimental setups the interested reader is referred to the given references in the corresponding sections. Beginning with an overview of the experimental setup in Section 2.3, the following sections deal with the generation of femtosecond pulses (Section 2.4), frequency conversion of laser pulses for ultrafast spectroscopy (Section 2.5), the basics of a pulse-shaper device (Section 2.6), and pulse characterization (Section 2.7). Subsequently, the ultrafast experiments which were employed in this thesis are described. The concepts of transient-absorption spectroscopy are given in Section 2.8. In Section 2.9 the principles of coherent two-dimensional (2D) spectroscopy are briefly described and both experimental realizations of 2D spectroscopy, employed in this thesis, are compared.

2.1 Molecular Transitions

In order to describe ultrafast light-induced processes within a molecular system it is essential to understand optical transitions in molecules, e.g., the absorption and emission of light. Upon the interaction of a molecule with a photon a transition from an initial energetic state $|\Psi_i^{mol}(\vec{r},\vec{R})\rangle$, which depends on the coordinates of the electrons $\vec{r}$ and of the nuclei $\vec{R}$, with energy ε_i to a final energetic state $|\Psi_f^{mol}(\vec{r},\vec{R})\rangle$ with energy ε_f can occur. These states are separated by the energy $\varepsilon_\gamma = \varepsilon_f - \varepsilon_i$. Depending on the value of ε_γ, possible molecular transitions involve rotational, vibrational, and electronic excitations. The corresponding energies of a molecule are calculated by solving the Schrödinger equation

$$\hat{H}(\vec{r},\vec{R})|\Psi^{mol}(\vec{r},\vec{R})\rangle = \varepsilon|\Psi^{mol}(\vec{r},\vec{R})\rangle, \tag{2.1.1}$$

of the molecular wave function $|\Psi^{mol}(\vec{r},\vec{R})\rangle$. Vibronic transitions involve both electronic and vibrational energy levels of a molecule and can be described by taking into account the electronic wave function $|\Psi^{el}(\vec{r},\vec{R})\rangle$ and the vibrational wave function $|\Psi^{vib}(\vec{r},\vec{R})\rangle$. In condensed phase rotational contributions can be neglected as they cannot be spectrally resolved as no free rotations of the molecules are possible due to the interaction with the solvent. Additionally, spin contributions are omitted as the spin wave functions are orthonormal. Therefore, their integral is either one or zero, which is referred to as “spin selection rule” [25].

By applying the Born-Oppenheimer approximation [26], the molecular wave function can be separated into the electronic and the nuclear contribution

$$|\Psi^{mol}(\vec{r},\vec{R})\rangle \approx |\Psi^{el}(\vec{r},\vec{R})\rangle|\Psi^{vib}(\vec{r},\vec{R})\rangle. \tag{2.1.2}$$

Equation (2.1.2) is valid for adiabatic conditions, i.e., for non-interacting electronic states, for which the coupling elements of nuclear wave functions between different electronic states can be neglected. However, in the case of (conical) intersections [27] of electronic potential energy surfaces different electronic states may interact and cause the Born-Oppenheimer approximation to break down.

In spectroscopy, the interaction of a molecule with light can be calculated by considering the molecular electronic dipole moment operator

$$\vec{\mu} = \int \rho(\vec{r})\vec{r}\mathrm{d}\vec{r} = -e\sum_j \vec{r}_j + \sum_k eZ_k\vec{R}_k, \tag{2.1.3}$$

where $\rho(\vec{r})$ denotes the charge distribution of the molecule, e the elementary charge, $\vec{r}_j$ the location of the j-th electron, Z_k the atomic number and $\vec{R}_k$ the location of the k-th nuclei. The probability per unit time $\frac{dP}{dt}$ for an optical transition between the states $|\Psi_i^{mol}\rangle$ and $|\Psi_f^{mol}\rangle$ is expressed by Fermi's golden rule [28, 29] for optical transitions,

$$\frac{dP}{dt} = \frac{2\pi}{\hbar}\left|\langle\Psi_f^{mol}|\vec{\mu}\cdot\vec{E}|\Psi_i^{mol}\rangle\right|^2 D, \tag{2.1.4}$$

with the reduced Planck constant $\hbar$, the electric field $\vec{E}$, and the density of states (DOS) D. In general, Fermi's golden rule is only applicable if the coupling term is a weak perturbation in comparison to the Hamiltonian $\hat{H}$ of the molecule. In the case of $\varepsilon_i < \varepsilon_f$, the DOS can be described via

$$D = g\delta(\varepsilon_f - \varepsilon_i - \hbar\omega), \tag{2.1.5}$$

where g is the degeneracy of the state $|\Psi_f^{mol}\rangle$ and the Dirac's delta function δ and thus Fermi's golden rule describes absorption. In the case of $\varepsilon_i > \varepsilon_f$ stimulated emission is described, and the DOS is given by

$$D = g\delta(\varepsilon_f - \varepsilon_i + \hbar\omega), \tag{2.1.6}$$

as the molecule has to emit a photon to obey energy conservation. Under the assumption that the molecule is small compared to the photon's wavelength, Eq. (2.1.4) can be written as

$$\frac{dP}{dt} = \frac{2\pi}{\hbar} E_0^2 |\mu_{fi}|^2 D, \tag{2.1.7}$$

with the transition dipole moment $\mu_{fi} = \langle \Psi_f^{mol} | \vec{\mu} | \Psi_i^{mol} \rangle$, such that the electric field caused by the photon is described by the amplitude component E_0 along the $\vec{\mu}$-direction. By combining the Born-Oppenheimer equation [Eq. (2.1.2)] and the electric dipole moment operator in Eq. (2.1.3), μ_{fi} reads

$$\mu_{fi} = \left[-e \sum_j \langle \psi_f^e | \vec{r}_j | \psi_i^e \rangle \right] \langle \psi_f^{vib} | \psi_i^{vib} \rangle, \tag{2.1.8}$$

for vibronic transitions. The factor within the square brackets is called electric dipole transition moment, which determines whether a molecular transition is allowed for an electric dipole interaction. The overlap integral between the vibrational states $|\psi_f^{vib}\rangle$ and $|\psi_i^{vib}\rangle$ is given by the second term. Its absolute square $\left| \langle \psi_f^{vib} | \psi_i^{vib} \rangle \right|^2$ is the so-called Franck-Condon factor. Thus, the greater the overlap of the vibrational part of the wave function in the initial and final state the larger the transition probability for the given vibronic transition, as illustrated in Fig. 2.1a. The oscillator strength for a molecular transition f is defined as

$$f = \frac{8\pi^2 m_e c \tilde{\nu}_{abs}}{3he^2} \mu^2, \tag{2.1.9}$$

with the electron mass m_e, the average reduced absorption energy $\tilde{\nu}_{abs} = \frac{\int \varepsilon d\tilde{\nu}}{\int \frac{\varepsilon}{\tilde{\nu}} d\tilde{\nu}}$, and the speed of light c. Additionally, Eq. (2.1.9) can be reformulated to describe the square of the transition moment

$$\mu^2 = \frac{3hc\varepsilon_0 \ln 10}{2000\pi^2 N_A} \frac{9n}{(n^2+2)^2} \int \frac{\varepsilon}{\tilde{\nu}} d\tilde{\nu}. \tag{2.1.10}$$

Here, h is Planck's constant, N_A Avogadro's number, n the refractive index of the medium, and the electric permittivity in vacuum ε_0.

Subsequent to the theoretical description of absorption and stimulated emission, different observable transitions which occur within the relaxation of a molecule are described qualitatively in the following. Apart from stimulated emission, there are four major pathways for the de-excitation of a molecule. All of these processes can be treated with Fermi's golden rule, however with a distinct (weak) coupling term, other than the electron-photon coupling term $\vec{\mu} \cdot \vec{E}$ used so far. Figure 2.1b depicts an overview of the transitions between electronic states, which is often referred to as Jablonksi diagram [30]. Molecular

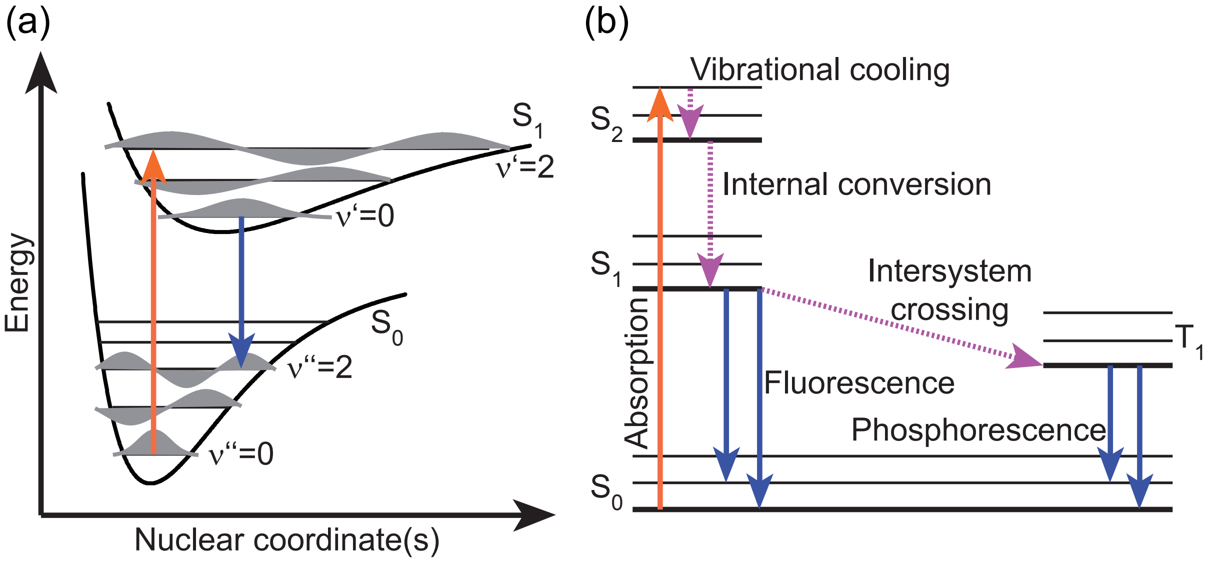

Figure 2.1: (a) Franck-Condon principle for a vibronic (simultaneous electronic and vibrational excitation) transition. In the depicted example the most probable transition occurs from the electronically, and vibrationally relaxed ($\nu'' = 0$), ground state S_0 to the $\nu' = 2$ vibrational level of the first excited electronic state S_1 (orange arrow), as the overlap of the vibrational wave functions (gray) is the largest for this transition. Similarly the highest probability for the fluorescence (blue arrow) from the vibrationally relaxed S_1 is observed towards $\nu'' = 2$ of the S_0. (b) Exemplary Jablonski diagram [30] which depicts an overview of possible non-radiative (dashed magenta arrows) and radiative (solid blue arrows) deactivation processes and molecular transitions within a molecular system upon excitation (orange arrow). A more detailed explanation is given in the text.

transitions include radiative processes, where the energy is released through emission of a photon, and non-radiative de-activation processes, i.e., internal conversion (IC) and inter-system crossing (ISC). In difference to fluorescence and IC, phosphorescence and ISC involve a spin flip (depicted in Fig. 2.1b from the first excited singlet state S_1 to the first excited triplet state T_1). Therefore, a spin-orbital coupling must be present to allow the spin of the electron to flip, which leads commonly to a lower transition rate in phosphorescence compared to fluorescence. The previously mentioned intramolecular transitions occur together with vibrational relaxation processes, which redistribute the vibrational energy by the so-called intramolecular vibrational redistribution (IVR) through the vibrational modes of the molecule. The relaxation energy of IVR is typically dissipated from the molecule towards the environment (i.e., the surrounding molecules or the solvent molecules).

2.2 Molecular Interactions

Molecules do not only act as individual separated systems undergoing molecular transitions upon excitation, as described in the previous section. They also interact with each other. These intermolecular interactions affect the properties of such a molecular ensemble, i.e., the absorption spectrum, and give access to additional relaxation pathways upon excitation. In the following, the concept of exciton coupling is discussed, which describes the change in linear absorption of interacting molecules in dependence on their relative orientation. Subsequently, two models which aim at describing the energy transfer between molecules and chromophores in aggregates or polymers are introduced. The basic understanding of molecular transitions and molecular interactions provide the key tools to investigate multichromophoric systems via their relaxation dynamics and structure (relative orientation).

2.2.1 Exciton Coupling

Small molecular systems, e.g., dimers, and complex molecular systems, e.g., polymers or aggregates, typically show considerable differences in their spectroscopic properties compared to their monomeric (sub-)units. In order to describe observable differences in the respective linear absorption spectra, molecular exciton theory was developed [31–33]. In the following, a simple introduction to this theory in the case of molecular dimers is presented. Subsequently, this approach is adopted and applied also for larger molecular systems. Finally, the effect of distinct relative chromophore orientations on the exciton splitting energy and transition moments is discussed.

Dimers

In the dimer model system, two identical molecules (labeled 1 and 2) with fixed distance and a distinct relative orientation of their transition dipole moments are considered, as depicted in Fig. 2.2a. Both molecules consist of two energy levels (the so-called two-level model system), respectively. For a given Hamiltonian $\hat{H}$, the eigenenergies ε_n^i and the associated eigenstates $|\varphi_n^i\rangle$ of the isolated molecules are given by

$$\hat{H}_n|\varphi_n^i\rangle = \varepsilon_n^i|\varphi_n^i\rangle, \tag{2.2.1}$$

where n represents the molecule (molecule $n = 1$ or $n = 2$) in the eigenstate i with $|\varphi_n^{i=0}\rangle$ for the ground state and $|\varphi_n^{i=1}\rangle$ for the excited state, respectively. The Hamilton operator for the dimer can be written as

$$\hat{H} = \hat{H}_1 + \hat{H}_2 + \hat{V}, \tag{2.2.2}$$

where $\hat{H}_1$ and $\hat{H}_2$ are the Hamilton operators for the isolated molecules, 1 and 2, and $\hat{V}$ is the intermolecular perturbation potential. The latter potential $\hat{V}$ is described with a coulomb potential, which is approximated by the point-dipole-point-dipole terms of the

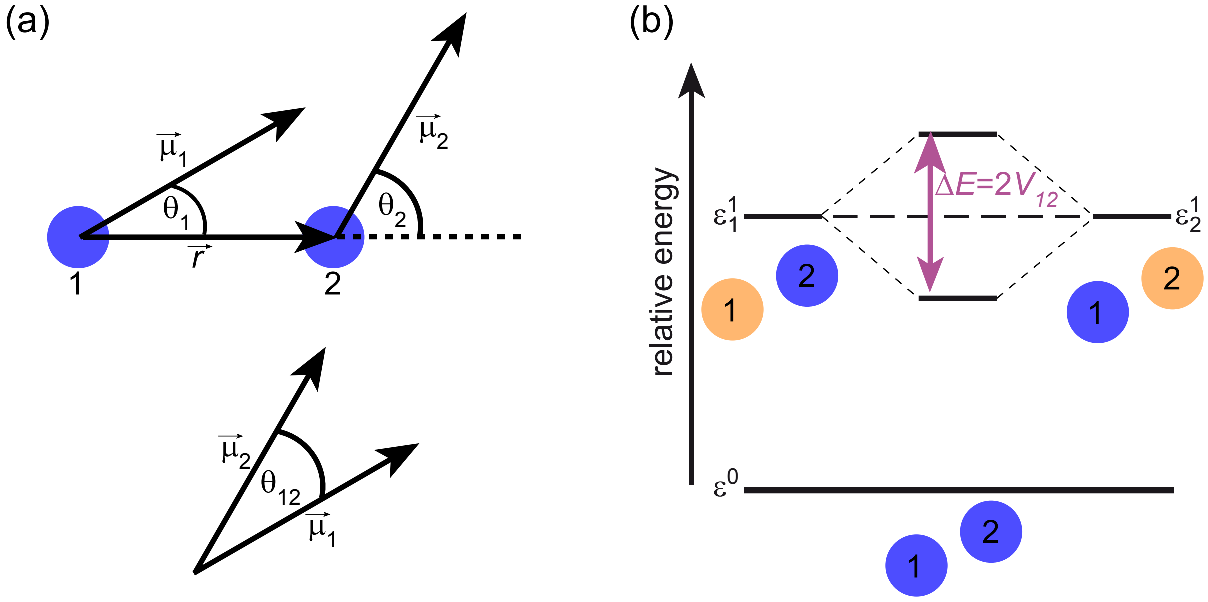

Figure 2.2: (a) Transitions dipole moments ($\vec{\mu}_1$ and $\vec{\mu}_2$) with an arbitrary relative orientation of two molecules (blue circles, 1 and 2) which are separated by the distance $\vec{r}$. The angles θ_1 and θ_2 refer to the angles enclosed by the respective transition dipole moment with the connection axis ($\vec{r}$) of the point-dipoles, and θ_{12} refers to the angle between both individual transition dipole moments. (b) In contrast to non-interacting, singly-excited molecules (orange circles, 1 and 2) with the corresponding energies ε_1^1 and ε_2^1, the interaction of two (identical) molecules leads to an energy splitting (magenta) resulting in two separated absorption bands in the linear absorption spectrum.

point-multipole expansion [34]

$$\hat{V} \approx \frac{\vec{\mu}_1 \cdot \vec{\mu}_2 - 3(\vec{\mu}_1 \cdot \vec{r})(\vec{\mu}_2 \cdot \vec{r})}{r^3}, \tag{2.2.3}$$

with the unit relative position vector

$$\vec{r} = \frac{\vec{r}_2 - \vec{r}_1}{|\vec{r}_2 - \vec{r}_1|}. \tag{2.2.4}$$

Here, $\vec{r}_n$ describes the center of the n-th molecule, for instance the center of mass. Based on the assumption of weak intermolecular interactions the eigenfunction of the dimer is equal to the product of the molecular eigenfunctions according to the Heitler-London approximation [35]. Thus, the dimer's electronic ground-state wave function $|\Psi^0\rangle$ and the lowest lying excited state(s) $|\Psi^f\rangle$ are given by

$$|\Psi^0\rangle = |\varphi_1^0 \varphi_2^0\rangle, \tag{2.2.5}$$

$$|\Psi^f\rangle = c_{f1}|\varphi_1^1 \varphi_2^0\rangle + c_{f2}|\varphi_1^0 \varphi_2^1\rangle, \tag{2.2.6}$$

with the normalized coefficients c_{f1} and c_{f2}. The excited state f of the coupled system is a linear combination of the contributions of individual excited molecules. These relative contributions are determined by the coefficients $c_{f1,2}$. The energy of the ground state of the dimer can be derived from the Schödinger equation

$$\mathcal{E}^0 = \langle \varphi_1^0 \varphi_2^0 | \hat{H} | \varphi_1^0 \varphi_2^0 \rangle, \tag{2.2.7}$$

which factors into

$$\mathcal{E}^0 = \varepsilon_1^0 + \varepsilon_2^0 + \langle \varphi_1^0 \varphi_2^0 | \hat{V} | \varphi_1^0 \varphi_2^0 \rangle. \tag{2.2.8}$$

Here, the ground-state energies of the isolated molecules are given by ε_1^0 and ε_2^0. The last term of Eq. (2.2.8) represents the van der Waals interaction energy between the ground states of molecules 1 and 2, which lowers the ground-state energy of the dimer.

The excited states or one-exciton eigenstates $|\Psi^+\rangle$ and $|\Psi^-\rangle$ can be rewritten as linear combinations of the product states where only individual molecules are excited, i.e., $|1\rangle = |\varphi_1^1 \varphi_2^0\rangle$ in which only molecule 1 is excited and $|2\rangle = |\varphi_1^0 \varphi_2^1\rangle$ in which only molecule 2 is excited. Therefore, in the case of a dimer

$$|\Psi^+\rangle = \cos\Theta |1\rangle - \sin\Theta |2\rangle, \tag{2.2.9}$$

$$|\Psi^-\rangle = \sin\Theta |1\rangle + \cos\Theta |2\rangle, \tag{2.2.10}$$

applies. The mixing angle Θ determines the relative contributions of the product states and is defined as $\Theta = \frac{1}{2} \arctan\left(\frac{V}{\Delta\mathcal{E}}\right)$ with the energy difference $\Delta\mathcal{E} = \varepsilon_1^1 - \varepsilon_2^1$ between the excited-state energies of the isolated molecules and the interchromophore coupling V_{12} (vide infra). In the case of a perfect homodimer (identical molecules) with $\Delta\mathcal{E} = 0$ and $V = \pm|V_{12}|$, Θ reaches the maximum/minimum value of $\Theta = \pm\frac{\pi}{4}$ which leads to

$$|\Psi^+\rangle = \frac{1}{\sqrt{2}} \left(|1\rangle + |2\rangle\right), \tag{2.2.11}$$

$$|\Psi^-\rangle = \frac{1}{\sqrt{2}} \left(|2\rangle - |1\rangle\right), \tag{2.2.12}$$

for $\Theta = -\frac{\pi}{4}$, and for $\Theta = +\frac{\pi}{4}$ to

$$|\Psi^+\rangle = \frac{1}{\sqrt{2}} \left(|1\rangle - |2\rangle\right), \tag{2.2.13}$$

$$|\Psi^-\rangle = \frac{1}{\sqrt{2}} \left(|1\rangle + |2\rangle\right). \tag{2.2.14}$$

Hence, both states $|\Psi^\pm\rangle$ contain the collective excitation of both molecules instead of a localized excitation of a single molecule.

By setting the ground-state energy of the isolated (identical) molecules equal to zero, i.e., $\varepsilon_i^0 = 0$, without loss of generality, the eigenenergies of the excitonic states $|\Psi^\pm\rangle$ are

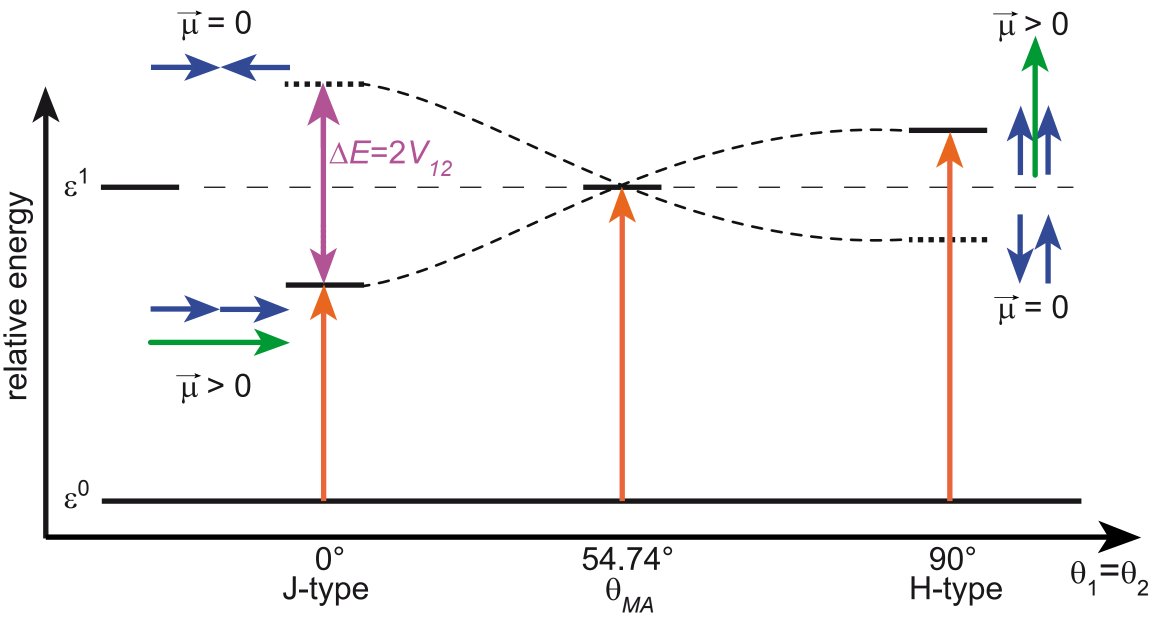

Figure 2.3: Exciton splitting energy (magenta) of a molecular dimer with coplanar ($\theta_{12} = 0°$) and parallel ($\theta_1 = \theta_2$) transition dipoles (blue arrows) in dependence of the angle enclosed by the respective transition dipole moment with the connection axis of the point-dipoles θ_1 (cf. Fig. 2.2a). The direction of the total transition dipole moment is shown by green arrows. Depending on θ_1, two limiting cases, the J-type ($\theta_1 = 0°$), H-type ($\theta_1 = 90°$), and the special case of $\theta_1 = \theta_{MA} = 54.7°$, i.e. the so-called magic angle [36], for which the exciton splitting energy vanisches, can be identified. Adapted from Ref. [31].

given by

$$\begin{aligned} \mathcal{E}^{\pm} &= \langle \Psi^{\pm} | \hat{H} | \Psi^{\pm} \rangle \\ &= \frac{1}{2}(\varepsilon_1^1 + \varepsilon_2^1 + \underbrace{\langle 1|\hat{V}|1\rangle}_{=:V_{11}} \pm \underbrace{\langle 1|\hat{V}|2\rangle}_{=:V_{12}} \pm \underbrace{\langle 2|\hat{V}|1\rangle}_{=:V_{21}} \pm \underbrace{\langle 2|\hat{V}|2\rangle}_{=:V_{22}}). \end{aligned} \tag{2.2.15}$$

For a homodimer $\varphi_1^n = \varphi_2^n =: \varphi^n$, $V_{11} = V_{22}$, $V_{12} = V_{21}$ applies and hence

$$\mathcal{E}^{\pm} = \varepsilon^1 + V_{11} \pm V_{12}, \tag{2.2.16}$$

holds. Equation (2.2.16) indicates that the energies of the excitonic states do not only shift by V_{11} with respect to ε^1, but additionally by $\pm V_{12}$ which leads to two distinct and separated energies ($\mathcal{E}^{\pm}$) split by $2V_{12}$ as shown in Fig. 2.2b. This splitting is called Davydov splitting or excitonic splitting and explains the presence of two absorption bands that are located near the monomeric ε^1-absorption in dimers. The exciton coupling energy V_{12} depends on the orientation and distance of the individual transition moments (μ_1, μ_2)

of the respective chromophores and is given by

$$V_{12} = \frac{1}{4\pi\varepsilon_0}\frac{\mu_1\mu_2}{r^3}\kappa, \tag{2.2.17}$$

where κ is the orientation factor

$$\kappa = \cos\theta_{12} - 3\cos\theta_1\cos\theta_2, \tag{2.2.18}$$

in which θ_{12} defines the angle between the transition moment vectors $\vec{\mu}_1$ and $\vec{\mu}_2$ of the chromophores 1 and 2, respectively. θ_1 and θ_2 are the angles between the respective transition moment vectors and the connection axis of the molecular centers (cf. Fig. 2.2). For two chromophores oriented parallel to each other ($\theta_1 = \theta_2$), the two limiting cases — J-type ($\theta_1 = \theta_2 = 0°$) and H-type ($\theta_1 = \theta_2 = 90°$) arrangement — can be derived by the variaton of θ_1 (cf. Fig. 2.3). In the special case of $\theta_1 = \arccos\left(\frac{1}{\sqrt{3}}\right) = 54.7°$, i.e. the so-called magic angle θ_{MA} [36], the interaction energy even vanishes. By insertion of the values for θ_1 in the three limiting cases in Eq. (2.2.17), it follows

$$\begin{aligned} \text{H-type:} \qquad V_{12} &= \frac{1}{4\pi\varepsilon_0}\frac{\mu_1\mu_2}{r^3} && (2.2.19)\\ \text{J-type:} \qquad V_{12} &= -\frac{1}{4\pi\varepsilon_0}\frac{2\mu_1\mu_2}{r^3} && (2.2.20)\\ \theta_{MA}: \qquad V_{12} &= 0. && (2.2.21) \end{aligned}$$

In general, for the aforementioned two absorption bands the total transition dipole moments (i.e., between ground state and one-exciton states) $\vec{M}_\pm = \langle 0|\vec{\mu}|\Psi^\pm\rangle$ read

$$\begin{aligned} \vec{M}_+ &= \cos\Theta\vec{\mu}_1 - \sin\Theta\vec{\mu}_2, && (2.2.22)\\ \vec{M}_- &= \cos\Theta\vec{\mu}_1 + \sin\Theta\vec{\mu}_2. && (2.2.23) \end{aligned}$$

Again, for a perfect homodimer, the molecules 1 and 2 are equal, i.e., $\Theta = \pm\frac{\pi}{4}$ and $\mu_1 = \mu_2$ holds, which results for $\Theta = -\frac{\pi}{4}$ in transition dipole moments of

$$\begin{aligned} \vec{M}_+ &= \tfrac{1}{\sqrt{2}}2\vec{\mu}_1, && (2.2.24)\\ \vec{M}_- &= 0. && (2.2.25) \end{aligned}$$

Equations (2.2.24) and (2.2.25) show that only one of the two transitions is allowed and will be observed in an absorption spectrum of a perfect homodimer. Since the oscillator strength f is proportional to the square of the transition moment [see Eq. (2.1.9)], it follows that the observed oscillator strength is twice that of the isolated chromophore.

Polymers and Aggregates

In analogy to the previous treatment of a dimer model system, the exciton theory of complex molecular systems, such as polymers and aggregates, are described in the following [32]. In general, for a molecular system consisting of N monomer units, the Heitler-London approximation [35] can be applied, similar to Eq. (2.2.6). The singly-excited states with the lowest energy is given by

$$\Phi^f = \sum_n c_n \varphi_n^f \prod_{m \neq n}^{N} \varphi_m^0, \tag{2.2.26}$$

i.e., as a linear combination of states where only individual molecules are excited. Due to a periodical distribution of the chromophores, Bloch's theorem [37] can be applied and the wave functions can be described as Wannier functions [38]

$$\Psi_k^f = \frac{1}{\sqrt{N}} \sum_{n=1}^{N} e^{2\pi i k n/N} |\Phi_n^f\rangle. \tag{2.2.27}$$

The eigenstate energies of the excited states are given by

$$E_k^f = E^1 + 2V_{12} \left(\frac{N-1}{N}\right) \cos\left(\frac{2\pi k}{N}\right), \tag{2.2.28}$$

where k is a quantum number taking on the values $k = 0, \pm1, \pm2, \ldots, \pm N/2$. The cosine term reaches its extremes for $k = 0$ and $k = \pm N/2$, which lead to the highest and lowest energies of the excitonic manifold. For an infinitely long polymer, the term $(N-1)/N$ approaches unity and therefore a maximum energy difference of $\Delta\mathcal{E} = \mathcal{E}_{\text{max}} - \mathcal{E}_{\text{min}} = 4V_{12}$ is achieved. This energy difference can be intuitively understood by the nearest-neighbor approximation, as each chromophore has two neighbors (no end-effect) instead of only one as in the case of a dimer.

It can easily be shown that Eq. (2.2.28) is valid for dimers. For a dimer $N = 2$ holds, and for $k = 0$ ($k = \pm\frac{N}{2}$) the cosine term becomes 1 (-1) and thus the respective energies are $\mathcal{E}^\pm = \varepsilon^1 \pm V_{12}$, as seen previously in Eq. (2.2.16). The magnitude of the exciton splitting energy $\Delta\mathcal{E}$ in the dimer is $2V_{12}$ while in the polymer $4V_{12}$ holds.

In the following three special cases for the orientation of transition moments within a polymer are considered which are a J-type (Fig. 2.4a), H-type (Fig. 2.4b), and an alternating zigzag (Fig. 2.4c) chain of molecules [32]. For simplicity, in all three cases the orientation of the single chromophores are chosen such that all of the transition dipole moments and main molecular axes are located in one plane.

For the J-type (Fig. 2.4a) and H-type (Fig. 2.4b), each chromophore is aligned parallel to its nearest neighbor (linear chain polymer), meaning that all chromophores are translatory equivalent. Hence, $\theta_1 = \theta_2$ and $\theta_{12} = 0°$ which reduces the exciton coupling energy in

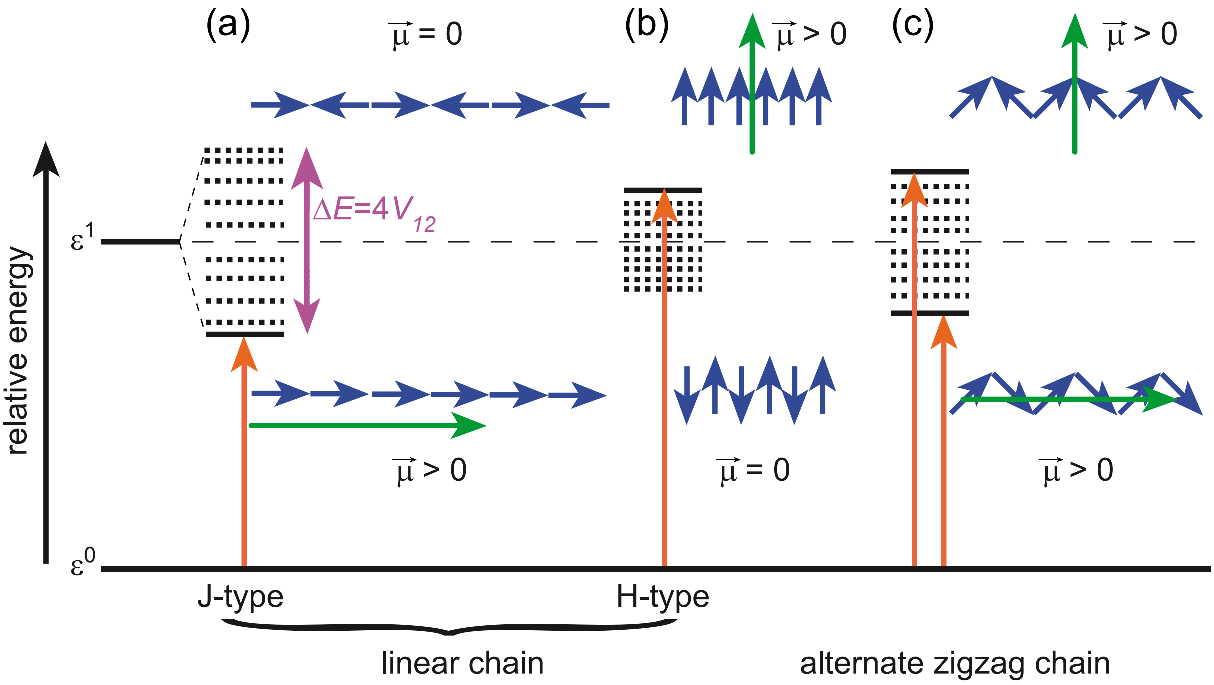

Figure 2.4: Exciton splitting energy (magenta) and allowed transitions (orange arrows to solid energy levels) for a polymer with J-type (a), H-type (b), and zigzag (c) orientated transition dipole moments. The direction of the resulting total transition moment is indicated by the green arrows. Adapted from Ref. [32].

Eq. (2.2.17) to

$$V_{12} = \frac{1}{4\pi\varepsilon_0}\frac{\mu_1\mu_2}{r^3}\left(1 - 3\cos^2\theta_1\right). \tag{2.2.29}$$

For all chromophores parallel to each other, the two limiting cases, H-type ($\theta_1 = 90°$) and the J-type ($\theta_1 = 0°$) arrangement, can be derived by the variation of θ_1. In the special case of $\theta_1 = \arccos\left(\frac{1}{\sqrt{3}}\right) = 54.7°$, i.e., the so-called magic angle θ_{MA} [36], the interaction energy even vanishes. By insertion of the values for θ_1 in the three limiting cases into Eq. (2.2.29), it follows

$$\begin{aligned}
\text{H-type:} \qquad V_{12} &= \frac{1}{4\pi\varepsilon_0}\frac{\mu_1\mu_2}{r^3} && (2.2.30)\\
\text{J-type:} \qquad V_{12} &= -\frac{1}{4\pi\varepsilon_0}\frac{2\mu_1\mu_2}{r^3} && (2.2.31)\\
\theta_{MA}: \qquad V_{12} &= 0. && (2.2.32)
\end{aligned}$$

For identical transition moments and distances, Eqs. (2.2.30) and (2.2.31) display an exciton splitting twice as large for a J-type arrangement than for an H-type arrangement. Furthermore, for an H-type alignment $V_{12} > 0$ while for a J-type arrangement $V_{12} < 0$, which leads to a shift of the absorption to higher or lower energy, respectively. Independent of θ_1, the transition moments for the linear chain polymers into the excited states are $\mu = 0$ for the forbidden and $\mu = \sqrt{N}\mu_1$ for the allowed excited state, where N accounts for the number of chromophores. Due to $f \propto \mu^2$ [cf. Eq. (2.1.9)] the oscillator strength in the polymer has the N-fold value compared to the monomer, which is in agreement with the example of the H-type dimer [cf. Eq. (2.2.24) and Eq. (2.2.25)].

In the case of an alternating zigzag chain of molecules, the transition moments are not parallel but are arranged in a zigzag arrangement (cf. Fig. 2.4c) for which two subsequent chromophores define one unit cell. The angles between the transition moments and the polymer axis are given with respect to θ_1 and are $\theta_2 = 180° - \theta_1$ and $\theta_{12} = 180° - 2\theta_1$. Hence, it follows that

$$V_{12} = -\frac{1}{4\pi\varepsilon_0}\frac{\mu_1\mu_2}{r^3}\left(1 + \cos^2\theta_1\right), \tag{2.2.33}$$

describes the exciton coupling energy.

For the cases of parallel and zigzag arrangement of the transition moments (Fig. 2.4a, b, and c) the exciton band width is $\Delta\mathcal{E} = 2V_{12}$ for a dimer and $\Delta\mathcal{E} = 4V_{12}$ in a polymer (cf. Fig. 2.4). For the polymer, the nearest-neighbor approximation is used, as each chromophore has two neighbors.

The intensity of the absorption band(s) for the alternating zigzag arrangement also depends on the exact geometry. The total transition moments to the lowest and highest exciton states of a dimer or polymer are

$$\vec{M}_+ = \sqrt{N}\vec{\mu}_1\cos\theta_1, \tag{2.2.34}$$

$$\vec{M}_- = \sqrt{N}\vec{\mu}_1\sin\theta_1, \tag{2.2.35}$$

where N again denotes the number of chromophores.

2.2.2 Energy Transfer

Interactions between molecules, being different molecules in the same solution or different centers in the same molecule, may not only lead to changes in the absorption spectrum as described in the previous section, but also to energy transfer from a chromophore/molecule D, called donor, to a second chromophore/molecule A, the acceptor, through dipole coupling. The two most common mechanisms used to describe such energy transfer between distinct sites are depicted in Fig. 2.5, the so-called Förster resonant energy transfer (FRET) [39] and Dexter energy transfer [40].

Figure 2.5a depicts the schematic energy level diagram for FRET. During the absorption process the donor is excited to a higher vibrational level of its first electronically-excited state. From this point the energy is converted by IVR to lower vibrational levels within the same excited state (cf. Sec. 2.1). Subsequently, the donor relaxes to the electronic ground state by spontaneous radiative or non-radiative processes. The excited-state lifetime τ_D of the donor and its relaxation rate k_D is determined by radiative τ_r and non-readiative τ_{nr}

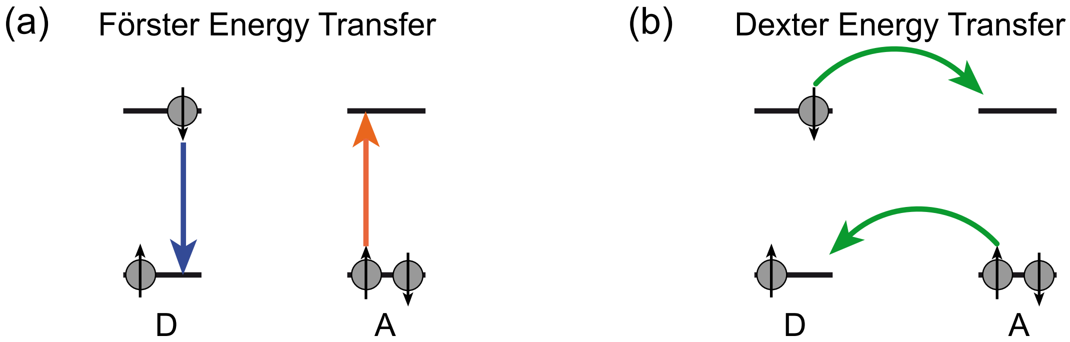

Figure 2.5: Principle of Förster resonant energy transfer (FRET) [39] (a) and Dexter energy transfer [40] (b). In FRET an electronically-excited donor (D) transfers the energy to an acceptor (A) unit, resulting in an excited A. Dexter energy transfer occurs as a concerted transfer within the electronically-excited and ground state of the D and A moiety, respectively, which again results in an excited A. Both mechanisms are based on dipole-dipole coupling between D and A.

deactivation mechanisms in the absence of energy transfer to other chromophores

$$k_D = \frac{1}{\tau_D} = \frac{1}{\tau_r} + \frac{1}{\tau_{nr}}. \tag{2.2.36}$$

Under the assumption that the energy difference for one of these possible deactivation processes of a donor molecule corresponds exactly to a possible absorption transition in a nearby acceptor molecule, with sufficient energetic coupling between these molecules both processes may occur simultaneously, resulting in a transfer of excitation from the donor to the acceptor. This assumption holds if the absorption spectrum of the acceptor overlaps with the fluorescence of the donor, which is typically given due to the broad spectra of polyatomic molecules in solution leading to a sufficient overlap between donor and acceptor transition. Additionally, at least some amount of mutual coupling between the electronic systems is required. Hence, it takes place only over limited distances. The coupling and interaction energy is of dipole-dipole nature, which is inversely proportional to the third power of the distance between donor and acceptor (R_{DA}^3). Thus, the probability of energy transfer which is proportional to the square of the coupling decreases to the sixth power of the distance (R_{DA}^6). A quantitative treatment of the energy transfer process from the donor to the acceptor $k_{DA} := k_{ET}$ leads to [39]

$$k_{DA} = \frac{k_D}{R_{DA}^6} \left[\frac{9 \ln 10}{128\pi^5 N_A} \frac{\Phi_D}{n^4} \kappa^2 \int \bar{I}_\lambda^D \epsilon_A(\lambda) \lambda^4 \mathrm{d}\lambda \right], \tag{2.2.37}$$

with the fluorescence spectrum (normalized to unit area) of the donor $\bar{I}_\lambda^D$, the extinction coefficient of the acceptor $\epsilon_A(\lambda)$, the fluorescence quantum yield of the donor Φ_D and its excited state decay rate k_D, both in the absence of energy transfer. n is the refractive index of the surrounding medium which shields the dipole fields. The orientation factor κ is defined identical to Eq. (2.2.18) as

$$\kappa = \cos\theta_{DA} - 3\cos\theta_D \cos\theta_A, \tag{2.2.38}$$

with the angle θ_{DA} between the two interacting dipole moments $\vec{\mu}_D$ and $\vec{\mu}_A$ of the donor and acceptor, respectively, and θ_D and θ_A are the angles between the respective transition dipole moment vectors and the connection line of the molecular centers. By recalling that the radiative rate constant is given by $k_r = \Phi_D k_D$, a dependence of the transfer rate k_{DA} on the radiative lifetime can be deduced. The shorter the radiative lifetime ($\tau_r = \frac{1}{k_r}$), the higher the transfer rate k_{DA}. A short radiative lifetime correlates with a large oscillator strength of the donor and therefore efficient dipole-dipole coupling. By defining the overlap-integral J as

$$J = \int \bar{I}_\lambda^D \epsilon_A(\lambda)\lambda^4 \mathrm{d}\lambda, \tag{2.2.39}$$

and introducing the Förster radius R_0, which is a characteristic quantity for a given Förster pair (donor and acceptor)

$$R_0^6 = \frac{9\ln 10}{128\pi^5 N_A}\frac{\Phi_D}{n^4}\kappa^2 J, \tag{2.2.40}$$

Eq. (2.2.37) can be rewritten to

$$k_{DA} = k_D \left(\frac{R_0}{R_{DA}}\right)^6. \tag{2.2.41}$$

In the case that donor and acceptor are separated by a distance of $R_{DA} = R_0$, the energy transfer rate equals the excited state decay rate of the donor, i.e., the transfer efficiency Φ_{ET}

$$\Phi_{ET} = \frac{k_{ET}}{k_D + k_{ET}} \tag{2.2.42}$$

reaches 50%.

In general, FRET is a strongly distance-depending mechanism (R^6), which requires overlapping fluorescence spectra of the donor and absorption spectrum of the acceptor (J), and a proper orientation reflected by the orientation factor κ. These characteristics make FRET an extremely powerful model for applications and methods to investigate energy-transfer processes and to derive intermolecular distances in biochemical applications [41].

Nevertheless, its applicability is limited in many investigations of strongly coupled multichromophore systems [42–44]. Some of the limitations can be directly inferred by considering Eq. (2.2.37). The donor and acceptor are approximated as transition point dipoles, which breaks down for intermolecular distances close to the size of individual molecules. For these distances transition charge densities are required rather than transition dipole moments. Moreover, optically dark states, which mediate energy transfer, e.g. in carotenoids, are not captured by the dipole approximation [45]. Additionally, in donor-acceptor dyads, which are covalently bound, through-bond contributions to the interaction have to be taken into account. For donor and acceptor molecules which are coherently coupled aggregates, similar effects have been observed for distances sufficiently small compared to their intra-molecular dimension. Furthermore, the spectral overlap integral J [cf. Eq. (2.2.39)] is calculated by the fluorescence of the donor molecule. Hence, FRET requires that the vibrational relaxation occurs faster than the actual energy transfer to the acceptor because the latter takes place from an equilibrated excited state. For small R_{DA}, the environment surrounding donor and acceptor may no longer be uncorrelated. Thus, a detailed analysis of the donor, acceptor, and solvent modes is necessary to correctly predict the energy transfer rates.

Another limitation of FRET is the inability to account for molecular transitions accompanied by a spin change, because the dipole-dipole interaction does not act on the spin wave functions. If the donor-acceptor distance allows direct orbital overlap and hence FRET is not allowed, energy transfer takes place by direct electron exchange, which was worked out by Dexter [40]. In the so-called Dexter mechanism the excited electron of the donor is transferred from its LUMO (lowest unoccupied molecular orbital) to the LUMO of the acceptor, while simultaneously an electron is transferred from the ground state of the acceptor to the ground state of the donor (see Fig. 2.5b). This corresponds to an energy transfer from donor to acceptor. Hence, energy transfer by the Dexter mechanism is a concerted two electron transfer. The rate of Dexter energy transfer k_{De} is [40]

$$k_{De} = 4\pi^2 cK \cdot Je^{-\frac{2R_{DA}}{L}}, \tag{2.2.43}$$

with the speed of light c, an experimental factor K, taking the geometric orbital interactions into account, and the overlap integral J defined in Eq. (2.2.39). The average Bohr radius L describes the most probable distance between the proton and the electron in a hydrogen atom in its ground state and is defined as

$$L = \frac{4\pi\varepsilon_0\hbar^2}{m_e e^2}. \tag{2.2.44}$$

The distance dependence of k_{De} is exponential, which is reasonable as the electron densities (included in L) of the approximated hydrogen-like orbitals are proportional to $e^{-\frac{1}{R}}$ (with the distance between the particular atom centers R). Besides the overlap of the emission spectra of the donor and the absorption spectra of the acceptor, Dexter energy transfer requires a direct orbital overlap between donor and acceptor. Thus, Dexter energy transfer becomes ineffective with increasing donor-acceptor separation and is typically limited to $R < 10$ Å. In contrast to FRET, a concerted two-electron transfer is not restricted to singlet-singlet energy transfer in Dexter energy transfer. Hence, triplet-triplet energy transfer is allowed because the acceptor provides two electrons with different spin orientation to balance the electron received from the excited donor.

2.3 Experimental Setup

Subsequent to the description of molecular transitions (Sec. 2.1) and interactions (Sec. 2.2), this section discusses the experimental setups which were employed to study ultrafast molecular processes. Figure 2.6 shows a schematic overview of the setups which were used to perform the ultrafast spectroscopy experiments in this thesis. The basic components are a Ti:Sapphire oscillator combined with a chirped-pulse amplifier system (Spectra Physics) followed by a noncollinear optical parametric amplifier (TOPAS White, Light Conversion Ltd), which allows a broadband tunability of the laser frequencies for pump laser spectra in the range from $500 - 1000$ nm. Subsequently, a home-built pulse shaper [48] allows for a manipulation which enables to create pulse sequences for pulse characterization, pulse compression, and for spectroscopic purposes. While pulse characterization for the transient-absorption experiments was performed collinearly with a SHG-crystal in a separate setup, pulse characterization for coherent two-dimensional spectroscopy in box geometry was performed noncollinearly in the setup itself. A mechanical motorized delay stage allows for a variable delay between the pump and the probe pulses up to about 4 ns. For transient-absorption experiments, every second pump pulse was blocked, which was realized by a phase-locked optical chopper. The actual experiments were performed in both, a home-built transient absorption [49] and coherent two-dimensional spectroscopy setup [47], respectively. In transient-absorption individual pump and probe pulses are temporally and spatially overlapped in a quartz flow cell. In the coherent two-dimensional spectroscopy setup four pulse replica are generated, which are again spatially and temporally overlapped in a flow cell containing the sample. Spectra of the employed probe laser pulses were detected by a spectrometer consisting of a spectrograph with two separated entrance slits and a two-dimensional CCD chip (Acton Spectra Pro 2500i equipped with a PIXIS 2K CCD camera). In the following, femtosecond pulse generation (Sec. 2.4), frequency-conversion (Sec. 2.5), laser pulse shaping (Sec. 2.6), and characterization (Sec. 2.7), transient absorption (Sec. 2.8), and coherent two-dimensional spectroscopy experiments (Sec. 2.9) are discussed.

2.4 Femtosecond Pulse Generation

Femtosecond laser pulses can be generated via oscillators consisting of three main components, namely a pump source, a gain medium, and an optical resonator [21]. The pump source serves as the energy source of the oscillator. Atoms or molecules within the gain medium need to be excited to higher-lying energetic states, which can be achieved by an electrical or optical excitation. The second component, the gain medium provides photons due to radiative relaxation processes of excited atoms or molecules to an energetically lower state (see Fig. 2.1b). Therefore, the energetical characteristics of the gain medium determines which longitudinal modes (i.e., modes along the propagation direction) are amplified and which pulse duration is achievable due to the spectral amplification width.

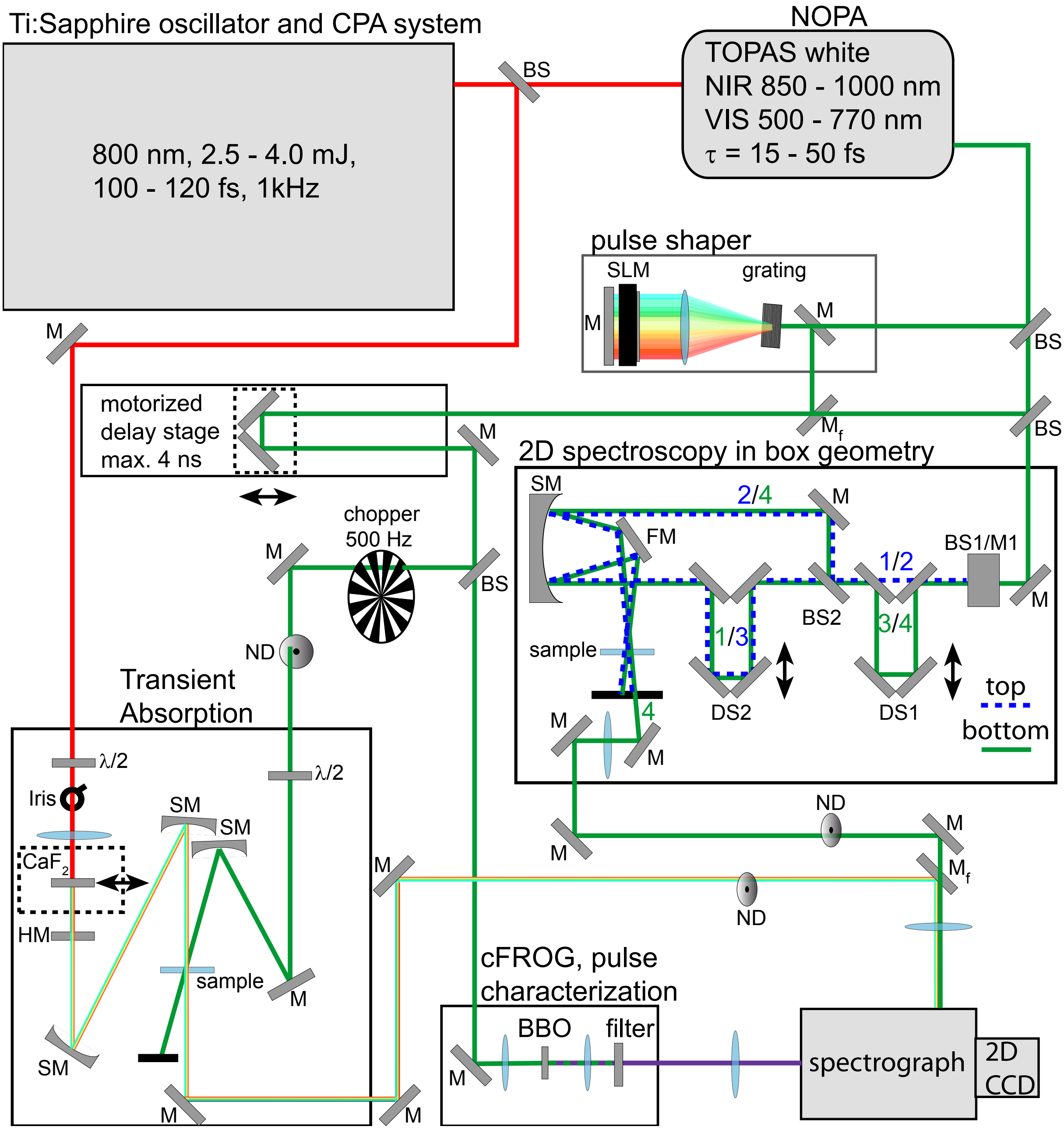

Figure 2.6: Schematic overview of the setups used for the ultrafast spectroscopy experiments presented in this thesis. The essential components include a Ti:Sapphire amplifier as the light source, frequency conversion by a NOPA, pulse shaping, pulse characterization, temporal pulse delay, transient absorption and coherent two-dimensional spectroscopy, and a spectrometer. Employed optical elements comprise lenses, beam splitters (BS), mirrors (M), flipped mirrors (M_f), neutral density filters (ND), a half-wave plate ($\frac{\lambda}{2}$), a hot mirror (HM), a folding mirror (FM), and spherical mirrors (SM). Partly adapted and modified from Refs. [46, 47]. Detailed descriptions are given in the text.

The third component is a resonator, which basically consists of two mirrors. These mirrors repeatedly reflect the emitted photons of the gain medium. Thus, a photon travels through the gain medium many times and stimulates the emission of further photons in the direction of itself. Still, to create short laser pulses an additional requirement has to be fulfilled. A fixed-phase relation between the longitudinal modes has to be induced by so-called mode-locking. At one point in time the “phase-locked” or “mode-locked” longitudinal modes superpose and add up to a short light pulse. Mode-locking can be induced either actively by electro-optical modulators or a Pockels cell, or passively by the Kerr-lens effect [17, 50, 51]. The Kerr-lens effect is an intensity-dependent effect, therefore, it causes an effective reflection of only ultrashort pulses with high peak intensities, whereas the continuous-wave (cw) modes are suppressed. Besides these three essential components of an oscillator, a prism pair is required to compensate the dispersion introduced by the gain medium.

All femtosecond experiments in this work were performed with a Ti:Sapphire oscillator (Ti:Sa) and regenerative amplifier [52] as a laser source. As a pump source a cw neodymium-doped yttrium orthovanadate (Nd:YVO_4) diode laser is used, which excites the gain medium, a titanium-doped sapphire (Al_2O_3). The repetition rate of the Ti:Sa oscillator is 80 MHz, which is determined by the mode spacing, i.e., the length of the optical resonator, with an output wavelength centered around 800 nm due to the amplification characteristics of the titanium-doped sapphire [17].

For molecules which do not absorb at 800 nm, it is essential to tune the frequency of the laser pulses. For this frequency conversion of the oscillator output typically higher pulse energies are required (cf. Sec. 2.5), which can be fulfilled with the help of chirped-pulse amplification (CPA) [53–55]. A typical CPA setup consists of three components, namely a stretcher, a regenerative amplifier, and a compressor. The stretcher and compressor consist of a grating pair which introduce a positive or negative chirp, respectively [56]. Chirp on pulses reduces the peak pulse intensity and is essential to avoid photo-damage of the gain medium. The stretcher applies a positive chirp leading to ≈ 1 ns pulse duration in the gain medium. Furthermore, as the compressor introduces a negative chirp, the compressor compensates the previously applied positive chirp by the stretcher and leads to nearly bandwidth-limited pulses with a higher peak energy of several millijoule. The repetition rate of 80 MHz is thus too high as subsequent pulses might temporally overlap for such high chirp values and lead to undesired interference effects. Therefore, the seed pulses from the oscillator need to be picked at a lower repetitation rate by a Pockels cell. In the employed laser sytem this pulse picking is performed at a repetition rate of 1 kHz and leads to a temporal and spatial overlap with a nanosecond pump pulse of a neodymium-doped yttrium lithium fluoride (Nd:YLF) laser in the Ti:Sa crystal of the CPA system. The achieved output pulses have a duration of $100 - 120$ fs, with a repetition rate of 1 kHz, and an output pulse energy of $2.5 - 4$ mJ which allows ultrashort spectroscopy and frequency conversion in subsequent processes that fit the requirements of the investigated molecules.

2.5 Frequency Conversion for Ultrafast Laser Spectroscopy

Studying molecular processes such as relaxation dynamics (Sec. 2.1) and energy transfer (Subsec. 2.2.2) requires a temporal resolution which is faster than these processes, i.e., on the order of tens of femtoseconds. The theoretical achievable minimal pulse duration is given by the bandwidth limit or Fourier limit [17] of a laser pulse

$$\tau_p \Delta\omega \geq 2\pi c_b, \tag{2.5.1}$$

with the temporal τ_p and spectral $\Delta\omega$ full width at half maximum (FWHM) of the intensity profile of the laser pulse, respectively. The constant c_b has different values for different types of spectral profiles, e.g., $c_b = \frac{4\ln 2}{2\pi} = 0.441$ for a Gaussian spectrum.

Apart from a high temporal resolution, it is necessary to tune the output laser pulses to frequencies which match the absorption of the studied molecules. Frequency conversion for the respective spectroscopic requirements can be performed by exploiting light-matter interactions. As all media are composed of charged particles on a microscopic scale, they respond to electromagnetic waves which propagate through them. The electromagnetic manifestation of this response is called polarisation P and modifies the applied field, as it is superimposed on it. The way a medium responds depends on how strong it is disturbed, which can be described by [17, 51, 57]

$$P = \epsilon_0 \left[\chi^{(1)} E_1 + \chi^{(2)} E_1 E_2 + \chi^{(3)} E_1 E_2 E_3 + \ldots + \chi^{(n)} E_1 \ldots E_n\right]. \tag{2.5.2}$$

Equation (2.5.2) includes n interactions ($i \leq n$) with the incident light fields E_i, the n-th order susceptibility $\chi^{(n)}$ of the nonlinear material, and the permittivity of vacuum ϵ_0. By considering that $\chi^{(2)} = 0$ in isotropic media, $\chi^{(3)}$ is the lowest nonlinear ($n > 1$) contribution. An exception are birefringent media for which $\chi^{(2)} \neq 0$. Due to nonlinear response of nonlinear media it is possible to convert the laser pulse frequency to other spectral regions, which is discussed in the following.

For the generation of the laser pulses in the ultrafast experiments several nonlinear processes were employed. Figure 2.7 displays an overview of nonlinear processes for frequency conversion of femtosecond laser pulses [58]. Second-harmonic generation (SHG, Fig. 2.7a) creates laser light with twice the frequency of an incident pulse [59]. In this process, a single fundamental beam with the frequency ω_1 is doubled in frequency to achieve $\omega_3 = 2\omega_1$. Moreover, SHG can be carried out in a noncollinear way when two beams of the same frequency ($\omega_1 = \omega_2$) are superimposed temporally and spatially in a χ^2-medium of adequate crystal symmetry.

By overlapping two pulses of different frequencies ($\omega_1 \neq \omega_2$) in an appropriate nonlinear medium of the right orientation either the sum of the frequencies ($\omega_3 = \omega_1 + \omega_2$) by sum-

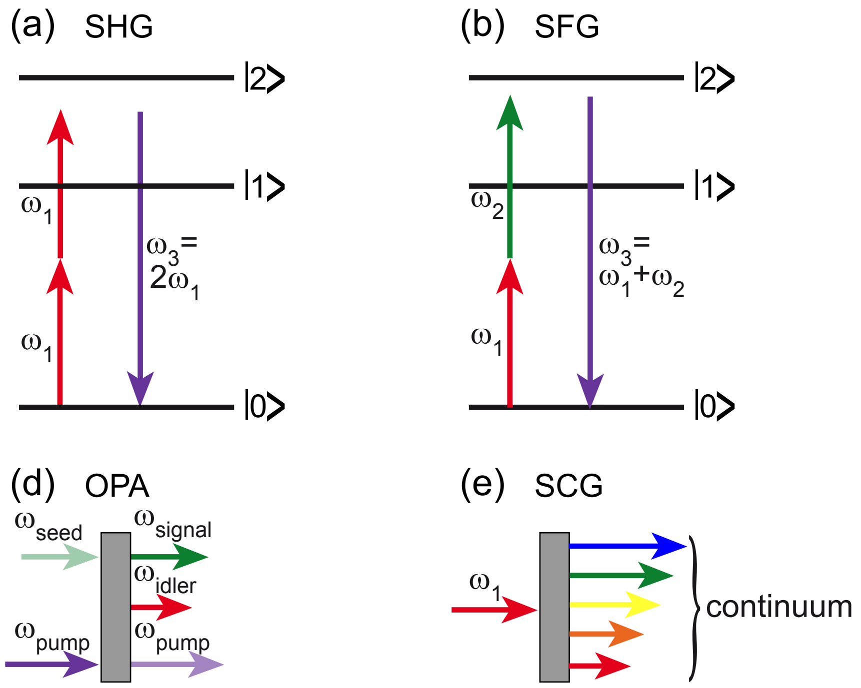

Figure 2.7: Nonlinear optical processes for frequency conversion, such as second harmonic generation (SHG, a), sum frequency generation (SFG, b), difference frequency generation (DFG, c), optical parametric amplification (OPA, d), and supercontinuum generation (SCG, f). See text for a detailed discussion of the nonlinear processes shown. Figure partly adapted from [58].

frequency generation (SFG, Fig. 2.7b) or the difference frequency ($\omega_3 = \omega_1 - \omega_2$, with $\omega_1 > \omega_2$) by difference-frequency generation (DFG, Fig. 2.7c) can be achieved.

In optical parametric amplification (OPA, Fig. 2.7d) a seed pulse is amplified by a pump pulse of higher energy and frequency. The output pulses of this process are an amplified signal pulse with $\omega_{signal} = \omega_{seed}$, an attenuated pulse with ω_{pump}, and an idler pulse with ω_{idler} being lower in frequency than that of the seed pulse. Optical parametric amplification provides an efficient process to create laser pulses for experiments in the visible regime. In such experiments, one part of the fundamental beam (800 nm output pulses of the Ti:Sa amplifier system) is frequency-doubled in a β-barium-borate (β-BaB_2O_4, BBO) crystal to obtain 400 nm pulses. Subsequently, these frequency-doubled pulses are overlapped with a broad white-light supercontinuum (described below) in another BBO crystal. Due to the orientation of the second BBO crystal and by adjusting the temporal overlap between the pump and the supercontinuum, different spectral parts of the seed supercontinuum are amplified for which the wavelength bandwidth phase matching is fulfilled [17, 60–62]. In this process an additional idler beam is generated (cf. Fig. 2.7d). Depending on the desired spectral bandwidth of the amplified signal pulse either collinear or noncollinear optical parametric amplifiers (NOPA) can be utilized. In a noncollinear arrangement of seed and pump pulses a broader amplification bandwidth can be generated. To achieve sufficiently high pulse energies for ultrafast spectroscopy (N) OPAs often use a second amplification stage.

Many transparent materials like sapphire (Al_2O_3) and calcium fluoride (CaF_2) show self-phase modulation (SPM) as a third-order response to an intense light field. The high intensity of the input pulse changes the temporal phase by varying the nonlinear refractive index of the medium (“optical Kerr effect”). Therefore, the instantaneous frequency is altered, leading to a spectrally broadened output pulse. Self-phase modulation is only one of the dominant processes in spectral broadening allowing for supercontinuum generation (SCG, Fig. 2.7e). The whole process of SCG is not fully understood yet as many other effects, e.g., self-steepening, Kerr lensing, material dispersion, and plasma formation have to be taken into account as well [63–66].

White-light supercontinua are typically used as seed pulses for (N)OPAs and as probe pulses for broadband optical probes in transient absorption spectroscopy. The spectral and temporal shape of the white-light continuum strongly depends on the pulse energy, the central frequency ω_1, pulse length as well as the photon flux per area of the pump pulse, and the nonlinear medium itself.

2.6 Femtosecond Laser Pulse Shaping

Femtosecond pulse-shaper devices provide the opportunity to manipulate the temporal and spectral properties of an ultrafast laser pulse [67–69]. Such devices are capable of modulating the pulse duration and even allow the generation of complex pulses, e.g., a sequence of laser pulses. In principle, a pulse-shaper device is based on a spatial separation of the frequency components of an ultrafast pulse. One option to perform this task are dispersive elements such as a grating or a prism. The resulting spatially separated frequency components can be temporally delayed against each other by the application of a frequency-dependent phase modulation [70]. Alternatively, a “spatial separation” can be realized with chirped pulses for which different frequency components are present at different positions in space along its propagation direction due to its temporal profile. Hence, different frequency components of a laser pulse are modulated at respective spatial positions, which is the working principle in acousto-optical modulators [71–75].

In this work, spatial frequency separation was employed by a grating in a pulse-shaper device with a liquid crystal display (LCD) in $4f$-geometry. The pulse-shaper device, which is explained briefly in the following (for experimental details see Ref. 48), was utilized for pulse compression, pulse characterization, and 2D spectroscopy (see Subsec. 2.9.1). The spectral components of an incoming beam are separated via a transmittive grating, which is located of the distance f of a focusing medium, i.e., a focusing mirror, which collimates the beam. In an additional distance of its focal length f the LCD is located. Depending on the applied voltage in single pixels of the LCD the orientation of liquid crystals can be varied which leads to a different refractive index within a pixel for the transmitted beam. Hence, applying a distinct frequency-dependent phase value for the ultrashort pulse. Subsequently to the phase-shaping of the LCD, the spectral components are refocused and recombined by a second lens and an additional grating. Such a symmetric implementation of the zero-dispersion compressor is also called $4f$-setup.

Additionally to pure phase shaping, independent phase and amplitude shaping is possible by employing a two-mask LCD [76]. The modulation axis of the LCD arrays is tilted by +45° and −45° with respect to the polarization of the incoming light, which is ensured by a linear polarizer before the LCD arrays. Linearly polarized light can be considered as a superposition of two orthogonal linearly polarized components. Thus, the two layers affect these two components independently and allow an arbitrary phase retardance of the two components. The resulting elliptically polarized and phase-shaped pulses after the two layers can be converted back to linearly polarized phase- and amplitude-shaped pulses by a second linear polarizer.

The utilized pulse-shaper device in this thesis is slightly modified in comparison to a zero-dispersion compressor setup [48]. The second mirror and grating were replaced by a folded mirror at the Fourier plane, which is called folded $4f$ setup. Hence, the LCD, consisting of two layers of 640 pixels (SLM-640, CRI), was displaced out of this plane, into the recollimated beam. Additionally, a cylindrical mirror was employed instead of a cylindric lens to avoid dispersion of the spectrally broad laser pulse.

2.7 Laser Pulse Characterization

The nonlinear processes described in Sec. 2.5 cannot only be used to generate electric fields for the actual experiment, but also provide the option to characterize them. Several methods allow a purely time-domain or frequency-domain characterization of laser pulses, e.g., intensity autocorrelation or spectral interferometry, respectively. A mixed time-frequency characterization is achieved by frequency-resolved optical gating (FROG) [77–79]. Pulse duration, spectrum, time-bandwidth product, and the value of the phase function can be determined via the FROG approach, while a few ambiguities remain depending on the FROG method [79].

Commonly, a second-harmonic FROG setup is implemented by spatially and temporally overlapping the unknown pulse with a copy of itself noncollinearly in a nonlinear medium (cf. Fig. 2.8a) in the same way as for an intensity autocorrelation. By detecting the corresponding nonlinear signal frequency-resolved, a phase-sensitive feedback is gained. The first pulse serves as a time gate for its copy by shifting one pulse continuously with respect to the other. The noncollinear geometry results in a background-free signal because the conservation of momentum leads to a signal emitted into the direction $\vec{k}_S = \vec{k}_1 + \vec{k}_2 \neq \vec{k}_1 \neq \vec{k}_2$, since $\vec{k}_1 \neq \vec{k}_2$. A FROG-trace $I_{FROG}^{SHG}(\omega, \tau)$ is measured by a systematic variation of the relative time delay between the two pulses τ, leading to

$$I_{FROG}^{SHG}(\omega, \tau) = \left| \int_{-\infty}^{\infty} E(t)E(t-\tau)e^{-i\omega t}\mathrm{d}t \right|^2, \tag{2.7.1}$$

which resolves the signal as a function of frequency and time delay. Subsequently to the measurement, the pulse is reconstructed by different iterative algorithms, allowing the identification of the electric field which generates the respective FROG-trace [80].

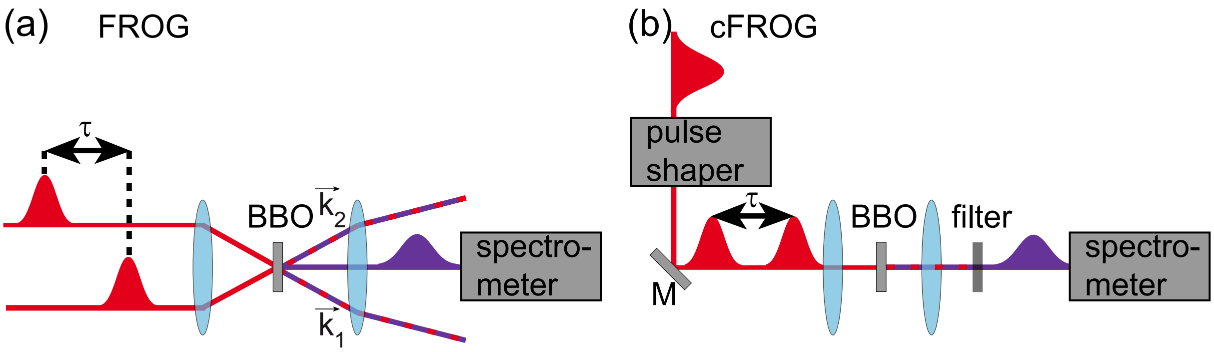

Figure 2.8: Scheme of a noncollinear SHG-FROG (a) and a collinear SHG-FROG (cFROG, b). In (a), two laser pulses (red pulses) from different directions create a background-free SHG signal (purple pulse) in the direction $\vec{k}_S = \vec{k}_1 + \vec{k}_2$. In (b), a double-pulse (red pulses) creates a SHG signal (purple pulse), which copropagates with the initial fundamental pulses (not explicitly shown). The latter fundamental needs to be spectrally filtered out in the experiment.

The calculation of I^{SHG}_{FROG} is repeated iteratively for different fields until calculation and experiment agree within the chosen convergence criteria [80].

While the generation of a pulse copy is easily achievable in theory, experimental limitation may favor a collinear FROG (cFROG) [81, 82] as depicted in Fig. 2.8b. The obtained signal in cFROG

$$I^{SHG}_{cFROG}(\omega,\tau) = \left| \int_{-\infty}^{\infty} \left[E(t) + E(t-\tau)\right] e^{-i\omega t} \mathrm{d}t \right|^2, \tag{2.7.2}$$

is no longer background free, as SHG contributions resulting from only one of the two pulse copies are emitted into the same direction. A cFROG requires the generation of collinearly propagating double pulses with a variable time delay τ, i.e., typically via a pulse shaping device [83, 84]. After the extraction of the term in Eq. (2.7.1) of the cFROG trace in Eq. (2.7.2), by low-pass Fourier filtering and subtraction of the permanent offset at long delay times the desired FROG trace is achieved. Hence, the pulse reconstruction can be performed by the same algorithms as for the noncollinear FROG.

2.8 Transient Absorption (TA) Spectroscopy

The principle of transient absorption (TA) spectroscopy, a special form of the pump–probe technique, is schematically illustrated in Fig. 2.9. The corresponding experimental setup is described in detail in Ref. [49]. In TA, an excitation pulse, typically labeled "pump pulse", excites a molecular sample to an excited state, which exhibits a different absorption spectrum than the molecular ground state. This difference is measured by a spectrally-resolved detection of the "probe pulse", which can be delayed by the pump-probe delay T (labeled population time in 2D spectroscopy), respective to the pump pulse.

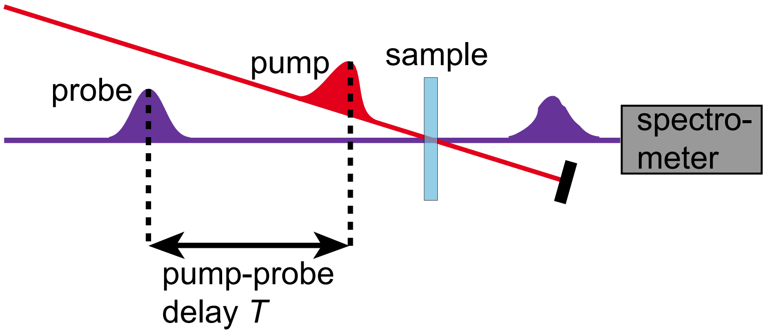

Figure 2.9: In TA, an excitation, or pump pulse (red pulse) excites the sample. The pump-induced difference in absorption is measured by a time-delayed probe pulse (purple pulse) as the spectral change of the probe pulse with and without a present excitation pulse. By measuring this change of absorption for different pump–probe delays T, the relaxation dynamics of a molecular system can be inferred.

By blocking every consecutive excitation pulse, the spectra of the probe pulse is measured with $[I^{*}(\lambda,T)]$ and without a pump pulse $[I(\lambda,T)]$. In this case a shot-to-shot detection scheme is beneficial due to the higher correlation between subsequent laser pulses [85, 86]. The change of absorption, which is often also called the change of optical density (ΔOD), is calculated via

$$\Delta OD(\lambda,T) = -\log\left(\frac{I^{*}(\lambda,T)}{I(\lambda,T)}\right) = \epsilon(\lambda)c(T)L, \tag{2.8.1}$$

and is directly connected to Lambert–Beer's law [87] by the extinction coefficient $\epsilon(\lambda)$, the time-dependent concentration $c(T)$, and the optical path length L. Upon excitation, different molecular transitions lead to changes in absorption, due to different contributions, namely ground-state bleach (GSB), stimulated emission (SE) and excited-state absorption (ESA), as illustrated in Fig. 2.10. As molecules in the ground state are excited by the pump pulse, the probe pulse can only excite remaining molecules from the ground state. Consequently, less light of the probe pulse is absorbed, which is reflected in a negative GSB contribution ($\Delta OD < 0$). With evolving time the GSB contribution decreases due to molecular relaxation processes, e.g., fluorescence or non-radiative relaxation pathways (cf. Sec. 2.1), called GSB recovery (GSBR). Furthermore, due to the interaction with the probe pulse, previously excited molecules can be stimulated by the probe to emit a photon at a distinct wavelength. This process is referred to as SE and has a negative contribution ($\Delta OD < 0$) as more photons are measured in the presence of a preceeding pump pulse. Positive contributions ($\Delta OD > 0$) can be observed for ESA as the previously excited molecules can be re-excited by the probe pulse to energetically-higher lying states. Additionally, a positive contribution can also be observed for a chemical reaction with a photo-induced product, e.g., an isomerization, for which typically a GSB of the initial excited reactant remains and the new absorption of the created product appears, which is called product absorption (PA).

Data interpretation in TA spectroscopy is performed by factorizing the measured ab-

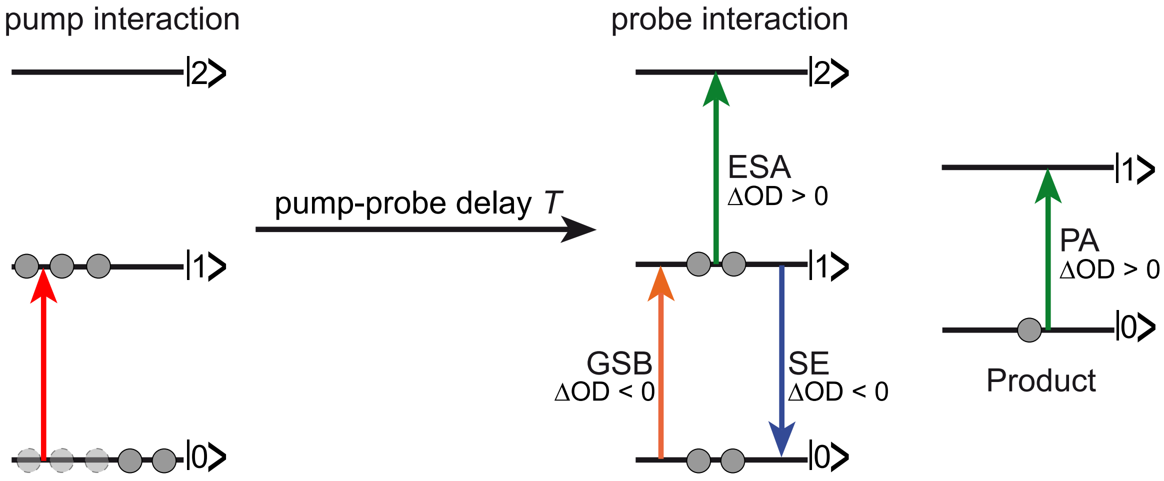

Figure 2.10: Signal contributions in TA. Upon interaction with the pump beam molecules are excited from the ground state ($|0\rangle$) to the excited state (in this case the first excited state $|1\rangle$). Subsequently, different (new) molecular transitions are accessible by the probe pulse which are classified as ground-state bleach (GSB), stimulated emission (SE), excited-state absorption (ESA), and in the case of a photo-induced reaction, product absorption (PA). Additionally, the sign of the observed changes in optical density (ΔOD) as defined via Eq. 2.8.1 are depicted next to each contribution.

sorption [$\Delta OD(T,\lambda)$] into

$$\Delta OD(T,\lambda) = \sum_{i=0}^{n-1} \epsilon_i(\lambda) c_i(T) L. \tag{2.8.2}$$

In this description, n chemical species interact with an external light-field. The index i identifies the portion of molecules in the species i with an energetic ascending order. Different relaxation models to analyze the transient absorption data are illustrated in Fig. 2.11. On the basis of mono-exponential decaying concentration profiles, the concentration of each species can be parametrized by a mono-exponential decay

$$c_i^{para}(T) = \exp(-k_i T), \tag{2.8.3}$$

with the rate k_i for the transition from the i-th species to the ground state. The reciprocal of the rate reflects the lifetime τ_i of the i-th species $\tau_i = \frac{1}{k_i}$. The mono-exponential decaying concentration profiles refer to a parallel (para) model, which is often called decay model. Applying a sequential rate model (seq) leads to the concentration profiles

$$c_i^{seq}(T) = \sum_{j=1}^{i} b_{ji} \exp(-k_j T), \tag{2.8.4}$$

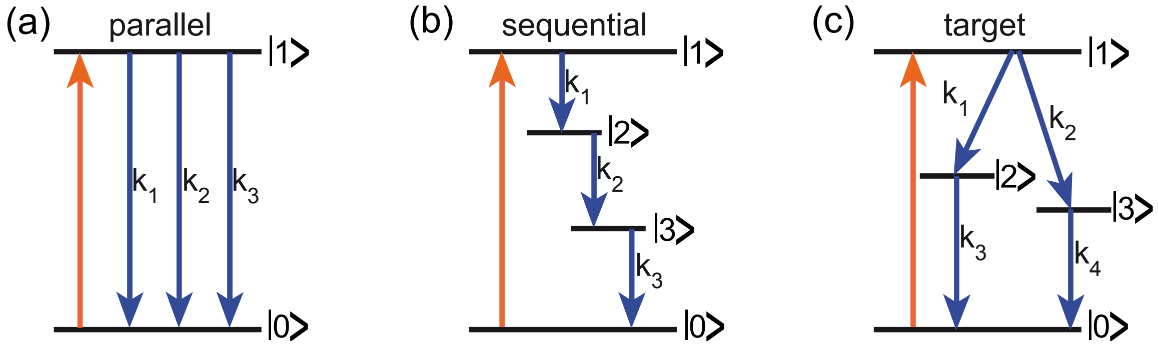

Figure 2.11: Different relaxation models for the description of deactivation processes in molecules. In the parallel model (a) the relaxation occurs from the same excited state, while the sequential relaxation (b) takes place stepwise from state to state. As molecules often relax in more complicated relaxation schemes (mixtures of parallel and sequential relaxation processes) a target model (c) is necessary to describe the (most probable) deactivation scheme which agrees with the experimental spectroscopic observations.

with the coefficients $b_{ji} = \prod_{m=1}^{i-1} k_m / \prod_{n=1,\neq j}^{i} (k_n - k_j)$. In the description of a sequential model, the excitation evolves from one state into the next state and the model is therefore often called evolution model.

The fitting function for the time-dependent change in absorption in a parallel rate model $\Delta OD^{para}(T, \lambda)$ (Fig. 2.11a) reads

$$\Delta OD^{para}(T, \lambda) = \sum_{i=0}^{n-1} DADS_i(\lambda) c_i^{para}(T), \tag{2.8.5}$$

where the free fitting parameter $DADS_i(\lambda)$ is the decay-associated difference spectrum of the i-th species. In the sequential model (Fig. 2.11b), the time-dependent change in absorption $\Delta OD^{seq}(T, \lambda)$ reads

$$\Delta OD^{seq}(T, \lambda) = \sum_{i=0}^{n-1} EADS_i(\lambda) c_i^{seq}(T), \tag{2.8.6}$$

with the free fitting parameter $EADS_i(\lambda)$ which is called evolution-associated difference spectrum of the i-th species. There is a linear relation between EADS and DADS, thus only one fitting process needs to be executed to determine both difference spectra (DS) [88]. If a target model (*target*) other than parallel or sequential model is fitted to the data (Fig. 2.11c) then the fitting function reads

$$\Delta OD^{target}(T, \lambda) = \sum_{i=0}^{n-1} SADS_i(\lambda) c_i^{target}(T), \tag{2.8.7}$$

with the free fitting parameter $SADS_i(\lambda)$, called species-associated difference spectrum of the i-th species. A target model fit can test whether or not a particular de-activation pathway of the measured system can be represented with that model. The computation of DADS and EADS is also referred to as global analysis, due to fitting of kinetics for many wavelengths instead of fitting kinetics at a single wavelength (local fit). The computation of SADS is also referred to as target analysis.

In a TA experiment, typically a white-light continuum (cf. Sec. 2.5) is employed as a probe pulse which allows to detect the relaxation dynamics over a broad spectral range ($\approx 350 - 770$ nm) [89, 90]. However, white-light probe pulses are strongly chirped. Hence, the different wavelengths of the continuum interact at different times with the sample. These variations in time can be corrected easily by measuring TA data in the pure solvent. For overlapping pump and probe pulses coherent non-resonant processes (e.g., cross-phase modulation [91–93], two-photon absorption [93, 94], and stimulated Raman processes [89]) lead to the formation of the "coherent artifact" [89, 90, 94]. Raw data is corrected by fitting the curvature of the coherent artifact with a polynomial function and shifting the correct arrival times for each wavelength based on the fit. In this thesis, data correction and analysis was performed by the software package Glotaran and TIMP [88, 95, 96]. Additionally to the chirp-correction, Glotaran provides the option to analyze the instrument response function [$IRF(T)$] by convoluting the results of the rate models with a Gaussian function, whose parameters are free fitting parameters.

2.9 Coherent Two-Dimensional (2D) Spectroscopy

Coherent two-dimensional (2D) spectroscopy can be qualitatively regarded as an extension to the previously described TA, by spectrally resolving the excitation energy. In the following, the vectorial character of all electric fields is neglected to simplify the description. The lowest order polarization which is relevant for both, TA and 2D spectroscopy, is the third-order polarization

$$\begin{aligned} P^{(3)}(\vec{r},t) = &\int_0^\infty dt_3 \int_0^\infty dt_2 \int_0^\infty dt_1 S^{(3)}(t_3,t_2,t_1) \\ &E(\vec{r},t-t_3)E(\vec{r},t-t_3-t_2)E(\vec{r},t-t_3-t_2-t_1). \end{aligned} \tag{2.9.1}$$

In Eq. (2.9.1) the time dependence of $P^{(3)}$ is captured via a systematic variation of the interactions times $t-t_3$, $t-t_3-t_2$, and $t-t_3-t_2-t_1$ of the extracted electric fields E. Thus, the real-valued third-order nonlinear response function in the time domain $S^{(3)}$, which contains the complete microscopic information about the system, can be obtained by 2D spectroscopy [24]. The response function itself is a real function in which causality is included, i.e., no response occurs before an interaction takes place.

Figure 2.12 depicts the pulse sequence and time-ordering of 2D spectroscopy. Three laser beams with the wave vectors $\vec{k}_1$, $\vec{k}_2$, and $\vec{k}_3$ irradiate the sample while a fourth one,

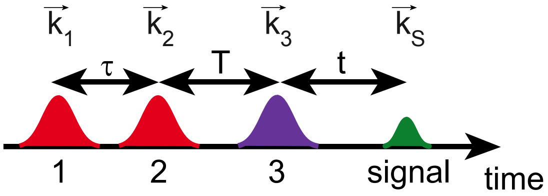

Figure 2.12: Pulse sequence and time definition for 2D spectroscopy. Three laser pulses (1, 2, 3) with their individual wave vectors $\vec{k}_i$ excite a sample (not shown), which emits a 2D signal with the wave vector $\vec{k}_S$. The timing between the pulses are defined as coherence time τ (between pulses 1 and 2), population time T (between pulses 2 and 3), and signal time t (between pulses 3 and the signal).

the signal, is emitted with the wave vector $\vec{k}_S$ by the sample [97]. Hence, 2D spectroscopy is a four-wave mixing (FWM) experiment. In FWM processes the signal is emitted in the direction determined by the phase-matching condition. The signal emitted in the direction $\vec{k}_S^R = -\vec{k}_1 + \vec{k}_2 + \vec{k}_3$ is called rephasing (R) part, while the non-rephasing (NR) part is emitted in the direction $\vec{k}_S^{NR} = \vec{k}_1 - \vec{k}_2 + \vec{k}_3$. The interaction times of the laser pulses with the sample are restricted to within the pulse envelopes due to a finite pulse duration. Thus, in a 2D experiment only the pulse envelopes are delayed with respect to each other. The time interval between interaction 1 and 2 is referred to as coherence time τ, while the interval between the second and third pulse interaction is labeled waiting or population time T in accordance with the pump-probe delay in conventional TA spectroscopy (for which $\tau = 0$, i.e. the pump pulse interacts twice with the sample). The signal detection time is t.

A 2D spectrum $S_{2D}(\omega_\tau, T, \omega_t)$ with two intuitive frequency axes (excitation frequency ω_τ and detection frequency ω_t) is obtained by a two-dimensional Fourier transform along the signal detection time t and coherence time τ to yield $iP^{(3)}(\omega_\tau, T, \omega_t)$ for a fixed population time T. However, due to the detection with a spectrometer, the signal field $E_S(\tau, T, \omega_t)$ rather than $E_S(\tau, T, t)$ is detected. Therefore, a second numerical Fourier transform (along t) is not necessary. The relationship between electric field and polarization is given by [97]

$$E_S(\tau, T, \omega_t) \sim \frac{i\omega_t}{n(\omega_t)} P^{(3)}(\tau, T, \omega_t). \tag{2.9.2}$$

Hence, performing the remaining Fourier transform along the τ-axis leads to

$$S_{2D}(\omega_\tau, T, \omega_t) = \int_{-\infty}^{\infty} iP^{(3)}(\tau, T, \omega_t) \exp(i\omega_\tau \tau) d\tau. \tag{2.9.3}$$

A 2D spectrum $S_{2D}(\omega_\tau, T, \omega_t)$ is a complex-valued quantity. The real part of $S_{2D}(\omega_\tau, T, \omega_t)$ describes changes of the absorption, while the imaginary part describes refractive index variations [98].

In 2D spectroscopy three laser pulses interact with the sample, which lead to a 2D signal, arising from exactly one interaction with each of the laser pulses. In general, the interacting electric field of the laser pulses is expressed as

$$\begin{aligned} E(t) = \quad & A_1(t+\tau+T)e^{-i\left[\omega_1 t-\vec{k}_1\vec{r}+\phi_1\right]} \\ + \quad & A_2(t+T)e^{-i\left[\omega_2 t-\vec{k}_2\vec{r}+\phi_2\right]} \\ + \quad & A_3(t)e^{-i\left[\omega_3 t-\vec{k}_3\vec{r}+\phi_3\right]} + c.c.\ , \end{aligned} \tag{2.9.4}$$

with the envelope function A_i, the center frequency ω_i, and the temporal phase $\phi_i = \Phi_0 + \varphi(t)$ of the i-th laser pulse. Substitution of Eq. (2.9.4) into Eq. (2.9.1) leads to $6{\cdot}6{\cdot}6 = 216$ terms in total which contribute to the third-order polarization $P^{(3)}$. Additionally, $P^{(3)}$ still contains contributions that arise from multiple interactions with the same pulse, which obscure the actually desired 2D signal. Hence, to obtain an isolated 2D signal, the amount of pulse contributions has to be reduced significantly. Considering the rotating-wave approximation (RWA) [99], the number of terms that contribute to $P^{(3)}$ is highly reduced. In RWA only slowly oscillating terms are relevant in the calculation of $P^{(3)}$, i.e., terms that are modulated with temporal electric-field envelope functions at frequencies $\omega_0 - \omega_{eg}$, with the carrier frequency ω_0 and the transition frequency ω_{eg}, while terms that oscillate at frequencies $\omega_0 + \omega_{eg}$ are neglected due to the integration [24]. By applying the RWA, the number of terms is reduced by a factor of 8 to $3 \cdot 3 \cdot 3 = 27$.

The number of remaining terms that contribute to $P^{(3)}$ is further reduced by taking into account the experimental conditions such as beam geometry and pulse ordering. In this thesis 2D spectroscopy in (partly collinear) pump–probe geometry ($2\mathrm{D}^{\mathrm{pp}}$) and in [fully noncollinear (nc)] box geometry ($2\mathrm{D}^{\mathrm{nc}}$) is performed.

The desired FWM signal is isolated in the former, $2\mathrm{D}^{\mathrm{pp}}$, by a systematic variation of the phases of the collinear excitation pulses 1 and 2, the so-called “phase cycling” [100, 100–107]. In $2\mathrm{D}^{\mathrm{nc}}$, the 2D signal isolation is based on the geometrical differences of the wave vectors of the three beams ($\vec{k}_1 \neq \vec{k}_2 \neq \vec{k}_3$), the so-called “phase matching” [97, 98]. Both experimental realizations of 2D spectroscopy which were employed in this thesis are discussed in the following (Subsec. 2.9.1 and Subsec. 2.9.2). Subsequently, similarities and differences in experimental requirements for performing a 2D experiment are pointed out (Subsecs. 2.9.3–2.9.7). Lastly, the advantages and disadvantages of both, $2\mathrm{D}^{\mathrm{pp}}$ and $2\mathrm{D}^{\mathrm{nc}}$, are briefly summarized and compared (Subsec. 2.9.8).

2.9.1 Coherent 2D Spectroscopy in Pump–Probe Geometry

Figure 2.13 displays the principle of 2D spectroscopy in pp geometry ($2\mathrm{D}^{\mathrm{pp}}$). In contrast to TA, in $2\mathrm{D}^{\mathrm{pp}}$ the excitation pulses (1 and 2) are generated and their time delay (coherence time τ) is varied by a pulse-shaper. The wave vectors of pulse 1 ($\vec{k}_1$) and pulse 2 ($\vec{k}_2$) are identical ($\vec{k}_1{=}\vec{k}_2$) and only the wave vector of the probe ($\vec{k}_3$) differs ($\vec{k}_1 = \vec{k}_2 \neq \vec{k}_3$). Consequently, TA contributions where either pulse 1 or 2 interacts twice with the sample ($\vec{k}_{TA} = \vec{k}_1 - \vec{k}_1 + \vec{k}_3 = \vec{k}_2 - \vec{k}_2 + \vec{k}_3 = \vec{k}_3$) are emitted in the same direction as the desired 2D signal. Furthermore, rephasing $k_S^R = -\vec{k}_1 + \vec{k}_2 + \vec{k}_3 = \vec{k}_3$ and non-

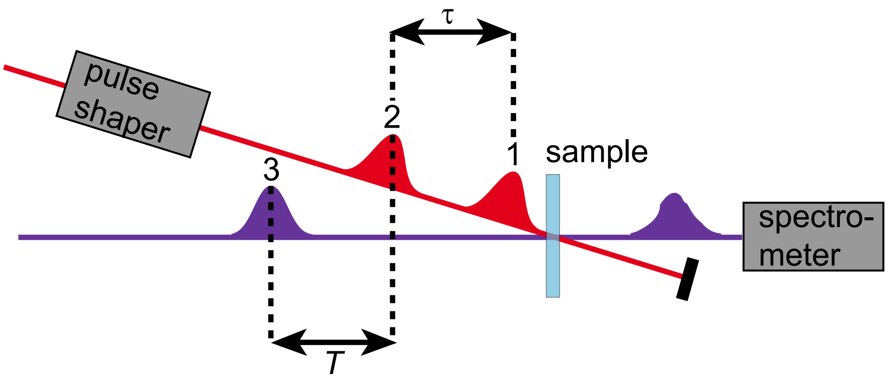

Figure 2.13: Coherent 2D spectroscopy in pp geometry. Compared to conventional TA (cf. Fig. 2.9) a pulse shaper is employed which creates a double-pulse sequence, variable in τ.

rephasing $\vec{k}_S^{NR} = \vec{k}_1 - \vec{k}_2 + \vec{k}_3 = \vec{k}_3$ contributions are emitted in the same signal direction.

The 2D signal is isolated from TA contributions by “phase cycling” [100, 100–107]. In phase cycling, a 2D signal $S_{2D}(\phi_{21})$ measured with a distinct phase difference between pulse 1 and 2 (ϕ_{21}) contains a weighted [$\exp(i\beta\phi_{21})$] summation of contributions $s(\beta)$ from different processes

$$S_{2D}(\phi_{21}) = \sum_\beta s(\beta)\exp(i\beta\phi_{21}), \tag{2.9.5}$$

with the integer β, which selects rephasing ($\beta = 1$) and non-rephasing signal terms ($\beta = -1$), respectively [104, 107]. In order to determine a distinct signal $s(\beta)$, it is necessary to perform several 2D experiments to obtain $S_{2D}(\phi_{21})$ with different ϕ_{21}. These $S_{2D}(\phi_{21})$ are linearly combined in a $1 \times L$ phase-cycling scheme

$$s_{1\times L}(\beta) = \frac{1}{L}\sum_{l=0}^{L-1} S_{2D}(l \cdot \Delta\phi_{21})\exp(-il\beta \cdot \Delta\phi_{21}), \tag{2.9.6}$$

with the integer l and the phase increment step $\Delta\phi_{21} = \frac{2\pi}{L}$ of the phase-cycling scheme. The value L is the number of phase-cycle intervals and determines the amount of 2D experiments which need to be performed. Subsequently to the summation in Eq. (2.9.6), a Fourier transform along τ is required to achieve the desired 2D spectrum. The possibility of varying the carrier phases of pulses 1 and 2 by a pulse-shaper allows a separate variation of the phases ϕ_1 and ϕ_2 in the (mask) transfer function

$$M(\omega) = \frac{1}{2}\left[e^{-i[\omega-(1-\gamma)\omega_0]\tau}e^{i\phi_1} + e^{i\phi_2}\right], \tag{2.9.7}$$

with the fundamental carrier frequency of the laser pulses ω_0. The value γ allows to shift the experiment from the laboratory frame into the rotating frame [104]. Thus, the signal oscillation as a function of τ is reduced by a factor of $\frac{1}{\gamma}$ and therefore less data points are required, as the Nyquist limit is reduced by the same factor. Furthermore, the signal

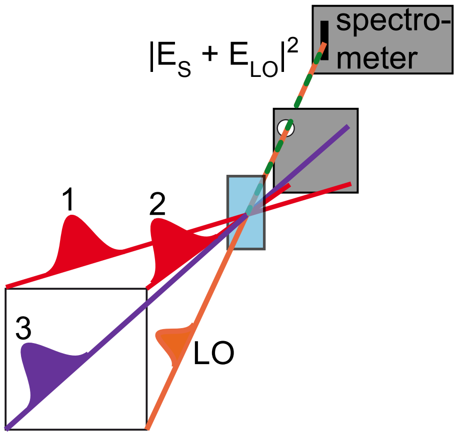

Figure 2.14: Coherent 2D spectroscopy in box geometry. Three excitation pulses $(1-3)$ arrive at the sample, which emits a signal field (E_S) in the phase-matching direction $\vec{k}_S = -\vec{k}_1 + \vec{k}_2 + \vec{k}_3$. The 2D signal is recorded with a spectrometer by heterodyne detection via a copropagating local oscillator (LO).

can be shifted from the reference frequency (typically the laser frequency) to frequencies which are less affected by experimental noise due to laser fluctuations and the climate in the laboratory.

2.9.2 Coherent 2D Spectroscopy in Box-Geometry

As alternative to "phase cycling" for isolating a 2D signal experimentally, a geometric approach can be employed, the so-called "phase matching" [97, 98]. In 2D spectroscopy in box geometry (2D$^{\mathrm{nc}}$) the excitation beams arrive at the sample from different directions and therefore with different wave vectors ($\vec{k}_1 \neq \vec{k}_2 \neq \vec{k}_3$) as depicted in Fig. 2.14. Due to the spatial separation of the excitation beams, their time delays (τ and T) are adjustable by mechanical delay stages (described in detail in Ref. [108]) but phase stability between the pulses is required (see Subsec. 2.9.6). The 2D signal is emitted in the phase-matching directions $\vec{k}_S^R = -\vec{k}_1 + \vec{k}_2 + \vec{k}_3$ and $\vec{k}_S^{NR} = \vec{k}_1 - \vec{k}_2 + \vec{k}_3$ corresponding to the rephasing (R) and non-rephasing (NR) components, respectively. Hence, the desired 2D signal is a weak background-free signal, which can be characterized completely by a copropagating local oscillator (LO, cf. Subsec. 2.9.4).

2.9.3 Chirp in 2D Spectroscopy

In 2D spectroscopy transform-limited laser pulses are desired, as chirped pulses lead to distortions in the resulting 2D spectra [109]. In TA spectroscopy, algorithms are able to correct for artifacts resulting from spectral phase of the probe pulses [89, 93, 110] which is more complicated in 2D spectroscopy as additionally the spectral phases of the excitation pulses affect the 2D spectrum [111].

In 2D$^{\mathrm{pp}}$ only pulses 1 and 2 are spectral replica (not all pulses as in the employed 2D$^{\mathrm{nc}}$) which provides the opportunity to use a white-light continuum to probe contributions which are spectrally far-off the excitation energies in the 2D spectrum. Especially for 2D$^{\mathrm{pp}}$ in the visible [101, 103, 112, 113] and ultraviolet [114, 115] region this is evident as electronic transitions typically possess much broader absorption bands than vibrational transitions in the infrared [102, 106, 116, 117]. However, the chirp of the probe pulse has a large influence on the waiting time T and leads to spectral distortions of the peak shapes in the 2D spectra. Chirp correction is crucial especially for the study of fast contributions at short population times. Thus, it is essential to correct for the probe chirp if population times on the order of the probe pulse duration (up to 600 fs for the used approach) are considered. Chirp correction is described in detail in Ref. [118] and is qualitatively analogous to the procedure in TA, but needs to be performed for every recorded excitation energy.

2.9.4 Heterodyne Detection

A highly sensitive detection technique is required to characterize the weak signal field in 2D spectroscopy. In $2\mathrm{D}^{\mathrm{pp}}$, the 2D signal is automatically heterodyned as it copropagates with beam 3. Still, the heterodyne detection can be optimized via polarization discrimination by setting the orientation of the pump and probe polarizations at 45° [103, 106]. Subsequently, an analyzer, which is initially perpendicular to the probe polarizer, is slightly rotated to provide the desired amplitude of beam 3, which serves as a local oscillator [103]. In this thesis all $2\mathrm{D}^{\mathrm{pp}}$ experiments were performed under magic angle polarization [36] between the pump (beam 1 and 2) and probe (beam 3) beams.

A common method in $2\mathrm{D}^{\mathrm{nc}}$ is to superimpose the weak signal field with a local oscillator (heterodyned detection). This leads to spectral interference (SI) between the signal field E_S and the electric field of the local oscillator E_{LO} [119, 120]. Assuming that the local oscillator is well characterized and time-delayed by t_{LO}, the spectrally-resolved intensity $I_{SI}(\omega_t)$ reads

$$\begin{aligned} I_{SI}(\omega_t) &= \left| E_S(\omega_t) e^{i\phi_S(\omega_t)} + E_{LO}(\omega_t) e^{i\phi_{LO}(\omega_t)} \right|^2 \\ &= I_S(\omega_t) + I_{LO}(\omega_t) + 2\sqrt{I_S(\omega_t) I_{LO}(\omega_t)} \cos\left[\phi_S(\omega_t) - \phi_{LO}(\omega_t)\right], \end{aligned} \tag{2.9.8}$$

with $I_i(\omega_t) = E_i(\omega_t)E_i(\omega_t)^*$. The complex signal field $E_S(\omega_t)$ and phase $\phi_S(\omega_t)$ can be determined by evaluating Eq. (2.9.8). The qualitative procedure is explained in the following. Firstly, Eq. (2.9.8) is Fourier transformed, which leads to three peaks in the time domain. Secondly, a Fourier filter around the time delay t_{LO} isolates the oscillatory part containing the signal field. Thirdly, an inverse Fourier transform of the filtered signal is performed. Finally, the signal field is obtained by dividing by the local oscillator amplitude and subtracting the LO phase. An appropriate delay t_{LO} is necessary which needs to be large enough to separate the peaks around $t = 0$ and $t = t_{LO}$ upon the first Fourier transform, and additionally t_{LO} is required to be small enough to not exceed the Nyquist limit such that the spectral fringes are still well resolved within the spectrometer.

Both, amplitude and phase of the signal field can be reconstructed by this approach. Additionally, heterodyne detection is a very sensitive technique. In particular, the direct measurement of the signal is proportional to $I_S(\omega_t)$. However, heterodyne detection measure the signal of an oscillating term which is proportional to $\sqrt{I_S(\omega_t) I_{LO}(\omega_t)}$. Thus, the detection sensitivity can be increased by $\sqrt{\frac{I_{LO}(\omega_t)}{I_S(\omega_t)}}$, since I_{LO} is much larger than I_S. The only limitation is the dynamic range of the spectrometer.

2.9.5 Scattered Light

Next to the chirp of the probe pulses (see Subsec. 2.9.3) scattered light distorts 2D spectra. In 2D$^{\mathrm{pp}}$ scattering contributions can be subtracted by performing a 4−step phase-cycling scheme [100, 105–107]. In this phase-cycling scheme, unwanted background scatter contributions are subtracted, while the signal is additive for all four signal contributions [106].

For 2D$^{\mathrm{nc}}$, Eq. (2.9.8) is an idealization, as scattered light from the excitation beams 1, 2, and 3 is also detected by spectral interferometry, despite the utilization of apertures [98]. Therefore,

$$\begin{aligned} I_{123LO} &= |E_1 + E_2 + E_3 + E_{LO} + E_S|^2 \\ &= (E_1 + E_2)^* E_3 + (E_1 + E_2) E_3^* + |E_1 + E_2|^2 + |E_S|^2 \\ &\quad + (E_1 + E_2)^* E_S + (E_1 + E_2) E_S^* + E_3^* E_S + E_3 E_S^* \\ &\quad + (E_1 + E_2)^* E_{LO} + (E_1 + E_2) E_{LO}^* + |E_3 + E_{LO}|^2 \\ &\quad + E_{LO}^* E_S + E_{LO} E_S^* \end{aligned} \tag{2.9.9}$$

is measured. The electric fields $E_i = \sqrt{I_i(\omega)} \exp[i \left(\phi_i(\omega) + \omega \tilde{t_i}\right)]$ contain not only the phases $\phi_i(\omega)$ and intensities $I_i(\omega)$, but also an additional phase term $\omega \tilde{t_i}$. The latter term results due to the different arrival times $\tilde{t_i}$ at the detector. Upon Fourier transformation only contributions from coherent scattering light remain, e.g., the light that contributes to the same Fourier window by interference with the local oscillator field. Thus, only contributions from the second-last line of Eq. (2.9.9) have to be taken into account. Therefore, it is necessary to measure

$$I_{3LO} = |E_3 + E_{LO}|^2 \tag{2.9.10}$$

and

$$I_{12LO} = |E_1 + E_2 + E_{LO}|^2 \tag{2.9.11}$$

separately by blocking the other beams (e.g., with shutters). Fourier evaluation of the signal $I_{123LO} - I_{3LO} - I_{12LO}$ yields the signal field, even if the coherently scattered light is of the same magnitude as the signal. However, the compensation of scattering light results in a longer measurement time.

2.9.6 Phase Stability

Phase stability between the single laser pulses in 2D spectroscopy is essential. For our implementation of 2D$^{\mathrm{pp}}$, the excitation pulses (1 and 2) are inherently phase stable, due to their generation by a pulse shaper and propagation along the same optical path. However, in 2D$^{\mathrm{nc}}$ mechanical vibrations of individual optical elements may lead to fluctuations of the individual path lengths of the beams, such that

$$\begin{aligned} \tilde{t}_i &\to \tilde{t}_i + \Delta\tilde{t}_i, \\ \tilde{t}_{LO} &\to \tilde{t}_{LO} + \Delta\tilde{t}_{LO}. \end{aligned} \tag{2.9.12}$$

Generally, these fluctuations introduce distortions of the recorded spectra [98]. These distortions can be minimized by delaying pulses in pairs via common optics

$$\begin{aligned} \Delta\tilde{t}_1 &= \Delta_{12} + \Delta_{13}, \\ \Delta\tilde{t}_2 &= \Delta_{12} + \Delta_{2LO}, \\ \Delta\tilde{t}_3 &= \Delta_{3LO} + \Delta_{13}, \\ \Delta\tilde{t}_{LO} &= \Delta_{3LO} + \Delta_{2LO}. \end{aligned} \tag{2.9.13}$$

In the case of pulse 1, the arrival time $\Delta\tilde{t}_1$ consists of Δ_{12} and Δ_{13}, where Δ_{ij} is the time jitter that both pulse i and j acquired during propagation via common optics [47, 98, 121]. Pairwise beam manipulation does not remedy all requirements on the stability of the optics, as some part of vibrations remain uncompensated, but simplifies the task to stabilize optics considerably. Alternatively, scattering can be effectively reduced via double-modulation lock-in detection by the implementation of choppers [122].

2.9.7 Phasing of 2D Spectra

As previously mentioned, 2D spectra are complex valued and consist of an absorptive (real) and a dispersive (imaginary) part (Sec. 2.9). In 2D$^{\mathrm{nc}}$, the absolute phase of a two-dimensional spectrum is a-priori not known as uncertainties remain in the signal arrival time with respect to the local oscillator. This is not the case in 2D$^{\mathrm{pp}}$ as the 2D signal is created and arrives with beam 3, respectively. In order to determine the absolute phase in 2D$^{\mathrm{nc}}$, spectrally resolved TA measurements with the same population time T are performed.

Phasing removes uncertainties in the interferometric phase relation of the LO with respect to pulse 3 and its arrival time [98]. The phasing procedure is based on the projection-slice theorem, which connects the projection of the 2D spectrum with corresponding TA data [97, 123, 124]. The real part of the 2D spectrum is projected onto the detection (ω_t) axis and multiplied by an adjustable phase term $e^{i\phi_c + i(\omega_t - \omega_0)t_c}$ with the correction factor for the phase ϕ_c and the arrival time t_c. The projection of the real part of the 2D spectrum

$$S_{TA} \overset{!}{\propto} \mathrm{Re}\left(\frac{\omega_t}{n(\omega_t)} E_{Pr}(\omega_t) \int_{-\infty}^{\infty} S_{2D}(\omega_\tau, T, \omega_t) e^{i\phi_c + i(\omega_t - \omega_0)t_c} d\omega_\tau \right), \tag{2.9.14}$$

is therefore fitted to the spectrally resolved TA signal field

$$S_{TA}(T, \omega_t) = \frac{\Delta OD(T, \omega_t)}{\sqrt{I^{pr}(\omega_t)}}, \tag{2.9.15}$$

with the change of absorption $\Delta OD(T, \omega_t)$ [cf. Eq. (2.8.1)] and the probe field $\sqrt{I^{pr}(\omega_t)}$ [98].

2.9.8 Coherent 2D Spectroscopy in TA vs. Box geometry

In this thesis, 2D spectroscopy is performed in (partly collinear) TA geometry and (non-collinear) box geometry for different molecular systems. Hence, a brief overview of advantages and drawbacks of both setups in regard to the previously mentioned requirements is given in the following.

In $2\mathrm{D}^{\mathrm{pp}}$, the desired 2D signal is obtained via phase cycling [100–107]. Therefore, the $2\mathrm{D}^{\mathrm{pp}}$ experiment can be easily realized by employing a pulse shaper in the beam path of the pump beam of a conventional TA setup. In contrast, $2\mathrm{D}^{\mathrm{nc}}$ requires phase matching [97, 98], which is realized by creating four spatially separated pulse replica by beam splitters or gratings.

Performing polarization-dependent 2D spectroscopy provides the opportunity to enhance and suppress distinct signal contributions in a 2D spectrum [125–127]. While the excitation beams (pulses 1 and 2) and pulse 3 are spatially separated in $2\mathrm{D}^{\mathrm{pp}}$, i.e., the pump and probe in TA, the polarization between pump and probe beam is easily adjustable. An individual manipulation of the polarization states of pulse 1 and pulse 2 requires a more sophisticated pulse-shaper device, which is capable of polarization-shaped multipulse sequences [128]. Due to the spatial separation of all beams in $2\mathrm{D}^{\mathrm{nc}}$, the beams can be individually manipulated, e.g., differently chopped or blocked to cancel out undesired signals, or adjustable in polarization to enhance specific signal contributions in polarization-dependent 2D spectroscopy [125–127].

Rephasing and non-rephasing 2D contributions cannot be measured directly in $2\mathrm{D}^{\mathrm{pp}}$, but by imposing causality in post data processing both contributions can be retrieved [103, 106]. In $2\mathrm{D}^{\mathrm{nc}}$, rephasing and non-rephasing contributions are directly accessible by simply recording negative (non-rephasing) and positive (rephasing) coherence times and detecting the signal in the phase-matching direction.

In $2\mathrm{D}^{\mathrm{pp}}$, the 2D signal can be interpreted as a directly heterodyned signal, as the probe beam (beam 3), initiates the desired 2D signal. Polarization discrimination allows an amplification of 2D signal by adjusting the amplitude of beam 3 compared to the

2D signal [103, 106]. In contrast, the 2D signal in $2D^{nc}$ is completely characterized by a fourth beam, the local oscillator, which allows a sensitive signal detection based on spectral interference [98]. Furthermore, an additional TA measurement in $2D^{nc}$ is required for the phasing procedure, which is irrelevant in $2D^{pp}$.

The implementation of a white-light supercontinuum as a probe beam gives access to a spectrally broad detection, but requires chirp correction [118], which results in an increase in the required time for an experiment. For both, $2D^{pp}$ and $2D^{nc}$, compressed excitation pulses are necessary, as chirped pulses produce artifacts and distortions in the 2D spectra [109], which cannot be corrected easily [111].

In comparison, $2D^{pp}$ has the advantage of a straight-forward experimental implementation with a broadband detection. By phase cycling, TA contributions and scattering contributions can be subtracted for the price of additional measurement time [103, 106]. Performing $2D^{nc}$ provides a background-free 2D signal, which gives direct access to non-rephasing and rephasing signal by measuring negative and positive coherence times, respectively. Additionally, all four beams (including the LO) can be individually manipulated, which provides the option to extract, amplify or suppress different 2D signal contributions [16, 129], while requiring a phase-stable $2D^{nc}$ setup [98].

Chapter 3

Multichromophoric Merocyanines

The relative orientation of chromophores is a key factor for determining the relationship between structure and functionality in molecular multichromophore assemblies. In the case of structurally flexible molecular systems one challenge is to rationalize the relevant effects of accessible chromophore orientations with spectroscopic observations. Especially for molecules in solution typical approaches like X-ray diffraction and NMR may not be applicable or comprehensive. In cooperation with the research group of Prof. Dr. Frank Würthner a series of merocyanine molecules that contain one, two or three highly dipolar ($\mu_g = 13.1$ D) dyes in close vicinity is investigated to study the influence of chromophore–chromophore interactions on the relative orientation of dyes and the photoinduced dynamics. Structural investigations via electro-optical absorption and density functional theory reveal a preferential molecular conformation which is driven by electrostatic interactions between highly polar merocyanines. Relaxation dynamics are probed via transient absorption and coherent two-dimensional spectroscopy. Furthermore, a general relaxation model is derived which can be applied for all merocyanines under investigation and can be used as a reference point for other dipolar donor–acceptor dyes. The intramolecular charge-transfer state of the monomeric merocyanine is stabilized by dipolar neighbor molecules in the bis- and tris-chromophoric dyes.

This chapter is organized as follows: The molecular series of mono- and multichromophoric merocyanines is introduced in Section 3.1. Then, molecular structure, i.e., the relative chromphore–chromophore orientation for the multichromophoric systems is investigated in Section 3.2. Subsequently, the influence of the molecular structure on the relaxation dynamics is investigated and discussed in Section 3.3. Chromophore–chromophore interactions are discussed in Section 3.4. Finally, the results of all experiments are summarized at the end of this chapter in Section 3.5.

3.1 Introduction

Chromophore–chromophore interactions play an important role in the functionality of supramolecular assemblies. In nature, the structure of these aggregates or polymers, such as photosynthetic light-harvesting systems or the DNA, is often determined by a particular molecular matrix environment, for example a protein. In artificially synthesized materials, the structure may also be due to self-assembly via interchromophore interactions [130]. In this case, attractive chromophore interactions between single molecules determine the first step of the chromophore arrangement and orientation. Therefore, these interactions have a high impact on the resulting supramolecular structure. In reverse, analyzing the molecular conformation in media allows deducing the interplay between structural arrangement and chromophore interactions. Furthermore, molecular interactions can serve as a rational control in the supramolecular design of functional organic materials for photonics and electronics.

The determination of molecular structures is commonly performed via X-ray crystallography [131–133] and nuclear magnetic resonance (NMR) spectroscopy [134]. These contemporary analytic techniques may be limited in the determination of a molecular structure, as, e.g., ambiguous couplings in the NMR analysis can occur or the molecular systems do not crystallize well enough for a thorough X-ray analysis. However, even if molecular crystals are accessible, the crystalline structure depends on conditions during crystallization such as the solvent and the ambient temperature and might not represent the preferential molecular structure in solution or other environments, e.g., in particular for J-aggregates it is not possible at all. Generally, molecules in solution display a higher structural degree of freedom than in solid phase which is additionally influenced by interactions between solute and solvent. Hence, even a dynamic distribution of molecular structures might be present.

Next to the aforementioned experimental techniques, theoretical calculations give access to molecular structures. In this case information is obtained by geometry optimization, e.g., in DFT calculations [135, 136], providing relative energies of different molecular conformations. Hence, the molecular geometry to start the optimization has to be chosen carefully to avoid local minima. Furthermore, obtained structures might not represent the actual geometry in solution as the molecular environment is typically neglected. More advanced theoretical calculations are capable of a molecular structure optimization in media by modelling the surrounding medium or by including correction parameters based on experimental results [137]. In consequence, these methods have to face higher computational costs.

Being confronted by the challenge of structure determination of multichromophoric molecular systems in solution, for which NMR and X-Ray do not provide unambiguous observations, linear absorption spectra have been proven to contain valuable structural information, e.g., by analyzing the orientation and distance dependence with exciton theory [31] or in the analysis of the aggregation process itself [130, 138–142]. Additionally, ultrafast laser pulses [143, 144] even in combination with X-ray absorption [145] have been shown to provide information on the molecular structure.

Merocyanines have been investigated frequently in the context of supramolecular design due to their outstanding molecular properties, e.g., high dipole moment and strong, usually narrow-band absorption in the visible. Merocyanines consist of a donor (D) and an acceptor (A) moiety which are linked by a polymethine bridge, which is variable in length. These donor–acceptor (D–A) systems can be described by two resonance structures, namely a neutral polyene structure and secondly, a zwitterionic resonance structure, due to delocalization of π electrons in merocyanines over D, A, and the polymethine linker. The equilibrium between these resonance structures depends on the D/A moiety and on the length of the connecting polymethine link. These structural properties of merocyanines allow versatile options of variation and therefore enable fine tuning of electronic and optical properties. This allows access to a large field of applications, e.g., in biology and medicine [146], nonlinear optics and photorefractive materials [147, 148], and as organic p-semiconducting materials in organic solar cells and field-effect transistors [149].

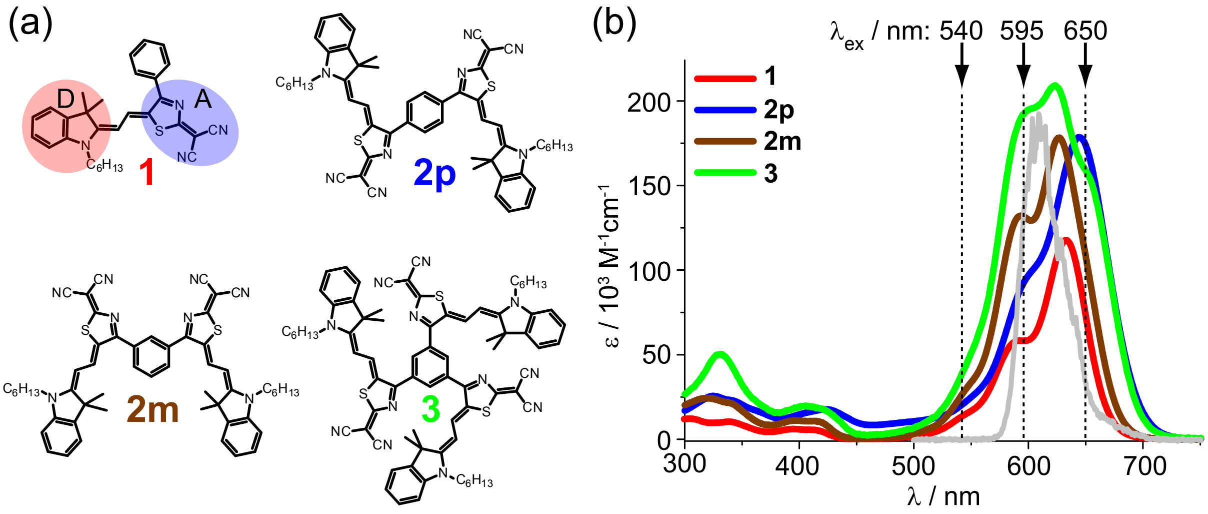

Figure 3.1: (a) Chemical structures of the studied monomer (**1**), consisting of an indolenine D and a thiazol A moiety which is attached to a benzene unit, and multichromophore (**2p**, **2m**, and **3**) dyes. Labels next to the chemical structures describe the number of chromophores. To distinguish the bis-merocyanines (**2**), the binding site relative to the other chromophore is labeled additionally (m = meta, p = para). The chromophores of **3** are all linked to each other in meta position at the benzene unit. (b) Linear absorption spectra for all dyes dissolved in DCM, displaying strong differences in their absorption maxima (λ_{max}) and relative absorption band intensities. The experiments of Subsections 3.3.1, 3.3.2, and 3.3.4 were performed with the laser spectrum depicted in gray. Black arrows and dashed lines indicate the different laser excitation wavelengths (λ_{ex}) of spectrally narrow pulses, which were set to determine the effect of excess energy on the molecular relaxation dynamics (Subsec. 3.3.3).

Furthermore, merocyanine and cyanine dyes often exhibit rather complex relaxation dynamics in solution. Recent studies of merocyanine and cyanine derivatives revealed isomerization processes due to a rotation along a double bond of the polymethine bridge [112, 150–154], as well as ultrafast ring-closure and -opening events from a merocyanine to a spiro compound (ring-closed form) [155–158]. Additionally, it is known that conical intersections can accelerate the relaxation pathways [159–163], and also the influence of protonation of merocyanines on the relaxation dynamics was studied [164]. Moreover, the ultrafast deactivation to a hot ground state, strongly depending on the environment (solvent), was investigated [165].

The present work goes beyond those mono-chromophoric studies and deals with chromophore–chromophore interactions between merocyanine dyes. Typically, these interactions can lead to shifts of the absorption bands and to changes of their relative intensities. Thus, a systematic merocyanine series (Fig. 3.1a) was synthesized, beginning with a single merocyanine chromophore consisting of an indolenine D and a thiazol A moiety. The A is directly linked to a benzene unit, which allows connecting further chemically identical merocyanine chromophores. The monomer (**1**) acts as a reference dye (since in this case chromophore–chromophore interactions are absent) for the multichromophore dyes (**2p**, **2m**, and **3**). Chromophore–chromophore interactions are introduced for bis-merocyanines, which are connected in para (**2p**) and meta (**2m**) position to each other, and a tris-merocyanine (**3**) for which all chromophores are in meta position to each other.

Figure 3.1b shows the linear absorption spectra in dichloromethane (DCM) of the investigated merocyanine dyes. In the following, spectral changes in the range from $\approx 500 - 750$ nm are discussed. The linear absorption spectrum of the monomer **1** (red in Fig. 3.1b) displays an absorption maximum at $\lambda_{\max} = 633$ nm. Furthermore, additional absorption bands around 595 nm and 540 nm can be attributed to a vibrational progression of the $S_0 \rightarrow S_1$ transition. In comparison to **1**, the para-linked dye **2p** (blue in Fig. 3.1b) displays a 12 nm bathochromically shifted absorption maximum at $\lambda_{\max} = 645$ nm with a small additional absorption band at 602 nm. The bathochromic shift of $\lambda_{\max}$ for a two-chromophore system in comparison to a monomer indicates either a J-type excitonic coupling of the two chromophores [31] or an increased conjugation length of the π-electron system. In contrast to **2p**, the meta-linked dye, **2m** (brown in Fig. 3.1b), displays a hypsochromically shifted absorption maximum at $\lambda_{\max} = 626$ nm with an intense additional absorption band at 593 nm. Lastly, the trimer **3** (green in Fig. 3.1b), for which all three chromophores are in meta position to each other, displays the most complex absorption spectrum. On the blue edge, the absorption maximum at $\lambda_{\max} = 623$ nm with an additional absorption band at 598 nm is similar to the absorption features of **2m**, on the red edge the third bathochromically shifted band at ≈ 652 nm is more similar to $\lambda_{\max}$ of **2p**.

Still, the origin and the nature of the observed chromophore interactions in linear absorption cannot be inferred easily. Hence, we address the question how chromophore interactions are reflected in the linear absorption spectra of multichromophoric merocyanines. Since such chromophore interactions and relaxation dynamics strongly depend on the relative chromophore orientation, the molecular structure in solution has to be determined to be able to resolve the origin of these interactions.

These questions are approached by initially determining the mutual chromophore–orientation of the multichromophoric merocyanines in Section 3.2. In the following, the structure-dependant relaxation dynamics are investigated in Section 3.3 to provide a relaxation scheme for all investagated dyes. Section 3.4 analyzes the linear absorption spectra based on the interactions of the chromophores. Finally, the key observations are summarized in Section 3.5.

3.2 Unraveling the Molecular Structure

In this section, the molecular structure, i.e., the relative chromophore orientations of the multichromophoric merocyanines, is investigated. The combination of electro-optical absorption (Subsec. 3.2.1) with density functional theory (Subsec. 3.2.2) provides a molecular structure, i.e., the preferential relative chromophore orientation, for the multichromophoric dyes. These assignments form the basis for the subsequent Sections 3.3 and 3.4, which analyze the influence of the determined molecular structure on the relaxation dynamics and on the linear absorption.

3.2.1 Electro-Optical Absorption

Electro-optical absorption (EOA) spectroscopy determines the difference in absorption of a molecular solution with $\left[\varepsilon^E(\varphi,\tilde{\nu})\right]$ and without $[\varepsilon(\tilde{\nu})]$ an externally applied electric field E, measured with light polarized parallel ($\varphi = 0°$) and perpendicular ($\varphi = 90°$) to the field direction of E. The relative change in absorption due to the effect of the applied external electric field can be described by the quantity $L(\varphi,\tilde{\nu})$, which is defined by

$$L(\varphi,\tilde{\nu}) = \frac{\varepsilon^E(\varphi,\tilde{\nu}) - \varepsilon(\tilde{\nu})}{\varepsilon(\tilde{\nu})} \times \frac{1}{E^2}. \tag{3.2.1}$$

It depends on the orientation of the molecules due to their ground state dipole moment μ_g, on the shift of the absorption band proportional to the dipole moment difference $\Delta\mu = \mu_e - \mu_g$, with the excited-state dipole moment μ_e, and on the electric field dependence of the transition dipole moment $\mu_{eg}(E)$ [166]. The analysis of the EOA response is conducted via multilinear regression of the EOA signal, in which spectral features as well as molecular properties are included. A detailed description of the multilinear regression is given by Liptay and Wortmann [167–169]. Additionally, information about the molecular μ_g can be retrieved by the linear combination

$$L_p(\varphi,\tilde{\nu}) = 6[L(0°,\tilde{\nu}) - 3L(90°,\tilde{\nu})], \tag{3.2.2}$$

which is proportional to μ_g^2.

Figure 3.2 displays the EOA response and the corresponding L_p values for all investigated dyes. Results of the multilinear analysis are collected in Table 3.1. Depending on the substitution pattern remarkable changes in the shape intensity of the EOA response are observable, which are discussed in detail in the following.

In case of **1** a positive electrodichroism $[L(0°) > L(90°)]$ is observable (cf. Fig. 3.2a). This indicates an angle in the range of 0° to 54.7° between μ_{eg} and μ_g $[\sphericalangle(\mu_{eg},\mu_g)]$. The linear regression and the wavenumber independence of L_p (Fig. 3.2b) support that only homogeneously polarized transitions are present. The obtained dipole moments are in accordance with previously reported values of highly dipolar merocyanine dyes with similar donor and acceptor moieties [170–174]. Furthermore, the determined $\Delta\mu$ values can be used together with μ_{eg} values to classify dyes by the square of the resonance parameter c^2, which is calculated, following Wortmann [172], via

$$c^2 = \frac{1}{2}\left(1 - \frac{\Delta\mu}{\sqrt{4\mu_{eg}^2 + \Delta\mu^2}}\right). \tag{3.2.3}$$

Dyes are classified to be polyene-like ($c^2 \approx 0; \Delta\mu > 0$), cyanine-like ($c^2 \approx 0.5; \Delta\mu \approx 0$), or betaine-like ($c^2 \approx 1; \Delta\mu < 0$). Hence, the values $c^2 = 0.518$ and $\Delta\mu = -2.4 \times 10^{-30}$ Cm

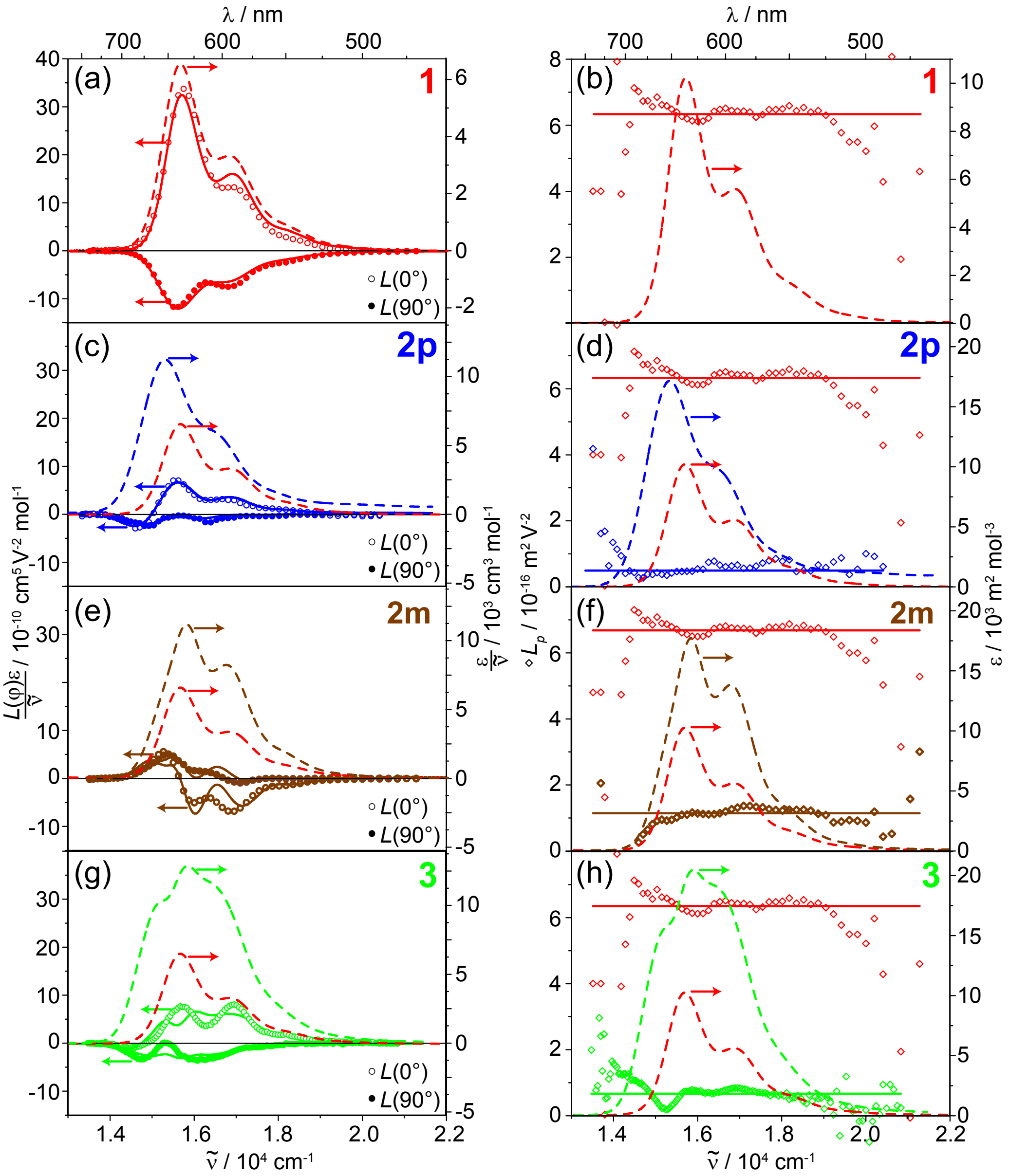

Figure 3.2: Linear absorption (dashed line) and EOA ($\varphi = 0°$: open symbol; $\varphi = 90°$: filled symbol) spectra as well as the multilinear regression (solid line) of **1** (a), **2p** (c), **2m** (e), **3** (g) chloroform at 298 K. (b) Linear absorption spectrum and the linear combination L_p (open symbol) of all dyes **1** (b), **2p** (d), **2m** (f), **3** (h) in chloroform at 298 K.

allow the classification of **1** as a cyanine-like dye.

The bis-merocyanine **2p** displays a positive electrodichroism $[L(0°) > L(90°)]$ in the EOA spectrum, however with a much smaller intensity than **1** (see Fig. 3.2c). This first indication for a smaller μ_g, compared to **1**, can be further visualized by the tremendously diminished L_p (compare Fig. 3.2d). The multilinear analysis reproduces the EOA spectrum well, which indicates the homogeneity of the investigated absorption bands, like in

Table 3.1: Overview of the results of the (electro-)optical properties determined by linear absorption and EOA[a] spectroscopy for all dyes in chloroform. For **3**, the transition dipole moment μ_{eg}, the dipole moment of the ground state μ_g, and of the excited state μ_e, were not determined as the multilinear regression analysis is not able to fit the experimental data appropriately.

Dye	**1**	**2p**	**2m**	**3**
λ_{ag}^{max} / nm	637	652	632	630
ε^{max} / $m^2 mol^{-1}$	10215	17200	17700	20400
μ_{eg} / 10^{-30} Cm	34.8	48.6	49.2	59.1
${\mu_g}^b$ / 10^{-30} Cm	$43.7 \pm 1.0\ (\parallel)$	$12.2 \pm 0.7\ (\parallel)$	$20.7 \pm 2.5\ (\perp)$	–
${\mu_e}^b$ / 10^{-30} Cm	$41.2 \pm 1.6\ (\parallel)$	$-1.1 \pm 1.6\ (\parallel)$	$35.7 \pm 2.0\ (\perp)$	–
$\Delta\mu^b$ / 10^{-30} Cm	$-2.4 \pm 1.2\ (\parallel)$	$-13.4 \pm 1.2\ (\parallel)$	$14.9 \pm 1.8\ (\perp)$	–

---

[a] Corrected to give "gas phase" dipole moments by Onsager cavity field correction. [175]

[b] Calculated under the approximation that $\sphericalangle(\mu_{eg}, \mu_g) = 0°$ and $\sphericalangle(\mu_{eg}, \mu_g) = 90°$ indicated by $(\parallel)$ and $(\perp)$, respectively.

the case of **1**. The analysis of the EOA measurement of **2p** thus reveals that two highly dipolar merocyanine dyes adopt a mean conformation with respect to the central spacer unit which compensates most of their individual μ_g. The most efficient compensation of μ_g is realized if both individual chromophores of **2p** perfectly point in opposite directions (cf. structure **2p**-I in Scheme 1, in contrast to structure **2p**-II). In this configuration two highly dipolar merocyanines are electrostatically favored as the donor moiety of one merocyanine is in proximity to the acceptor moiety and in remoteness to the donor moiety of the other chromophore. In such a configuration, **2p** would display an inversion center which would result in $\mu_g = 0$. However, due to structural flexibility, individual chromophores can break this symmetry and generate a μ_g which is close to zero, i.e., reduced vastly compared to the μ_g of **1**. Regarding the spectral changes of $L(0°)$ and $L(90°)$ for **2p** (cf. Fig. 3.2c), an increasing absorption for $L(0°)$ is observable which displays a similar spectral shape as the absorption spectrum of **1**. Additionally, a decrease of the absorp-

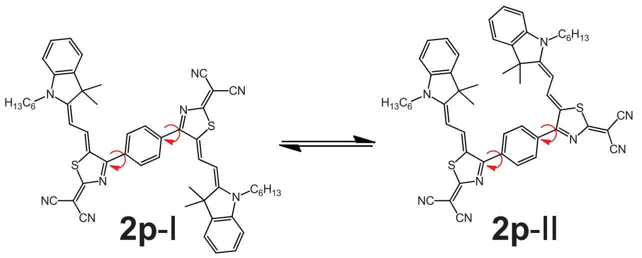

Scheme 1: Different conformations of **2p** through rotation of one or two chromophores around the benzene bridge. The structures **2p**-I and **2p**-II depict anti-parallel and parallel chromophore orientations for **2p**, respectively.

tion at the low-energetic spectral edge of the absorption band is detectable for both, $L(0°)$ and $L(90°)$. This indicates that the applied electric field results in orientational changes of the initially isotropic molecular distribution and thereby creating dimeric molecules with monomeric character, i.e., localized excitation on single chromophores [167, 171]. Hence, the chromophore–chromophore interactions are reduced, or even canceled out, for a subensemble of molecules, which is observable in the decrease of spectral components in $L(0°)$ and $L(90°)$ at the low-energy edge. Furthermore, for a localized excitation within a single dimer with an inversion center, $\mu_e^{\mathbf{2p}} = \mu_e^{\mathbf{1}} - \mu_g^{\mathbf{1}}$ would hold [167]. From the determined values (cf. Table 3.1) it follows that $\mu_e^{\mathbf{1}} - \mu_g^{\mathbf{1}} = -2.5 \times 10^{-30}$ Cm, which matches the value for $\Delta\mu$ from **2p** within the estimated error intervall. This indicates once more only small deviations from a perfectly symmetric configuration with an inversion center (**2p**-I in Scheme 1).

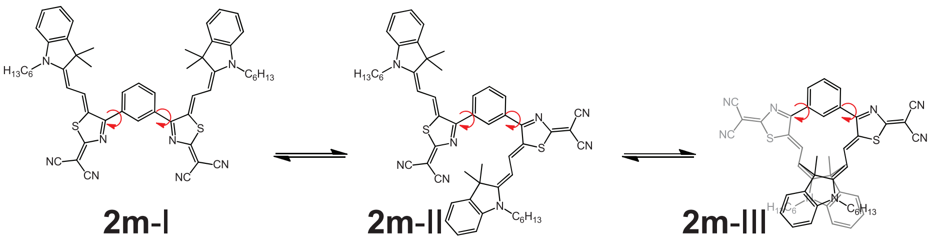

Scheme 2: Different conformations of **2m** through rotation of one or two chromophores around the bridge. The structures **2m**-I, **2m**-II and **2m**-III depict different limiting structures of **2m** with predominantly parallel (I and III) and anti-parallel (II) chromophore orientation.

The electro-optical response of **2m** (Fig. 3.2e) is again reduced in comparison to **1**. In contrast to **1** and **2p**, **2m** exhibits a negative electrodichroism [$L(0°) < L(90°)$], which indicates that μ_{eg} has an angle between 54.7° and 90° relative to μ_g. The decrease in dipolarity can be further visualized by a smaller L_p (Fig. 3.2f). In contrast to **1** and **2p**, the analysis of **2m** does not reproduce the spectral band structure of the EOA spectra, indicating heterogeneous bands within the linear absorption spectrum. Still, the L_p of the EOA measurements of **2m** leads to the conclusion that the two highly dipolar merocyanine dyes adopt a conformation which compensates most of their individual μ_g within the bis-merocyanine. Hence, both chromophores have to point again in predominantly different directions to reduce the total μ_g of the dimer (cf. structures **2m**-II in Scheme 2, in contrast to predominantly parallel orientations of structures **2m**-I and **2m**-III). However, the dipole moment is not reduced as efficiently as in case of **2p**, which might be rationalized by the closer proximity of both chromophores, since they are oriented in meta position of the bridging spacer unit within **2m**. An orientation of the two chromophores whose ground-state dipole moments point in predominantly opposite directions is electrostatically favored due to the proximity of the donor moiety of one merocyanine to the acceptor moiety of the other chromophore and vice versa. Still, due to the meta substitution pattern an inversion center of the molecular structure is not possible as in the case of **2p**. Spectral changes of the EOA response in **2m** are visible at the low-energetic edge, where both $L(0°)$ and $L(90°)$ are increasing (compare Fig. 3.2e). Moreover, $L(0°)$ displays a strong decrease of two spectrally sharp bands at higher energies. Comparing the linear absorption spectra of **1** and **2m** (dashed lines in Fig. 3.2e), the two sharp bands of **2m** resemble how both linear absorption spectra differ. Hence, due to the applied electric field, localized excitations on single chromophores are created, leading to a decrease of the spectrally sharp absorption bands of **2m**.

The electro-optical response of **3** is again reduced in comparison to **1**, exhibiting also a positive electrodichroism $[L(0°) > L(90°)]$. Experimental data for **3** could not be fitted appropriately by multilinear regression analysis (cf. Fig. 3.2g), which indicates again heterogeneous bands. The reason might originate from the overlap of multiple differently polarized transitions of one or several species/conformers present in solution. This assumption is supported by the energy dependence of L_p (see Fig. 3.2h) over the whole region of the absorption band. Although a quantitative analysis at this point is not possible without the knowledge of the individual band shapes of the overlapping transitions, one can deduce that the overall dipolarity of **3** is, like in the case of the bis-merocyanines **2p** and **2m**, reduced. This is in accordance with the assumption that the repulsive electrostatic interactions of the highly dipolar merocyanine dyes leads to a conformation which compensates most of their individual ground-state dipole moment μ_g. An efficient compensation of μ_g could be realized, e.g., by a propeller-like arrangement, where the donor moiety of one highly dipolar merocyanine is in proximity to the next chromophore. The EOA response displays two increasing bands for $L(0°)$ at the spectral positions of the absorption of **1**. Additionally, a decrease in $L(90°)$ at the low-energy edge of the absorption of **3** and a spectrally broad band around 1.65×10^4 cm^{-1} can be observed. Again, the rise of spectral bands in $L(0°)$ indicates a localization of the excitation but in this case without the distinct shape of the absorption spectrum of **1**. This might be due to the structural and electrostatic complexity of **3**, which might hamper a localization by the electrostatic field on a distinct chromophore.

3.2.2 Density Functional Theory

In the previous section, distinct structural chomophore orientations were proposed for the bis-merocyanines, **2p** and **2m**, based on the spectral changes in EOA measurements and presumed electrostatic interactions. In order to validate the previously described observations, density functional theory (DFT, B3LYP/def2-SVP level) calculations were performed for the mono- (**1**) and the two bis-merocyanines (**2p** and **2m**). Figure 3.3 depicts the results of the geometry optimization and the resulting electron density for **1**, **2p** and **2m** (starting from different chromophore orientations, i.e., parallel or antiparallel).

For **1** the electron density of the highest occupied molecular orbital (HOMO) is localized on the merocyanine chromophore, without extending over the directly linked benzene unit. In contrast, the electron density of the lowest unoccupied molecular orbital (LUMO) is extended over the merocyanine chromophore and the benzene unit. Furthermore, the transition dipole moment of **1** could be determined to $\mu_{eg} = 34.7 \times 10^{-30}$ Cm, which corresponds nicely to the experimentally determined value of $\mu_{eg} = 34.8 \times 10^{-30}$ Cm (cf.

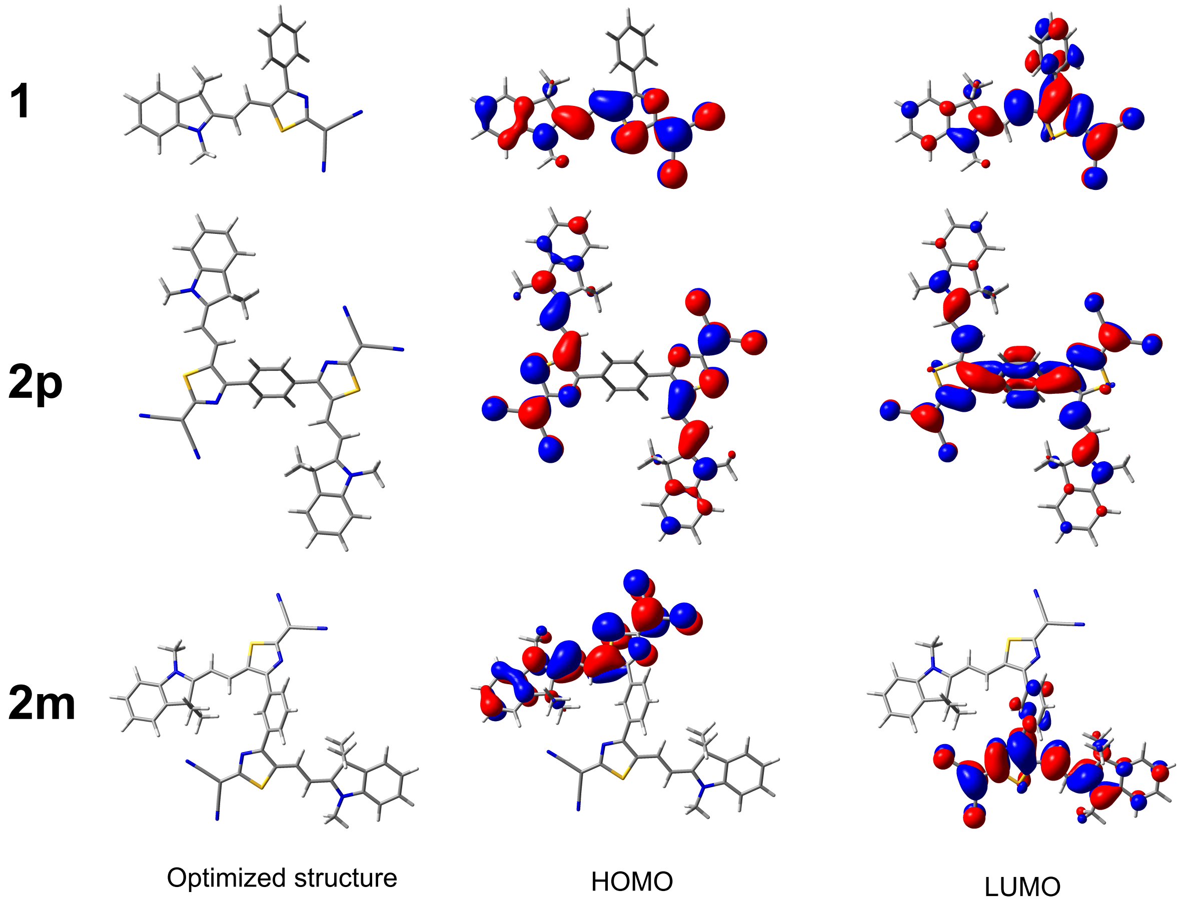

Figure 3.3: Structure optimization (B3LYP/def2-SVP level) of **1**, **2p**, **2m** and electron density of the related HOMO and LUMO.

Table 3.1).

In the case of **2p**, the geometry-optimized structure displays two merocyanine chromophores which are almost in one plane, pointing in opposite directions. The bridging benzene unit is rotated out of this plane, possibly due to sterical hindrance. Concerning the electron density, a localization, again on the single chromophores, similar to **1**, is observed for the HOMO of **2p**. Due to structural symmetry, both merocyanines are energetically degenerate, which explains why the electron density is located on both chromophores in the HOMO. The electron distribution of the LUMO displays an elongation from the acceptor moieties of both merocyanine chromophores over the bridging benzene unit, which is in agreement with the conjugation of the $\pi-$electron system. The structural optimization of **2p** thus strongly agrees with the proposed structure (structure **2p**-I in Scheme 1) based on the EOA measurements.

The geometry optimization of **2m** leads to an energetically favored anti-parallel orientation of the two merocyanine subunits (similar to **2m**-II in Scheme 2). In this configuration, the two chromphores point in different directions, similar to **2p**, but in this case the chromophores are twisted. Like in the case of **1** and **2p**, the electron density of the HOMO for **2m** is localized on the merocyanine unit. However, in stark contrast to **2p**, the localization is only on one of the two merocyanine chromophores. The electron distribution of the LUMO of **2m** is localized also on a single chromophore, with small contributions on the benzene bridging unit. Importantly, comparing HOMO and LUMO of **2m**, the electron density is located on the other chromophore. Hence, both chromophores of **2m** are not degenerate as for **2p**. A possible explanation is the proximity to the acceptor moiety of the other merocyanine chromophore, thus being in an electrostatically favored geometry. In further consequence, the donor moiety of the second chromophore is in a larger distance to the acceptor moiety of the first merocyanine dye.

3.3 Relaxation Dynamics of Multichromophoric Merocyanines

The previous Section 3.2 provided a structural assignment of the relative chromophore orientation for **2p** and **2m**. This section investigates, how the different structures and corresponding interactions between individual chromophores for the multichromophoric merocyanines, affect the relaxation dynamics. The relaxation dynamics of the single merocyanine **1** in solution are investigated by transient absorption (TA) spectroscopy (Subsec. 3.3.1) and subsequently compared to both bis- and the tris-merocyanine (Subsec. 3.3.2). The influence of the excitation energy on the relaxation is investigated for all merocyanines (Subsec. 3.3.3). Furthermore, the results of coherent 2D spectroscopy (Subsec. 3.3.4) in TA geometry are presented. All results of the ultrafast spectroscopy experiments are combined to a relaxation model, which was applied to all investigated merocyanine dyes (Subsec. 3.3.5).

3.3.1 Relaxation Dynamics of the Mono-Merocyanine 1

Figure 3.4a depicts the TA map of **1** (with ≈ 0.3 OD) upon excitation with ≈ 20 fs pulses centered at 630 nm (see gray spectrum in Fig. 3.1b). Negative signals (blue/black) in the region of 550 – 750 nm correspond to ground-state bleach (GSB) and stimulated emission (SE), positive signals (yellow/red) around 400 – 550 nm originate from excited-state absorption (ESA). Initially, an ultrafast (≈ 200 fs) relaxation is observable as the ESA and SE shift towards longer wavelengths. Subsequently, the signal decays within tens of picoseconds, resulting in a small remaining signal (≈ 0.75 mOD) of GSB at 633 nm and photoinduced absorption at 660 nm up to a maximum delay of 3.6 ns. Corresponding kinetic traces at selected wavelengths are presented in Fig. 5.1b. The initial ultrafast relaxation is observable through a different signal evolution in the ESA for 500 nm (black) and 517 nm (red). The shift of the SE is visible as a small initial rise at 660 nm (green) and 720 nm (pink). Furthermore, oscillatory behavior can be observed at 633 nm (blue, GSB) during the first 2 ps. To achieve a more detailed interpretation of the relaxation

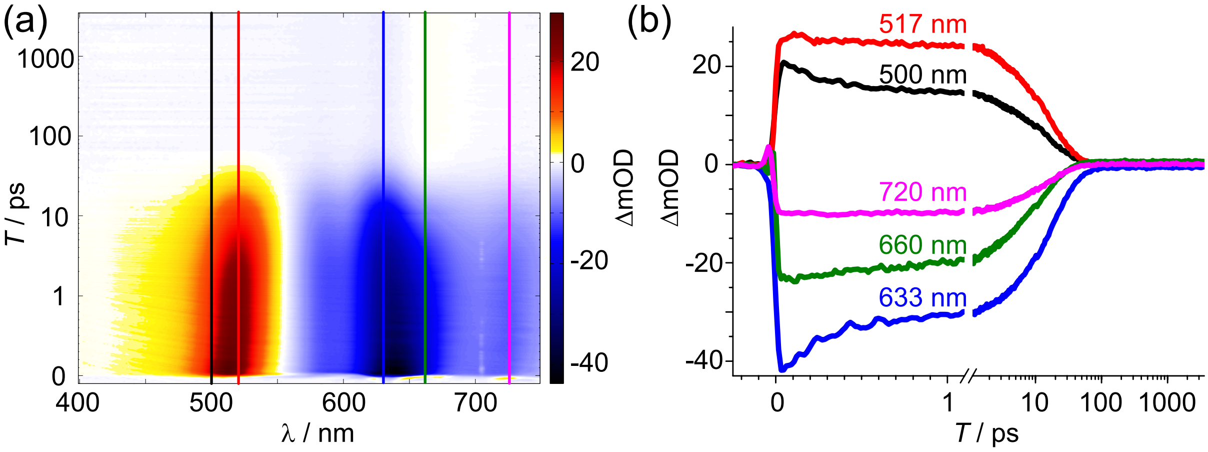

Figure 3.4: (a) Chirp-corrected transient absorption (TA) map of the monomer **1** in DCM upon 630 nm excitation as a function of detection wavelength λ and waiting time T. The T axis is plotted in linear scale up to 1 ps and logarithmically afterwards. Negative signals (blue/black) in the region of 550 − 750 nm correspond to ground-state bleach (GSB) and stimulated emission (SE), positive signals (yellow/red) around 400 − 550 nm originate from excited-state absorption (ESA). The "uneven" vertical signal at ≈ 705 nm is due to a defective pixel of the CCD camera in the spectrometer. (b) Exemplary transients (included as colored vertial lines in (a) display the time evolution of the signals at certain wavelengths. Transients are plotted linearly up to 1.1 ps and logarithmically afterwards, which is indicated by a double break in the T axis, without neglecting data points.

dynamics of **1**, we performed a global analysis of the time-resolved data. Five decay times were prerequisite to fit the data properly. In order to account for permanent remaining signal contributions, one of the time scales was fixed at 10 ns, which is larger than our experimentally accessible delay time. The additional time constants for **1** were found to be $\tau_1 = 213$ fs, $\tau_2 = 1.4$ ps, $\tau_3 = 10$ ps, and $\tau_4 = 17$ ps.

Figure 3.5 shows the decay-associated difference spectra (DADS) for **1** upon 630 nm excitation. The DADS of the ultrafast (213 fs) decay (black) possesses negative contributions around 535 and 635 nm and positive ones around 505, 675 and 735 nm. The shape of the DADS for such an ultrashort time constant leads to the conclusion that the system performs an initial motion away from the Franck–Condon region towards lower-energetic regions of the S_1 potential energy surface (PES). The $\tau_2 = 1.4$ ps component (red) displays a shift towards larger wavelengths in the ESA (510 − 535 nm) and SE (650 − 745 nm) regions. This process can be assigned to vibrational cooling. The $\tau_3 = 10$ ps component (blue) displays a small rise of ESA at 435 nm and a loss of ESA at 515 nm. Furthermore, the SE decays at 658 and 725 nm. The spectral shape of the 10 ps DADS indicates a shift of the GSB and SE signals to shorter wavelengths as the SE decreases stronger than the GSB. The $\tau_4 = 17$ ps component (pink) has the largest amplitude of all DADS. Displaying ESA ($<$ 550 nm), GSB (550 − −660 nm), and SE ($>$ 660 nm) features, it describes the decay of excited-state population to the ground state as all contributions decrease almost completely. The ESA feature can be attributed to the absorption from the first excited state (S_1) to energetically higher-lying excited states (S_n). Furthermore,

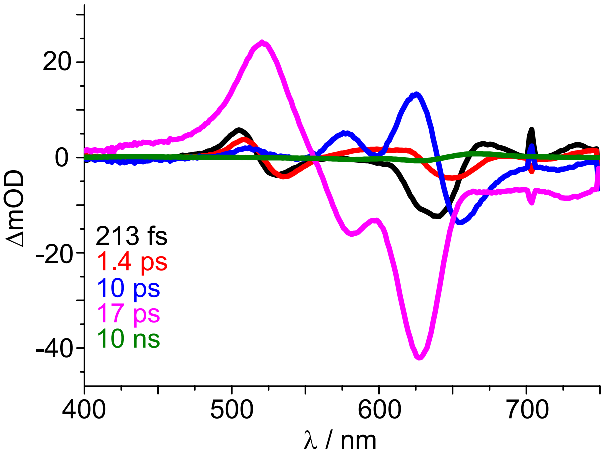

Figure 3.5: DADS and corresponding relaxation times of **1** in DCM upon 630 nm excitation. Five time components are necessary to describe the data properly. The 10 ns time component (green) was fixed to describe the remaining signal at a maximal population time of $T = 3.6$ ns.

the 17 ps component displays a shallow and unstructured SE from $660 - 750$ nm. As mentioned above, the $\tau_5 = 10$ ns component (green) describes a small remaining signal (< 1 mOD) which consists of a GSB and a photoinduced absorption component at 670 nm.

The transient at 633 nm in Fig. 5.1b displays distinct oscillations with a period of $\approx$ 200 fs which decay within the first 2 ps. Such behavior was interpreted as wave-packet motion on the excited-state PES in other merocyanine dyes [152, 153]. Hence, in order to analyze the observed wave-packet dynamics, the underlying decay contribution (determined by the global fit of Fig. 3.5) was subtracted from the raw data. The remaining fit residuals as a function of probe wavelength λ and pump–probe delay T, up to 2.8 ps, are shown in Fig. 3.6a. Distinct oscillations along T are visible in the ESA region at $\approx 500 - 550$ nm and in the GSB and SE region at $\approx 620 - 750$ nm as alternating positive (yellow/red) and negative signals (blue) along T. Prior to a Fourier transformation along T, TA data up to $T = 50$ fs were neglected to exclude distortions in the fit residuals due to the coherent artifact at $T = 0$. Figure 3.6b shows the Fourier transform of the fit residuals along T, yielding two major modes at $\tilde{\nu} = 190$ and 360 cm^{-1}. In the already mentioned recent study of similar dyes, these two modes were assigned to a torsional and vibrational stretching motion, respectively [152, 153]. The resulting phase at the horizontal cut at $\tilde{\nu} = 190$ cm^{-1} of the Fourier-transformed data is shown in the bottom of Fig. 3.6b. Two phase jumps of $\Delta\Phi \approx \pi$ are observable at 533 and 666 nm. These phase jumps correspond to the minimum of the amplitude between the turning points of an oscillating wave packet as observed in another merocyanine system [152, 153] and also in other molecular systems [176, 177]. The maxima of the amplitudes can be assigned to the spectral signatures at the turning points of the wave packet. At one of the turning points an increased transient population with SE at 642 nm and ESA at 512 nm can be observed, whereas on the other reversal point the SE at 682 nm and ESA at 543 nm are enhanced. Thus, we assign the oscillating features to a wave-packet motion in the excited state, as the signatures appear in the spectral regions of ESA and SE.

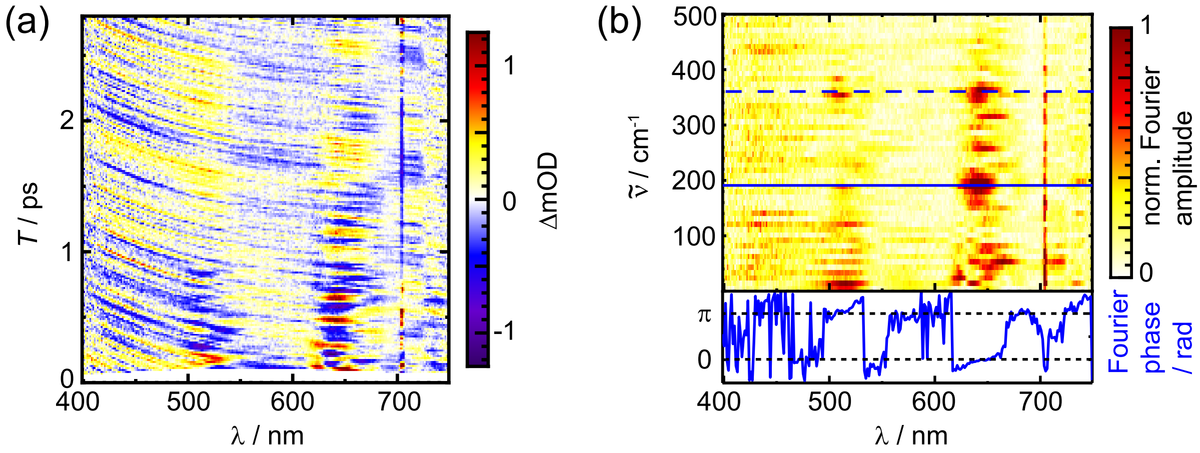

Figure 3.6: (a) Fit residuals of the chirp-corrected TA map of Fig. 5.1a as a function of probe wavelength λ and delay time T up to 2.8 ps. Data up to $T = 50$ fs were neglected to exclude distortions of the coherent artifact. Alternating positive (yellow) and negative (blue) signals along T at $\approx 500-550$ nm and $\approx 620-750$ nm indicate signatures of a coherent vibrational wave packet. (b) Absolute values of the Fourier transform (top) of the residuals along T, displaying distinct amplitudes at 190 cm^{-1} (horizontal solid line) and 360 cm^{-1} (horizontal dashed line), respectively. The phase at 190 cm^{-1} is depicted as a function of probe wavelength λ (bottom).

3.3.2 Relaxation Dynamics of 2p, 2m, and 3

Transient absorption maps, which were measured under the same experimental conditions as for **1** (Subsec. 3.3.1), and DADS for **2p**, **2m**, and **3** are shown in Fig. 3.7. Similar to the TA map of **1** (Fig. 3.4a), all dyes display a (spectrally) broad ESA ($\approx 400-565$ nm) and combined GSB and SE ($\approx 565-720$ nm) signals. Furthermore, a shift towards shorter wavelengths is observable from $\approx 10-100$ ps for the GSB and SE band.

Like for the monomer (**1**) five decay time constants were needed to fit the relaxation dynamics properly for all other molecules (**2p**, **2m**, and **3**). The results of the global analysis are depicted as DADS (like in Fig. 4.6) in Fig. 3.7 (right) for the multichromophore dyes. All dyes display similar relaxation dynamics and spectral changes. The ultrafast relaxation processes occur with ≈ 175 fs and ≈ 1 ps. Subsequently, all dyes are still in the excited state, deducible from the distinct SE and ESA with a lifetime of $10-17$ ps. From the latter excited state two different processes are observable: a partial recovery of the ground state and the appearance of a new ESA at $\approx 400-500$ nm, accompanied by a SE with unstructured, shallow spectral shape. Despite the similar spectral behavior, the lifetime of the excited state is significantly different for the different molecules as it rises from 17 ps (**1**) over 51 ps (**2p**) up to 77 ps (**2m**) and 81 ps (**3**). Furthermore, a 10 ns component (fixed during global analysis) was needed to describe the small (< 1 mOD) remaining GSB and photoinduced absorption signal for all dyes.

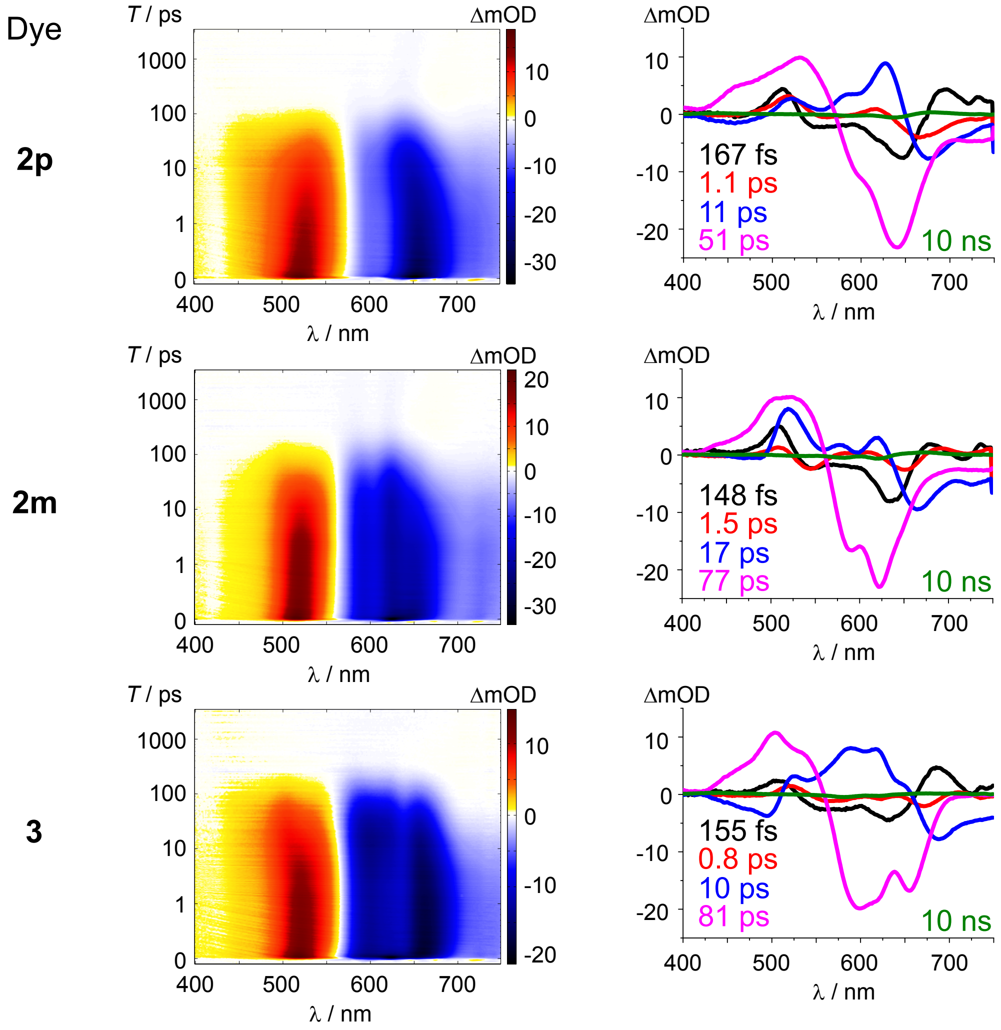

Figure 3.7: Left side: TA maps of **2p**, **2m**, and **3** (from top to bottom) in DCM upon 630 nm excitation. Negative signals (blue/black) in the region of 550 − 750 nm correspond to GSB and SE, positive signals (yellow/red) around 400 − 550 nm originate from ESA. The T axis is plotted with a linear scale up to 1 ps and logarithmically afterwards. Right side: DADS and relaxation time scales resulting from global analysis. Five time components are necessary to describe the data properly. The 10 ns time component (green) was fixed to describe the tiny remaining signal at $T = 3.6$ ns.

3.3.3 Influence of Excitation Wavelength

In order to investigate the influence of excess energy on the relaxation dynamics, we performed TA measurements with narrowband ($\approx 15 - 30$ nm) fs laser pulses centered at 540 nm, 595 nm, and 650 nm, as depicted by arrows in Fig. 3.1b. Similar to the 633 nm excitation in the previous Sections 3.3.1 and 3.3.2, five decay times were necessary to model the time-resolved data properly. The DADS and relaxation time scales result from a global fit and are depicted in Fig. 3.8. The general results and interpretation are comparable to the previous detailed discussion. Hence, here we focus on the qualitative

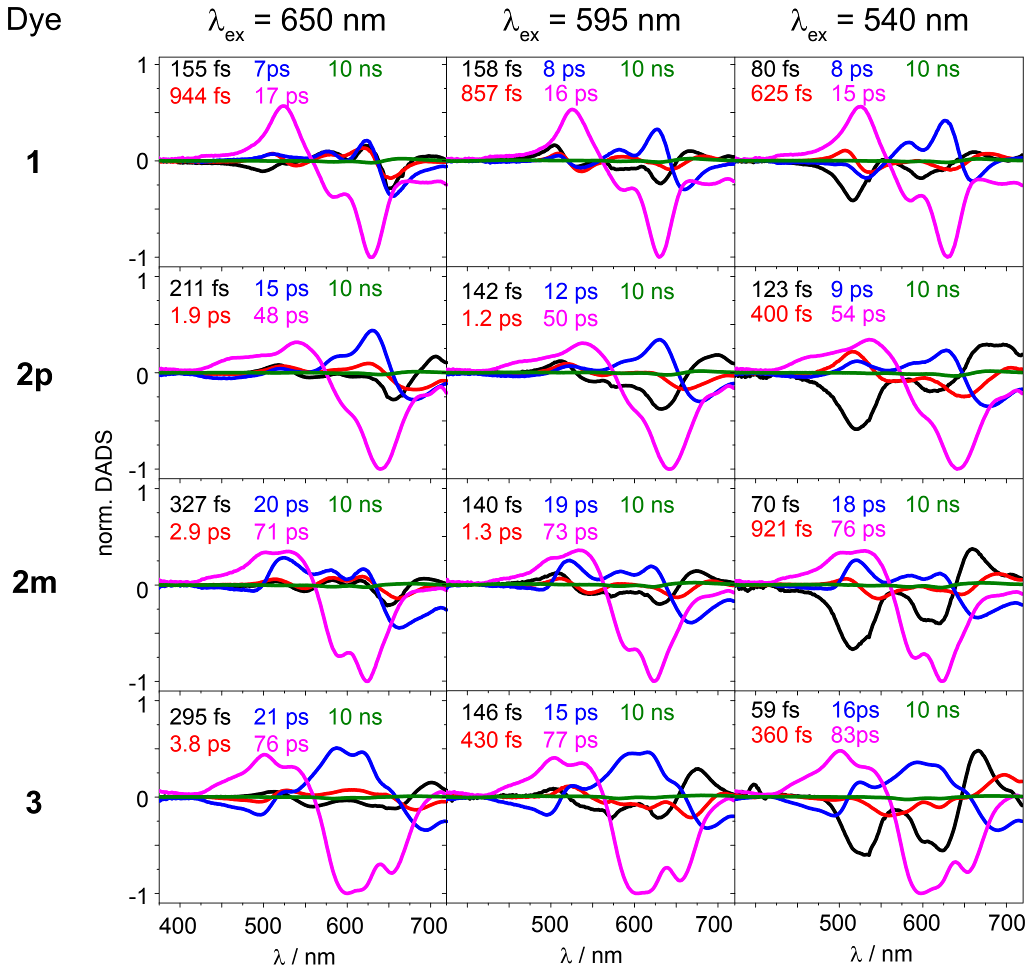

Figure 3.8: Overview of DADS and relaxation times (included in the plots) resulting from global analysis for all dyes (different rows, in the order **1**, **2p**, **2m**, **3** from top to bottom) at different excitation wavelengths λ_{ex} (different columns), namely 650 nm (left), 595 nm (middle), and 540 nm (right). The longest time scale, 10 ns, was kept fixed during fitting to resemble the tiny offset signal for large T values.

trends of the relaxation time scales upon different excitation wavelength.

Comparing the results for the individual dyes in Fig. 3.8 to the previously obersved relaxation dynamics (cf. Fig. 3.5 and Fig. 3.7), the three longest time components τ_3, τ_4, and τ_5 (blue, pink, and green DADS in Fig. 3.8, respectively) display similar spectral and temporal behavior independently of the excitation wavelength. The fixed 10 ns component (τ_5, green) is necessary to fit the remaining GSB and photoinduced absorption and does not change with varying excitation energy. Furthermore, τ_4 (pink) reflects the lifetime in the excited state, while the EADS and DADS of τ_3 (blue) show the loss of SE and a decrease of GSB. Comparing the relaxation time scales and spectral behavior, the three latter relaxation processes (τ_3, τ_4, τ_5) only display minor dependence on the excitation wavelength.

In clear contrast, the first and second relaxation times τ_1 and τ_2 (black and red DADS in Fig. 3.8, respectively) show a significant dependence on the excitation wavelength. For all dyes a smaller excitation wavelength (higher excitation energy) leads to a decrease of the relaxation time scale for both initial relaxation times. The first relaxation time scale τ_1 decreases from a few hundred fs down to a sub-100 fs component. Similarly, the subsequent relaxation τ_2 decreases from a few ps at 650 nm excitation down to a sub-ps time scale at 540 nm. Hence, excitation with higher energy leads to faster initial relaxation. It is difficult to discriminate one concrete process, which leads to this wavelength dependency, as it can either imply a relaxation via an energetic barrier which has to be overcome [164], a different initial starting point on the PES, or it can comprise ultrafast dynamics due to an intramolecular charge-transfer (ICT) state known to be formed by merocyanines.

3.3.4 Coherent 2D Spectroscopy

Coherent 2D spectroscopy gives access to additional information in comparison to TA spectroscopy, as not only the detection axis for every waiting/population time T is energy-resolved, but also the excitation axis. Thus, this auxiliary observable of the correlation between excitation and detection energy allows direct identification of couplings between different absorption bands and the influence of the excitation energy on dynamics. More specifically, one can deduce the energy transfer between different states and observe chemical processes, e.g., a photoinduced isomerization of an initially excited reactant. Coherent 2D spectroscopy was performed in the previously mentioned TA setup with laser excitation pulses depicted in Fig. 3.1 (gray). To obtain 2D data in TA geometry, the coherence time τ was varied by the pulse shaper, from 0 fs up to 109.5 fs in 1.5 fs steps, for every T, applying a three-fold phase-cycling scheme [103, 104, 107, 178]. Purely absorptive 2D spectra were generated by Fourier transformation along τ and taking the real part. 2D spectra for short population times were chirp corrected by measuring T from -600 to $+600$ fs in steps of 30 fs and subsequently from $T = 700$ fs to $T = 1.3$ ps in 100 fs steps [118]. 2D spectra for population times from 10 to 70 ps were not chirp corrected.

Figure 3.9 shows 2D spectra for all dyes of this study at selected T, ranging from 30 fs (left column) up to 70 ps (right column). To facilitate the comparison to the previous TA studies, signals corresponding to GSB and SE (blue/black) are plotted as negative signals, while ESA contributions (yellow/red) are plotted as positive signals.

At $T = 30$ fs all dyes display strong diagonal ($|\tilde{\nu}_\tau| = |\tilde{\nu}_t|$, compare black line) signal contributions, which are coupled to distinct SE features at $\tilde{\nu}_t \approx 1.4 \times 10^4$ cm^{-1} and ESA features at $\tilde{\nu}_t \approx 1.9 \times 10^4$ cm^{-1}, respectively, rather independently of $\tilde{\nu}_\tau$. With evolving population time T, the 2D signal for all dyes changes from a diagonally elongated 2D signal at $T = 30$ fs to horizontally orientated peaks at $T \approx 1$ ps. From $T = 1$ ps up to $T = 70$ ps, besides an overall signal decay, a vertical shift to higher $\tilde{\nu}_t$ of the GSB and SE signal can be observed. Similar to the observations and interpretations of the previous TA studies, this shift can be explained by a faster decay of SE, at lower $\tilde{\nu}_t$ than the remaining GSB, during the relaxation processes. After $T \approx 1$ ps all dyes display only a minor wavelength dependence of the 2D signal. This is in distinct difference to previously studied merocyanine systems, which displayed excitation-wavenumber-dependent signatures for a photoinduced isomerization [152, 153]. Thus, coherent 2D spectroscopy

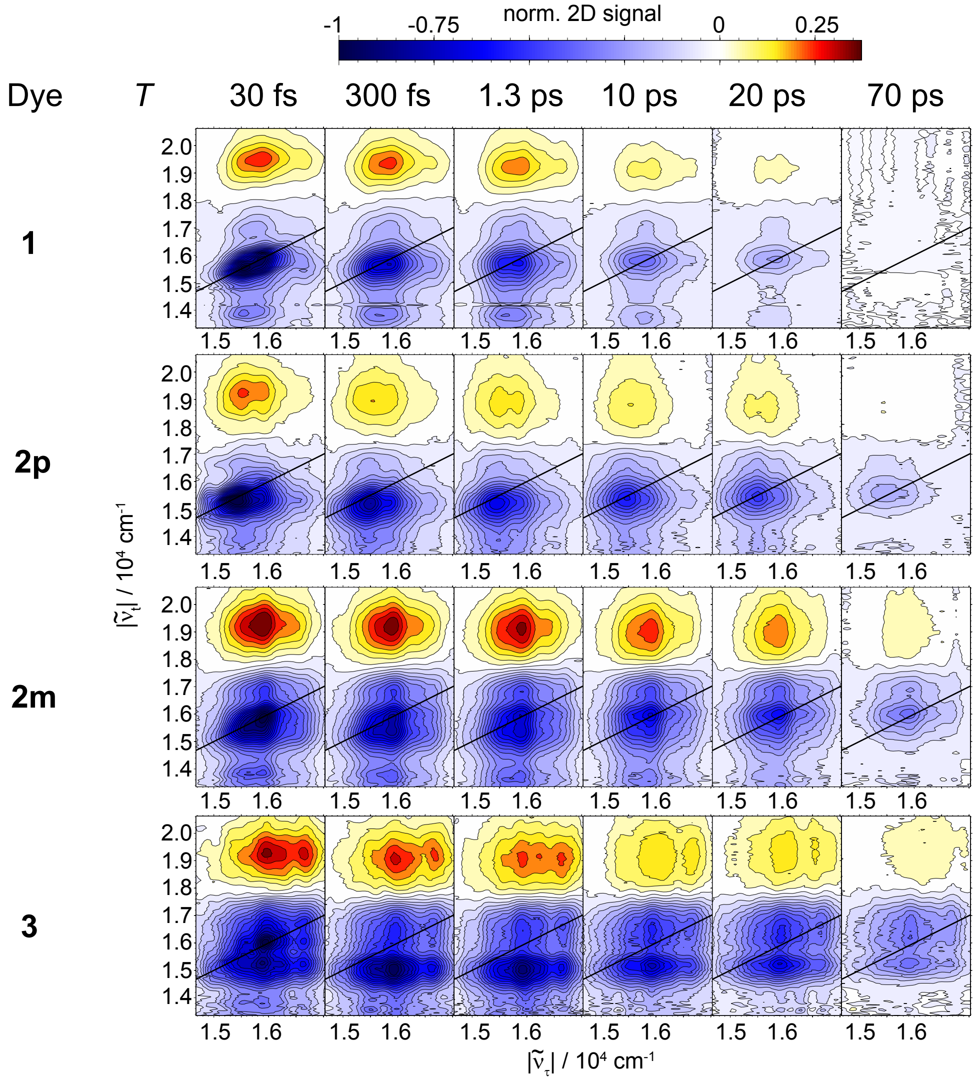

Figure 3.9: Absorptive 2D spectra for (from top to bottom row) **1**, **2p**, **2m**, and **3**, are plotted as a function of excitation $\tilde{\nu}_\tau$ and detection wavenumber $\tilde{\nu}_t$ for selected population times (different columns). Negative signals (blue/black) are plotted to correspond to ground-state bleach (GSB) and stimulated emission (SE), positive signals (yellow/red) originate from excited-state absorption (ESA). Contours are plotted in steps of 5% of the maximal, normalized signal at $T = 30$ fs.

allows the exclusion of an isomer equilibrium in solution prior to excitation and photoinduced isomerization reactions as dominant reaction channels for all investigated dyes of this study.

Regarding the interaction between the different absorption bands (compare Fig. 3.1) the 2D signals for the corresponding range ($\tilde{\nu}_\tau$ and $\tilde{\nu}_t$ from $\approx 1.5 - 1.7 \times 10^4$ cm^{-1}) are discussed in the following. The monomer **1** displays two distinct cross peaks at $(\tilde{\nu}_\tau, \tilde{\nu}_t) = (1.58, 1.68) \times 10^4$ cm^{-1} and $(\tilde{\nu}_\tau, \tilde{\nu}_t) = (1.68, 1.58) \times 10^4$ cm^{-1}, which correspond to the absorption maximum at 633 nm and the absorption band of the vibrational progression (as coupling to other chromophores can be excluded) at 595 nm, respectively. Thus, if one of the absorption bands is excited, both bands display a GSB due to the coupling via a common ground state. The diagonal peak at $(\tilde{\nu}_\tau, \tilde{\nu}_t) = (1.68, 1.68) \times 10^4$ cm^{-1} displays only a small GSB signal which indicates either a fast relaxation to lower energetic states, a weaker signal due to a smaller extinction coefficient of the higher energetic band (see Fig. 3.1), or alternatively an overlapping ESA contribution.

Similar to **1**, **2p** exhibits distinct cross peaks for all T up to 20 ps between its absorption bands at $(\tilde{\nu}_\tau, \tilde{\nu}_t) = (1.55, 1.66) \times 10^4$ cm^{-1} and $(\tilde{\nu}_\tau, \tilde{\nu}_t) = (1.66, 1.55) \times 10^4$ cm^{-1} (645 and 602 nm). Furthermore, a weak higher-energetic diagonal peak at $(\tilde{\nu}_\tau, \tilde{\nu}_t) = (1.66, 1.66) \times 10^4$ cm^{-1} is observable. The increase in lifetime of **2p** compared to **1** can be inferred indirectly by the stronger remaining 2D signal contributions at $T = 70$ ps.

2D spectra of **2m** display a more complex structure than those of **1** and **2p**. Additionally to the cross peaks between the absorption maxima (626 and 598 nm) at $(\tilde{\nu}_\tau, \tilde{\nu}_t) = (1.60, 1.69) \times 10^4$ cm^{-1}, the cross peak $(\tilde{\nu}_\tau, \tilde{\nu}_t) = (1.69, 1.60) \times 10^4$ cm^{-1} is only indicated as the signal at $\tilde{\nu}_t = 1.60 \times 10^4$ cm^{-1} is elongated to larger $\tilde{\nu}_\tau$. Furthermore, a distinct signal at $\tilde{\nu}_t = 1.54 \times 10^4$ cm^{-1} is observable up to 1.3 ps, which displays the coupling from GSB to SE. With evolving population time, the SE decays stronger than the GSB and ESA, leading to a rather small SE signal contribution with remaining GSB and ESA at 70 ps.

For **3**, the three absorption bands at 652, 623, and 598 nm are already visible in the 2D spectrum at $T = 30$ fs as diagonal peaks at $\tilde{\nu}_\tau = \tilde{\nu}_t = 1.53$, 1.61, and 1.67×10^4 cm^{-1}, respectively. Furthermore, the coupling between the latter absorption bands is visible as cross peaks to energetically lower absorption bands below the diagonal ($\tilde{\nu}_t < \tilde{\nu}_\tau$). Already at $T = 300$ fs most of the signal relaxed to a strong combined GSB and SE signal at $\tilde{\nu}_t = 1.53 \times 10^4$ cm^{-1}. For larger T, the SE decays similar to **1**, **2p**, and **2m**, leading to a weak SE with GSB and ESA remaining at 70 ps.

In general, 2D spectroscopy of all studied dyes displays the coupling between the different absorption bands observed in linear absorption. Due to the pulse duration of $\tau_p \approx$ 20 fs and the limited spectral width of the pulses an unambiguous determination of the coupling mechanism (purely excitonic, vibronic, or a mixture of both) of the absorption bands is difficult. Extremely broadband laser pulses might lead to a clear discrimination of the origin of the absorption spectra in future studies. Nevertheless, already the current 2D spectra allow us to conclude that there is no significant mixture of isomers in solution. Furthermore, no indication for a photoinduced isomerization process is observed, in contrast to previous studies performed on other merocyanine systems [150–153, 155–157].

3.3.5 Relaxation Model

Having described the results of TA and 2D spectroscopy, we now aim at proposing a general relaxation model for all investigated (multi)chromophoric dyes. Figure 3.10 shows the relaxation scheme based on the spectroscopic observations for **1**, which indeed can be adapted successfully to all multichromophore dyes (**2p**, **2m**, and **3**) as shown below. Directly upon laser excitation (orange arrow) the population in the first excited state

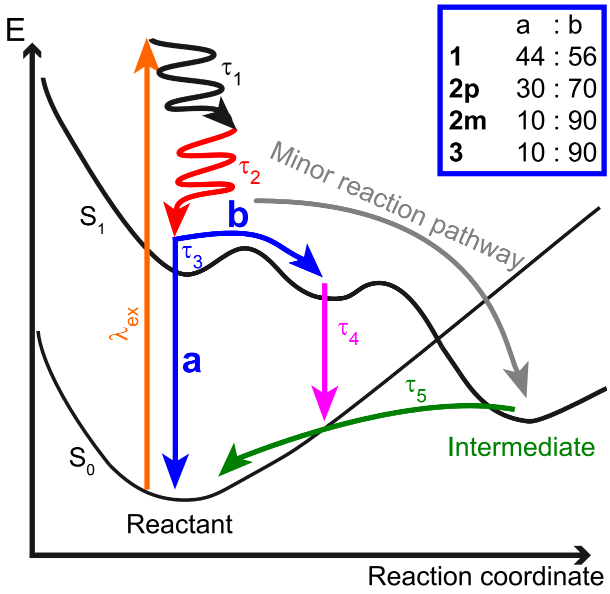

Figure 3.10: Relaxation scheme for all studied dyes based on the performed spectroscopic measurements. Upon vertical $S_0 \rightarrow S_1$ excitation (orange, λ_{ex}) the energy relaxes via a wave-packet motion (wiggly arrows) dynamically to a local minimum on the PES which is described by two initial relaxation processes τ_1 (black) and τ_2 (red). From this local minimum the relaxation pathway splits up within τ_3 (blue). Either the system relaxes back to the initial ground state via pathway a, or it further relaxes to another minimum via pathway b. From the latter minimum the relaxation back to the ground state occurs with τ_4 (pink), which determines the S_1 lifetime of the dye. Small spectral indications, i.e., the remaining GSB and photoinduced absorption, suggest a further minor relaxation pathway (gray) to a long-lived intermediate state that relaxes back to the electronic ground state with τ_5 (green), beyond our accessible experimental time window. Results of the target analysis displaying the relaxation pathway ratios for pathways a and b are stated in the inset.

(S_1) moves away from the Franck–Condon window within ≈ 175 fs, which is reflected in τ_1 (black arrow). Furthermore, vibrational relaxation takes place within ≈ 1 ps (τ_2, red arrow). The first 2 ps of the relaxation processes are accompanied by ultrafast oscillations with a period of ≈ 200 fs, which can be assigned to torsional and vibrational modes of **1**, as previously observed for other merocyanines [152–154]. Therefore, after excitation the system effectively dissipates excess energy by nuclear motions, namely torsion and vibration. It should be mentioned that an assignment of two primary relaxation time scales might be a physically incorrect description as a typical wave-packet motion is a dynamic and not a kinetic process [165]. However, the description with two kinetic time constants is sufficient to model the data phenomenologically. After these initial relaxation steps, the system is still in the excited state, as observable from the SE and ESA features for all studied molecules. From this stationary point of the PES the proposed relaxation scheme splits up within τ_3 into pathways a and b (labeled blue arrows). Pathway a directly repopulates the electronic ground state S_0, leading to a partial GSB recovery. Most of the population relaxes via pathway b to another minimum of the excited-state PES which is characterized by a shallow SE and a new ESA band at shorter wavelengths. The rise of an ESA band is explicitly observable as a negative contribution in the blue DADS between 400 and 500 nm for **2p**, **2m**, and **3** (Fig. 4.6). We assign this state to a minimum on the S_1, which relaxes with τ_4 (pink arrow), as it clearly displays ESA and SE features, in contrast to a supposed hot ground state or a relaxed isomer. Thus, the relaxation time scale τ_4 determines the lifetime of the excited state for all dyes. There is probably a further pathway (gray arrow) which leads to a long-lived intermediate and

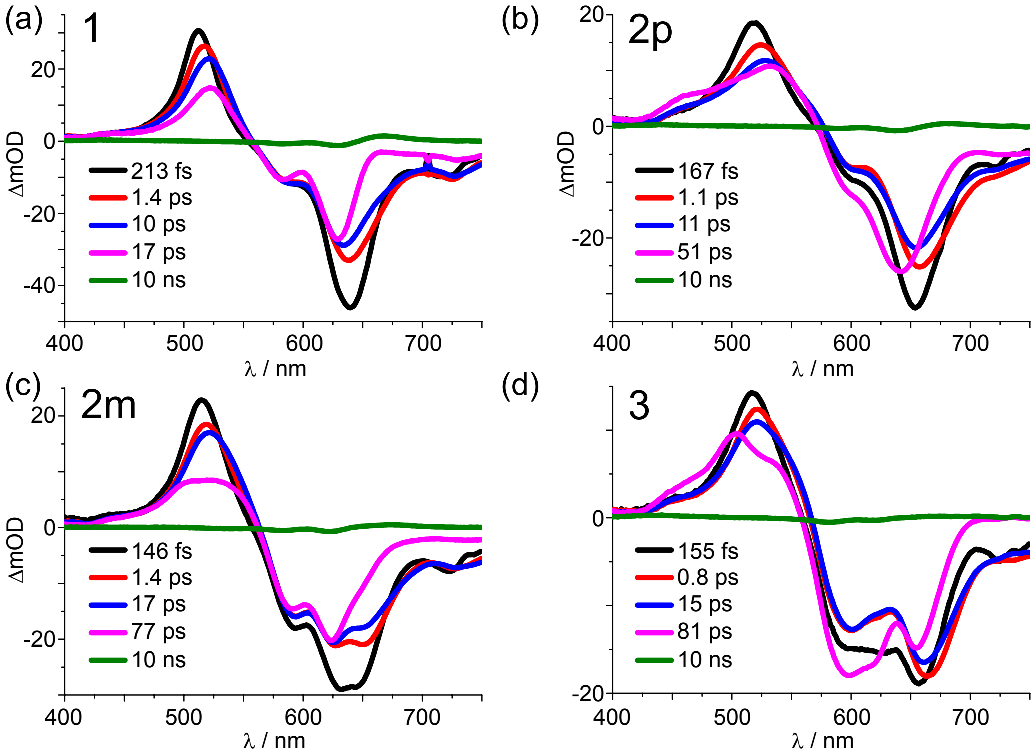

Figure 3.11: Species-associated difference spectra of **1** (a), **2p** (b), **2m** (c), and **3** (d) for TA data with excitation pulses centered at 630 nm (see gray spectrum in Fig. 3.1).

thus to the remaining GSB and photoinduced absorption that may return to the initial ground state only after times of $\tau_5 > 10$ ns (green arrow), compare the DADS in Fig. 4.6. As the spectral indications of this component are rather small (< 1 mOD), we assign the latter process to a minor relaxation pathway, perhaps evolving through a conical intersection [159–163, 179].

To validate and quantify the proposed relaxation scheme in Fig. 3.10, a target analysis was performed, investigating the branching ratio from the excited state relaxing with τ_3 towards the ground state (pathway a) and towards the additional minimum in the excited-state PES relaxing with τ_4 (pathway b), respectively. As a feedback for the target it was required that the GSB from the species-associated difference spectra (SADS, see Fig. 3.11) which relaxes with τ_4 (SADS$_4$) should not have a larger amplitude than SADS$_3$. For **2p** and **3** such a behavior of the GSB was observed in some spectral regions, as the overlapping ESA contributions decay faster. Therefore, we fitted a branching ratio that could reproduce the GSB at ≈ 650 nm. The ratio b:a (cf. Fig. 3.10) can be interpreted as an upper limit for the fraction of the excited-state population which relaxes via the longer-lived second minimum on the excited-state minimum, i.e., species SADS$_4$, compared to the fraction of the excited-state population which directly undergoes internal conversion to the ground state. For all investigated dyes this scheme could be applied, leading to the ratios summarized in the inset of Fig. 3.10. For **1** the target model leads to a relaxation branching ratio of almost equal amounts in pathways a and b. This result might be affected by the similarity of the relaxation time scales τ_3 and τ_4 for **1**. Thus, the contributions of the relaxation occurring with τ_3 and τ_4 cannot be distinguished unambiguously. For **2p** a major fraction of the population relaxes by pathway b to SADS$_4$, instead of directly relaxing to the ground state. For **2m** and **3** almost all of the population relaxes via pathway b. The branching ratios of the dyes echo the trend observed for the lifetimes nicely, as for the increase of the lifetime from **1**, over **2p**, to **2m**, and finally to **3**, the branching ratios display a favored relaxation by pathway b.

Similar relaxation models with double-minimum excited-state PES were proposed for other D–A systems, rationalized by a change of electron density or conformation [154, 159–161, 164, 180–183]. Changes of the electron density occur upon localized excitation, i.e., exciting only the D or A moiety of a merocyanine (first minimum), which is equilibrated with a CT state (second minimum) [180–183]. Hence, the relaxation might occur from the locally excited or the CT state. For merocyanines which are close to the cyanine-limit, this szenario is rather unlikely as the delocalization of the electron density does not change upon excitation [170]. Still, it cannot be excluded that an initially excited CT state relaxes to an additional CT state which displays a complete charge separation. Additionally to changes in the electron density, the double minimum on the excited-state PES was proposed to originate from conformational changes, e.g., a planarized or twisted structure. Such structural changes break the conjugation of the π-electron system and might lead to an isomerization as observed for similar merocyanine systems [112, 150–154]. The oscillatory behavior within the first few picoseconds of the relaxation for **1** indicates enhanced vibrational and rotational motion of the polyene linker upon excitation. Additionally, the small photoinduced absorption feature up to $T = 3.6$ ns indicates an isomerization via the minor relaxation pathway. Thus, the double minimum on the excited-state PES might be based on structural changes in the excited state, which is followed by a structural relaxation back to the initially excited conformation.

3.4 Chromophore Interaction and Orientation

The presented results in the Sections 3.2 and 3.3 demonstrate clearly that the chromophores of the bis- and tris-merocyanines under investigation are interacting. This becomes obvious from the substantial differences in the linear absorption spectra presented in Fig. 3.1 already, but also the results of EOA and TA experiments show deterministic variations; the origin of the chromophore interactions is now discussed.

Within perturbation theory the interaction between chromophores can be distinguished between the strong and the weak coupling regime, which leads to a delocalized or a localized excitation, respectively. In the weak coupling regime, the interaction between chromophores is described either via coulomb interaction or exchange interaction. The former interaction is characterized by a strong, long-range and through-space coupling, which leads in the weak-coupling regime to Förster energy transfer [39]. Alternatively, the coupling is described via exchange interaction, which is a weak, short range and through-bond coupling. The exchange interaction leads to the so-called Dexter energy

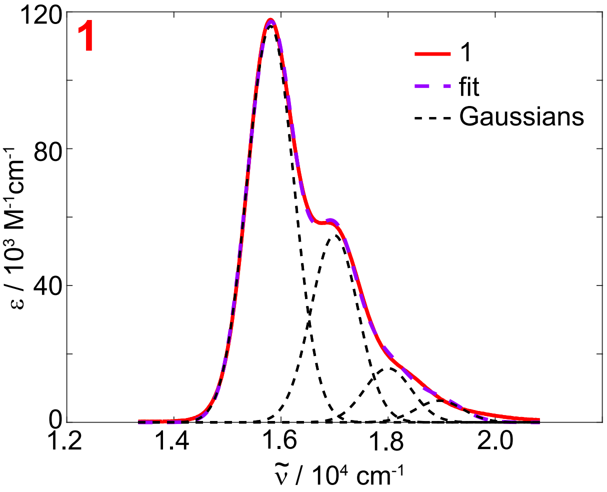

Figure 3.12: Linear absorption of **1** (red), fitted by four Gaussians with identical widths (439 cm^{-1}), and fit result (purple, dashed). Details of the fitting routine are given in the text.

transfer [40].

The molecules under study are not fluorescent at all, such that Förster energy transfer is not applicable, leaving us with the possibility of a Dexter-like energy transfer. This requires a rather close proximity of donor and acceptor chromophore below one nanometer. Since the benzene bridge is only about 0.4 nm in size this interaction mechanism seems possible. The corresponding electron transfer from one chromophore to the other would thus lead to a charge-transfer state in the excited state, which can be elucidated in TA experiments. The time-resolved results however display a longer excited-state lifetime for **2m** compared to **2p** while the distance between the chromophores is smaller in **2m** (cf. Table 3.2). Hence, Dexter energy transfer seems also not applicable.

In the case of a strong inter-chromophoric coupling, molecular excitation leads to a delocalized excitation, which can be treated via exciton theory, following the seminal work of Kasha [31]. The exciton coupling energy V in dipole–dipole approximation can be calculated via

$$V = \frac{1}{4\pi\varepsilon_0}\frac{|\mu_A||\mu_B|}{R^3}\left[\cos(\theta_{\mathrm{AB}}) - 3\cos(\theta_{\mathrm{A}})\cos(\theta_{\mathrm{A}})\right], \tag{3.4.1}$$

where ε_0 corresponds to the dielectric constant in vacuum, while μ_A and μ_B correspond to the two interacting transition dipole moments which are separated by the distance R. The angles θ_{A} and θ_{B} refer to the angles enclosed by the respective transition dipole moment with the connection axis of the point dipoles, and θ_{AB} refers to the angle between both transition dipole moments. In Table 3.2, the corresponding values derived from the geometry optimization of the DFT calculations (cf. Sec. 4.2) are presented. The results indicate an exciton coupling energy V_{DFT} for **2m** which is roughly twice the one of **2p**.

To compare these values with experimental results we turn again to the linear absorption spectra and try to model these. The spectrum for **1** can be modeled with four Gaussians corresponding to the $\mathrm{S}_0 \rightarrow \mathrm{S}_1$ transition and its vibrational progressions. Hence, the four Gaussians were forced to have the same width. The resulting energetic distances (see Fig. 3.12) are thus approximately identical. To resolve the excitonic splitting, two more

Table 3.2: Overview of the determined angles and distances between two chromophores for **2p** and **2m** based on the structural optimization by DFT. Additionally, the exciton coupling energies, which are determined by exciton theory V_{DFT} and determined by the fit of Gaussian functions to the linear absorption spectra V_{fit} (cf. Fig. 3.13), are given.

Dye	θ_A / °	θ_B / °	θ_{AB} / °	R / Å	V_{DFT} / cm^{-1}	V_{fit} / cm^{-1}
2p	119.50	119.55	0.00	8.39	249	700
2m	105.70	131.53	18.60	7.33	568	647

Gaussians (again with the identical width) were included to model the absorption spectra for **2p** and **2m** since no pure H- or J-type coupling can be expected. For this fit the positions (and widths) of the four Gaussians used to fit the spectrum of **1** were kept fixed and only their amplitudes were allowed to vary. The results (see Fig. 3.13 and Tab. 3.2) indicate coupling energies of $V_{\mathrm{fit}}^{\mathbf{2p}} = 700\ \mathrm{cm}^{-1}$ and $V_{\mathrm{fit}}^{\mathbf{2m}} = 647\ \mathrm{cm}^{-1}$. Both values ($V_{\mathrm{fit}}$) are larger than the theoretical ones (V_{DFT}, cf. Tab. 3.2). This observation can be rationalized by taking into account that V_{DFT} values are based on the geometry-optimzed structures of the DFT calculations and represent the energetically minimized structures in the gas phase. Already in the EOA measurements a certain degree of flexibility and structural distribution could be deduced. Therefore, to evaluate the influence of the relative chromophore orientation on V, the exciton splitting energy for slight deviations of the DFT results were calculated. In these calculations of V one chromophore of the bischromophoric systems (**2p** and **2m**) was fixed in space with the coordinates obtained by DFT. Figure 3.14 depicts the chemical structures and calculated V by variation of the

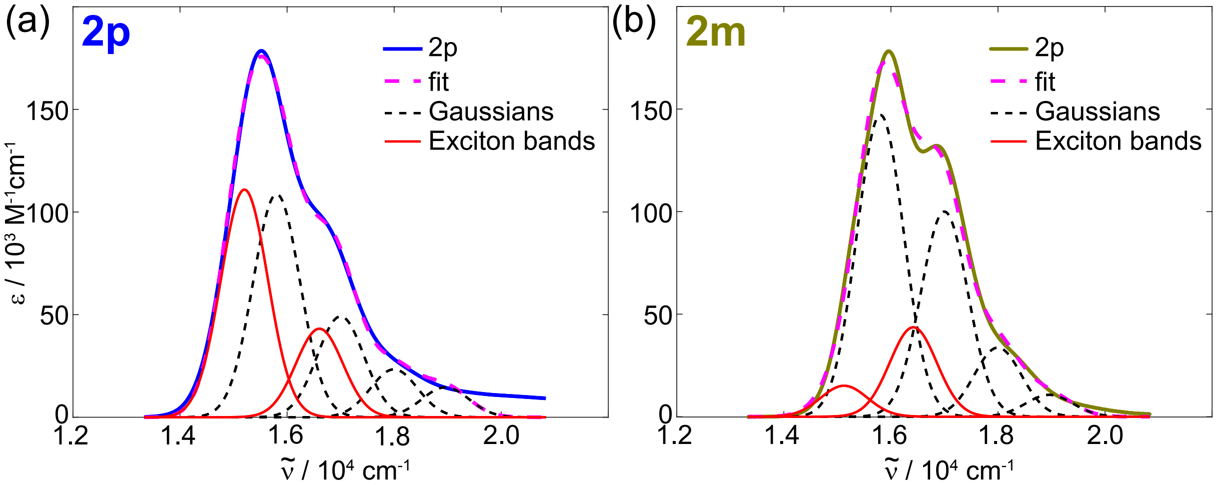

Figure 3.13: Linear absorption (blue and brown), four Gaussians with the positions of the fitted absorption spectrum of **1** (black, dashed) with optimized amplitudes (see Fig. S3 and Tab. S1), and additional two gaussians to represent the excitonic bands (red, solid) for **2p** (a) and **2m** (b), respectively. The fit result for both dimers is shown in dashed pink lines. Details of the fitting routine are given in the SI.

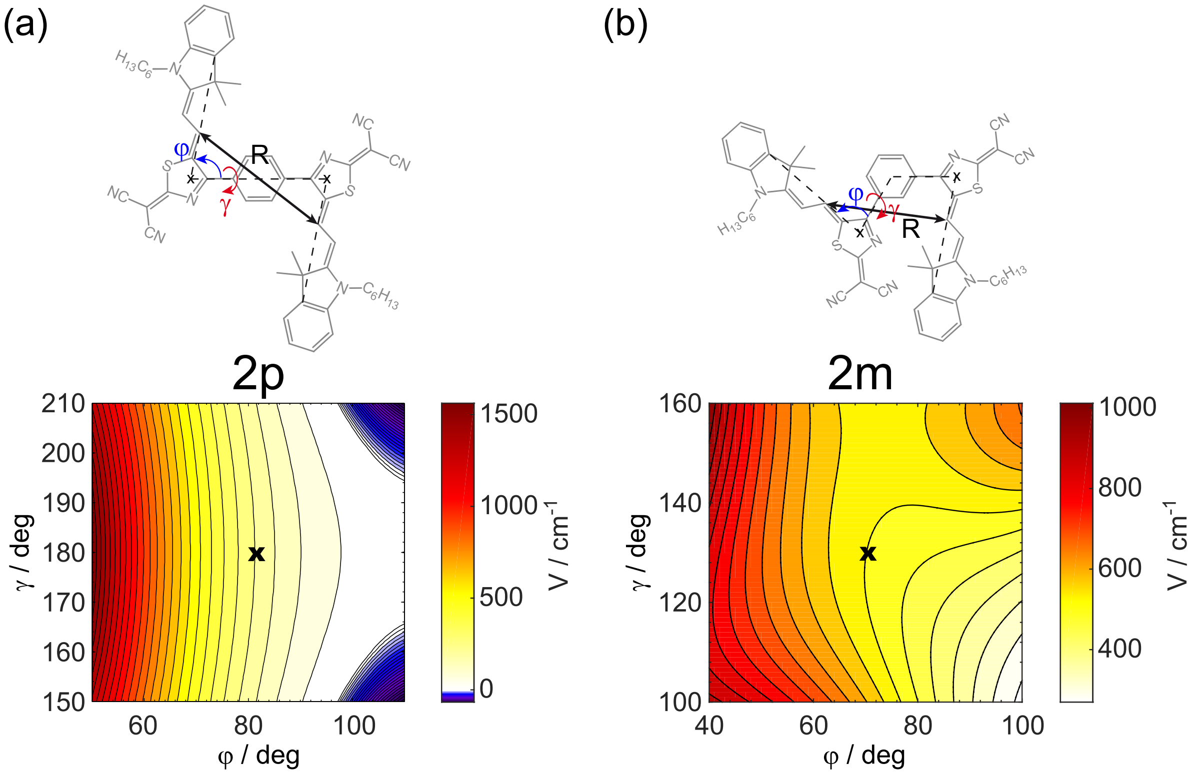

Figure 3.14: Molecular structure and exciton splitting energy V in dependence on the chromophore tilting angle φ and the rotation angle γ for **2p** (a) and **2m** (b), respectively. For the calculation of V the optimized structures of the DFT calculations were set as starting geometries (marked as crosses in the center of the lower two maps). Subsequently, one chromophore was fixed in this geometry, the other chromophore was varied in φ and γ. The resulting R, θ_{AB}, θ_A, and θ_B values were utilized to calculate V via Eq. 3.4.1.

second chromophore by its tilting angle γ and rotation angle φ (which are not identical to θ_{AB}, θ_A, and θ_B, but determine the latter angles and R for Eq. 3.4.1). While V of **2p** only displays minor changes in the variation of γ, a distinct dependence on φ can be observed. Changes of φ of $\approx 10°$ easily approach $V \approx 700$ cm^{-1}, which are obtained by $V_{\text{fit}}^{\mathbf{2p}}$ (cf. Tab. 3.2). In contrast, **2m** displays strong variations in V in dependence on both angles, φ and γ. This observation can be rationalized by the proximity of the two chromophores in **2m**. Similarly to **2p**, $V_{\text{fit}}^{\mathbf{2m}}$ are accessed by small variations of φ and γ by $\approx 10°$ of one chromophore. As only one chromophore is varied in its orientation to the fixed other chromophore, it should be pointed out that large V values are accessible already by the flexibility of one chromophore and are even more probable for variations of both chromophores.

The fits of the linear spectra of **2p** and **2m** (cf. Fig. 3.13) can be interpreted as quasi-flexible systems which consist of a contribution of a "monomer" and a "dimer" spectrum. For distinct relative chromophore orientations, V might be rather small and negligable compared to the absorption bandwidth and the merocyanine dimer displays a monomer-like absorption spectrum. In contrast, small variations in the tilting angle lead to rather large V values which can be described by exciton theory [31]. Additionally, the strong interaction between the chromophores leads to a distinct increase in excited-state lifetime as observed by TA spectroscopy. The flexibility of the molecular systems and the accompanied influence on the linear absorption spectra make it comprehensible why an unambiguous structural characterization by NMR and X-ray can be difficult or even impossible, like in this case, for such systems.

3.5 Conclusion

Molecular structure determination is a fundamental step in the investigation of reaction mechanisms and supramolecular design. Experimental and theoretical approaches provide excellent tools for the determination of energetically stable structures. Still, each approach exhibits its own limitations, e.g., a crystal structure depends on the crystallization conditions, couplings in NMR may be absent, and DFT geometry optimization can approach a local and not the global minimum of a molecular structure. Alternative approaches are helpful to investigate interactions between chromophores, and thus obtain insight into structure and function.

Electro-optical absorption (EOA) provided structural information for multichromophoric merocyanines by measuring the dipole moments in the excited and ground states. Additionally, spectral changes indicated a localization of the excitation on a single chromophore by the applied external electric field in dimeric compounds. These observations led to a conformational assignment for the multichromophoric system that compensates most of the ground-state dipole moment of the individual chromophores.

This structural assignment could be supported by DFT calculations. Starting from different geometries, the para-substituted dimer (**2p**) displayed the energetically most stable conformation with the two chromophores pointing in mutually opposite directions. For the meta-substituted dimer (**2m**) an orientation for which both chromophores point in different directions was observed.

Additionally, transient absorption and 2D spectroscopy data led to a relaxation model which described all measurements. The relaxation model comprises two local minima in the first excited state. Directly after laser excitation a coherent wave packet could be observed, which relaxes into the first local minimum. From there the relaxation splits up either directly towards the ground state as internal conversion or towards another local minimum. This second local minimum on the potential energy surface is assigned to an intramolecular charge-transfer (ICT) state. Due to the varying substitution pattern with dipolar chromophores in the neighborhood the ICT state is stabilized in different amounts, leading to a strong variation in excited-state lifetime.

Lastly, by analyzing the effect of chromophore orientation on the exciton splitting energy (V), it could be shown that experimentally observed values are accessible by slight changes of the relative chromophore orientation. The linear spectra thus display a superposition of monomeric and excitonic contributions validating the conclusions from EOA, DFT, and TA spectroscopy. By combining experimental results (EOA and TA spectroscopy) and calculations (DFT) all information are funneled with the help of exciton theory into an extended understanding of a flexible multichromophoric molecular system in solution. This approach will lead also to valuable results for other comparable molecular systems and might be a useful tool for elucidating new insights into supramolecular design.

CHAPTER 4

Energy Transfer Between Squaraine Polymer Sections

In comparison to the previous studied mono-, di- and trimer merocyanines in Chapter 3, the polymeric squaraine dyes investigated in this chapter display an increasing structural complexity. Still, squaraines and merocyanines are highly related as both are classified as cyanine-like chromophores. The work presented in this chapter is a cooperation with the research groups of Prof. Dr. Christoph Lambert, who previously synthesized the polymer [184] and performed transient absorption experiments, and the group Prof. Dr. Roland Mitrić, who performed advanced density functional theory calculations. The content of Sections 4.1–4.5 has previously been published in Ref. [3].

The absorption spectrum of the investigated squaraine polymer indicated the presence of two different structural species within a polymer. Hence, this unique situation provides the opportunity to study the relaxation and interaction of different structural segements within a single polymer strand. These observations allow a comparison of squaraine polymers to other polymers based on very small monomers, e.g., MEH-PPV, which is studied in Chapter 5.

After a brief introduction and literature overview of conjugated polymers in Section 4.1, computations are presented in Section 4.2, which confirm the previously assigned features in the linear spectra to *zigzag* and *helix* segments within the squaraine polymer. Subsequently, TA experiments and both the affiliated global and target analysis is presented, which describes the complex relaxation within and between the different structural confirmations of the polymer. In addition, coherent 2D spectroscopy in Section 4.4 confirms the ultrafast relaxation dynamics. Lastly, the results are summarized in Section 4.5.

4.1 Introduction

For the development of various optoelectronic devices, e.g., organic photovoltaics, understanding energy-transfer processes in conjugated polymers is essential [185–194]. Low-molecular-weight polymers typically exhibit structural flexibility on timescales of several nanoseconds. In contrast, conjugated polymers may behave totally differently due to their larger molecular weight, which leads to slower structural dynamics. Additionally, conjugated polymers usually display a distribution of local conformations, which influences ultrafast dynamics of electronic processes in optical devices, e.g., exciton diffusion or charge migration [195–205]. In order to understand fundamental properties of conjugated polymers, it is crucial to gather insights into the relation of electronic processes in conjugated polymers and their microscopic or superstructure in solution and in the solid state [206]. Studying conjugated polymers in solution allows a restriction to defined polymer structures. These results can be attributed to properties of local structures within a bulk material [207–211]. However, the information of the influence of different local structures within a single polymer strand is still lacking. The latter information is rather important as conjugated polymers display a variety of local structures, which complicates the assignment of discrete energy transfer processes, as e.g., indications for energy transfer along a polymer strand (intramolecular energy transfer) and between different polymers (intermolecular energy transfer) may overlap. Studying conjugated polymers under diluted conditions excludes interactions between different polymers (e.g. intermolecular energy transfer), thus, allows to study different local structures within a single polymer chain. Recently studied squaraine homopolymers under diluted conditions displayed a different amount of *zigzag* and *helix* segments within a single polymer strand depending on the solvent [184, 212–215]. Hence, squaraine homopolymers allow a detailed investigation of photo-induced dynamics within a conjugated polymer strand depending on the local superstructure, which can be tuned by the choice of the solvent.

Generally, polymeric low-molecular-weight squaraines have gained much attention in recent years [216] due to their cyanine-like behavior, i.e., strong and narrow absorption in the red of the visible spectrum, and intense fluorescence with a rather small Stokes shift [217–222]. These properties are advantageous for many applications, ranging from dye-sensitized solar cells and organic photovoltaic applications [212, 223–245] to ion sensors [246–250] and biolabeling [251–259]. Polymers based on very small monomers as styrene (e.g. MEH-PPV) or tiophene (e.g. P3HT) display completely different optical behavior from their monomers [260]. On the other hand, squaraine polymers and copolymers are based on monomers which already display a narrow and strong absorption in the red of the visible spectrum [184, 212–215, 261]. The optical properties of polymeric squaraines can be explained by excitonic coupling of the transition moments of localized squaraine chromophores. In general, this leads to a broad and red-shifted absorption spectrum (compared to the monomer), which reflects the excitonic manifold of states.

Figure 4.1 depicts the linear absorption spectra of the monomer and conjugated polymers in different solvents. Depending on the solvent, the squaraine homopolymer $[\mathrm{SQB}]_n$ ($M_w = 46700$, $\mathrm{PDI} = 1.8$, and $X_n = 36$) displays different spectral features [184]. The latter observations can be used to assign the polymer structure by exciton coupling theory. In dichloromethane (DCM) and chloroform ($\mathrm{CHCl_3}$) the polymer displays a red-shifted absorption compared to the monomer. The latter observation can be explained by a stretched conformation due to a J-aggregate behavior, i.e., a head-to-tail arrangement of transition moments. In contrast, the polymer displays a *helix* structure in acetone, which displays a blue-shifted absorption (compared to the monomer) of the most intense absorption of the exciton manifold due to a H-aggregate behavior, i.e., a face-to-face arrangement of transition moments [213]. In dimethylformamide (DMF) a mixture of both superstructures is present within one polymer. The assignment of these superstructures is based on calculations (semiempirical AM1 method) of different structural models whose calculated absorption spectra (INDO method) were in agreement with expermeintal absorption spectra by superimposing different ratios of *zigzag* and *helix* conformations in different solvents. Although this description is highly simplistic, it is able to explain the

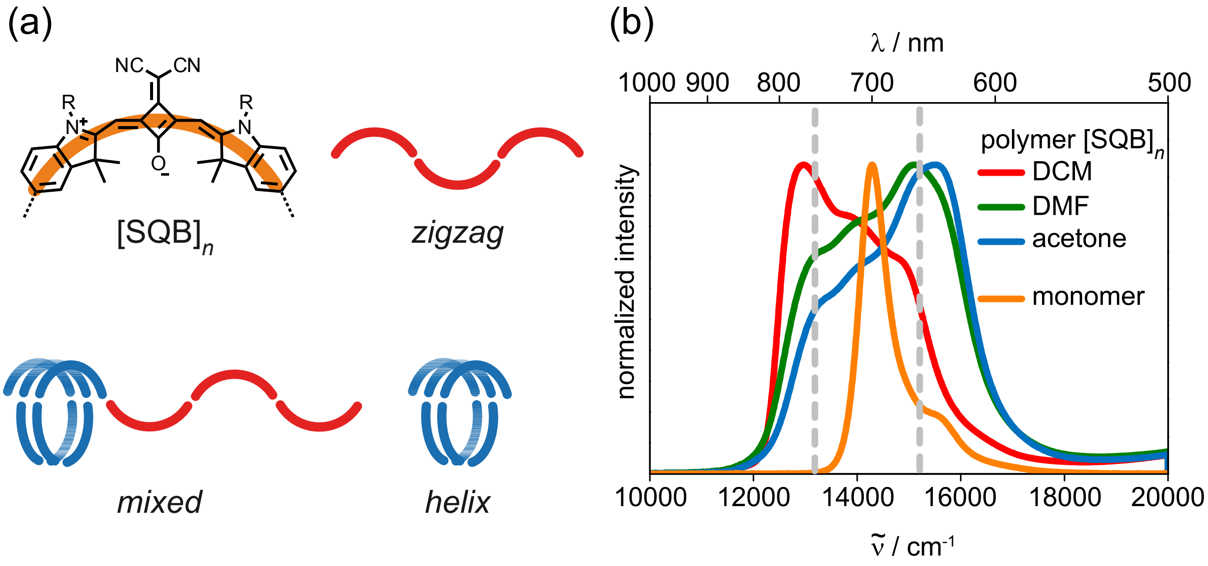

Figure 4.1: Chemical structure and proposed polymer structures of [SQB]$_n$ (a). Absorption spectra of the monomer and the polymer in diverse solvents (b). Gray dashed lines in (b) indicate the excitation wavenumbers of the transient absorption experiments in Section 4.3. Adapted with permission from Ref. [3]. © (2015) American Chemical Society.

main spectral features very well.

The results of this chapter are the result of a cooperation with the research group of Prof. Dr. Christoph Lambert, University of Würzburg, where the investigated compounds were synthesized and transient absorption (TA) spectroscopy was performed. In the following, the structural assignment of *zigzag* and *helix* sections for [SQB]$_n$ is investigated by more elaborated DFT calculations (Section 4.2), performed by the group of Dr. Roland Mitric, University of Würzburg. Subsequently, the relaxation dynamics of [SQB]$_n$ in DCM and DMF are compared by transient absorption (TA) spectroscopy (Section 4.3). In addition to TA spectroscopy, a global target analysis determines a relaxation model for [SQB]$_n$ providing information about the relaxation with different domains of the exciton manifold and the energy transfer dynamics between *zigzag* and *helix* segments within the polymer strand. Lastly, the results from the global target analysis are supported by coherent two-dimensional (2D) spectroscopy (Section 4.4).

4.2 Computations

Optical spectra of the *zigzag* and *helix* conformation of the model [SQB]$_n$ hexamer ([SQB]$_6$) were calculated by long-range-corrected tight-binding time-dependent density functional theory (lc-TDDFTB) [262]. For a detailed description of lc-TDDFTB and the performed optimization procedure based on previously performed semiempirical AM1

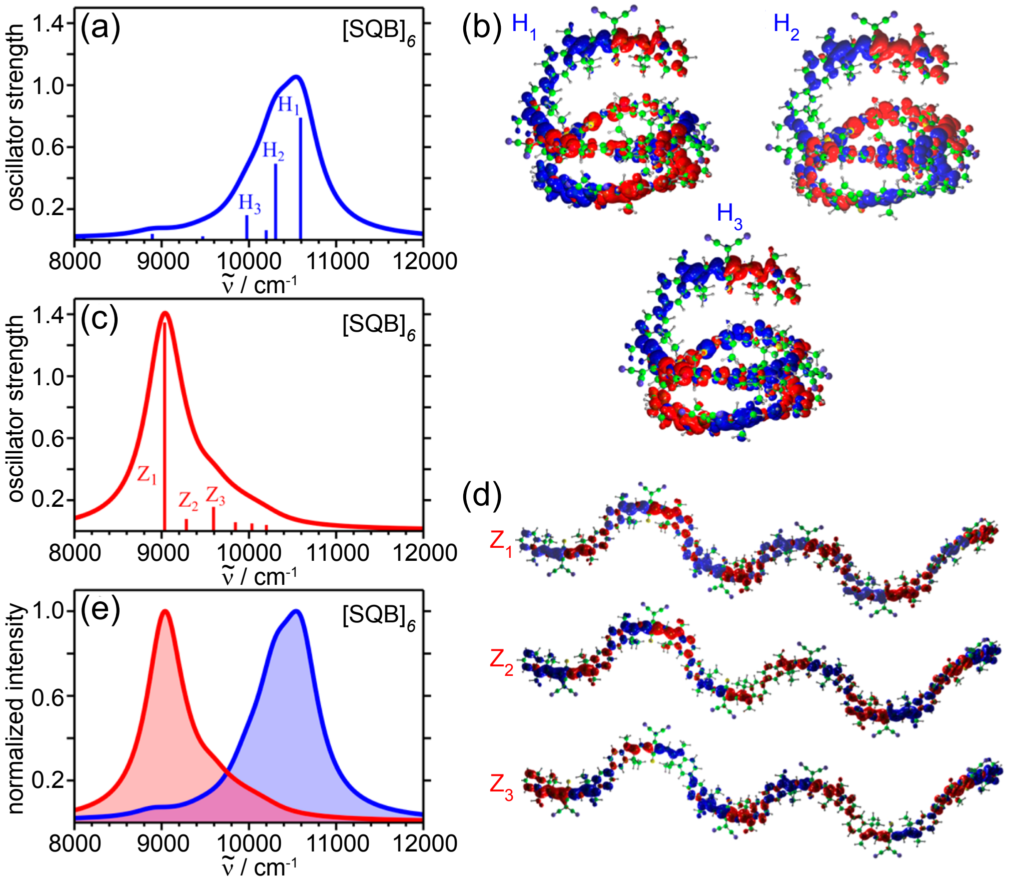

Figure 4.2: Calculated absorption spectra and transition densities for the three most intense transitions of the *helix* (a and b, respectively) and *zigzag* (c and d, respectively) transition densities for the superstructure of a model [SQB]$_n$ hexamer ([SQB]$_6$). The labels H$_1$–H$_3$ and Z$_1$–Z$_3$ denote the three most intense transitions for the helix and zigzag conformer, respectively. (e) Comparison of the theoretical normalized absorption spectra for both conformers. Adapted with permission from Ref. [3]. © (2015) American Chemical Society.

calculations [184], the interested reader is referred to the references [3] and [262].

Figure 4.2a depicts the calculated absorption spectra for the *helix* superstructures of [SQB]$_6$. The absorption spectrum consists of six transitions with a bandwidth of ≈ 1750 cm^{-1} from the highest to the lowest energy transition. The most intense transition is located at 10600 cm^{-1} (assigned to the H$_1$ state), accompanied by two additional weaker, lower energetic bands at 10300 cm^{-1} (assigned to the H$_2$ state) and 9980 cm^{-1} (assigned to the H$_3$ state), respectively. These three bands arise due to the electronic coupling between the first excited states of six individual monomeric units. Thus, the bands can be attributed to the first exciton manifold. Furthermore, the excitonic character for H$_1$−H$_3$ is illustrated by calculated transition densities shown in Fig. 4.2b. The transition densities for all three states (H$_1$−H$_3$) are delocalized along the *helix* structures and differ by the sign (phase) on the individual monomeric units.

Figure 4.2c shows the calculated absorption spectra for the *zigzag* superstructure of a

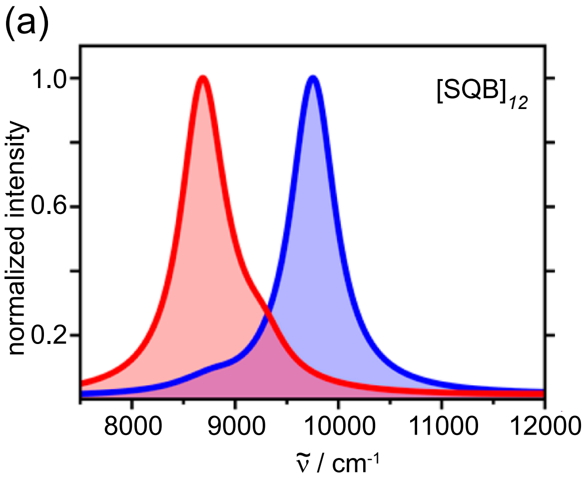

Figure 4.3: Calculated absorption spectra of the squaraine (a) 12mer ([SQB$_{n=12}$]) and (b) 22mer ([SQB$_{n=12}$]). Red and blue curves correspond to the *zigzag* and *helix* conformations, respectively. The peak intensities have been normalized to unity, and the lines have been broadened by a Lorentzian function with the width of 1000 cm^{-1}. Adapted with permission from Ref. [3]. © (2015) American Chemical Society.

model SQB hexamer. In contrast to the helix structure, the six transitions of the extended zigzag conformer display a narrower bandwidth of ≈ 1200 cm^{-1}, which is in agreement with the linear absorption spectra in Fig. 4.1. The most intense transition is located at 9000 cm^{-1} (assigned to the Z_1 state), accompanied by two weaker, higher energetic absorption bands at 9280 cm^{-1} (assigned to the Z_2 state) and 9600 cm^{-1} (assigned to the Z_3 state). Figure 2d depicts the transition densities for the Z_1–Z_3 states, which are delocalized over the extended structure and reflect the coupling of transition dipole moments on individual monomers. In the case of the most intense transition (Z_1), all monomers are coupled in a head-to-tail manner. All transition dipole moments point in the same direction, which is characteristic for a J-aggregate behavior.

The calculated absorption spectra for both superstructures, i.e., *helix* and *zigzag*, are juxtaposed in Fig. 4.2 next to each other. The elongated structure displays a strongly red-shifted absorption with respect to the *helix* conformation. Structural assignments for the conjugated polymers can be performed by comparing the results of the theoretical approach with the experimental absorption spectra. Hence, the absorption spectrum of $[\mathrm{SQB}]_n$ in solvents, as e.g., DCM (red in Fig. 4.1) can be assigned to a predominant *zigzag* structure. In the case of $[\mathrm{SQB}]_n$ in acetone (blue in Fig. 4.1) and DMF (green in Fig. 4.1), the calculations support the assignment of a predominant *helix* conformation. Additionally, these assignments are supported by calculations of larger oligomers containing $n = 12$ and $n = 22$ units, as depicted in Fig. 4.3a and Fig. 4.3b, respectively. A slight blue-shift of the absorption spectra can be observed for an increasing number of oligomer units n. Furthermore, the difference between the absorption maxima for *helix* and *zigzag* increases with increasing n: in the case of $[\mathrm{SQB}]_{n=12}$ the spectral difference is 3000 cm^{-1}, and increases for $[\mathrm{SQB}]_{n=22}$ to ≈ 4000 cm^{-1}. The latter energetic difference of the absorption maxima is in good agreement with the absorption maxima of $[\mathrm{SQB}]_n$ dissolved in DCM and acetone in Fig. 4.1.

4.3 Transient Absorption

4.3.1 Transient Absorption Experiments

TA spectroscopy of $[\mathrm{SQB}]_n$ (with an optical density OD ≈ 0.3 at the respective excitation wavenumber) was performed with excitation pulses generated by an OPA either centered at 13200 or at 15200 cm^{-1} (compare gray, dashed lines in Fig. 4.1) and probing by a white-light continuum. The instrumental response was ≈ 110 fs as determined by fitting the coherent artifact signals of the pure solvent. In order to avoid multiphoton absorption effects, the measurements were done at either 50 or 100 nJ pulse^{-1}.

Figure 4.4a depicts selected difference spectra (DS) of $[\mathrm{SQB}]_n$ in DCM upon exciting the highest ε of *zigzag* segments at ≈ 13200 cm^{-1}. The DS display the strongest GSB signal at ≈ 13000 cm^{-1}, with additional, much weaker GSB contributions at ≈ 15000 cm^{-1} and $\approx 25000 - 26000$ cm^{-1}. Furthermore, a spectrally broad, but weak ESA contribution is present between ≈ 16000 cm^{-1} and ≈ 24000 cm^{-1}. With evolving waiting time T, all these contributions decay without large spectral changes. Transients at 12900 cm^{-1} and 15200 cm^{-1} in Fig. 4.4b approximately reflect the relaxation of excited *zigzag* and *helix* conformations of $[\mathrm{SQB}]_n$, respectively. This assignment is supported by TDDFT computations in Sec. 4.2. Thus, upon 13200 cm^{-1} excitation, *zigzag* segments which relax to the ground state are excited almost exclusively.

Figure 4.4c shows the DS of $[\mathrm{SQB}]_n$ in DCM upon excitation of the fewer polymer sections which possess a *helix* conformation at 15200 cm^{-1}. The DS upon 15200 cm^{-1} excitation display similar spectral features as upon 13200 cm^{-1} excitation (Fig. 4.4a), e.g., a strong GSB feature at ≈ 13000 cm^{-1}. In contrast to the latter experiment, a distinct GSB at ≈ 15000 cm^{-1} is observable at $T = 0.58$ ps (blue DS in Fig. 4.4c), which probes almost exclusively excited *helix* conformational units. The GSB at 15000 cm^{-1} decays more rapidly than at 13000 cm^{-1} as observable in the transients at 15200 cm^{-1} and 12900 cm^{-1} in Fig. 4.4d, respectively. Initially, the transient at 15200 cm^{-1} decays rapidly within the first ps (marked by a red circle in Fig. 4.4d) and subsequently decays similar as in the case of 13200 cm^{-1} excitation (see transients at 15200 cm^{-1} in Fig. 4.4b and Fig. 4.4d, respectively). Hence, after 1 ps the DS display the relaxation dynamics of excited *zigzag* sections. This observation indicates an energy transfer from initially *helix* structures to *zigzag* structures along one polymer strand (intramolecular energy transfer) within the first ps. The alternative explanation for the relaxation dynamics after 1 ps by a parallel excitation of *helix* and *zigzag* conformers can be excluded as it would not explain the rapid and strong decay of the 15200 cm^{-1} signal. Additionally, energy transfer between different polymer strands (intermolecular energy transfer) can be ruled out due to the very diluted experimental conditions.

In order to further investigate the influence of different superstructures within one poly-

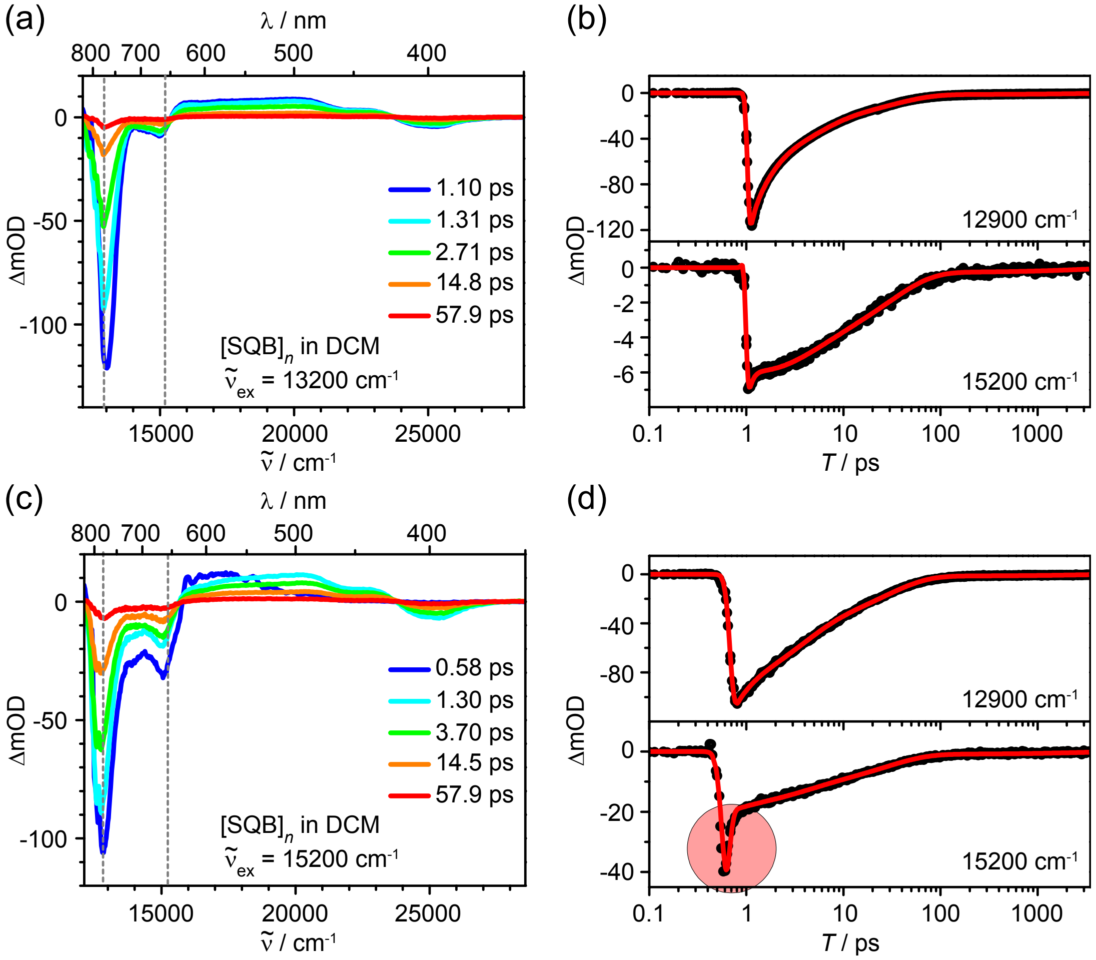

Figure 4.4: Selected (stray light and chirp corrected) transient absorption spectra and selected time traces with global fit (red lines) of [SQB]$_n$ in DCM at 13200 cm^{-1} pump wavenumber (a, b) and at 15200 cm^{-1} pump wavenumber (c, d). The probe wavenumbers of the transients are depicted by gray dashed lines in the diagrams of the transient absorption spectra. Adapted with permission from Ref. [3]. © (2015) American Chemical Society.

mer strand on photo-induced dynamics, TA experiments with 13200 cm^{-1} and 15200 cm^{-1} excitation were additionally performed for [SQB]$_n$ in DMF. In DMF, the polymer strands of [SQB]$_n$ predominantly possess a *helix* conformation. Figure 4.5a depicts the DS of [SQB]$_n$ in DMF upon 13200 cm^{-1} excitation. The DS display a strong GSB at ≈ 13200 cm^{-1} with additional weaker GSB and ESA features at higher wavenumbers similar to the previous TA experiments for [SQB]$_n$ in DCM (Fig. 4.4). Within the first ps, the GSB at ≈ 13200 cm^{-1} displays a small red-shift and decays to ≈ 2/3 of its initial signal intensity. At the same time, the GSB at ≈ 15000 cm^{-1} grows in, which is depicted in the transient at 15200 cm^{-1} in Fig. 4.5b (marked by a red circle). Within the first 10 ps, the GSB intensities at ≈ 13000 cm^{-1} and ≈ 15000 cm^{-1} display a change in magnitude. For T > 20 ps the GSB at ≈ 13000 cm^{-1} almost disappeared. Thus, almost exclusively GSB of excited *helix* segments remain, which indicates energy transfer from *zigzag* to

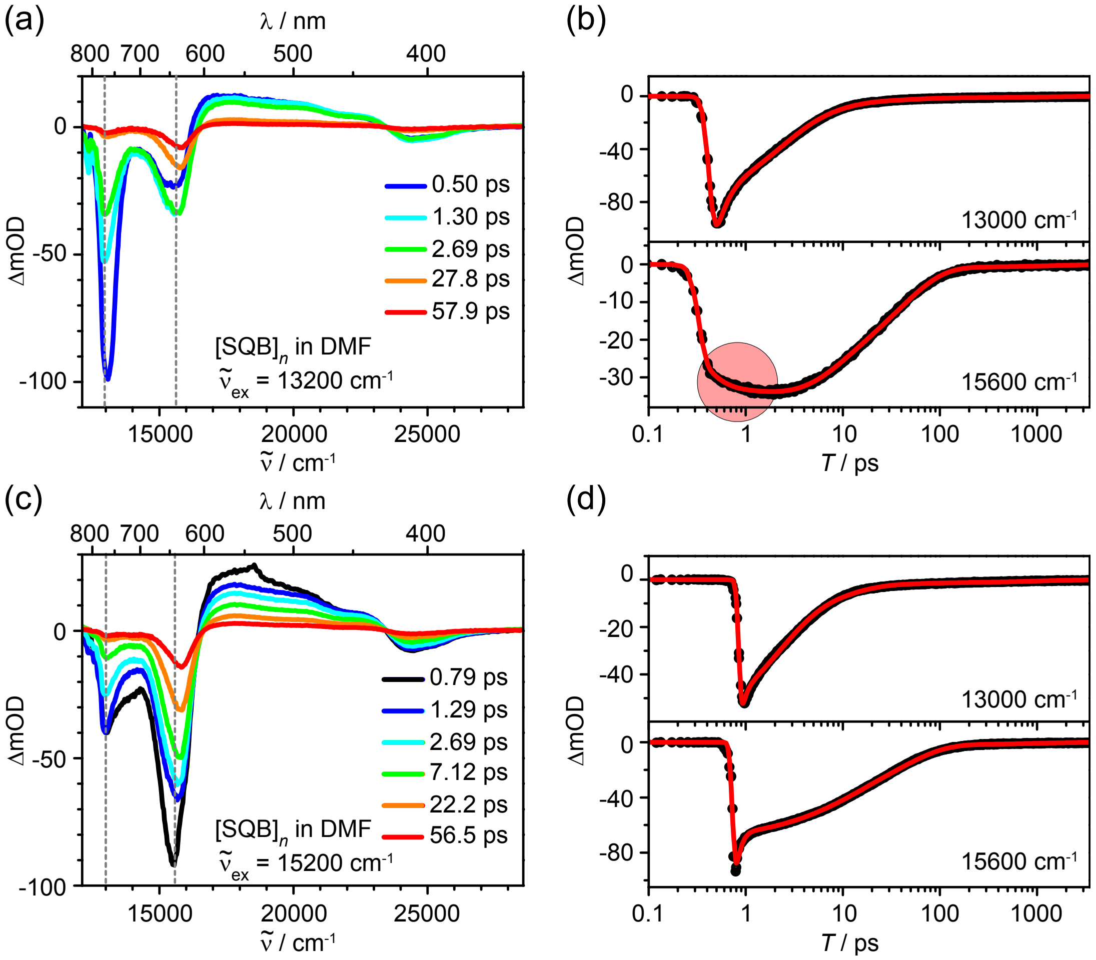

Figure 4.5: Selected (stray light and chirp corrected) transient absorption spectra and selected time traces with global fit (red lines) of [SQB]$_n$ in DMF at 13200 cm^{-1} pump wavenumber (a, b) and at 15200 cm^{-1} pump wavenumber (c, d). The probe wavenumbers of the transients are depicted by gray dashed lines in the diagrams of the transient absorption spectra. Adapted with permission from Ref. [3]. © (2015) American Chemical Society.

helix structures.

Figure 4.5c depicts the DS for [SQB]$_n$ in DMF upon 15200 cm^{-1} excitation. Hence, in this experiment, almost exclusively *helix* segments are excited. Initially, the DS display a pronounced GSB at 15600 cm^{-1} and ≈ 13000 cm^{-1}, respectively. The former GSB signal decays within the first 100 fs and from then on more slowly as depicted in the 15200 cm^{-1} transient in Fig.4.5d. In contrast, the transient at 12900 cm^{-1} does not display a very rapid decay at the beginning, but decays much faster overall at later times than the GSB at 15200 cm^{-1}. From 20 ps on, the DS only display a strong GSB at ≈ 15600 cm^{-1}. Thus, almost exclusively excited-state population of *helix* conformers are probed.

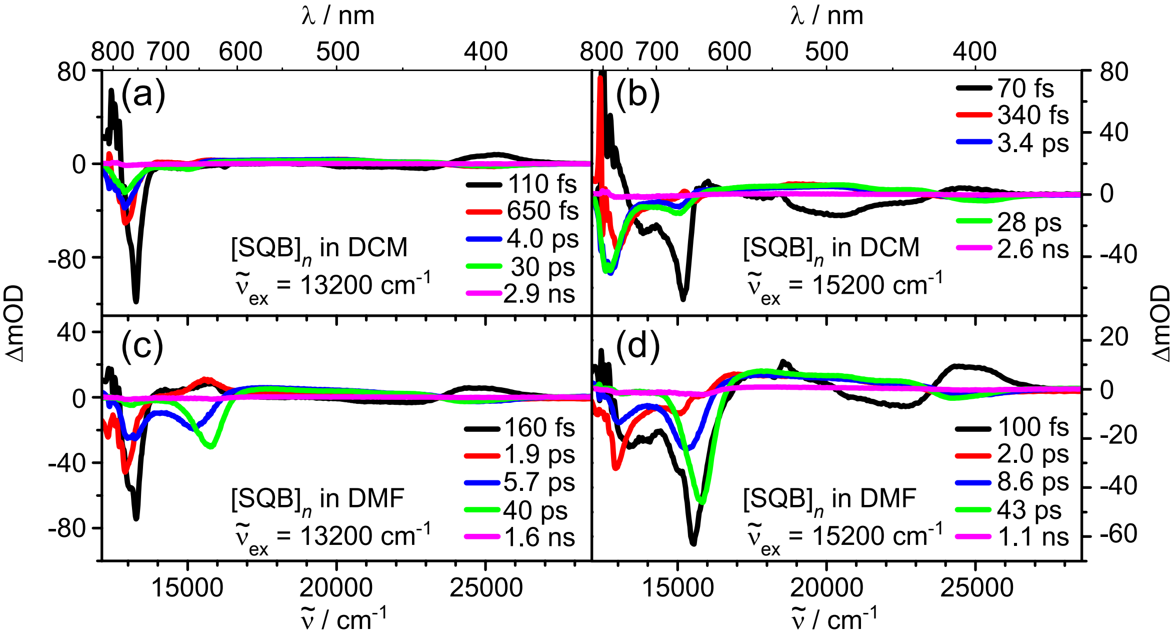

Figure 4.6: Decay-associated difference spectra (DADS) and associated lifetimes of $[\mathrm{SQB}]_n$ in (a) DCM upon 13200 cm^{-1} excitation, (b) DCM upon 15200 cm^{-1} excitation, (c) DMF upon 13200 cm^{-1} excitation, and (d) DMF upon 15200 cm^{-1} excitation. Adapted with permission from Ref. [3]. © (2015) American Chemical Society.

4.3.2 Global Analysis

The performed TA experiments in DCM and DMF with predominantly excitation of *zigzag* and *helix* segments of $[\mathrm{SQB}]_n$, respectively, indicate energy-transfer processes from *helix* to *zigzag* sections (TA in DCM upon 15200 cm^{-1} excitation, Fig. 4.4c,d) and from *zigzag* to *helix* sections (TA in DMF upon 13200 cm^{-1} excitation, Fig. 4.5a,b). These observations should only be valid if the energetic lowest excited state has *zigzag* structure in DCM and *helix* structure in DMF. A global analysis was performed to determine the number of spectral components of the transient maps. Figure 4.6 depicts the DADS and corresponding timescales resulting from the global analysis for all TA experiments. Five decay components were the prerequisite to properly reproduce the relaxation dynamics in each TA experiment. The fifth decay component displays only a very small amplitude, which was necessary to fit the remaining signals at ≈ 2 ns and will be neglected in the following.

The initial DADS (τ_1 = 110 fs, black in Fig. 4.6a) corresponding to the TA experiment in DCM upon 13200 cm^{-1} excitation displays a strong negative signal at 13000 cm^{-1} and a positive signal at ≈ 12500 cm^{-1}. Such a derivative shape indicates a spectral shift which is furthermore observable at spectral changes in the range from 15000 − 27000 cm^{-1}. Subsequent DADS (DADS$_2$-DADS$_4$) display a similar spectral shape with a pronounced negative amplitude around 13000 cm^{-1}. Hence, upon excitation of the exciton manifold at 13200 cm^{-1}, an initial relaxation to the lowest excitonic state takes place within $\tau_1 = 110$ fs. From the latter state the system undergoes structural relaxation with $\tau_2 = 650$ fs (red in Fig. 4.6a) and 4.0 ps (blue in Fig. 4.6a). Finally, the relaxation to the ground state takes place with $\tau_4 = 30$ ps (green in Fig. 4.6a).

Figure 4.6b depicts the DADS for the TA experiment in DCM upon 15200 cm^{-1} excitation. In contrast to the previous analysis, the shortest lifetime ($\tau_1 = 70$ fs, black in Fig. 4.6b) displays a pronounced negative signal at 15200 cm^{-1} and a positive amplitude around 13000 cm^{-1}. One possible explanation would be a direct deactivation of the *helix* species to the ground state, which is quite improbable on this ultrafast timescale. Thus, the initial dynamics indicate an ultrafast energy transfer from the *helix* to the *zigzag* segments. Subsequent dynamics (DADS_2-DADS_4) are similar to the DADS upon 13200 cm^{-1} excitation described above.

The DADS for TA experiments in DMF exciting at 13200 cm^{-1} are shown in Fig. 4.6c. The two initial dynamics $\tau_1 = 160$ fs (black DADS in Fig. 4.6c) and $\tau_2 = 1.9$ ps (red DADS in Fig. 4.6c) display a negative signal at $\approx$ 13000 cm^{-1}, similar to the TA experiment in DCM upon 13200 cm^{-1} excitation. However, the DADS corresponding to $\tau_3 = 5.6$ ps (blue DADS in Fig. 4.6c) displays two negative signals, one at $\approx$ 13000 cm^{-1} and an additional one at $\approx$ 15200 cm^{-1}. The latter signal is even more pronounced and shifts to higher wavenumbers at the DADS with $\tau_4 = 40$ ps (green DADS in Fig. 4.6c). The signal at $\approx$ 15000 cm^{-1} grows in accompanied by the loss of the signal at $\approx$ 13000 cm^{-1}. Thus, the energy from initially excited *zigzag* segments transfers to *helix* segments with 1.9 ps is indicated. Subsequently, the photo-excited polymer conformational units undergo structural relaxation with 5.7 ps and decay to the ground state with 40 ps. These processes are somewhat slower in DMF than in DCM.

Figure 4.6d depicts the DADS for $[\mathrm{SQB}]_n$ in DMF upon 15200 cm^{-1} excitation. The initial DADS ($\tau_1 = 100$ fs, black in Fig. 4.6d) displays a strong signal at 15400 cm^{-1} with some additional intensity around $13000-14300$ cm^{-1}. The following DADS corresponding to $\tau_2 = 2.0$ ps (red in Fig. 4.6d) shows an increased negative amplitude at 13000 cm^{-1} with a strongly decreased signal at higher wavenumbers. These features are reversed for the third DADS ($\tau_3 = 8.6$ ps, blue in Fig. 4.6d), which has the strongest negative amplitude at 15200 cm^{-1}. The following fourth DADS with $\tau_4 = 43$ ps (green in Fig. 4.6d) displays again a strong negative amplitude at 15700 cm^{-1}. These observations indicate an energy transfer from initially excited *helix* structures to *zigzag* structures, as observed above in the TA for exciting at 15200 cm^{-1} in DCM. Subsequently, before the energy relaxes to the ground state, the energy at *zigzag* segments transfers back to *helix* segments as observed in TA for exciting at 13200 cm^{-1} in DMF. Thus, the observations for $[\mathrm{SQB}]_n$ in DMF upon 15200 cm^{-1} excitation indicate both energy-transfer processes, i.e., *zigzag* to *helix* and *helix* to *zigzag*, along one polymer strand.

4.3.3 Target Analysis

A target analysis was performed in order to investigate the photo-excited relaxation based on TA experiments of $[\mathrm{SQB}]_n$ with different excitation energies in DCM and DMF. In advance, two requirements were provided in order to optimize the ratios for different

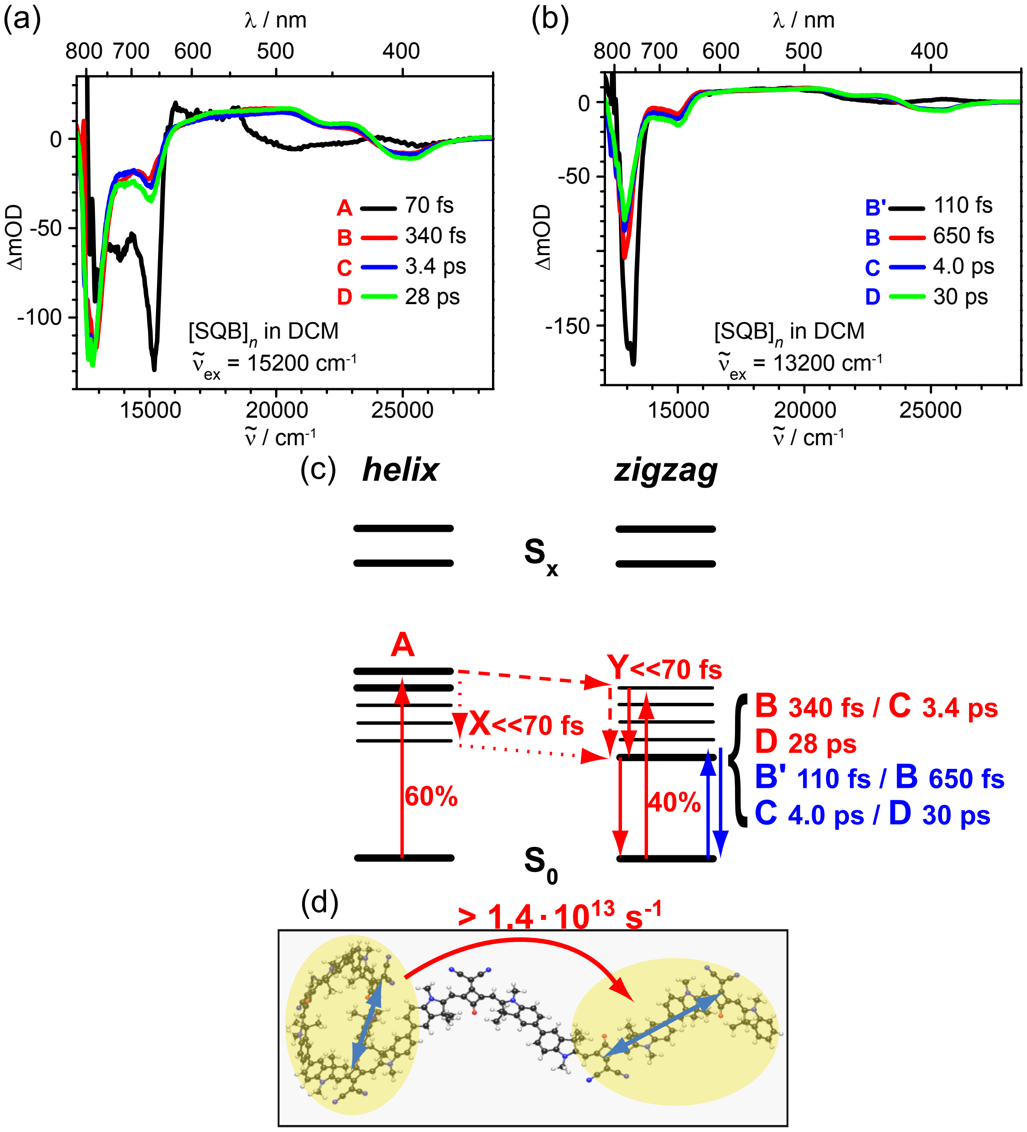

Figure 4.7: Species-associated difference spectra (SADS) of $[\mathrm{SQB}]_n$ in DCM upon 15200 cm^{-1} excitation (a) and upon 13200 cm^{-1} excitation (b). State diagrams (with an arbitrary number of exciton states) of *helix* and *zigzag* sections (c). Assignments and data given in red pertain to the SADS in (a), those given in blue to (b). Energy-transfer processes assigned to the corresponding superstructures (d) which are indicated by the target analysis. Adapted with permission from Ref. [3]. © (2015) American Chemical Society.

relaxation pathways. Firstly, energy transfer from *helix* to *zigzag* and from *zigzag* to *helix* are included to reflect results of the performed TA experiments. Secondly, the ESA contribution at ≈ 18800 cm^{-1} is equal for all transient species to energetically higher-lying states, as ESA to higher-lying state is assumed to have the same extinction coefficient. These requirements lead to relaxation pathways connecting the transient species and allow the adjustment of the efficiencies for each relaxation pathway.

Figure 4.7 depicts the results of the target analysis for both excitation energies in DCM. Upon 15200 cm^{-1} excitation (Fig. 4.7a), the target analysis leads to a parallel excitation of the states “A” with 60% and “Y” with 40%, which describe excited states in *helix* and *zigzag* conformation, respectively. The SADS of A display a prominent GSB at 15200 cm^{-1}, while Y is not visible in the spectra due to an ultrafast relaxation process ($\tau \ll 70$ fs) to state B. Species A relaxes with $\tau(\mathrm{A}) = 70$ fs to B accompanied by spectral changes of the ESA around $18200 - 25000$ cm^{-1} via two possible relaxation pathways. Firstly, the energy might relax through the exciton manifold of *helix* segments to X, from which an energy transfer from *helix* to *zigzag* to state B occurs (dotted relaxation pathway in Fig. 4.7c). In this case, species X would not display any spectral indications due to the low intermediate concentration. Secondly, an initial *helix* to *zigzag* energy transfer occurs from A to Y, which relaxes with an ultrafast process to B (dashed relaxation pathway in Fig. 4.7c). Both relaxation pathways can not be discriminated by solely the target analysis. Still, an upper boundary for the energy-transfer rate from *helix* to *zigzag* can be given by 1/(70 fs) ($k_{A\rightarrow B} = 1.4 \times 10^{13}$ s^{-1}). Subsequent SADS for the species B–D display a quite similar spectral shape with a prominent GSB at 13200 cm^{-1}. Thus, comprised relaxation processes from B–D occur within *zigzag* sections of the polymer. From state B over C to D two structural relaxation processes occur with $\tau(B) = 340$ fs and $\tau(C) = 3.4$ ps, respectively. Species D decays to the ground state with $\tau(D) = 28$ ps.

Upon 13200 cm^{-1} excitation (Fig. 4.7b), in DCM mainly *zigzag* segments are excited. Initially, an ultrafast relaxation from B’ to B occurs with $\tau(\mathrm{B'}) = 110$ fs accompanied by spectral changes of the ESA between $20000 - 25000$ cm^{-1}. From B structural relaxation and depopulation of the excited state occur similar in spectral shape of the SADS and similar in the timescale to the previously described analysis of the TA experiment exciting at 15200 cm^{-1} in DCM.

Figure 4.8 depicts the results of the target analysis for both excitation energies in DMF. Upon 13200 cm^{-1} excitation (Fig. 4.8b), the SADS of B’ displays a very strong GSB at $\approx$ 13000 cm^{-1}. Unlike the TA experiments in DCM, in DMF the SADS for B’ to D display a stepwise change of GSB intensities at 13000 cm^{-1} and 16000 cm^{-1}. The latter observation can be explained by a broader distribution of *helix* and *zigzag* structures within a polymer strand in DMF compared to DCM. The sequence of SADS indicates an energy transfer from *zigzag* to *helix* segments. The *zigzag* to *helix* energy transfer was attributed to the $\tau(\mathrm{B}) = 1.9$ ps timescale, which displays the strongest change of intensities at 13000 cm^{-1} and 16000 cm^{-1}, respectively. The spectral changes of the ESA around $21000 - 27000$ cm^{-1} from B’ to B are attributed to the relaxation within the exciton manifold. Hence, the excitation of the sample at the maximum of the lowest energetic band is still somewhat higher in energy than the lowest exciton state.

Upon 15200 cm^{-1} excitation (Fig. 4.8a), in DMF the series of SADS display a decreasing GSB at 15000 cm^{-1}. The GSB at 13000 cm^{-1} decreases only with a small magnitude from the first to the second SADS. In the following, the latter GSB decays rapidly up to the SADS corresponding to 43 ps, which displays only spectral features of *helix* states. In analogy to the observations in DCM upon 15200 cm^{-1} excitation, the findings can be interpreted with an energy transfer from *helix* to *zigzag* segments with $\tau(\mathrm{A}) = 100$ fs.

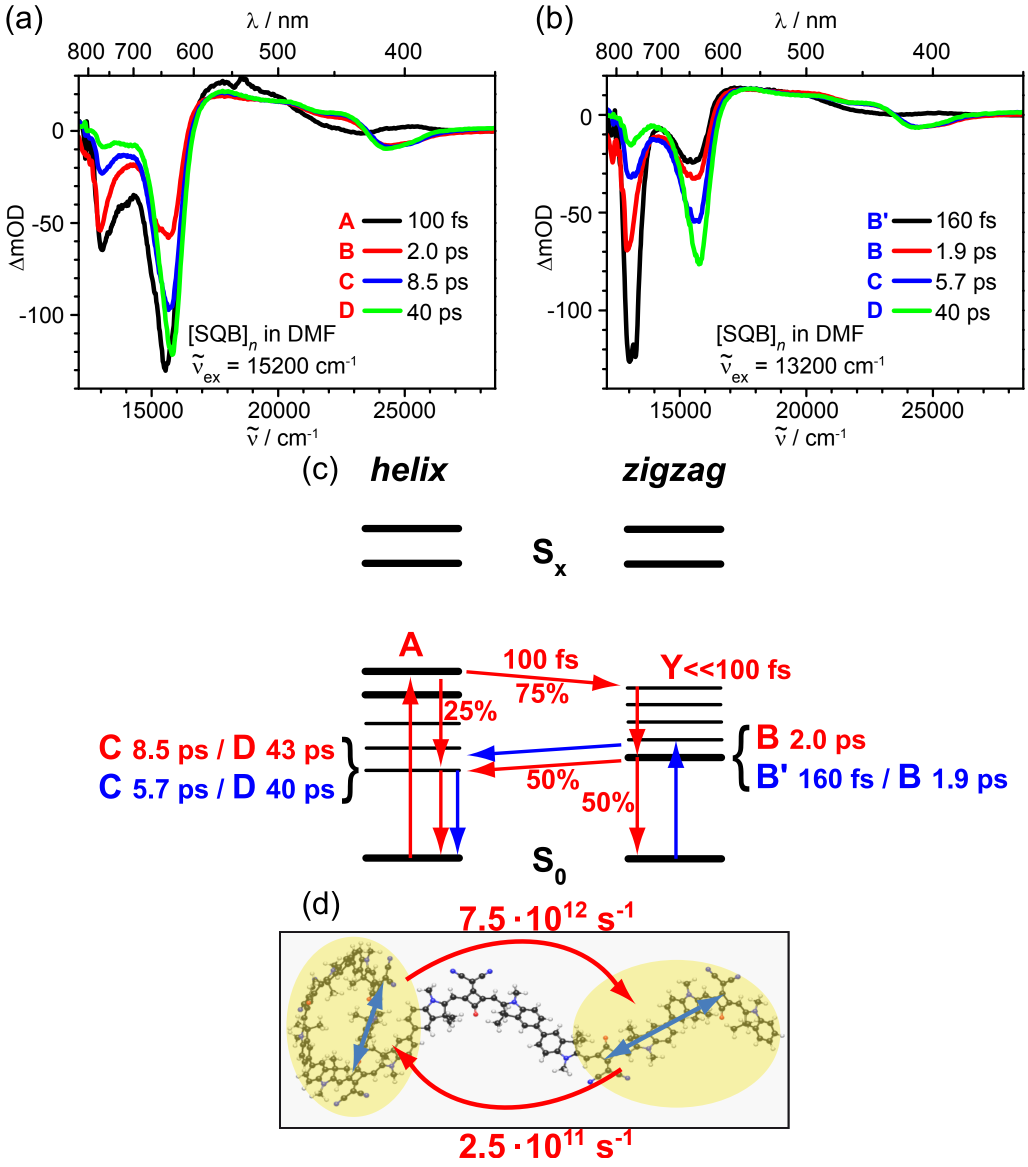

Figure 4.8: Species-associated difference spectra (SADS) of $[\mathrm{SQB}]_n$ in DMF upon 15200 cm^{-1} excitation (a) and upon 13200 cm^{-1} excitation (b). State diagrams (with an arbitrary number of exciton states) of *helix* and *zigzag* sections (c). Assignments and data given in red pertain to the SADS in (a), those given in blue to (b). Energy-transfer processes assigned to the corresponding superstructures (d) which are indicated by the target analysis. Adapted with permission from Ref. [3]. © (2015) American Chemical Society.

The efficiency of the latter energy transfer is 75%, which leads to an energy-transfer rate of $k_{A \to B} = 7.5 \times 10^{12}$ s^{-1}. Subsequently, an ultrafast energy relaxation within the exciton manifold leads to species B. This excited species has a lifetime of 2.0 ps (very similar to $\tau = 1.9$ ps for excitation at 13200 cm^{-1} in DMF) and undergoes back-energy transfer to C with a rate of $k_{B \to C} = 2.5 \times 10^{12}$ s^{-1} and an efficiency of 50%. Subsequent relaxation from C to D occurs with $\tau(\mathrm{C}) = 8.5$ ps, which is followed by the relaxation to the ground state with $\tau(\mathrm{D}) = 43$ ps. An equally good target fit was obtained by assuming a parallel excitation of *helix* and *zigag* sections followed by energy transfer from *zigzag* to *helix* segments. Based on the target analysis this pathway can not be ruled out. Still, the latter relaxation pathway is still unlikely as an energy transfer from *helix* to *zigzag* sections was previously observed in DCM upon 15200 cm^{-1} excitation. The energy transfer from *helix* to *zigzag* sections requires the relaxation within the exciton manifold of the *helix* segments being much slower than the energy-transfer step. Based on this requirement, the relaxation pathway which relaxes within the exciton manifold upon 15200 cm^{-1} excitation in DCM can be ruled out.

The target analysis for both excitation energies in both solvents leads to three major points. Firstly, in DCM the lowest exciton states of the *zigzag* segments are energetically lower than the lowest exciton states for the *helix* conformers. This assignment is reversed in DMF. Secondly, the relaxation within the exciton manifold of the *helix* segments is much slower than the relaxation within the exction manifold of the *zigzag* conformations. Thirdly, the energy transfer from *helix* to *zigzag* is an order of magnitude faster than from *zigzag* to *helix*.

The exciton coupling and consequently the exciton bandwidth in a *helix* structure might be larger than in a *zigzag* structure, because the distance between individual squaraine chromophores can be much smaller due to the face-to-face arrangement in a *helix*. Thus, the electronic structure depends on the supramolecular structure. A somewhat smaller bandwidth with a higher-lying lowest energetic exciton state is expected for a looser helix arrangement in DCM than in DMF. The relaxation within the exciton manifold and energy-transfer processes depend on the Franck-Condon overlap of states. Generally, the relaxation within the exciton manifold depends strongly on the exciton-vibrational coupling and may also lead to “transient population trapping” [263] in vibrationally excited states. Although these effects are hardly predictable in complex systems such as $[\mathrm{SQB}]_n$, they may influence the relative relaxation rates within the exciton manifold and between the different polymer sections.

4.4 Coherent 2D Spectroscopy

To visualize the initial interactions and relaxation dynamics between the absorption bands of $[\mathrm{SQB}]_n$ (OD ≈ 0.3) we performed coherent 2D spectroscopy using a laser spectrum covering the absorption maxima at ≈ 13000 cm^{-1} and ≈ 14000 cm^{-1}. Laser pulses were generated by a noncollinear optical parametric amplifier (Topas White, Light Conversion), with a pulse duration of 22 fs as determined from SHG-FROG in a 10 μm β-barium borate (BBO) crystal. For each population time T, the coherence time τ was varied by $\tau = \pm 120.69$ fs in steps of $\Delta\tau = 4.47$ fs. Real-valued 2D spectra, reflecting the change in absorption, were obtained by phasing with transient absorption data within the same experimental setup using beam 3 as a probe.

Figure 4.9 depicts the results for $[\mathrm{SQB}]_n$ in DCM (a) and DMF (d) for selected population times T. Excitation corresponds to the horizontal $\tilde{\nu}_\tau$ wavenumbers, whereas detection

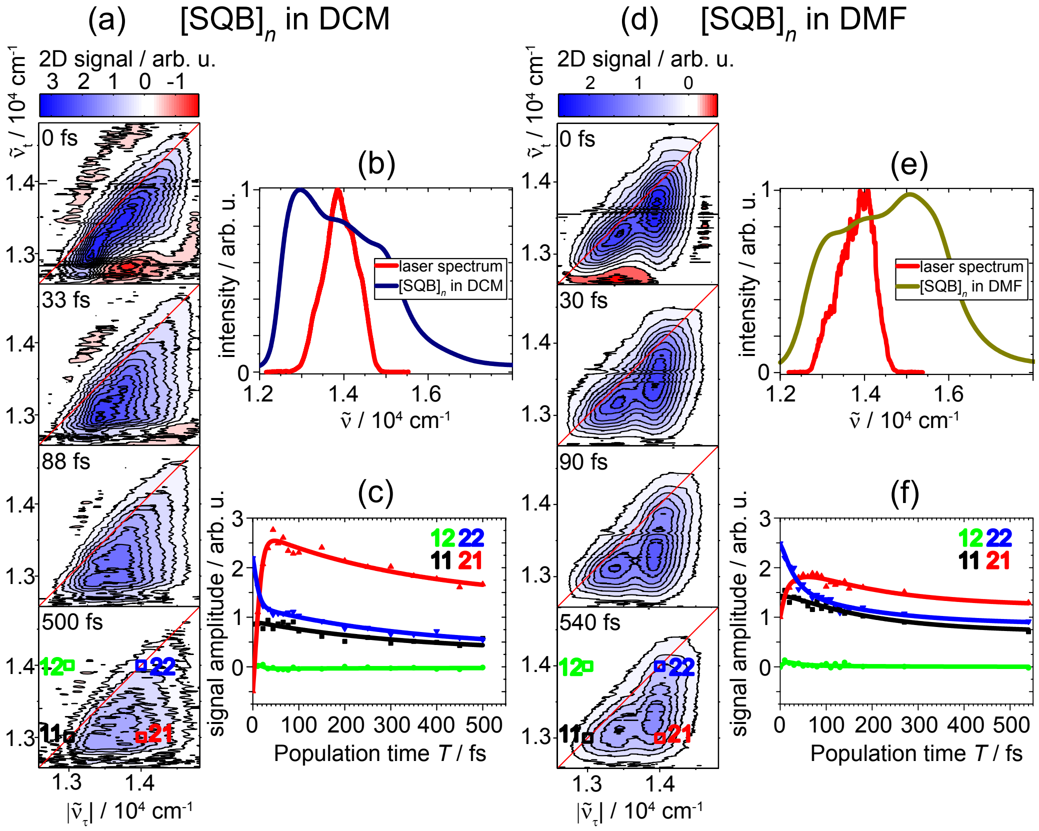

Figure 4.9: Coherent 2D spectroscopy of [SQB]$_n$ in (a) DCM and (d) DMF for selected population times. 2D spectra have been normalized to the maximum of the $T = 0$ fs spectrum and contour lines are drawn in steps of 10% starting from 95%. (b,e) Laser spectrum (red) and absorption spectrum during the 2D scan in DCM (b, blue) and DMF (e, gold). (c,f) Dynamics of the diagonal and off-diagonal signal amplitudes for four regions of interest as marked in the bottom 2D spectrum for [SQB]$_n$ in DCM (c) and DMF (f). Adapted with permission from Ref. [3]. © (2015) American Chemical Society.

corresponds to the vertical $\tilde{\nu}_t$ wavenumbers. Blue (positive) signals display GSB and SE signal contributions, while red (negative) signals display ESA contributions. This sign convention is opposite to that in transient absorption above, because in 2D spectroscopy the emitted signal magnitude is generally recorded and plotted, rather than the absorbance change. As a consequence of the limited laser pulse bandwidth (Fig. 4.9b for [SQB]$_n$ in DCM and Fig. 4.9e for [SQB]$_n$ in DMF), covering ≈ 1500 cm^{-1} of the spectrally broad absorption band, the dynamics within these bands are visible as 2D line-shape modifications rather than clearly separated peaks. For the population time $T = 0$ fs, signal contributions of the solvent have to be taken into account. Furthermore, "phase twist" contributions originating from the temporal overlap of the third pulse with the first two may occur.

The laser pulses centered at 13700 cm^{-1} mainly excite intermediate sections of the polymer which are energetically between the absorption of *zigzag* and *helix* segments. Qualitative similarities can be found in the real-valued 2D spectra of [SQB]$_n$ in DCM and DMF: The $T = 0$ fs spectrum is mainly elongated along the diagonal for excitation wavenumbers of $|\tilde{\nu}_\tau| \lesssim 13750\ \mathrm{cm}^{-1}$, i.e., excitation and emission frequencies are correlated. For higher excitation wavenumbers, a coupling to lower detection wavenumbers is observable as a larger shift of the signal below the diagonal. The subsequent dynamics within the first 90 fs are governed by an ultrafast component that is associated with changes in the 2D lineshape: At high excitation wavenumbers the signal loses its amplitude and gains intensity at lower detection wavenumbers. Between 90 fs and 500 fs, an overall decay of the signal can be observed. In order to get a better impression of the signal amplitude progression in the 2D spectra, we chose four square regions of interest (ROI) with a side length of $\approx 115\ \mathrm{cm}^{-1}$ centered at the diagonal $\tilde{\nu}_\tau = \tilde{\nu}_t$ and off-diagonal $\tilde{\nu}_\tau \neq \tilde{\nu}_t$ positions corresponding to absorption maxima at $\approx 13000\ \mathrm{cm}^{-1}$ and $\approx 14000\ \mathrm{cm}^{-1}$. The signal evolution of these ROIs is shown in Fig. 4.9c for $[\mathrm{SQB}]_n$ in DCM and Fig. 4.9f for $[\mathrm{SQB}]_n$ in DMF as a function of population time (symbols). Starting at $T = 0$ fs, the diagonal peaks (11 and 22) have the highest amplitude. With increasing T, the strongest changes are the initial decrease of the 22 peak accompanied by the rise of the corresponding off-diagonal peak 21. After this process the overall amplitude of all components decreases up to our measurement limit of $T \approx 500$ fs.

To quantify these processes we performed for each solvent global fits of the four ROI signals over time, i.e., sharing the rates while amplitudes and offset were free parameters. For $[\mathrm{SQB}]_n$ in DCM the fit resulted in two time constants of $1/k = 9 \pm 2$ fs and 349 ± 118 fs, and in DMF the time constants were $1/k = 28 \pm 7$ fs and 201 ± 53 fs. In both solvents we observed ultrafast energy transfer from initially excited states towards energetically lower-lying states on the order of our pulse duration. According to the global fit, the cross peak 21 rises with the same time constant as the decay of the corresponding diagonal peak 22. This indicates an ultrafast relaxation within the excitonic manifold towards the lowest states in energy as was assumed in the global target fit in Fig. 4.7 and Fig. 4.8. From the latter states further relaxation processes occur which lead to an overall decay of the signal without a change in line-shape within our spectral and population time window. The subsequent relaxation displays the relaxation of the *zigzag* segments in DCM with $1/k = 349$ fs and in DMF with $1/k = 201$ fs. The time of 349 fs (from the 2D analysis) fits well with the lifetime of B observed in the transient absorption experiment 2, whereas the time of 201 fs in DMF (from the 2D analysis) fits well with the lifetime of B' in the transient absorption experiment 3. In the 2D spectroscopy experiments, mainly energetically intermediate states of the polymer were excited. In DCM, an ultrafast relaxation towards the lowest *zigzag* energy takes place, followed by a further relaxation of this state. In DMF, the coupling between intermediate states and *zigzag* states is already visible in the $T = 0$ fs 2D spectrum as a pronounced off-diagonal signal. Subsequently, the energy relaxes towards the *zigzag* states within $1/k = 28$ fs, from where further relaxation towards the energetically more stable *helix* (in DMF) may occur with $1/k = 201$ fs. This is interpreted as an energy-driven process: in DCM there are mainly *zigzag* segments which are the lowest in energy. The excited intermediate states relax initially towards these *zigzag* states in DCM, while in DMF the relaxation from the excited intermediate states towards the *helix* segments is coupled via the *zigzag* conformations.

4.5 Summary and Conclusions

Combining theoretical calculations and experimental observations, the optical properties of the squaraine homopolymer $[\mathrm{SQB}]_n$ were assigned to a *zigzag* conformation, which displays a J-type behavior and *helix* conformation with H-type behavior depending on the solvent. Based on this structural model, the relaxation dynamics were analyzed by a target analysis of transient absorption experiments exciting different structural domains. In the target analysis different relaxation processes could be distinguished. Firstly, the relaxation within the exciton manifold of *zigzag* and *helix* segments, and additionally the energy transfer between both superstructures within a polymer strand. The latter dynamics could be confirmed by coherent two-dimensional (2D) spectroscopy experiments.

Upon exciting *helix* sections in DCM at higher energies, the excited energy is initially transferred from *helix* to *zigzag* segments with a rate of $k \approx 10^{13}\ \mathrm{s}^{-1}$. In DMF the photo-induced dynamics of $[\mathrm{SQB}]_n$ are more complex. Upon excitation of the *zigzag* domains (at low energies), an energy-transfer from *zigzag* to *helix* can be observed. However, if the *helix* segments are excited, initially the energy is transferred from *helix* to *zigzag* with $k \approx 10^{13}\ \mathrm{s}^{-1}$, which is followed by the back-energy transfer to *helix* segments with $k \approx 10^{11}\ \mathrm{s}^{-1}$. Thus, for $[\mathrm{SQB}]_n$ the energy transfer between different structures within one polymer (intramolecular energy transfer) is faster than the relaxation within the exciton manifold. This observation supports the recent assumption of energy-transfer processes in squaraine polymers may be well below the subpicosecond timescale [213]. For other conjugated polymers, as e.g., MEH-PPV intramolecular energy transfer is typically one order of magnitude slower than intermolecular energy transfer [187, 264]. The difference of the rate for intramolecular energy transfer can be explained by the spectral matching of the donor and acceptor density of states. Squaraine polymers display most likely a matching of the density of states due to very small reorganization energy in the class of cyanine-like chromophores [213]. In contrast, conventional-type polymers as polyphenylenevinylene and polythiophene display a much weaker energy-state matching as can be seen by a strong Stokes shift and the small spectral overlap of absorption and fluorescence spectra [265]. Thus, if an efficient ultrafast energy transfer within a polymer strand is desired, the use of polymers based on cyanine-like chromophores as squaraines may be advantageous.

CHAPTER 5

Relaxation Dynamics in the Low-Temperature Phase of MEH-PPV

The polymer Poly[2-methoxy-5-(2-ethylhexyloxyl)-1,4-phenylenevinylene] (MEH-PPV) is a soundly investigated polymer at room temperature, which was already studied in polymer solar cells. By investigating the aggregated phase of MEH-PPV at low temperatures, the molecular complexity is again increased compared to the systematic series of merocyanines in Chapter 3 and squaraine polymers in Chapter 4. The work in this chapter was conducted in cooperation with the group of Prof. Dr. Anna Köhler at the University of Bayreuth, who previously investigated the phase transition of MEH-PPV upon cooling [266].

The aggregated phase of MEH-PPV allows studying the effect of aggregation on exciton relaxation and energy transfer. Subsequently to a brief literature overview and the description the phase transition of MEH-PPV (Section 5.1), the photo-induced dynamics are explored by transient absorption (TA) and coherent two-dimensional (2D) spectroscopy (Section 5.2). By combining both results of the techniques a discrimination between population dynamics (Subsec. 5.3.1) and energy transfer and relaxation (Subsec. 5.3.2) is given in Section 5.3. Finally, a comprehensive picture of the photo-induced dynamics within the aggregated phase of MEH-PPV is provided in Section 5.4.

5.1 Introduction

Conjugated polymers combine a high absorption cross section with low-cost production and the possibility to deposit them on top of flexible substrates [267–269]. These molecular properties make the class of conjugated polymers a promising molecular functional material for applications in organic electronics and photovoltaics. Despite the advantageous characteristics, the efficiencies of solar cells based on conjugated polymers are still limited to $< 11\%$ [12].

The performance of organic photovoltaics is significantly influenced by the efficiency of energy transport from the bulk of the donor material towards the donor-acceptor interface. Photoinduced dynamics, e.g., excited energy transport and energy relaxation, depend on the interactions of polymer structural units (monomer) within a single polymer chain and to neighboring polymer chains in aggregated structures. These interactions have an influence on a variety of properties of the excited-state relaxation dynamics, namely the population yield of mobile excitons versus nonmobile species (e.g., excimers), the capability to transport the absorbed energy over long distances, the formation of charge-transfer states, and their dissociation into free charges in proximity of the donor-acceptor interface.

Structural variations as conformational disorder in conjugated polymers break the conjugation along the polymer chains, thus forming short conjugated segments, so called "conformational subunits" [187, 270]. Upon photoexcitation, an exciton is populated initially, which is typically delocalized over several conformational subunits. Within a sub-100 fs timescale these delocalized excitons localize on smaller domains due to dynamic coupling between electronic and nuclear degrees of freedom [271]. From these spatially smaller domains the excited energy is transported spatially on a longer timescale by a sequence of Förster energy transfer steps between localized excitons [272, 273]. Intermediate regimes of energy transfer have been reported for MEH-PPV in chloroform [274]. Strong differences in the timescale of energy transfer along a polymer chain (intramolecular) and between different chains (intermolecular) can be observed. Intramolecular energy transfer is typically one to two orders of magnitude slower than intermolecular energy transfer [188, 198, 275, 276]. Thus, the presence of intermolecular acceptor sites can explain the more efficient energy transport in films compared to isolated polymer chains [264, 276, 277].

Although this generalized picture of exciton dynamics can be applied for conjugated polymers, strong differences in the dynamics of the photoexcited species, as well as the rate, the efficiency, and the length scale of energy transport can be observed for systems with different structure and morphology [206, 276, 278–281]. Hence, understanding the key factors of exciton dynamics requires the capability to control and tune the structure of aggregates. A promising approach is to study systems for which aggregation and the morphology of the self-aggregated phase can be controlled by external parameters, i.e., solvent or temperature.

The polymer MEH-PPV is an excellenct candidate to study the exciton dynamics depending on the structure as two classes of chromophores were observed in solution. Firstly, chromophores which emit from high-energy states ("blue sites") and secondly, chromophores emitting from low-energy states ("red sites") [207, 282–284]. Single molecular spectroscopy revealed that the ratio between blue and red sites is dependent on interactions between segments of the polymer contacted by chain folding. Furthermore, the red sites have been characterized by an increased conjugation length in comparison to the blue sites [284, 285]. Additionally, the formation of red sites was related to aggregation [207, 286]. A phase-transition from a coiled phase ("blue phase") at room temperature (RT) to an aggregated and planarized phase ("red phase") at low temperatures has recently been observed for a concentrated solution of MEH-PPV in 2-methyltetrahydrofuran (MeTHF). Moreover, the red phase was characterized by a very large conjugation length [266]. The formation of the red phase was accompanied by the appearance of a low-energy band in both absorption and emission spectra [266, 287]. In the following, the red (blue) phase will be referred to as aggregated (coiled) phase.

The ultrafast dynamics of MEH-PPV have been extensively studied at RT in solution and films, thus characterizing the coiled phase [198, 206, 283, 288, 289]. However, ul-

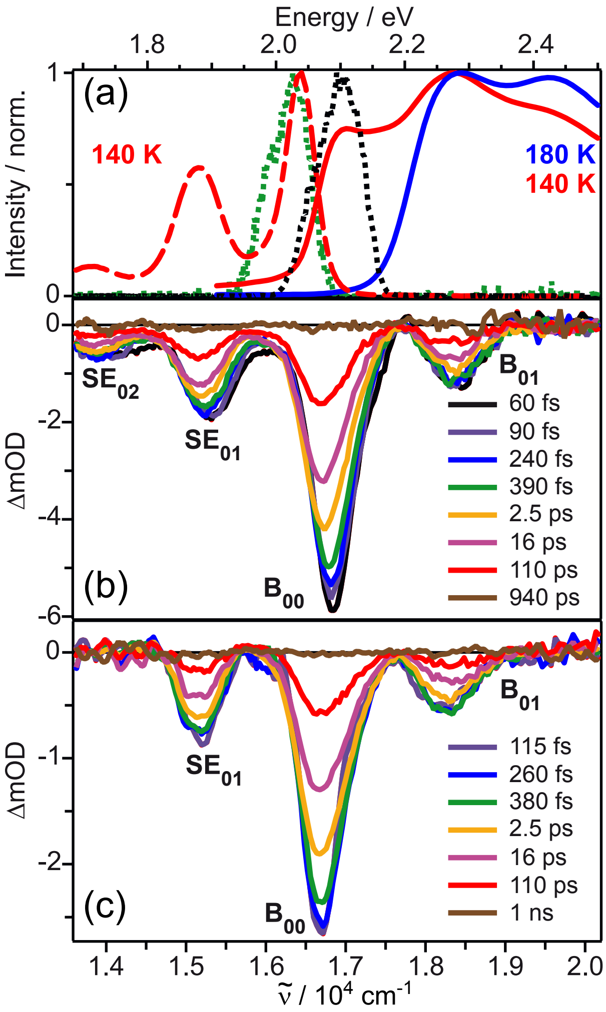

Figure 5.1: (a) Linear absorption (red, solid) and emission (red, dash-dotted) of the aggregated phase of MEH-PPV at 140 K and linear absorption (blue, solid) of the coiled phase of MEH-PPV at 180 K. Additionally, the laser spectra (black and green dotted) used in the experiments to investigate the ultrafast dynamics of the aggregated phase of MEH-PPV are shown. Selected difference spectra at 140 K for different population times are depicted upon excitation at 2.10 eV (b) and 2.03 eV (c). Reprinted with permission from Ref. [4]. © (2015), AIP Publishing LLC.

trafast dynamics for the aggregated phase are still sparse. As a consequence, transient absorption (Subsec. 5.2.1) and coherent 2D spectroscopy (Subsec. 5.2.2) experiments were performed to investigate the regimes of energy transfer in the aggregated phase of MEH-PPV. Furthermore, the energy hopping dynamics between different polymer segments were investigated and conclusively compared with typical values for red-emitting sites in single molecules (Section 5.3).

5.2 Results and Analysis

5.2.1 Transient Absorption

Figure 5.1a depicts the linear absorption and fluorescence spectrum of MEH-PPV at 140 K, and the linear absorption spectrum at 180 K, as well as the pump spectra for TA experiments. At 180 K, MEH-PPV displays a spectrally broad absorption profile with maxima at ≈ 2.27 eV and ≈ 2.45 eV. Upon cooling the sample of MEH-PPV below the transition temperature of 204 K, the absorption profile changes, devoloping a new absorption band at 2.10 eV (red spectrum at 140 K in Fig. 5.1a).

Transient absorption experiments were performed with excitation pulses centered at 2.10 eV and 2.03 eV with pulse durations of 42 fs and 60 fs, respectively. Pulse intensities at the sample position were set to 9.4×10^{13} photons/cm^2 and 4.9×10^{14} photons/cm^2 for 2.10 eV and 2.03 eV, respectively. Beam sizes at the sample were ≈ 50 μm for the pump and ≈ 30 μm for the probe beam. A white-light continuum covering the complete visible spectrum was used as probe pulses in all TA experiments.

With the selected pump spectra only the respective red-edge of the sample was excited. The resulting difference spectra (DS) are shown in Fig. 5.1b and 5.1c for the TA experiments at 140 K exciting at 2.10 eV and 2.03 eV, respectively. All DS display three distinct bands at 2.27 eV, 2.08 eV, and 1.88 eV. Upon 2.10 eV excitation, a fourth band is observable at 1.72 eV. This band is not visible in the DS exciting at 2.03 eV, as the magnitude of the band is within the experimental noise. Spectral bands in the DS can be ascribed by comparing them with the inverse linear absorption and fluorescence spectra. The band at 2.27 eV (B_{01}) displays the GSB of the vibronic 0-1 transition. The band at 2.08 eV (B_{00}) is composed of contributions from the GSB and SE of the 0-0 transition. Lastly, the negative bands at 1.88 eV (SE_{01}) and 1.72 eV (SE_{02}) can be assigned to SE from the 0-1 and 0-2 vibronic transitions, respectively.

The GSB features (B_{00} and B_{01}) do not resemble the complete absorption spectrum. As no positive contributions are observable in the DS, this can be interpreted either as the absence of an ESA contribution or as overlapping contributions of ESA and GSB which compensate each other. Under the first assumption of the lack of an ESA contribution, only a fraction of the steady-state absorption stems from the states absorbing at 2.10 eV. Thus, the latter states can be attributed to the planarized, aggregated phase of MEH-PPV. Generally, planarization of conjugated polymers affects a fraction of $40 - 60\%$ of all chromophores [290, 291]. As a result, the absorption of the polymer above 2.10 eV, which is not reflected by the transient bleach signal, can be assigned to the non-planarized, coiled phase which was not excited by the pump laser.

Regarding the relaxation dynamics, the GSB recovers within 1 ns as observable from the DS in Fig. 5.1b and Fig. 5.1c for both excitation energies. Still, depending on the excitation energies, distinct differences can be observed within the first 10 ps. Upon 2.10 eV excitation, all bands display a bathochromic spectral shift, most pronounced in the SE. In contrast, the amplitude of the shift is almost completely suppressed upon exciting the low-energy edge of the aggregated-phase absorption at 2.03 eV.

In general, the bands of the DS display a decay in amplitude and a spectral shift with evolving waiting time. These two spectral changes might occur on a similar timescale, thus hampering a distinct identification and separation of molecular relaxation processes in a global analysis. Due to the fact that all bands observed in TA are spectrally separated without indications for an ESA contribution, a band analysis was performed. The latter analysis allows the separation of the decay contributions originating from population dynamics from the band-shifts, via spectral moments. The first two spectral moments M

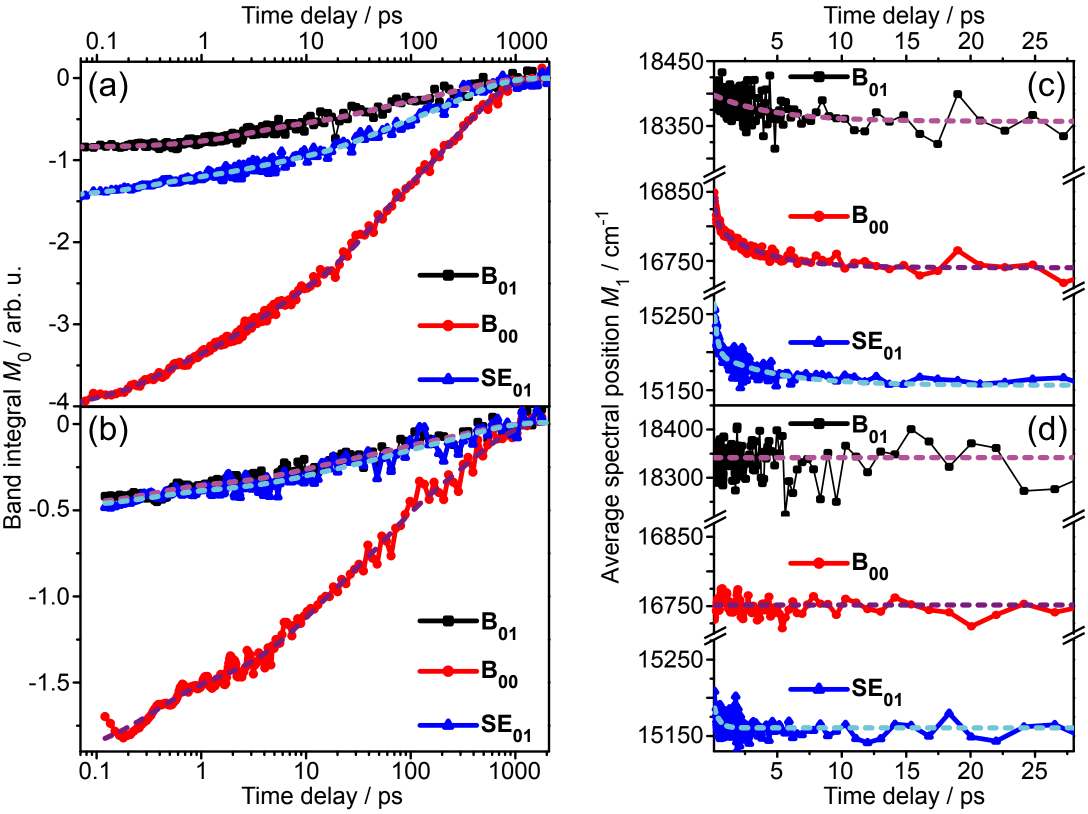

Figure 5.2: Spectral moments of the three major bands (B_{01}, B_{00}, and SE_{01}) observed in the transient absorption experiments as a function of the population time T: Integrated intensity $M_0^{(i)}$ (Eq. 5.2.1a) of the three major bands for excitation at (a) 2.10 eV and (b) 2.03 eV and their average spectral position $M_1^{(i)}$ (Eq. 5.2.1b) upon excitation at (c) 2.10 eV and (d) 2.03 eV. The temporal dependence of the spectral moments is fitted by a multi-exponential kinetics (dashed lines) consistent with the results of the maximum entropy method analysis. Reprinted with permission from Ref. [4]. © (2015), AIP Publishing LLC.

are defined as

$$M_0^{(i)}(T) = \sum_{\nu=\nu_1^{(i)}}^{\nu_2^{(i)}} I(\nu, T) \cdot \Delta\nu, \tag{5.2.1a}$$

$$M_1^{(i)}(T) = \frac{1}{M_0^{(i)}(T)} \sum_{\nu=\nu_1^{(i)}}^{\nu_2^{(i)}} \nu \cdot I(\nu, T) \cdot \Delta\nu, \tag{5.2.1b}$$

with the absorbance change $I(\nu, T)$ at frequency ν and population time T, the frequency summation limits for each band i, $\nu_1^{(i)}$ and $\nu_2^{(i)}$, and the frequency interval between data points $\Delta\nu$. Population dynamics are probed exclusively by the band integrals $M_0^{(i)}$ (zero-order spectral moments), as they are not sensitive to variations in the shape or position of the bands, under the given premise that the bands do not overlap spectrally. Band shifts are directly monitored by the first spectral moments $M_1^{(i)}$, which reflect the average spectral position of the bands.

Figure 5.2a and Figure 5.2b show the results of the zeroth order spectral moments $M_0^{(i)}$ of SE_{01}, B_{00}, and B_{01}, as function of T upon 2.10 eV and 2.03 eV excitation, respectively. The temporal behavior of the population can be described either by a broad distribution of rates or by several distinct kinetic processes due to the wide distribution of polymer lengths and possible conformations. The former case is typically described by a Kohlrausch-Williams-Watts (KWW) function [292], i.e., a stretched exponential function,

$$M_1^{(0)}(T) = Ae^{-\left(\frac{T}{\tau}\right)^{\beta}}, \tag{5.2.2}$$

where A is the amplitude, τ is the characteristic time and β is the distribution width. Previously investigated independent, parallel single-step processes as well as sequential multistep processes in disordered structures revealed a stretched exponential dynamical behavior by theoretical models [292–299]. In the case of several distinct kinetic processes, a multi-exponential fit function

$$M_1^{(0)}(T) = \sum_{j=1}^{4} A_j e^{-\frac{T}{\tau_j}}, \tag{5.2.3}$$

with amplitudes A_j and characteristic times τ_j, is used.

The maximum entropy method (MEM), via the open-source program MemEXP [300, 301], is performed to discriminate between both cases without initial bias. Figure 5.3 depicts the results of the MEM analysis for the temporal evolution of M_0 for B_{01} and B_{00} upon excitation at 2.10 eV and 2.03 eV, respectively. As the MEM analysis in Fig. 5.3

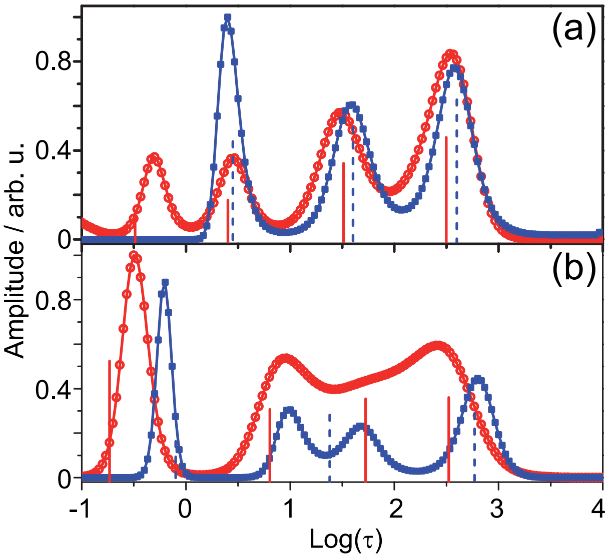

Figure 5.3: Best rate distributions describing the temporal evolution of M_0 for the bleach bands B_{01} (blue squares) and B_{00} (red circles), upon excitation at (a) 2.10 eV and (b) 2.03 eV, as retrieved via the maximum entropy method analysis. Vertical blue dashed (red solid) lines show the best rate constants and corresponding amplitudes for the multi-exponential fit of the B_{01} and B_{00} population dynamics. Reprinted with permission from Ref. [4]. © (2015), AIP Publishing LLC.

Table 5.1: Characteristic time constants obtained from a multi-exponential global fit and from a stretched exponential global fit of the integrated signals $M_0^{(i)}(T)$, respectively, and from the independent fits of the average spectral position $M_1^{(i)}(T)$ of the three major bands (i = B_{01}, B_{00} and SE_{01}) of the transient absorption data described in Section 5.2.1. Reprinted with permission from Ref. [4]. © (2015), AIP Publishing LLC.

	Excitation energy	2.10 eV	2.10 eV	2.03 eV
	Temperature	120 K	140 K	140 K
Population decay $M_0(T)$ $M_0(T) = \sum_{j=1}^{4} A_j \mathrm{e}^{-\frac{T}{\tau_j}}$	τ_1 [fs]	220 ± 50	290 ± 40	240 ± 60
	τ_2 [ps]	2.6 ± 0.2	2.5 ± 0.3	5 ± 2
	τ_3 [ps]	41 ± 4	32 ± 3	41 ± 8
	τ_4 [ps]	320 ± 20	312 ± 11	380 ± 50
Population decay $M_0(T)$ $M_0(T) =$ $A_1 \mathrm{e}^{-\frac{T}{\tau_1}} + A_2 \mathrm{e}^{-(\frac{T}{\tau_2})^{\beta}}$	τ_1 [ps]	1.18 ± 0.12	0.88 ± 0.07	0.26 ± 0.17
	τ_2 [ps]	74 ± 3	94 ± 3	63 ± 3
	β [ps]	0.48 ± 0.01	0.49 ± 0.01	0.45 ± 0.02
Band shift $M_1^{\mathrm{B}_{01}}(T)$	τ_1^{s} [fs]	–	–	–
	τ_2^{s} [ps]	3.9 ± 0.8	4.8 ± 0.8	–
Band shift $M_1^{\mathrm{B}_{00}}(T)$	τ_1^{s} [fs]	200 ± 80	230 ± 70	< 100
	τ_2^{s} [ps]	2.9 ± 0.5	3.6 ± 0.6	–
Band shift $M_1^{\mathrm{SE}_{01}}(T)$	τ_1^{s} [fs]	170 ± 40	250 ± 50	400 ± 200
	τ_2^{s} [ps]	2.8 ± 0.6	4.7 ± 1.1	–

contains four distinct time scale peaks, the temporal behavior is described by several kinetic processes in favor of a broad distribution of rates. Resulting fit constants in Table 5.1 should be interpreted as average constants of different rate distributions, as these discrete processes might be still distributed to a certain degree. In comparison, the fit results for the case of a broad distribution of rates are also listed in Table 5.1 below the results of the multi-exponential global fit.

The results of the first moment spectral moment $M_1^{(i)}$ analysis are depicted in Fig. 5.2c and Fig. 5.2d and listed in Table 5.1 for excitation energies at 2.10 eV and 2.03 eV, respectively. Upon 2.10 eV excitation, all bands display a spectral shift within the first 15 ps. On the one hand, an initial spectral shift on the order of $\tau_1^s \approx 200 - 250$ fs can be observed for the bands containing contributions from SE, i.e., SE_{01} and B_{00}. On the other hand, a ≈ 4 ps shift in all bands is observed. The former sub-300 fs shift can be ascribed to processes in the excited state as only bands with SE contribution are affected. Furthermore, the absence of this shift in the GSB band B_{01} is an additional evidence for the lack of a ESA contribution overlapping in this spectral region. The ≈ 4 ps bathochromic shift is observed for the average spectral positions of all bands. For B_{01} and SE_{01} the ≈ 4 ps shift occurs with similar amplitudes.

Except for a very small initial shift in the SE_{01} band on a sub-500 fs time scale, no spectral evolution of the average spectral band position is observed upon 2.03 eV excitation,

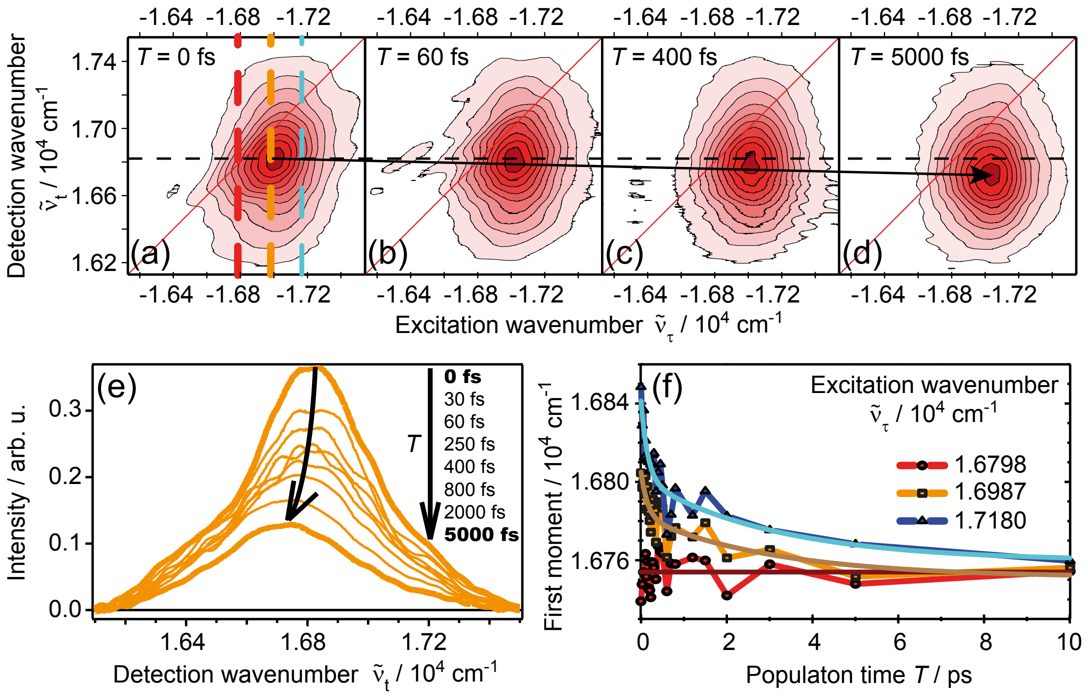

Figure 5.4: Selected normalized 2D spectra of MEH-PPV at different population times T: (a) 0 fs, (b) 60 fs, (c) 400 fs, and (d) 5000 fs. Contour lines are plotted from 5% (light pink) to 95% (dark red) in steps of 10%. The dashed horizontal line marks the $T = 0$ average spectral position of the 2D signal at $\tilde{\nu}_\tau = 1.6987 \times 10^4$ cm^{-1}, while the black arrow indicates the shift of the 2D signal towards lower detection wavenumbers as a function of the population time T. (e) Spectral evolution of the signal along the detection axis for excitation at $\tilde{\nu}_\tau = 1.6987 \times 10^4$ cm^{-1} (orange vertical dashed line in panel a). (f) Temporal evolution of the first moment $M_1(T)$ (i.e., average spectral position) of the signal along the detection axis (symbols) for the different excitation wavenumbers shown by the vertical lines in panel (a). Overlayed solid lines show the best individual bi-exponential fit of each trace. Reprinted with permission from Ref. [4]. © (2015), AIP Publishing LLC.

which indicates that no excess energy is in the system.

5.2.2 Coherent 2D Spectroscopy

Coherent 2D spectroscopy in box geometry was performed with 35 fs laser pulses centered at 2.10 eV. The time delay between the third pulse and the local oscillator (t_{34}) was set to 2.8 ps. The coherence time τ was scanned in the range of ±145 fs in steps of $\Delta\tau = 5.5$ fs.

Figure 5.4 depicts normalized 2D spectra of MEH-PPV at selected population times. At $T = 0$, the 2D spectrum is elongated along the diagonal ($-\tilde{\nu}_\tau = \tilde{\nu}_t$), displaying a cross-peak below the diagonal. With progressing population time, the 2D spectra loses the diagonal shape and shifts to lower detection wavenumbers $\tilde{\nu}_t$, depicted by the black arrow in Fig. 5.4. In addition to this bathochromic shift in $\tilde{\nu}_t$, the 2D spectra change to a round and symmetric shape.

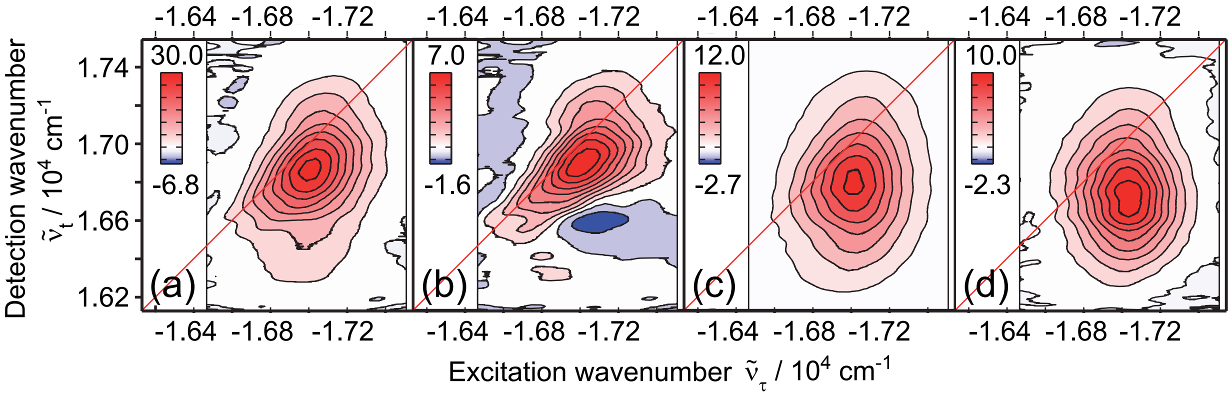

Figure 5.5: Two-dimensional decay-associated spectra (2D-DAS) obtained from global analysis of the 2D data and associated with (a) sub-30 fs, (b) 290 fs, (c) 2.9 ps, and (d) $\gg$ 10 ps kinetics. The data at the lowest excitation wavenumbers, where no signal was detected, were removed from the analysis. Contour lines are drawn from 0 to the maximum (minimum) value in steps of 12.5%. Reprinted with permission from Ref. [4]. © (2015), AIP Publishing LLC.

Dynamical changes of the 2D spectra are shown for an exemplary cut along $\tilde{\nu}_t$ at $\tilde{\nu}_\tau = -1.6987 \times 10^4$ cm^{-1} in Fig. 5.4e. Similar to the analysis performed for the TA experiments, the first moment $M_1(\tilde{\nu}_\tau, T)$ of the cuts along $\tilde{\nu}_t$ are evaluated for three $\tilde{\nu}_\tau$ values as a function of T and presented in Fig. 5.4f. While the cut at $\tilde{\nu}_\tau = -1.6798 \times 10^4$ cm^{-1} displays no shift, a red-shift which increases with raising $\tilde{\nu}_\tau$ can be observed for the other temporal evolutions of the first moment (at -1.6987×10^4 cm^{-1} and -1.7180×10^4 cm^{-1}, respectively). The shift is finished within 10 ps resulting in an asymptotic value of $\tilde{\nu}_t = -1.6750 \times 10^4$ cm^{-1}, independent of $\tilde{\nu}_\tau$.

The temporal evolution of $M_1(\tilde{\nu}_\tau, T)$ at all $\tilde{\nu}_\tau$ was fitted in analogy to the previous TA with bi-exponential kinetics. For $\tilde{\nu}_\tau < 1.6790 \times 10^4$ cm^{-1} the first time constant is allowed to be different, as an ultrafast ($<$ 40 fs) hypsochromic shift is observed. A small increase of both time constants was observed with increasing $\tilde{\nu}_\tau$ in an independent fit. This indicates a transfer from high- to low-energy exciton states, as the energy from high energy states can proceed through more intermediate steps than from the lower-energy states. However, due to the signal-to-noise ratio of the data, an accurate analysis of the $\tilde{\nu}_\tau$ dependece of the shift rates was not possible. Thus, a global analysis of the time evolution of $M_1(\tilde{\nu}_\tau, T)$ was performed with the same time constants for all $\tilde{\nu}_\tau$. The latter analysis results in two time constants, i.e., 180 ± 30 fs and 4.5 ps, which should be treated as average values over the observed spectral range. Both time constants are in good agreement with the time scales of the bandshifts observed in the TA data (compare Table 5.1).

Figure 5.5 depicts the two-dimensional decay-associated spectra (2D-DAS), the 2D assemblies of DADS in TA, resulting from a global analysis of the 2D spectra [302–304]. The dynamics of MEH-PPV in 2D spectroscopy were fitted by four exponential functions. These results should again be interpreted as average timescales for processes in the polymer. Four time scales were prerequisite to fit the temporal behavior of the 2D data properly, namely $\tau_1^{2D} < 30$ fs, $\tau_2^{2D} = 290 \pm 60$ fs, $\tau_3^{2D} = 2.9 \pm 0.5$ ps, and a τ_4^{2D} >> 10 ps. The latter timescale was necessery to reproduce the remaining 2D signal at 5 ps. The observed timescales of the 2D analysis are quite similar to the ones observed in the TA study (compare Table 5.1). The initial 2D-DAS corresponding to $\tau_1^{2D} < 30$ fs displays the decay (positive contribution) of the diagonal contribution in the 2D spectrum. Subsequently, the 2D-DAS for $\tau_2^{2D} = 290$ fs consists of a decay component along the diagonal and a rising component (negative contriubution) below the diagonal. Thus, the latter 2D-DAS spectrum represents a bathochromic shift to lower $\tilde{\nu}_t$.

The underlying process can be assigned to a shift of the SE, due to the similar timescale for the SE shift in the TA analysis. At all $\tilde{\nu}_\tau$ the amplitude of decay is larger than the rise of the cross-peak below the diagonal. Hence, the decaying components overlap with the red-shift of the SE. Lastly, the two 2D-DAS corresponding to the timescales $\tau_3^{2D} = 2.9$ ps and $\tau_4^{2D} \gg 10$ ps display a similar symmetric round shape. However, the 2D-DAS of $\tau_4^{2D} \gg 10$ ps peaks at lower $\tilde{\nu}_t$ than $\tau_3^{2D} = 2.9$ ps.

5.3 Discussion

5.3.1 Population Dynamics

Rather versatile and complex relaxation dynamics have been previously reported for solutions, films, and isolated molecules of MEH-PPV [207, 283, 285, 286, 288, 305, 306]. In isolated chains, a mono-exponential decay in the range of $0.4 - 1.2$ ns was observed [283, 286]. In contrast, aggregates [283, 286], films [208, 278, 307], and collapsed chains [282, 308] of MEH-PPV display a non-exponential decay with a strongly reduced photoluminescence quantum yield. The latter observation was assigned due to the presence of non-emissive species which absorb above 2.07 eV [277, 283, 309–311]. Alternatively, the non-emissive species were assigned to excimers, aggregates, polarons, and polaron pairs, which were directly photo-excited or accessed by the quenching of singlet excitons [205, 206, 277, 305, 308, 312, 313].

Transient absorption (Sec. 5.2.1) and 2D spectroscopy (Sec. 5.2.2) displayed complex relaxation dynamics within the aggregated phase of MEH-PPV. In addition to the TA analysis, 2D-DAS revealed a < 30 fs decay of the diagonal component. This relaxation time scale is faster than the experimental instrument response and possibly comprises solvent contributions. Nevertheless, a similar ultrafast (≤ 30 fs) relaxation was observed in a three pulse photon echo peak shift (3PEPS) study of MEH-PPV [289, 314, 315], which was assigned to exciton localization. Furthermore, depolarization of anisotropy due to several competing relaxation processes was observed, explained by exciton relaxation and localization processes [198, 205]. The latter processes agree with the observed loss of the diagonal contribution in the 2D spectra, thus leading to the assignment of the ≤ 30 fs processes to exciton relaxation and localization.

In the TA, 2D experiments and affiliated analysis of the temporal behavior, no indications for ESA contributions were observed. Typically, one would expect an ESA contribution close to the one-exciton absorption due to the excitation to a two-exciton band. Deviations from this behavior are known in literature in the presence of strong electron correlation, which is for example present in polyenes. Although the lack of an ESA contribution can not be excluded for all wavenumbers, no dominant contribution can be observed. In 2D spectroscopy, the spectrum at $T = 0$ peaks below the diagonal. Either the 2D signal is shifted to lower $\tilde{\nu}_t$ due to an overlapping ESA contribution above the diagonal or due to an initial relaxation within the experimental time-resolution. Albeit it is not possible to distinguish between both scenarios based on the experimental observations, an initial relaxation is expected due to ultrafast exciton localization. An experimental approach to distinguish between the initial shift and the overlapping ESA contribution would be two-dimensional double-quantum coherence spectroscopy [316]. Such an experiment would provide a direct way to measure the energy position of the two-exciton states in a system, as well as the correlation to the one-exciton states.

Former observed complex dynamics were described by a linear combination of single exponential functions (Eq. 5.2.3) and a stretched exponential decay (Eq. 5.2.2). For both models a similar interpretation for the relaxation processes can be concluded as described in the following.

For the initial dynamics ($<$ 10 ps) a significant fraction of GSB recovery can be observed as well as a simultaneous decay of SE and GSB. Furthermore, exciton relaxation and energy transfer fall into the time regime $<$ 10 ps, as seen by the analysis of the average band positions $[M_0(T)]$. Hence, the repopulation of the ground state up to $T = 10$ ps is assigned to non-radiative internal conversion processes mediated by defects in the aggregated phase [282]. This interpretation is consistent with the previously observed decrease of emission quantum yield for MEH-PPV films and aggregates compared to single solvated chains [283, 310, 311, 317].

A complete recovery of the GSB is observed occurring on a $>$ 10 ps timescale. As energy transfer between excitons can be observed within a $<$ 10 ps timescale, the processes occurring with $>$ 10 ps dynamics can be assigned to the $S_1 \rightarrow S_0$ relaxation of the exciton states at the bottom of the density of states. Upon 2.10 eV excitation a $\approx$ 40 ps and a $\approx$ 320 ps timescale were observed in transient absorption for 140 K and 120 K. Comparing the experiments for both temperatures, the $\approx$ 40 ps occurred with a relative intensity of the total amplitude of 25% and 43%, while the $\approx$ 320 ps component occurred with 38% and 32% at 140 K and 120 K, respectively. Two relaxation timescales were reported previously and were assigned to intramolecular energy transfer [318]. Furthermore, the faster timescale was assigned to a non-radiative decay of polaron pairs [318]. As in our study the decay is obsered in the GSB and SE, a non-radiative decay can be excluded. Thus, the $\approx$ 40 ps is assigned to a radiative $S_1 \rightarrow S_0$ transition, which is quenchend by defect states in the aggregated phase. Conclusively, the $\approx$ 320 ps time scale occurs from states which are further away from defect states. Hence, the latter states are not quenched and decay on a longer timescale. For the analysis with a stretched exponential function, the $>$ 10 ps dynamics were fitted with $\beta = 0.48$, which indicates a highly distributed $S_1 \rightarrow S_0$ relaxation process. A β-value close to 0.5 indicates a dispersive energy transfer by dipole-dipole coupling to lower energies from where the energy is efficiently quenched by defect states [272, 319, 320]. Due to the spatial distribution of defect states, the dynamics occur highly distributed, thus leading to a stretched exponential behavior of the GSB and SE decay. A density of electron traps with a 0.7 eV depth on the order of 1023 m^{-3} was determined for the structurally related alkoxy-PPV-derivate OC1C10-PPV. These electron traps are present in π-conjugated polymers at about the same density as they are likely to arise from some kind of water-oxygen complex [321, 322]. It has been suggested that these complexes act as exciton traps and therefore limit the exciton diffusion length [323].

A distinct statement can be made for the presence of long-lived states (which display lifetimes on a > 1 ns timescale). These states are suggested to originate from repopulation of emissive single exciton state in MEH-PPV films. Such species were observed in literature for excitation energies above 2.14 eV [277, 278, 283, 305, 308, 312, 313], where the coiled phase absorbs. Thus, the generation of long-lived species can be excluded for the energies of the pulses in the performed experiments.

5.3.2 Energy Transport and Relaxation

The analysis of the average spectral band position $\left[M_1^{(i)}(T)\right]$ in TA and 2D spectroscopy revealed two relaxation processes: one on the order of ≈ 200 fs and the other with ≈ 4 ps.

In TA, the former process can be detected as a bathochromic shift exclusively for bands which contain SE contributions. Figure 5.6 depicts the amplitude of the ≈ 200 fs along $\tilde{\nu}_t$ for the B_{00} band as observed in 2D spectroscopy for different $\tilde{\nu}_\tau$. For increasing excitation energies an increase in the amplitude can be observed. In general, a ≈ 200 fs bathochromic shift can be explained by exciton relaxation, vibrational relaxation, or conformational relaxation in the excited states. A (Förster) energy transfer between different conformational subunits can be excluded, as it would result in an additional bathochromic shift for the GSB contribution. Previously, a shift on a similar timescale ($\approx 200 - 400$ fs) was observed for the room-temperature (RT) phase of MEH-PPV by transient grating (TG) and 3PEPS experiments [289, 314]. In these studies, the shift was explained by exciton relaxation. Furthermore, a bathochromic shift of the emission for PPV-based polymers at RT was observed, which was absent in small oligomers. Thus, the bathochromic shift can therefore not be explained by exclusively vibrational relaxation or solvation relaxation dynamics [324, 325]. Conformational dynamics play an important role in the relaxation of photo-excited polymers and could lead to a bathochromic shift in SE, e.g. by planarization. Ultrafast structural relaxation on the timescale of high-frequency vibrational modes have been attributed to be responsible for ultrafast exciton localization in MEH-PPV [205, 271, 289, 315]. In contrast, torsional relaxation and excited state planarization are expected to take place on a timescale of few ps or longer for MEH-PPV in solution at RT [195, 306, 326]. In the aggregated phase, these processes are expected to be even slower. Thus, the bathochromic shift in SE occurs due to exciton relaxation within the manifold of electronic states sharing the same ground state.

In opposition to the former shift, the additional ≈ 4 ps process appears in the GSB and SE bands for 2.10 eV laser excitation, while it is missing upon 2.03 eV excitation. A ≈ 4 ps shift of the GSB band can either be explained by a spectral diffusion process in the electronic ground state or by a (Förster) energy transfer from high-energy to low-

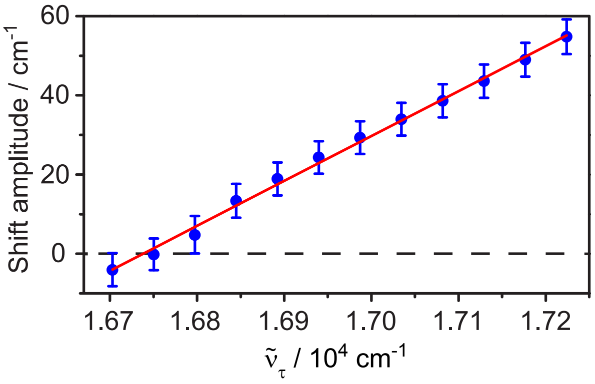

Figure 5.6: Amplitude of the ≈ 4.5 ps red-shift along the detection axis observed in the 2D experiment as a function of the excitation wavenumber $\tilde{\nu}_\tau$, obtained from the bi-exponential global fit of the $M_1(\tilde{\nu}_\tau, T)$. The data is phenomenologically described by a linear fit (red line) with a slope of 0.113±0.002. The standard deviation of the linear fit is denoted as error bars of $\pm\sigma$. Reprinted with permission from Ref. [4]. © (2015), AIP Publishing LLC.

energy states located at different sites in the aggregate (i.e., exciton hopping). Spectral diffusion in the electronic ground state is based on an inhomogeneous distribution of transition energies within an absorptive lineshape. Laser excitation which is spectrally narrower than the linewidth of the ensemble only excites a sub-ensemble of the spectral linewidth. Thus, a spectral hole is created in the electronic ground state. Before this hole is repopulated by the excited state, it can be refilled by environment-induced fluctuations in the transition energy of non-photoexcited chromophores. Depending on the spectral position of the initial excited sub-ensemble, whether it is located at the center or the edge of the transition energy distribution, spectral diffusion appears as a spectral broadening or as a spectral shift. (Förster) energy transfer generally occurs between different excited states with little or no orbital overlap by dipole-dipole coupling. In a polymer, the energy is typically transferred within the excitonic density of states. Due to different ground states of donor and acceptor, energy transfer leads to the recovery of the high-energy tail of the GSB, while the low-energy side GSB increases due to the excitation from the donor to acceptor unit.

In contrast to TA, 2D spectroscopy allows to distinguish between spectral diffusion and (Förster) energy transfer. Spectral diffusion leads to a loss of memory of the initial excitation energy. Thus, due to spectral diffusion a 2D signal loses the diagonal elongation ($\tilde{\nu}_\tau = \tilde{\nu}_t$), becomes spectrally broader and changes into a round shape. None of these features is observed on a timescale larger than 200 fs. Hence, the ≈ 4 ps process can not originate from spectral diffusion. Energy transfer between different states can be observed by 2D spectropscopy as excitation energy $\tilde{\nu}_\tau$ and $\tilde{\nu}_t$ are correlated. Thus, the energy transfer from a high-energy state to a low-energy state leads to a cross-peak below the diagnoal. The high exciton density of MEH-PPV prevents the observation of a distinct cross-peak, but appears as a bathochromic shift of the 2D signal along the detection axis $\tilde{\nu}_t$. Thus, 2D spectroscopy allows the identification of the ≈ 4 ps process as an energy transfer between excitonic states. Consistently, the amplitude of the bathochromic shift with ≈ 4 ps rises for increasing excitation energies, as higher energetic states are accessed.

In addition, 2D spectroscopy provides the option to analyze the energy transfer dynamics as function of excitation wavenumber $\tilde{\nu}_\tau$. Figure 5.6 depicts the amplitude of the ≈ 4.5 ps bathochromic shift determined by the global analysis of $M_1^{(i)}(T)$ in 2D spectroscopy as a function of $\tilde{\nu}_\tau$. The $\tilde{\nu}_\tau$ depending amplitude of the signal shift re-

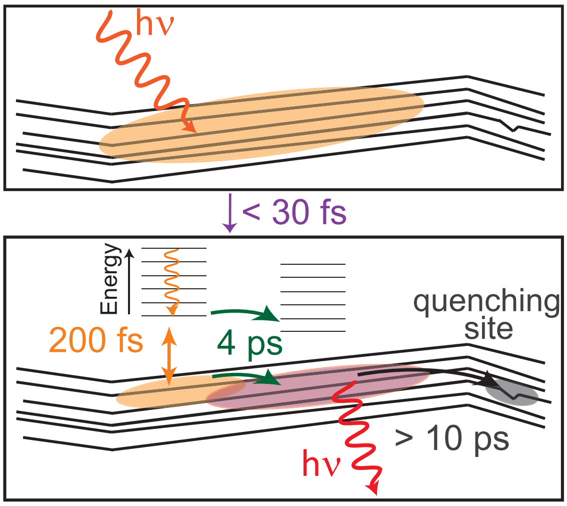

Figure 5.7: Schematic representation of the photophysics of the aggregated phase of MEH-PPV. Initially photoexcited delocalized exciton states (upper frame) localize on an ultrafast (< 30 fs) timescale on smaller domains on the aggregate chains (lower frame). Within the following ≈ 200 fs, exciton relaxation within these smaller domains occurs and leads to the population of the exciton states at the bottom of the density of states. On a ≈ 4 ps timescale, Förster energy transfer leads to migration of the exciton towards the lowest energy states of the aggregated phase, from which energy transfer to defect states and radiative relaxation take place. Reprinted with permission from Ref. [4]. © (2015), AIP Publishing LLC.

flects the amount of energy relaxation since the GSB and SE components of the signal shift simultaneously and with the same amplitude as previously shown by the analysis of the first moments of $M_1^{\mathrm{B}_{01}}$ and $M_1^{\mathrm{SE}_{01}}$ upon 2.01 eV excitation (cf. Table 5.1). For $\tilde{\nu}_\tau < 1.6750 \times 10^4$ cm^{-1} no shift is observed within the experimental signal-to-noise, except for a small < 40 fs blue-shifted component ascribed to the initial loss of the diagonal elongation. Hence, the position of the 0-0 transition for the lowest exciton states in the aggregated phase of MEH-PPV is $\tilde{\nu} = (16750 \pm 50)$ cm^{-1}, with a confidence value of 50 cm^{-1}, which is given by the wavenumber separation between consecutive $\tilde{\nu}_\tau$ points in Fig. 5.6.

Independent of $\tilde{\nu}_\tau$, the values of $M_1(\tilde{\nu}_\tau, T)$ reach the same asymptotic value (cf. Fig. 5.4f). The ≈ 4.5 ps shift accounts only for a small fraction of the energy relaxation, i.e., ≈ 55 cm^{-1} at $\tilde{\nu}_\tau = 1.7224$ cm^{-1} (Fig. 5.6). Therefore, most of the energy relaxation occurs on time scales much faster than 4.5 ps and populates low-energy exciton states, which are at most ≈ 55 cm^{-1} higher in energy than the lowest energy states on the aggregated phase. Thus, Förster energy transfer occurs at the bottom of the density of states.

5.4 Summary and Conclusions

Figure 5.7 summarizes the relaxation dynamics of the aggregated phase of MEH-PPV based on broadband transient absorption and coherent 2D spectroscopy. Upon excitation, initially delocalized excitons localize within sub-30 fs to spatially smaller conjugated domains [271]. Depending on the excitation energy, different conjugated domains can be accessed. Within ≈ 200 fs excited energy relaxes within the exciton manifold, sharing a common ground state. Hence, the lowest exciton states are populated. Analysis of coherent 2D spectroscopy revealed that the accessed exciton states after ≈ 200 fs are located

$\approx$ 55 cm^{-1} higher in energy than the lowest exciton states. Subsequently, the energy relaxes by exciton diffusion to the bottom of the density of states of the aggregate. From the latter states exciton transfer occurs with a broad distribution of time scales longer than 10 ps either towards defect states or back to the ground state.

Generally, planarization dynamics are expected on a $>$ 10 ps time scale. Due to the degree of planarization of the studied aggregated phase of MEH-PPV, these effects are too small to be detected in the performed experiments. Future studies could reveal planarization effects by detecting the emission with a higher spectral resolution.

Coherent 2D spectroscopy is a particularly suited technique to study the relaxation dynamics in complex systems as a function of the excitation energy. By the combination of coherent 2D and TA spectroscopy the aggregated phase of MEH-PPV was characterized. Most photoexcited excitons relax on an ultrafast timescale with only little spatial displacement energy. Subsequently, due to the initial $\approx$ 200 fs relaxation and the $\approx$ 4 ps energy transfer, 95% of the excitons are located at the low-energy excitonic states within the first $\approx$ 12 ps after excitation.

Chapter 6

Conclusion

The aim of this work was to investigate photoinduced relaxation dynamics of multichromophoric molecular systems in dependence on their structure. Results of such an investigation are essential to enhance the efficiency of photo-electronic devices, especially in polymeric solar cells. For this purpose, well-defined molecular structures in solution were chosen, which allowed to study the influence of their morphology and related chromophore–chromophore interactions on the relaxation dynamics of polymers by ultrafast spectroscopy.

Transient absorption (TA) and coherent two-dimensional (2D) spectroscopy have been applied to reveal effects of chromophore interactions in multichromophoric systems of increasing molecular complexity: mono-, di-, and trimeric merocyanines in cooperation with the group of Prof. Dr. Frank Würthner at the University of Würzburg, squaraine polymers in cooperation with the groups of Prof. Dr. Christoph Lambert and Prof. Dr. Roland Mitrić, both at the University of Würzburg, and aggregated MEH-PPV polymers in cooperation with the group of Prof. Dr. Anna Köhler at the University of Bayreuth.

With a defined number of chromophores and substitution patterns attached to a benzene linker, which was designed by synthesis, the systematic series of merocyanines in Chapter 3 represents an ideal model system to study the influence of chromophore orientation on chromophore interactions and relaxation dynamics. In the linear absorption spectra distinct differences between the monomer, both para- and meta-substituted dimer, and the meta-substituted trimer were observed. These spectral changes could not be explained solely by applying exciton theory. Based on the ultrafast relaxation dynamics by TA, a general relaxation scheme with two minima in the excited-state potential energy surface was derived which was applied to all studied merocyanine systems. The increase in excited-state lifetime from the monomeric merocyanine (17 ps) over the para-substituted bichromophore (51 ps) and the meta-substituted dimer (77 ps) to the meta-substituted trimer (81 ps) was proposed to originate from the stabilization of one of the excited-state minima with intramolecular-charge transfer character. Additionally, 2D spectroscopy allowed to exclude an isomerization process as a major deactivation channel during the relaxation process.

By combining structural assignments via electro-optical absorption (EOA) and density functional theory (DFT) with the relaxation model derived from TA and 2D spectroscopy, the increase in excited-state lifetime for the multichromophoric merocyanines could be confirmed by a stabilization of an intramolecular charge-transfer state due to dipole-dipole interactions, which is even more efficient in the meta-substituted dimer and trimer due to the proximity of chromophores compared to the para-substituted merocyanine.

In addition, the structural insights by EOA and DFT provided a starting point in the calculation of the exciton-splitting energy in dependence on the chromophore orientation. Due to the flexibility of individual chromophores this approach explicitly took changes in chromophore-chromophore distance and orientation into account. The linear absorption spectra of the multichromophoric merocyanines could be qualitatively explained by a superposition of monomeric and excitonic character which originates from the flexibility of the chromophores. Thus, based on molecular synthesis an intramolecular charge-transfer state could be stabilized which gives access to an approximately five times longer excited-state lifetime compared to the monomer.

By going from mono-, di-, and trimeric merocyanines to the polymeric squaraine $[\mathrm{SQB}]_n$ in Chapter 4, the structural complexity of the studied molecular system increased noticeably. However, as several chromophores of the polymer act as conjugation subunits, the description of the polymer is reduced. Recently, distinct changes of the linear absorption spectra of $[\mathrm{SQB}]_n$ in dependence of the solvent were assigned to a different superposition of *helix* and *zigzag* segments within $[\mathrm{SQB}]_n$, thus allowing for a comparison of the effect of the predominant structures on the relaxation dynamics of conjugated polymers by the choice of solvent.

Long-range-corrected tight-binding time-dependent DFT calculations displayed the effect of chromophore orientation on the linear absorption spectra and confirmed the presence of predominantly *zigzag* segments in dichloromethane (DCM) and *helix* structures in dimethylformamide (DMF), which can be treated as H- and J-aggregates, respectively.

Individual TA experiments of $[\mathrm{SQB}]_n$ were performed in DCM and DMF, thereby exciting either *zigzag* or *helix* structures, respectively. To exclude interactions between polymer strands, all spectroscopic experiments were performed under diluted conditions. The results of TA and an affiliated target analysis revealed energy transfer from initially excited *helix* segments in DCM to *zigzag* segments within hundreds of femtoseconds. Upon excitation of *zigzag* domains in DMF, energy transfer to *helix* domains was observed. However, if *helix* domains are excited in advance, energy is transferred within hundreds of femtoseconds to *zigzag* domains which transfer the energy back to *helix* domains within several tens of picoseconds.

This energy transfer between *zigzag* and *helix* segments was confirmed by 2D spectroscopy in which predominantly intermediate states (energetically located between *helix* and *zigzag* structures) of the polymer were excited. For $[\mathrm{SQB}]_n$ in DCM, an ultrafast relaxation to *zigzag* segments was observed which subsequently relax to the ground state. In DMF, intermediate excited segments relax towards the *zigzag* segments within tens of femtoseconds. Afterwards, the energy is transferred back to *helix* segments for which the most stable excitonic state is energetically favored in DMF.

The combination of the structural assignment based on theoretical calculations with ultrafast spectroscopy resulted in a comprehensive picture of the interactions between different structural domains within a single polymer. Ultrafast and efficient energy transfer within a polymer strand of $[\mathrm{SQB}]_n$ is based on the matching of the density of states between donor and acceptor sites. Hence, if an opto-electronic application requires an ultrafast energy transfer within a single polymer, cyanine-like polymers should be considered.

The molecular complexity is further increased in Chapter 5 by turning from relaxation dynamics within single strands of conjugated polymers towards aggregated polymers. Recently it was shown that Poly[2-methoxy-5-(2-ethylhexyloxyl)-1,4-

phenylenevinylene] (MEH-PPV) undergoes a phase transition from a coiled, disordered phase to an aggregated, planarized phase upon cooling. Thus, MEH-PPV allows studying the effect of changes of the morphology on photoinduced dynamics by comparing the extensively investigated coiled phase of MEH-PPV at room temperature with its aggregated phase upon cooling.

In TA ultrafast relaxation dynamics were observed and an associated band analysis allowed to discriminate between population decay to the ground state and other relaxation processes. Additionally, a maximum entropy method allowed an assignment of the population decay to exponential processes with a certain degree of distribution, in favor of highly distributed processes, typically described by stretched exponential functions.

Performing 2D spectroscopy in combination with a global analysis revealed an additional ultrafast population decay. In summary, the sub-10 ps population dynamics were assigned to a sub-30 fs localization of initially delocalized excitons, and the repopulation of the ground state by non-radiative internal conversion within several picoseconds. On timescales larger than 10 ps, a radiative relaxation from the first excited state to the ground state is observed with about 40 ps. This process is quenched by defect states within the aggregated phase of MEH-PPV. Additionally, the relaxation to the ground state occurs with about 320 ps which was attributed to a larger spatial distance to the previously mentioned quenching sites.

Relaxation processes in TA and 2D spectroscopy displayed two exponential timescales for relaxation of about 200 fs and 4 ps. The former component could be attributed to exciton relaxation as it solely contributed to spectral bands which contain stimulated emission. However, this 200 fs process relaxation does not result in the population of the excitonic states with the lowest energy. By the analysis of the 2D spectra, spectral diffusion could be excluded as an origin for the 4 ps component, which was assigned to energy transfer processes to the bottom of the excitonic manifold. Thus, in the aggregated phase of MEH-PPV 95 % of mobile excitons are located at the low-energy excitonic state within about 12 ps.

For all studied molecular systems it was shown that TA and 2D spectroscopy are complementary techniques, which efficiently allowed to analyze the relaxation dynamics of complex molecular systems. Especially, the additional information content of 2D spectroscopy was able to enlighten processes which were only indirectly inferable by TA alone. The observed dynamics and chromophore interactions provide suitable conditions to generate polymeric solar cells. A systematic interplay between synthesis, parameter-dependent analysis, and device production paves the path towards highly efficient polymeric solar cells which are able to compete with the state-of-the-art silicon-based solar cells.

Bibliography

[1] F. Koch, A. Steinbacher, C. Consani, A. Zitzler-Kunkel, M. Stolte, F. Würthner, and T. Brixner, *The Role of the Dipolar Neighborhood on the Relaxation Dynamics of Multichromophoric Merocyanines.*
Submitted on April 12, 2016.

[2] F. Koch, M. Stolte, D. Bialas, A. Zitzler-Kunkel, A. Steinbacher, T. Brixner, and F. Würthner, *Unraveling the Molecular Structure of Interacting Multichromophoric Merocyanines in Solution.*
In preparation, status April 12, 2016.

[3] C. Lambert, F. Koch, S. F. Völker, A. Schmiedel, M. Holzapfel, A. Humeniuk, M. I. S. Röhr, R. Mitric, and T. Brixner,
Energy Transfer Between Squaraine Polymer Sections: From Helix to Zigzag and All the Way Back.
Journal of the American Chemical Society **137**, 7851–7861 (2015).

[4] C. Consani, F. Koch, F. Panzer, T. Unger, A. Köhler, and T. Brixner,
Relaxation dynamics and exciton energy transfer in the low-temperature phase of MEH-PPV.
The Journal of Chemical Physics **142**, 212429 (2015).

[5] F. Koch, M. Kullmann, U. Selig, P. Nuernberger, D. C. G. Götz, G. Bringmann, and T. Brixner,
Coherent two-dimensional electronic spectroscopy in the Soret band of a chiral porphyrin dimer.
New Journal of Physics **15**, 025006 (2013).

[6] P. K. Verma, F. Koch, A. Steinbacher, P. Nuernberger, and T. Brixner,
Ultrafast UV-induced photoisomerization of intramolecularly H-bonded symmetric β-diketones.
Journal of the American Chemical Society **136**, 14981–14989 (2014).

[7] P. K. Verma, A. Steinbacher, F. Koch, P. Nuernberger, and T. Brixner,
Monitoring ultrafast intramolecular proton transfer processes in an unsymmetric β-diketone.
Physical Chemistry Chemical Physics **17**, 8459–8466 (2015).

[8] T. Unger, F. Panzer, C. Consani, F. Koch, T. Brixner, H. Bässler, and A. Köhler,
Ultrafast Energy Transfer between Disordered and Highly Planarized Chains of Poly[2-methoxy-5-(2-ethylhexyloxy)-1,4-phenylenevinylene] (MEH-PPV).
ACS Macro Letters **4**, 412–416 (2015).

[9] J. Luther, M. Nast, M. N. Fisch, D. Christoffers, F. Pfisterer, D. Meissner, and J. Nitsch,
Solar Technology. In *Ullmann's Encyclopedia of Industrial Chemistry.*
Wiley-VCH Verlag GmbH & Co. KGaA (2000).

[10] M. Jørgensen, K. Norrman, and F. C. Krebs,
Stability/degradation of polymer solar cells.
Solar Energy Materials and Solar Cells **92**, 686–714 (2008).

[11] R. Po, C. Carbonera, A. Bernardi, F. Tinti, and N. Camaioni,
Polymer- and carbon-based electrodes for polymer solar cells: Toward low-cost, continuous fabrication over large area.
Solar Energy Materials and Solar Cells **100**, 97–114 (2012).

[12] J. You, L. Dou, K. Yoshimura, T. Kato, K. Ohya, T. Moriarty, K. Emery, C.-C. Chen, J. Gao, G. Li, and Y. Yang,
A polymer tandem solar cell with 10.6% power conversion efficiency.
Nature Communications **4**, 1446 (2013).

[13] M. C. Scharber, D. Mühlbacher, M. Koppe, P. Denk, C. Waldauf, A. J. Heeger, and C. J. Brabec,
Design Rules for Donors in Bulk-Heterojunction Solar Cells—Towards 10 % Energy-Conversion Efficiency.
Advanced Materials **18**, 789–794 (2006).

[14] T. M. Clarke, A. M. Ballantyne, J. Nelson, D. D. C. Bradley, and J. R. Durrant,
Free Energy Control of Charge Photogeneration in Polythiophene/Fullerene Solar Cells: The Influence of Thermal Annealing on P3HT/PCBM Blends.
Advanced Functional Materials **18**, 4029–4035 (2008).

[15] M. Wollenhaupt, A. Assion, and T. Baumert,
Femtosecond Laser Pulses: Linear Properties, Manipulation, Generation and Measurement. In *Springer Handbook of Lasers and Optics.*
Springer Science+Business Media, New York (2007).

[16] G. D. Reid and K. Wynne,
Ultrafast Laser Technology and Spectroscopy. In *Encyclopedia of Analytical Chemistry: Instrumentation and Applications.*
John Wiley & Sons, Chichester (2000).

[17] J.-C. Diels and W. Rudolph,
Ultrashort Laser Pulse Phenomena. Second edition.
Academic Press, Burlington (2006).

[18] C. Rullière,
Femtosecond Laser Pulses: Principles and Experiments. Second edition.
Springer, New York, NY (2005).

[19] P. Hannaford,
Femtosecond Laser Spectroscopy.
Springer Science & Business Media, New York (2005).

[20] A. M. Weiner,
Ultrafast Optics. First edition.
John Wiley & Sons Inc., Hoboken (2009).

[21] W. Demtröder,
Laser Spectroscopy: Basic Principles. Volume 1. Fourth edition.
Springer, Berlin (2008).

[22] D. J. Tannor,
Introduction to Quantum Mechanics: A Time-Dependent Perspective.
University Science Books, Sausalito (2007).

[23] B. M. Garraway and K.-A. Suominen,
Wave-packet dynamics: new physics and chemistry in femto-time.
Reports on Progress in Physics **58**, 365–419 (1995).

[24] S. Mukamel,
Principles of Nonlinear Optical Spectroscopy. First edition.
Oxford University Press, New York (1995).

[25] D. C. Harris and M. D. Bertolucci,
Symmetry and Spectroscopy: An Introduction to Vibrational and Electronic Spectroscopy.
Courier Corporation (1978).

[26] M. Born and R. Oppenheimer,
Zur Quantentheorie der Molekeln.
Annalen der Physik **389**, 457–484 (1927).

[27] W. Domcke and D. R. Yarkony,
Role of Conical Intersections in Molecular Spectroscopy and Photoinduced Chemical Dynamics.
Annual Review of Physical Chemistry **63**, 325–352 (2012).

[28] E. Fermi,
Nuclear Physics: A Course Given by Enrico Fermi at the University of Chicago.
University of Chicago Press (1974).

[29] P. a. M. Dirac,
The Quantum Theory of the Emission and Absorption of Radiation.
Proceedings of the Royal Society of London A: Mathematical, Physical and Engineering Sciences **114**, 243–265 (1927).

[30] A. Jabłoński,
Efficiency of Anti-Stokes Fluorescence in Dyes.
Nature **131**, 839–840 (1933).

[31] M. Kasha, H. R. Rawls, and M. Ashraf El-Bayoumi,
The Exciton Model in Molecular Spectroscopy.
Pure and Applied Chemistry **11**, 371–392 (1965).

[32] E. G. McRae and M. Kasha.
The Molecular Exciton Model. In *Physical Processes in Radiation Biology.*
Academic Press (1964).

[33] H. van Amerongen, L. Valkunas, and R. van Grondelle,
Photosynthetic Excitons.
World Scientific Publishing Co. Pte. Ltd. (2000).

[34] A. R. Edmonds,
Angular Momentum in Quantum Mechanics.
Princeton University Press (1996).

[35] W. Heitler and F. London,
Wechselwirkung neutraler Atome und homöopolare Bindung nach der Quantenmechanik.
Zeitschrift für Physik **44**, 455–472 (1927).

[36] S. Schott, A. Steinbacher, J. Buback, P. Nuernberger, and T. Brixner,
Generalized magic angle for time-resolved spectroscopy with laser pulses of arbitrary ellipticity.
Journal of Physics B: Atomic, Molecular and Optical Physics **47**, 124014 (2014).

[37] F. Bloch,
Über die Quantenmechanik der Elektronen in Kristallgittern.
Zeitschrift für Physik **52**, 555–600 (1929).

[38] G. H. Wannier,
The Structure of Electronic Excitation Levels in Insulating Crystals.
Physical Review **52**, 191–197 (1937).

[39] T. Förster,
Zwischenmolekulare Energiewanderung und Fluoreszenz.
Annalen der Physik **437**, 55–75 (1948).

[40] D. L. Dexter,
A Theory of Sensitized Luminescence in Solids.
The Journal of Chemical Physics **21**, 836–850 (1953).

[41] D. L. Andrews and A. A. Demidov,
Resonance Energy Transfer.
Wiley (1999).

[42] S. E. Braslavsky, E. Fron, H. B. Rodríguez, E. S. Román, G. D. Scholes, G. Schweitzer, B. Valeur, and J. Wirz,
Pitfalls and limitations in the practical use of Förster's theory of resonance energy transfer.
Photochemical & Photobiological Sciences **7**, 1444–1448 (2008).

[43] D. Beljonne, C. Curutchet, G. D. Scholes, and R. J. Silbey,
Beyond Förster resonance energy transfer in biological and nanoscale systems.
The Journal of Physical Chemistry. B **113**, 6583–6599 (2009).

[44] A. Olaya-Castro and G. D. Scholes,
Energy transfer from Förster–Dexter theory to quantum coherent light-harvesting.
International Reviews in Physical Chemistry **30**, 49–77 (2011).

[45] P. J. Walla, P. A. Linden, C. P. Hsu, G. D. Scholes, and G. R. Fleming,
Femtosecond dynamics of the forbidden carotenoid S1 state in light-harvesting complexes of purple bacteria observed after two-photon excitation.
Proceedings of the National Academy of Sciences **97**, 10808–10813 (2000).

[46] S. Rützel,
Pulse-Sequence Approaches for Multidimensional Electronic Spectroscopy of Ultrafast Photochemistry.
Dissertation. Universität Würzburg (2014).

[47] U. Selig, F. Langhojer, F. Dimler, T. Löhrig, C. Schwarz, B. Gieseking, and T. Brixner,
Inherently Phase-Stable Coherent Two-Dimensional Spectroscopy Using only Conventional Optics.
Optics Letters **33**, 2851–2853 (2008).

[48] T. Quast,
Spectroscopic Investigation of Charge-transfer Processes and Polarisation Pulse Shaping in the Visible Spectral Range.
Dissertation. Universität Würzburg (2012).

[49] J. Buback,
Femtochemistry of Pericyclic Reactions and Advances towards Chiral Control.
Dissertation. Universität Würzburg (2011).

[50] U. Morgner, F. X. Kärtner, S. H. Cho, Y. Chen, H. A. Haus, J. G. Fujimoto, E. P. Ippen, V. Scheuer, G. Angelow, and T. Tschudi,
Sub-two-cycle pulses from a Kerr-lens mode-locked Ti:sapphire laser.
Optics Letters **24**, 411–413 (1999).

[51] R. W. Boyd,
Nonlinear Optics. Third edition.
Academic Press, Burlington (2008).

[52] D. E. Spence, P. N. Kean, and W. Sibbett,
60-fsec pulse generation from a self-mode-locked Ti:sapphire laser.
Optics Letters **16**, 42–44 (1991).

[53] D. Strickland and G. Mourou,
Compression of amplified chirped optical pulses.
Optics Communications **56**, 219–221 (1985).

[54] P. Maine, D. Strickland, P. Bado, M. Pessot, and G. Mourou,
Generation of Ultrahigh Peak Power Pulses by Chirped Pulse Amplification.
IEEE Journal of Quantum Electronics **24**, 398–403 (1988).

[55] G. Cheriaux, P. Rousseau, F. Salin, J. P. Chambaret, B. Walker, and L. F. DiMauro,
Aberration-free stretcher design for ultrashort-pulse amplification.
Optics Letters **21**, 414–416 (1996).

[56] E. Treacy,
Optical pulse compression with diffraction gratings.
IEEE Journal of Quantum Electronics **5**, 454–458 (1969).

[57] Y. R. Shen,
Principles of Nonlinear Optics. Wiley classics edition.
Wiley & Sons, New York, NY (2002).

[58] D. Meschede,
Optics, light and lasers. Second edition.
Wiley-VCH, Weinheim (2007).

[59] P. A. Franken, A. E. Hill, C. W. Peters, and G. Weinreich,
Generation of Optical Harmonics.
Physical Review Letters **7**, 118 (1961).

[60] R. Menzel,
Photonics. Second edition.
Springer, Berlin [u.a.] (2007).

[61] M. Bass,
Handbook of Optics. Second edition.
McGraw-Hill, New York (1995).

[62] D. Eimerl, L. Davis, S. Velsko, E. K. Graham, and A. Zalkin,
Optical, mechanical, and thermal properties of barium borate.
Journal of Applied Physics **62**, 1968–1983 (1987).

[63] G. Yang and Y. R. Shen,
Spectral broadening of ultrashort pulses in a nonlinear medium.
Optics Letters **9**, 510–512 (1984).

[64] B. Gross and J. T. Manassah,
Supercontinuum in the anomalous group-velocity dispersion region.
Journal of the Optical Society of America B **9**, 1813–1818 (1992).

[65] A. L. Gaeta,
Catastrophic Collapse of Ultrashort Pulses.
Physical Review Letters **84**, 3582–3585 (2000).

[66] J. M. Dudley, G. Genty, and S. Coen,
Supercontinuum generation in photonic crystal fiber.
Reviews of Modern Physics **78**, 1135 (2006).

[67] A. Monmayrant, S. Weber, and B. Chatel,
A newcomer's guide to ultrashort pulse shaping and characterization.
Journal of Physics B: Atomic, Molecular and Optical Physics **43**, 103001 (2010).

[68] A. M. Weiner,
Ultrafast optical pulse shaping: A tutorial review.
Optics Communications **284**, 3669–3692 (2011).

[69] A. M. Weiner,
Femtosecond pulse shaping using spatial light modulators.
Review of Scientific Instruments **71**, 1929 (2000).

[70] A. M. Weiner, D. E. Leaird, J. S. Patel, and J. R. Wullert,
Programmable shaping of femtosecond optical pulses by use of 128-element liquid crystal phase modulator.
IEEE Journal of Quantum Electronics **28**, 908–920 (1992).

[71] I. Chang,
Acoustooptic Devices and Applications.
IEEE Transactions on Sonics and Ultrasonics **23**, 2–21 (1976).

[72] P. Tournois,
Acousto-optic programmable dispersive filter for adaptive compensation of group delay time dispersion in laser systems.
Optics Communications **140**, 245–249 (1997).

[73] V. Y. Molchanov, S. I. Chizhikov, O. Y. Makarov, N. P. Solodovnikov, V. N. Ginzburg, E. V. Katin, E. A. Khazanov, V. V. Lozhkarev, and I. V. Yakovlev,
Adaptive acousto-optic technique for femtosecond laser pulse shaping.
Applied Optics **48**, C118–C124 (2009).

[74] F. Verluise, V. Laude, Z. Cheng, C. Spielmann, and P. Tournois,
Amplitude and Phase Control of Ultrashort Pulses by Use of an Acousto-Optic Programmable Dispersive Filter: Pulse Compression and Shaping.
Optics Letters **25**, 575–577 (2000).

[75] F. Verluise, V. Laude, J.-P. Huignard, P. Tournois, and A. Migus,
Arbitrary Dispersion Control of Ultrashort Optical Pulses with Acoustic Waves.
Journal of the Optical Society of America B **17**, 138–145 (2000).

[76] M. M. Wefers and K. A. Nelson,
Generation of high-fidelity programmable ultrafast optical waveforms.
Optics Letters **20**, 1047–1049 (1995).

[77] D. J. Kane and R. Trebino,
Characterization of arbitrary femtosecond pulses using frequency-resolved optical gating.
IEEE Journal of Quantum Electronics **29**, 571–579 (1993).

[78] R. Trebino,
Frequency-Resolved Optical Gating: The Measurement of Ultrashort Laser Pulses.
Springer (2002).

[79] R. Trebino, K. W. DeLong, D. N. Fittinghoff, J. N. Sweetser, M. A. Krumbügel, B. A. Richman, and D. J. Kane,
Measuring Ultrashort Laser Pulses in the Time-Frequency Domain Using Frequency-Resolved Optical Gating.
Review of Scientific Instruments **68**, 3277–3295 (1997).

[80] R. Trebino and D. J. Kane,
Using phase retrieval to measure the intensity and phase of ultrashort pulses: frequency-resolved optical gating.
Journal of the Optical Society of America A **10**, 1101–1111 (1993).

[81] I. Amat-Roldán, I. Cormack, P. Loza-Alvarez, E. Gualda, and D. Artigas,
Ultrashort Pulse Characterisation with SHG Collinear-FROG.
Optics Express **12**, 1169–1178 (2004).

[82] G. Stibenz and G. Steinmeyer,
Interferometric frequency-resolved optical gating.
Optics Express **13**, 2617–2626 (2005).

[83] A. Galler and T. Feurer,
Pulse shaper assisted short laser pulse characterization.
Applied Physics B **90**, 427–430 (2008).

[84] D. E. Wilcox and J. P. Ogilvie,
Comparison of pulse compression methods using only a pulse shaper.
Journal of the Optical Society of America B **31**, 1544–1554 (2014).

[85] D. Linde,
Characterization of the noise in continuously operating mode-locked lasers.
Applied Physics B Photophysics and Laser Chemistry **39**, 201–217 (1986).

[86] F. Kanal, S. Keiber, R. Eck, and T. Brixner,
100-kHz shot-to-shot broadband data acquisition for high-repetition-rate pump–probe spectroscopy.
Optics Express **22**, 16965–16975 (2014).

[87] A. Beer,
Bestimmung der Absorption des rothen Lichts in farbigen Flüssigkeiten.
Annalen der Physik **162**, 78–88 (1852).

[88] I. H. M. van Stokkum, D. S. Larsen, and R. van Grondelle,
Global and target analysis of time-resolved spectra.
Biochimica et Biophysica Acta (BBA) - Bioenergetics **1657**, 82–104 (2004).

[89] S. A. Kovalenko, A. L. Dobryakov, J. Ruthmann, and N. P. Ernsting,
Femtosecond Spectroscopy of Condensed Phases with Chirped Supercontinuum Probing.
Physical Review A **59**, 2369–2384 (1999).

[90] U. Megerle, I. Pugliesi, C. Schriever, C. Sailer, and E. Riedle,
Sub-50 fs Broadband Absorption Spectroscopy with Tunable Excitation: Putting the Analysis of Ultrafast Molecular Dynamics on Solid Ground.
Applied Physics B: Lasers and Optics **96**, 215–231 (2009).

[91] K. Ekvall, P. van der Meulen, C. Dhollande, L.-E. Berg, S. Pommeret, R. Naskrecki, and J.-C. Mialocq,
Cross Phase Modulation Artifact in Liquid Phase Transient Absorption Spectroscopy.
Journal of Applied Physics **87**, 2340 (2000).

[92] B. Dietzek, T. Pascher, V. Sundström, and A. Yartsev,
Appearance of coherent artifact signals in femtosecond transient absorption spectroscopy in dependence on detector design.
Laser Physics Letters **4**, 38–43 (2007).

[93] M. Lorenc, M. Ziolek, R. Naskrecki, J. Karolczak, J. Kubicki, and A. Maciejewski,
Artifacts in Femtosecond Transient Absorption Spectroscopy.
Applied Physics B: Lasers and Optics **74**, 19–27 (2002).

[94] M. Rasmusson, A. N. Tarnovsky, E. Åkesson, and V. Sundström,
On the use of two-photon absorption for determination of femtosecond pump–probe cross-correlation functions.
Chemical Physics Letters **335**, 201–208 (2001).

[95] J. J. Snellenburg, S. P. Laptenok, R. Seger, K. M. Mullen, and I. H. M. van Stokkum,
Glotaran: a Java-Based Graphical User Interface for the R-Package TIMP.
Journal of Statistical Software **49**, 1–22 (2012).

[96] K. M. Mullen and I. H. M. van Stokkum,
TIMP: An R Package for Modeling Multi-way Spectroscopic Measurements.
Journal of Statistical Software **18**, 1–46 (2007).

[97] D. M. Jonas,
Two-dimensional femtosecond spectroscopy.
Annual Review of Physical Chemistry **54**, 425–463 (2003).

[98] T. Brixner, T. Mančal, I. V. Stiopkin, and G. R. Fleming,
Phase-stabilized two-dimensional electronic spectroscopy.
The Journal of Chemical Physics **121**, 4221–4236 (2004).

[99] T. Brabec and F. Krausz,
Nonlinear Optical Pulse Propagation in the Single-Cycle Regime.
Physical Review Letters **78**, 3282 (1997).

[100] S. Yan and H.-S. Tan,
Phase cycling schemes for two-dimensional optical spectroscopy with a pump–probe beam geometry.
Chemical Physics **360**, 110–115 (2009).

[101] P. F. Tekavec, J. A. Myers, K. L. M. Lewis, and J. P. Ogilvie,
Two-Dimensional Electronic Spectroscopy with a Continuum Probe.
Optics Letters **34**, 1390–1392 (2009).

[102] E. M. Grumstrup, S.-H. Shim, M. A. Montgomery, N. H. Damrauer, and M. T. Zanni,
Facile collection of two-dimensional electronic spectra using femtosecond pulse-shaping technology.
Optics Express **15**, 16681–16689 (2007).

[103] J. A. Myers, K. L. Lewis, P. F. Tekavec, and J. P. Ogilvie,
Two-Color Two-Dimensional Fourier Transform Electronic Spectroscopy with a Pulse-Shaper.
Optics Express **16**, 17420–17428 (2008).

[104] Z. Zhang, K. L. Wells, E. W. J. Hyland, and H.-S. Tan,
Phase-cycling schemes for pump–probe beam geometry two-dimensional electronic spectroscopy.
Chemical Physics Letters **550**, 156–161 (2012).

[105] P. Tian, D. Keusters, Y. Suzaki, and W. S. Warren,
Femtosecond phase-coherent two-dimensional spectroscopy.
Science **300**, 1553–1555 (2003).

[106] S.-H. Shim and M. T. Zanni,
How to Turn Your Pump–Probe Instrument into a Multidimensional Spectrometer: 2D IR and VIS Spectroscopies via Pulse Shaping.
Physical Chemistry Chemical Physics **11**, 748–761 (2009).

[107] H.-S. Tan,
Theory and Phase-Cycling Scheme Selection Principles of Collinear Phase Coherent Multi-Dimensional Optical Spectroscopy.
The Journal of Chemical Physics **129**, 124501 (2008).

[108] U. Selig-Parthey,
Methods of Nonlinear Femtosecond Spectroscopy in the Visible and Ultraviolet Regime and Their Application to Coupled Multichromophore Systems.
Dissertation (2012).

[109] G. S. Schlau-Cohen, A. Ishizaki, and G. R. Fleming,
Two-dimensional electronic spectroscopy and photosynthesis: Fundamentals and applications to photosynthetic light-harvesting.
Chemical Physics **386**, 1–22 (2011).

[110] S. A. Kovalenko, N. P. Ernsting, and J. Ruthmann,
Femtosecond hole-burning spectroscopy of the dye DCM in solution: the transition from the locally excited to a charge-transfer state.
Chemical Physics Letters **258**, 445–454 (1996).

[111] P. F. Tekavec, J. A. Myers, K. L. M. Lewis, F. D. Fuller, and J. P. Ogilvie,
Effects of Chirp on Two-Dimensional Fourier Transform Electronic Spectra.
Optics Express **18**, 11015–11024 (2010).

[112] M. Kullmann, S. Ruetzel, J. Buback, P. Nuernberger, and T. Brixner,
Reaction Dynamics of a Molecular Switch Unveiled by Coherent Two-Dimensional Electronic Spectroscopy.
Journal of the American Chemical Society **133**, 13074–13080 (2011).

[113] J. A. Myers, K. L. M. Lewis, F. D. Fuller, P. F. Tekavec, C. F. Yocum, and J. P. Ogilvie,
Two-Dimensional Electronic Spectroscopy of the D1-D2-cyt b559 Photosystem II Reaction Center Complex.
The Journal of Physical Chemistry Letters **1**, 2774–2780 (2010).

[114] C.-H. Tseng, S. Matsika, and T. C. Weinacht,
Two-dimensional ultrafast Fourier transform spectroscopy in the deep ultraviolet.
Optics Express **17**, 18788–18793 (2009).

[115] N. Krebs, I. Pugliesi, J. Hauer, and E. Riedle,
Two-dimensional Fourier transform spectroscopy in the ultraviolet with sub-20 fs pump pulses and 250–720 nm supercontinuum probe.
New Journal of Physics **15**, 085016 (2013).

[116] S.-H. Shim, D. B. Strasfeld, Y. L. Ling, and M. T. Zanni,
Automated 2D IR Spectroscopy Using a Mid-IR Pulse Shaper and Application of This Technology to the Human Islet Amyloid Polypeptide.
Proceedings of the National Academy of Sciences **104**, 14197–14202 (2007).

[117] L. P. DeFlores, R. A. Nicodemus, and A. Tokmakoff,
Two-dimensional Fourier transform spectroscopy in the pump-probe geometry.
Optics Letters **32**, 2966–2968 (2007).

[118] P. A. Tekavec, K. L. Lewis, F. D. Fuller, J. A. Myers, and J. P. Ogilvie,
Toward Broad Bandwidth 2-D Electronic Spectroscopy: Correction of Chirp From a Continuum Probe.
IEEE Journal of Selected Topics in Quantum Electronics **18**, 210–217 (2012).

[119] L. Lepetit, G. Chériaux, and M. Joffre,
Linear Techniques of Phase Measurement by Femtosecond Spectral Interferometry for Applications in Spectroscopy.
Journal of the Optical Society of America B **12**, 2467–2474 (1995).

[120] C. Dorrer, N. Belabas, J.-P. Likforman, and M. Joffre,
Experimental implementation of Fourier-transform spectral interferometry and its application to the study of spectrometers.
Applied Physics B: Lasers and Optics **70**, 99–107 (2000).

[121] A. Nemeth, J. Sperling, J. Hauer, H. F. Kauffmann, and F. Milota,
Compact phase-stable design for single- and double-quantum two-dimensional electronic spectroscopy.
Optics Letters **34**, 3301–3303 (2009).

[122] R. Augulis and D. Zigmantas,
Two-dimensional electronic spectroscopy with double modulation lock-in detection: enhancement of sensitivity and noise resistance.
Optics Express **19**, 13126–13133 (2011).

[123] R. R. Ernst,
Principles of nuclear magnetic resonance in one and two dimensions.
Clarendon Press, Oxford (2004).

[124] R. Mersereau and A. Oppenheim,
Digital reconstruction of multidimensional signals from their projections.
Proceedings of the IEEE **62**, 1319–1338 (1974).

[125] R. M. Hochstrasser,
Two-dimensional IR-spectroscopy: polarization anisotropy effects.
Chemical Physics **266**, 273–284 (2001).

[126] J. Dreyer, A. M. Moran, and S. Mukamel,
Tensor Components in Three Pulse Vibrational Echoes of a Rigid Dipeptide.
Bulletin of the Korean Chemical Society **24**, 1091–1096 (2003).

[127] E. L. Read, G. S. Engel, T. R. Calhoun, T. Mančal, T. K. Ahn, R. E. Blankenship, and G. R. Fleming,
Cross-peak-specific two-dimensional electronic spectroscopy.
Proceedings of the National Academy of Sciences **104**, 14203–14208 (2007).

[128] T. Brixner and G. Gerber,
Femtosecond polarization pulse shaping.
Optics Letters **26**, 557–559 (2001).

[129] P. Hamm and M. Zanni,
Concepts and Methods of 2D Infrared Spectroscopy.
Cambridge University Press (2011).

[130] F. Würthner, T. E. Kaiser, and C. R. Saha-Möller,
J-Aggregates: From Serendipitous Discovery to Supramolecular Engineering of Functional Dye Materials.
Angewandte Chemie International Edition **50**, 3376–3410 (2011).

[131] Y. Waseda, E. Matsubara, and K. Shinoda,
X-Ray Diffraction Crystallography: Introduction, Examples and Solved Problems.
Springer Science & Business Media (2011).

[132] M. F. C. Ladd and R. A. Palmer,
Structure Determination by X-Ray Crystallography.
Springer US, Boston, MA (1995).

[133] M. S. Smyth and J. H. J. Martin,
x Ray crystallography.
Molecular Pathology **53**, 8–14 (2000).

[134] G. Harald,
NMR Spectroscopy: Basic Principles, Concepts and Applications in Chemistry. Third edition.
Wiley-VCH (2013).

[135] R. G. Parr and Y. Weitao,
Density-Functional Theory of Atoms and Molecules.
Oxford University Press (1994).

[136] W. Koch and M. C. Holthausen,
A Chemist's Guide to Density Functional Theory.
Wiley (2001).

[137] J. Tomasi, B. Mennucci, and R. Cammi,
Quantum Mechanical Continuum Solvation Models.
Chemical Reviews **105**, 2999–3094 (2005).

[138] O. Kühn and S. Lochbrunner,
Quantum Dynamics and Spectroscopy of Excitons in Molecular Aggregates.
arXiv:1108.4834 [physics] (2011).

[139] D. Möbius,
Scheibe Aggregates.
Advanced Materials **7**, 437–444 (1995).

[140] X.-Q. Li, X. Zhang, S. Ghosh, and F. Würthner,
Highly Fluorescent Lyotropic Mesophases and Organogels Based on J-Aggregates of Core-Twisted Perylene Bisimide Dyes.
Chemistry – A European Journal **14**, 8074–8078 (2008).

[141] H. Marciniak, X.-Q. Li, F. Würthner, and S. Lochbrunner,
One-Dimensional Exciton Diffusion in Perylene Bisimide Aggregates.
The Journal of Physical Chemistry A **115**, 648–654 (2011).

[142] G. A. Lott, A. Perdomo-Ortiz, J. K. Utterback, J. R. Widom, A. Aspuru-Guzik, and A. H. Marcus,
Conformation of self-assembled porphyrin dimers in liposome vesicles by phase-modulation 2D fluorescence spectroscopy.
Proceedings of the National Academy of Sciences **108**, 16521–16526 (2011).

[143] M. Gruebele and A. H. Zewail,
Femtosecond wave packet spectroscopy: Coherences, the potential, and structural determination.
The Journal of Chemical Physics **98**, 883–902 (1993).

[144] A. H. Zewail,
Femtochemistry: atomic-scale dynamics of the chemical bond.
The Journal of Physical Chemistry A **104**, 5660–5694 (2000).

[145] H. N. Chapman, P. Fromme, A. Barty, T. A. White, R. A. Kirian, A. Aquila, M. S. Hunter, J. Schulz, D. P. DePonte, U. Weierstall, R. B. Doak, F. R. N. C. Maia, A. V. Martin, I. Schlichting, L. Lomb, N. Coppola, R. L. Shoeman, S. W. Epp, R. Hartmann, D. Rolles, A. Rudenko, L. Foucar, N. Kimmel, G. Weidenspointner, P. Holl, M. Liang, M. Barthelmess, C. Caleman, S. Boutet, M. J. Bogan, J. Krzywinski, C. Bostedt, S. Bajt, L. Gumprecht, B. Rudek, B. Erk, C. Schmidt, A. Hömke, C. Reich, D. Pietschner, L. Strüder, G. Hauser, H. Gorke, J. Ullrich, S. Herrmann, G. Schaller, F. Schopper, H. Soltau, K.-U. Kühnel, M. Messerschmidt, J. D. Bozek, S. P. Hau-Riege, M. Frank, C. Y. Hampton, R. G. Sierra, D. Starodub, G. J. Williams, J. Hajdu, N. Timneanu, M. M. Seibert, J. Andreasson, A. Rocker, O. Jönsson, M. Svenda, S. Stern, K. Nass, R. Andritschke, C.-D. Schröter, F. Krasniqi, M. Bott, K. E. Schmidt, X. Wang, I. Grotjohann, J. M. Holton, T. R. M. Barends, R. Neutze, S. Marchesini, R. Fromme, S. Schorb, D. Rupp, M. Adolph, T. Gorkhover, I. Andersson, H. Hirsemann, G. Potdevin, H. Graafsma, B. Nilsson, and J. C. H. Spence,
Femtosecond X-ray protein nanocrystallography.
Nature **470**, 73–77 (2011).

[146] A. V. Kulinich and A. A. Ishchenko,
Merocyanine dyes: synthesis, structure, properties and applications.
Russian Chemical Reviews **78**, 141–164 (2009).

[147] F. Würthner, R. Wortmann, and K. Meerholz,
Chromophore Design for Photorefractive Organic Materials.
ChemPhysChem **3**, 17–31 (2002).

[148] B. Kippelen, F. Meyers, N. Peyghambarian, and S. R. Marder,
Chromophore Design for Photorefractive Applications.
Journal of the American Chemical Society **119**, 4559–4560 (1997).

[149] L. Huang, M. Stolte, H. Bürckstümmer, and F. Würthner,
High-Performance Organic Thin-Film Transistor Based on a Dipolar Organic Semiconductor.
Advanced Materials **24**, 5750–5754 (2012).

[150] A. Yartsev, J.-L. Alvarez, U. Åberg, and V. Sundström,
Overdamped wavepacket motion along a barrierless potential energy surface in excited state isomerization.
Chemical Physics Letters **243**, 281–289 (1995).

[151] Z. Wang, S. Chu, S. Wang, and Q. Gong,
Ultrafast excited-state dynamics associated with the photoisomerization of a cyanine dye.
The Journal of Chemical Physics **137**, 164502 (2012).

[152] S. Ruetzel, M. Diekmann, P. Nuernberger, C. Walter, B. Engels, and T. Brixner,
Photoisomerization among ring-open merocyanines. I. Reaction dynamics and wave-packet oscillations induced by tunable femtosecond pulses.
The Journal of Chemical Physics **140**, 224310 (2014).

[153] C. Walter, S. Ruetzel, M. Diekmann, P. Nuernberger, T. Brixner, and B. Engels,
Photoisomerization among ring-open merocyanines. II. A computational study.
The Journal of Chemical Physics **140**, 224311 (2014).

[154] P. Nuernberger, S. Ruetzel, and T. Brixner,
Multidimensional Electronic Spectroscopy of Photochemical Reactions.
Angewandte Chemie International Edition **54**, 11368–11386 (2015).

[155] R. S. S. Kumar, L. Lüer, D. Polli, M. Garbugli, and G. Lanzani,
Primary photo-events in a metastable photomerocyanine of spirooxazines.
Optical Materials Express **1**, 293 (2011).

[156] N. P. Ernsting,
Transient optical absorption spectroscopy of the photochemical spiropyran-merocyanine conversion.
Chemical Physics Letters **159**, 526–531 (1989).

[157] N. Tamai and H. Masuhara,
Femtosecond transient absorption spectroscopy of a spirooxazine photochromic reaction.
Chemical Physics Letters **191**, 189–194 (1992).

[158] J. Buback, P. Nuernberger, M. Kullmann, F. Langhojer, R. Schmidt, F. Würthner, and T. Brixner,
Ring-closure and isomerization capabilities of spiropyran-derived merocyanine isomers.
The Journal of Physical Chemistry A **115**, 3924–3935 (2011).

[159] A. Sanchez-Galvez, P. Hunt, M. A. Robb, M. Olivucci, T. Vreven, and H. B. Schlegel,
Ultrafast Radiationless Deactivation of Organic Dyes: Evidence for a Two-State Two-Mode Pathway in Polymethine Cyanines.
Journal of the American Chemical Society **122**, 2911–2924 (2000).

[160] P. Nuernberger, G. Vogt, G. Gerber, R. Improta, and F. Santoro,
Femtosecond study on the isomerization dynamics of NK88. I. Ground-state dynamics after photoexcitation.
The Journal of Chemical Physics **125**, 044512 (2006).

[161] G. Vogt, P. Nuernberger, G. Gerber, R. Improta, and F. Santoro,
Femtosecond study on the isomerization dynamics of NK88. II. Excited-state dynamics.
The Journal of Chemical Physics **125**, 044513 (2006).

[162] X. F. Xu, A. Kahan, S. Zilberg, and Y. Haas,
Photoreactivity of a Push-Pull Merocyanine in Static Electric Fields: A Three-State Model of Isomerization Reactions Involving Conical Intersections.
The Journal of Physical Chemistry A **113**, 9779–9791 (2009).

[163] A. Toniolo, G. Granucci, and T. J. Martínez,
Conical Intersections in Solution: A QM/MM Study Using Floating Occupation Semiempirical Configuration Interaction Wave Functions.
The Journal of Physical Chemistry A **107**, 3822–3830 (2003).

[164] C. Burda, M. H. Abdel-Kader, S. Link, and M. A. El-Sayed,
Femtosecond Dynamics of a Simple Merocyanine Dye: Does Deprotonation Compete with Isomerization?
Journal of the American Chemical Society **122**, 6720–6726 (2000).

[165] A. Kahan, A. Wand, S. Ruhman, S. Zilberg, and Y. Haas,
Solvent Tuning of a Conical Intersection: Direct Experimental Verification of a Theoretical Prediction.
The Journal of Physical Chemistry A **115**, 10854–10861 (2011).

[166] S. Beckmann, K.-H. Etzbach, P. Krämer, K. Lukaszuk, R. Matschiner, A. J. Schmidt, P. Schuhmacher, R. Sens, G. Seybold, R. Wortmann, and F. Würthner,
Electrooptical Chromophores for Nonlinear Optical and Photorefractive Applications.
Advanced Materials **11**, 536–541 (1999).

[167] W. Liptay, R. Wortmann, H. Schaffrin, O. Burkhard, W. Reitinger, and N. Detzer,
Excited state dipole moments and polarizabilities of centrosymmetric and dimeric molecules. I. Model study of a bichromophoric molecule.
Chemical Physics **120**, 429–438 (1988).

[168] W. Liptay, R. Wortmann, R. Böhm, and N. Detzer,
Excited state dipole moments and polarizabilities of centrosymmetric and dimeric molecules. II. Polyenes, polyynes and cumulenes.
Chemical Physics **120**, 439–448 (1988).

[169] R. Wortmann, K. Elich, and W. Liptay,
Excited state dipole moments and polarizabilities of centrosymmetric and dimeric molecules. III. Model calculations for 1,8-diphenyl-1,3,5,7-octatetraene.
Chemical Physics **124**, 395–409 (1988).

[170] F. Würthner, G. Archetti, R. Schmidt, and H.-G. Kuball,
Solvent Effect on Color, Band Shape, and Charge-Density Distribution for Merocyanine Dyes Close to the Cyanine Limit.
Angewandte Chemie International Edition **47**, 4529–4532 (2008).

[171] F. Würthner, S. Yao, T. Debaerdemaeker, and R. Wortmann,
Dimerization of Merocyanine Dyes. Structural and Energetic Characterization of Dipolar Dye Aggregates and Implications for Nonlinear Optical Materials.
Journal of the American Chemical Society **124**, 9431–9447 (2002).

[172] F. Würthner, C. Thalacker, R. Matschiner, K. Lukaszuk, and R. Wortmann,
Optimization of neutrocyanine chromophores based on five-membered heterocycles for photorefractive applications.
Chemical Communications, 1739–1740 (1998).

[173] C. Brückner, C. Walter, M. Stolte, B. Braïda, K. Meerholz, F. Würthner, and B. Engels,
Structure–Property Relationships for Exciton and Charge Reorganization Energies of Dipolar Organic Semiconductors: A Combined Valence Bond Self-Consistent Field and Time-Dependent Hartree-Fock and DFT Study of Merocyanine Dyes.
The Journal of Physical Chemistry C **119**, 17602–17611 (2015).

[174] V. Parthasarathy, R. Pandey, M. Stolte, S. Ghosh, F. Castet, F. Würthner, P. K. Das, and M. Blanchard-Desce,
Combination of Cyanine Behaviour and Giant Hyperpolarisability in Novel Merocyanine Dyes: Beyond the Bond Length Alternation (BLA) Paradigm.
Chemistry – A European Journal **21**, 14211–14217 (2015).

[175] L. Onsager,
Electric Moments of Molecules in Liquids.
Journal of the American Chemical Society **58**, 1486–1493 (1936).

[176] M. H. Vos, F. Rappaport, J.-C. Lambry, J. Breton, and J.-L. Martin,
Visualization of coherent nuclear motion in a membrane protein by femtosecond spectroscopy.
Nature **363**, 320–325 (1993).

[177] Q. Wang, R. W. Schoenlein, L. A. Peteanu, R. A. Mathies, and C. V. Shank,
Vibrationally Coherent Photochemistry in the Femtosecond Primary Event of Vision.
Science **266**, 422–424 (1994).

[178] H.-S. Tan,
Theory and phase-cycling scheme selection principles of collinear phase coherent multi-dimensional optical spectroscopy.
The Journal of Chemical Physics **129**, 124501 (2008).

[179] E. Teller,
The Crossing of Potential Surfaces.
The Journal of Physical Chemistry **41**, 109–116 (1937).

[180] K. A. Zachariasse, M. Grobys, T. von der Haar, A. Hebecker, Y. V. Il'ichev, Y. B. Jiang, O. Morawski, and W. Kühnle,
Intramolecular charge transfer in the excited state. Kinetics and configurational changes.
Journal of Photochemistry and Photobiology A: Chemistry **102**, 59–70 (1996).

[181] Z. R. Grabowski, K. Rotkiewicz, and W. Rettig,
Structural Changes Accompanying Intramolecular Electron Transfer: Focus on Twisted Intramolecular Charge-Transfer States and Structures.
Chemical Reviews **103**, 3899–4032 (2003).

[182] T. Yoshihara, S. I. Druzhinin, and K. A. Zachariasse,
Fast Intramolecular Charge Transfer with a Planar Rigidized Electron Donor/Acceptor Molecule.
Journal of the American Chemical Society **126**, 8535–8539 (2004).

[183] S. I. Druzhinin, N. P. Ernsting, S. A. Kovalenko, L. P. Lustres, T. A. Senyushkina, and K. A. Zachariasse,
Dynamics of Ultrafast Intramolecular Charge Transfer with 4-(Dimethylamino)benzonitrile in Acetonitrile.
The Journal of Physical Chemistry A **110**, 2955–2969 (2006).

[184] S. F. Völker and C. Lambert,
Exciton Coupling Effects in Polymeric cis-Indolenine Squaraine Dyes.
Chemistry of Materials **24**, 2541–2553 (2012).

[185] J.-L. Brédas, D. Beljonne, V. Coropceanu, and J. Cornil,
Charge-Transfer and Energy-Transfer Processes in π-Conjugated Oligomers and Polymers: A Molecular Picture.
Chemical Reviews **104**, 4971–5004 (2004).

[186] G. D. Scholes,
Long-Range Resonance Energy Transfer in Molecular Systems.
Annual Review of Physical Chemistry **54**, 57–87 (2003).

[187] I. Hwang and G. D. Scholes,
Electronic Energy Transfer and Quantum-Coherence in π-Conjugated Polymers.
Chemistry of Materials **23**, 610–620 (2011).

[188] E. Hennebicq, G. Pourtois, G. D. Scholes, L. M. Herz, D. M. Russell, C. Silva, S. Setayesh, A. C. Grimsdale, K. Müllen, J.-L. Brédas, and D. Beljonne,
Exciton Migration in Rigid-Rod Conjugated Polymers: An Improved Förster Model.
Journal of the American Chemical Society **127**, 4744–4762 (2005).

[189] D. Beljonne, G. Pourtois, C. Silva, E. Hennebicq, L. M. Herz, R. H. Friend, G. D. Scholes, S. Setayesh, K. Müllen, and J. L. Brédas,
Interchain vs. intrachain energy transfer in acceptor-capped conjugated polymers.
Proceedings of the National Academy of Sciences **99**, 10982–10987 (2002).

[190] K. Becker and J. M. Lupton,
Efficient Light Harvesting in Dye-Endcapped Conjugated Polymers Probed by Single Molecule Spectroscopy.
Journal of the American Chemical Society **128**, 6468–6479 (2006).

[191] N. Banerji,
Sub-picosecond delocalization in the excited state of conjugated homopolymers and donor–acceptor copolymers.
Journal of Materials Chemistry C **1**, 3052–3066 (2013).

[192] T. L. Andrew and T. M. Swager.
Structure Property Relationships for Exciton Transfer in Conjugated Polymers. In *Charge and Exciton Transport through Molecular Wires.*
Wiley-VCH Verlag GmbH & Co. KGaA (2011).

[193] F. Laquai, Y.-S. Park, J.-J. Kim, and T. Basché,
Excitation Energy Transfer in Organic Materials: From Fundamentals to Optoelectronic Devices.
Macromolecular Rapid Communications **30**, 1203–1231 (2009).

[194] C. Gadermaier and G. Lanzani,
Photophysics of conjugated polymers: the contribution of ultrafast spectroscopy.
Journal of Physics: Condensed Matter **14**, 9785 (2002).

[195] P. Parkinson, C. Müller, N. Stingelin, M. B. Johnston, and L. M. Herz,
Role of Ultrafast Torsional Relaxation in the Emission from Polythiophene Aggregates.
The Journal of Physical Chemistry Letters **1**, 2788–2792 (2010).

[196] M. M. L. Grage, T. Pullerits, A. Ruseckas, M. Theander, O. Inganäs, and V. Sundström,
Conformational disorder of a substituted polythiophene in solution revealed by excitation transfer.
Chemical Physics Letters **339**, 96–102 (2001).

[197] M. M.-L. Grage, P. W. Wood, A. Ruseckas, T. Pullerits, W. Mitchell, P. L. Burn, I. D. W. Samuel, and V. Sundström,
Conformational disorder and energy migration in MEH-PPV with partially broken conjugation.
The Journal of Chemical Physics **118**, 7644–7650 (2003).

[198] T. E. Dykstra, E. Hennebicq, D. Beljonne, J. Gierschner, G. Claudio, E. R. Bittner, J. Knoester, and G. D. Scholes,
Conformational Disorder and Ultrafast Exciton Relaxation in PPV-family Conjugated Polymers.
The Journal of Physical Chemistry B **113**, 656–667 (2009).

[199] B. J. Schwartz,
Conjugated Polymers: What makes a chromophore?
Nature Materials **7**, 427–428 (2008).

[200] K. Becker, M. Fritzsche, S. Höger, and J. M. Lupton,
Phenylene-Ethynylene Macrocycles as Model Systems of Interchromophoric Interactions in π-Conjugated Macromolecules.
The Journal of Physical Chemistry B **112**, 4849–4853 (2008).

[201] M. R. Talipov, A. Boddeda, Q. K. Timerghazin, and R. Rathore.
Key Role of End-Capping Groups in Optoelectronic Properties of Poly-p-phenylene Cation Radicals
The Journal of Physical Chemistry C **118**, 21400–21408 (2014).

[202] G. M. Newbloom, S. M. Hoffmann, A. F. West, M. C. Gile, P. Sista, H.-K. C. Cheung, C. K. Luscombe, J. Pfaendtner, and L. D. Pozzo,
Solvatochromism and Conformational Changes in Fully Dissolved Poly(3-alkylthiophene)s.
Langmuir **31**, 458–468 (2015).

[203] R. J. O. M. Hoofman, M. P. de Haas, L. D. A. Siebbeles, and J. M. Warman,
Highly mobile electrons and holes on isolated chains of the semiconducting polymer poly(phenylene vinylene).
Nature **392**, 54–56 (1998).

[204] S. Cho, B. S. Rolczynski, T. Xu, L. Yu, and L. X. Chen,
Solution Phase Exciton Diffusion Dynamics of a Charge-Transfer Copolymer PTB7 and a Homopolymer P3HT.
The Journal of Physical Chemistry B **119**, 7447–7456 (2015).

[205] A. Ruseckas, P. Wood, I. D. W. Samuel, G. R. Webster, W. J. Mitchell, P. L. Burn, and V. Sundström,
Ultrafast depolarization of the fluorescence in a conjugated polymer.
Physical Review B **72**, 115214 (2005).

[206] B. J. Schwartz,
Conjugated polymers as molecular materials: how chain conformation and film morphology influence energy transfer and interchain interactions.
Annual Review of Physical Chemistry **54**, 141–172 (2003).

[207] T.-Q. Nguyen, V. Doan, and B. J. Schwartz,
Conjugated polymer aggregates in solution: Control of interchain interactions.
The Journal of Chemical Physics **110**, 4068–4078 (1999).

[208] M. Yan, L. J. Rothberg, E. W. Kwock, and T. M. Miller,
Interchain Excitations in Conjugated Polymers.
Physical Review Letters **75**, 1992–1995 (1995).

[209] A. Ruseckas, M. Theander, L. Valkunas, M. R. Andersson, O. Inganäs, and V. Sundström,
Energy transfer in a conjugated polymer with reduced inter-chain coupling.
Journal of Luminescence **76–77**, 474–477 (1998).

[210] A. Watanabe, T. Kodaira, and O. Ito,
Time-resolved emission spectra of poly(3-octylthiophene): energy migration in the π-conjugated polymer chain.
Chemical Physics Letters **273**, 227–231 (1997).

[211] J. Z. Zhang, M. A. Kreger, Q.-S. Hu, D. Vitharana, L. Pu, P. J. Brock, and J. C. Scott,
Femtosecond studies of exciton dynamics in a novel main chain chiral conjugated poly(arylenevinylene).
The Journal of Chemical Physics **106**, 3710–3720 (1997).

[212] S. F. Völker, S. Uemura, M. Limpinsel, M. Mingebach, C. Deibel, V. Dyakonov, and C. Lambert,
Polymeric Squaraine Dyes as Electron Donors in Bulk Heterojunction Solar Cells.
Macromolecular Chemistry and Physics **211**, 1098–1108 (2010).

[213] S. F. Völker, A. Schmiedel, M. Holzapfel, K. Renziehausen, V. Engel, and C. Lambert,
Singlet–Singlet Exciton Annihilation in an Exciton-Coupled Squaraine-Squaraine Copolymer: A Model toward Hetero-J-Aggregates.
The Journal of Physical Chemistry C **118**, 17467–17482 (2014).

[214] S. F. Völker, T. Dellermann, H. Ceymann, M. Holzapfel, and C. Lambert,
Synthesis, electrochemical, and optical properties of low band gap homo- and copolymers based on squaraine dyes.
Journal of Polymer Science Part A: Polymer Chemistry **52**, 890–911 (2014).

[215] S. F. Völker, A. Schmiedel, M. Holzapfel, C. Böhm, and C. Lambert,
Charge transfer dynamics in squaraine–naphthalene diimide copolymers.
Physical Chemistry Chemical Physics **15**, 19831–19844 (2013).

[216] J.-Q. Jiang, C.-L. Sun, Z.-F. Shi, and H.-L. Zhang,
Squaraines as light-capturing materials in photovoltaic cells.
RSC Advances **4**, 32987–32996 (2014).

[217] A. Ajayaghosh,
Chemistry of Squaraine-Derived Materials: Near-IR Dyes, Low Band Gap Systems, and Cation Sensors.
Accounts of Chemical Research **38**, 449–459 (2005).

[218] L. Beverina and P. Salice,
Squaraine Compounds: Tailored Design and Synthesis towards a Variety of Material Science Applications.
European Journal of Organic Chemistry **2010**, 1207–1225 (2010).

[219] S. Sreejith, P. Carol, P. Chithra, and A. Ajayaghosh,
Squaraine dyes: a mine of molecular materials.
Journal of Materials Chemistry **18**, 264–274 (2008).

[220] S. Yagi and H. Nakazumi.
Squarylium Dyes and Related Compounds. In *Heterocyclic Polymethine Dyes.*
Springer Berlin Heidelberg (2008).

[221] L. Hu, Z. Yan, and H. Xu,
Advances in synthesis and application of near-infrared absorbing squaraine dyes.
RSC Advances **3**, 7667–7676 (2013).

[222] L. Beverina and M. Sassi,
Twists and Turns Around a Square: The Many Faces of Squaraine Chemistry.
Synlett **25**, 477–490 (2014).

[223] F. Silvestri, M. D. Irwin, L. Beverina, A. Facchetti, G. A. Pagani, and T. J. Marks,
Efficient Squaraine-Based Solution Processable Bulk-Heterojunction Solar Cells.
Journal of the American Chemical Society **130**, 17640–17641 (2008).

[224] V. Y. Merritt and H. J. Hovel,
Organic solar cells of hydroxy squarylium.
Applied Physics Letters **29**, 414–415 (1976).

[225] D. L. Morel, A. K. Ghosh, T. Feng, E. L. Stogryn, P. E. Purwin, R. F. Shaw, and C. Fishman,
High-efficiency organic solar cells.
Applied Physics Letters **32**, 495–497 (1978).

[226] S. Wang, E. I. Mayo, M. D. Perez, L. Griffe, G. Wei, P. I. Djurovich, S. R. Forrest, and M. E. Thompson,
High efficiency organic photovoltaic cells based on a vapor deposited squaraine donor.
Applied Physics Letters **94**, 233304 (2009).

[227] U. Mayerhöffer, K. Deing, K. Gruß, H. Braunschweig, K. Meerholz, and F. Würthner,
Outstanding Short-Circuit Currents in BHJ Solar Cells Based on NIR-Absorbing Acceptor-Substituted Squaraines.
Angewandte Chemie International Edition **48**, 8776–8779 (2009).

[228] B. Fan, Y. Maniglio, M. Simeunovic, S. Kuster, T. Geiger, R. Hany, F. Nüesch, B. Fan, Y. Maniglio, M. Simeunovic, S. Kuster, T. Geiger, R. Hany, and F. Nüesch,
Squaraine Planar-Heterojunction Solar Cells, Squaraine Planar-Heterojunction Solar Cells.
International Journal of Photoenergy **2009** (2009).

[229] G. Wei, R. R. Lunt, K. Sun, S. Wang, M. E. Thompson, and S. R. Forrest,
Efficient, Ordered Bulk Heterojunction Nanocrystalline Solar Cells by Annealing of Ultrathin Squaraine Thin Films.
Nano Letters **10**, 3555–3559 (2010).

[230] G. Wei, S. Wang, K. Renshaw, M. E. Thompson, and M. E. Thompson,
Solution-Processed Squaraine Bulk Heterojunction Photovoltaic Cells.
ACS Nano **4**, 1927–1934 (2010).

[231] L. Beverina, M. Drees, A. Facchetti, M. Salamone, R. Ruffo, and G. A. Pagani,
Bulk Heterojunction Solar Cells – Tuning of the HOMO and LUMO Energy Levels of Pyrrolic Squaraine Dyes.
European Journal of Organic Chemistry **2011**, 5555–5563 (2011).

[232] G. Wei, X. Xiao, S. Wang, J. D. Zimmerman, K. Sun, V. V. Diev, M. E. Thompson, and S. R. Forrest,
Arylamine-Based Squaraine Donors for Use in Organic Solar Cells.
Nano Letters **11**, 4261–4264 (2011).

[233] S. Wang, L. Hall, V. V. Diev, R. Haiges, G. Wei, X. Xiao, P. I. Djurovich, S. R. Forrest, and M. E. Thompson,
N,N-Diarylanilinosquaraines and Their Application to Organic Photovoltaics.
Chemistry of Materials **23**, 4789–4798 (2011).

[234] G. Wei, X. Xiao, S. Wang, K. Sun, K. J. Bergemann, M. E. Thompson, and S. R. Forrest,
Functionalized Squaraine Donors for Nanocrystalline Organic Photovoltaics.
ACS Nano **6**, 972–978 (2012).

[235] C.-H. Chen, W.-T. Cheng, M.-L. Tsai, and K.-T. Huang,
Fabrication and Performance of Copper Phthalocyanine/Squaraine Dye/Perylene Composite with Bulk Heterojunctions by the Solution Blending Process.
Industrial & Engineering Chemistry Research **51**, 3630–3638 (2012).

[236] X. Xiao, G. Wei, S. Wang, J. D. Zimmerman, C. K. Renshaw, M. E. Thompson, and S. R. Forrest, *Small-Molecule Photovoltaics Based on Functionalized Squaraine Donor Blends.* Advanced Materials **24**, 1956–1960 (2012).

[237] K. C. Deing, U. Mayerhöffer, F. Würthner, and K. Meerholz, *Aggregation-dependent photovoltaic properties of squaraine/PC61BM bulk heterojunctions.* Physical Chemistry Chemical Physics **14**, 8328–8334 (2012).

[238] W. Kylberg, Y. Zhang, A. Aebersold, F. A. d. Castro, T. Geiger, J. Heier, S. Kuster, C.-Q. Ma, P. Bäuerle, F. Nüesch, J.-N. Tisserant, and R. Hany, *Oligothiophene dendron-decorated squaraine dyes: Synthesis, thin film formation, and performance in organic solar cells.* Organic Electronics **13**, 1204–1212 (2012).

[239] T. Maeda, T. Tsukamoto, A. Seto, S. Yagi, and H. Nakazumi, *Synthesis and Characterization of Squaraine-Based Conjugated Polymers With Phenylene Linkers for Bulk Heterojunction Solar Cells.* Macromolecular Chemistry and Physics **213**, 2590–2597 (2012).

[240] D. Bagnis, L. Beverina, H. Huang, F. Silvestri, Y. Yao, H. Yan, G. A. Pagani, T. J. Marks, and A. Facchetti, *Marked Alkyl- vs Alkenyl-Substitutent Effects on Squaraine Dye Solid-State Structure, Carrier Mobility, and Bulk-Heterojunction Solar Cell Efficiency.* Journal of the American Chemical Society **132**, 4074–4075 (2010).

[241] H. Choi and P. V. Kamat, *CdS Nanowire Solar Cells: Dual Role of Squaraine Dye as a Sensitizer and a Hole Transporter.* The Journal of Physical Chemistry Letters **4**, 3983–3991 (2013).

[242] T. Maeda, S. Arikawa, H. Nakao, S. Yagi, and H. Nakazumi, *Linearly π-extended squaraine dyes enable the spectral response of dye-sensitized solar cells in the NIR region over 800 nm.* New Journal of Chemistry **37**, 701–708 (2013).

[243] T. Maeda, H. Nakao, H. Kito, H. Ichinose, S. Yagi, and H. Nakazumi, *Far-red absorbing squarylium dyes with terminally connected electron-accepting units for organic dye-sensitized solar cells.* Dyes and Pigments **90**, 275–283 (2011).

[244] T. Maeda, Y. Hamamura, K. Miyanaga, N. Shima, S. Yagi, and H. Nakazumi, *Near-infrared Absorbing Squarylium Dyes with Linearly Extended π-Conjugated Structure for Dye-sensitized Solar Cell Applications.* Organic Letters **13**, 5994–5997 (2011).

[245] T. Maeda, N. Shima, T. Tsukamoto, S. Yagi, and H. Nakazumi, *Unsymmetrical squarylium dyes with π-extended heterocyclic components and their application to organic dye-sensitized solar cells.* Synthetic Metals **161**, 2481–2487 (2011).

[246] J. V. Ros-Lis, R. Martínez-Máñez, F. Sancenón, J. Soto, M. Spieles, and K. Rurack, *Squaraines as Reporter Units: Insights into their Photophysics, Protonation, and Metal-Ion Coordination Behaviour.* Chemistry – A European Journal **14**, 10101–10114 (2008).

[247] J. V. Ros-Lis, R. Martínez-Máñez, and J. Soto,
A selective chromogenic reagent for cyanide determination.
Chemical Communications, 2248–2249 (2002).

[248] A. Ajayaghosh, E. Arunkumar, and J. Daub,
A Highly Specific Ca^{2+}*-Ion Sensor: Signaling by Exciton Interaction in a Rigid–Flexible–Rigid Bichromophoric "H" Foldamer.*
Angewandte Chemie International Edition **41**, 1766–1769 (2002).

[249] B. Radaram, T. Mako, and M. Levine,
Sensitive and selective detection of cesium via fluorescence quenching.
Dalton Transactions **42**, 16276–16278 (2013).

[250] B. Ananda Rao, H. Kim, and Y.-A. Son,
Synthesis of near-infrared absorbing pyrylium-squaraine dye for selective detection of Hg^{2+}*.*
Sensors and Actuators B: Chemical **188**, 847–856 (2013).

[251] K. D. Volkova, V. B. Kovalska, A. L. Tatarets, L. D. Patsenker, D. V. Kryvorotenko, and S. M. Yarmoluk,
Spectroscopic study of squaraines as protein-sensitive fluorescent dyes.
Dyes and Pigments **72**, 285–292 (2007).

[252] A. L. Tatarets, I. A. Fedyunyayeva, T. S. Dyubko, Y. A. Povrozin, A. O. Doroshenko, E. A. Terpetschnig, and L. D. Patsenker,
Synthesis of water-soluble, ring-substituted squaraine dyes and their evaluation as fluorescent probes and labels.
Analytica Chimica Acta **570**, 214–223 (2006).

[253] E. Terpetschnig, H. Szmacinski, A. Ozinskas, and J. R. Lakowicz,
Synthesis of Squaraine-N-Hydroxysuccinimide Esters and Their Biological Application as Long-Wavelength Fluorescent Labels.
Analytical Biochemistry **217**, 197–204 (1994).

[254] J. Thomas, D. B. Sherman, T. J. Amiss, S. A. Andaluz, and J. B. Pitner,
Synthesis and Biosensor Performance of a Near-IR Thiol-Reactive Fluorophore Based on Benzothiazolium Squaraine.
Bioconjugate Chemistry **18**, 1841–1846 (2007).

[255] B.-L. Renard, Y. Aubert, and U. Asseline,
Fluorinated squaraine as near-IR label with improved properties for the labeling of oligonucleotides.
Tetrahedron Letters **50**, 1897–1901 (2009).

[256] F.-P. Gao, Y.-X. Lin, L.-L. Li, Y. Liu, U. Mayerhöffer, P. Spenst, J.-G. Su, J.-Y. Li, F. Würthner, and H. Wang,
Supramolecular adducts of squaraine and protein for noninvasive tumor imaging and photothermal therapy in vivo.
Biomaterials **35**, 1004–1014 (2014).

[257] E. Arunkumar, N. Fu, and B. D. Smith,
Squaraine-Derived Rotaxanes: Highly Stable, Fluorescent Near-IR Dyes.
Chemistry – A European Journal **12**, 4684–4690 (2006).

[258] J. J. Gassensmith, E. Arunkumar, L. Barr, J. M. Baumes, K. M. DiVittorio, J. R. Johnson, B. C. Noll, and B. D. Smith,

Self-Assembly of Fluorescent Inclusion Complexes in Competitive Media Including the Interior of Living Cells.
Journal of the American Chemical Society **129**, 15054–15059 (2007).

[259] Z. Xiang, E. E. Nesterov, J. Skoch, T. Lin, B. T. Hyman, T. M. Swager, B. J. Bacskai, and S. A. Reeves,
Detection of Myelination Using a Novel Histological Probe.
Journal of Histochemistry & Cytochemistry **53**, 1511–1516 (2005).

[260] K. Müllen and G. Wegner (Eds.),
Electronic Materials: The Oligomer Approach.
Wiley-VCH Verlag GmbH (2008).

[261] C. Lambert, T. Scherpf, H. Ceymann, A. Schmiedel, and M. Holzapfel,
Coupled Oscillators for Tuning Fluorescence Properties of Squaraine Dyes.
Journal of the American Chemical Society **137**, 3547–3557 (2015).

[262] A. Humeniuk and R. Mitric,
Long-range correction for tight-binding TD-DFT.
arXiv:1503.01714 [physics] (2015).

[263] S. Polyutov, O. Kühn, and T. Pullerits,
Exciton-vibrational coupling in molecular aggregates: Electronic versus vibronic dimer.
Chemical Physics **394**, 21–28 (2012).

[264] T.-Q. Nguyen, J. Wu, V. Doan, B. J. Schwartz, and S. H. Tolbert,
Control of Energy Transfer in Oriented Conjugated Polymer-Mesoporous Silica Composites.
Science **288**, 652–656 (2000).

[265] K. M. Gaab and C. J. Bardeen,
Wavelength and Temperature Dependence of the Femtosecond Pump-Probe Anisotropies in the Conjugated Polymer MEH-PPV: Implications for Energy-Transfer Dynamics.
The Journal of Physical Chemistry B **108**, 4619–4626 (2004).

[266] A. Köhler, S. T. Hoffmann, and H. Bässler,
An Order–Disorder Transition in the Conjugated Polymer MEH-PPV.
Journal of the American Chemical Society **134**, 11594–11601 (2012).

[267] K. M. Coakley and M. D. McGehee,
Conjugated Polymer Photovoltaic Cells.
Chemistry of Materials **16**, 4533–4542 (2004).

[268] B. Zhao, Z. He, X. Cheng, D. Qin, M. Yun, M. Wang, X. Huang, J. Wu, H. Wu, and Y. Cao,
Flexible polymer solar cells with power conversion efficiency of 8.7%.
Journal of Materials Chemistry C **2**, 5077–5082 (2014).

[269] B. Muhsin, R. Roesch, G. Gobsch, and H. Hoppe,
Flexible ITO-free polymer solar cells based on highly conductive PEDOT:PSS and a printed silver grid.
Solar Energy Materials and Solar Cells **130**, 551–554 (2014).

[270] S. T. Hoffmann, H. Bässler, and A. Köhler,
What determines inhomogeneous broadening of electronic transitions in conjugated polymers?
The Journal of Physical Chemistry B **114**, 17037–17048 (2010).

[271] W. J. D. Beenken and T. Pullerits,
Spectroscopic Units in Conjugated Polymers: A Quantum Chemically Founded Concept?
The Journal of Physical Chemistry B **108**, 6164–6169 (2004).

[272] L. M. Herz, C. Silva, A. C. Grimsdale, K. Müllen, and R. T. Phillips,
Time-dependent energy transfer rates in a conjugated polymer guest-host system.
Physical Review B **70**, 165207 (2004).

[273] R. Q. Albuquerque, C. C. Hofmann, J. Köhler, and A. Köhler,
Diffusion-limited energy transfer in blends of oligofluorenes with an anthracene derivative.
The Journal of Physical Chemistry B **115**, 8063–8070 (2011).

[274] E. Collini and G. D. Scholes,
Coherent Intrachain Energy Migration in a Conjugated Polymer at Room Temperature.
Science **323**, 369–373 (2009).

[275] G. Padmanaban and S. Ramakrishnan,
Conjugation Length Control in Soluble Poly[2-methoxy-5-((2'-ethylhexyl)oxy)-1,4-phenylenevinylene] (MEHPPV): Synthesis, Optical Properties, and Energy Transfer.
Journal of the American Chemical Society **122**, 2244–2251 (2000).

[276] B. J. Schwartz, T.-Q. Nguyen, J. Wu, and S. H. Tolbert,
Interchain and intrachain exciton transport in conjugated polymers: ultrafast studies of energy migration in aligned MEH-PPV/mesoporous silica composites.
Synthetic Metals **116**, 35–40 (2001).

[277] I. B. Martini, A. D. Smith, and B. J. Schwartz,
Exciton-exciton annihilation and the production of interchain species in conjugated polymer films: Comparing the ultrafast stimulated emission and photoluminescence dynamics of MEH-PPV.
Physical Review B **69**, 035204 (2004).

[278] T.-Q. Nguyen, I. B. Martini, J. Liu, and B. J. Schwartz,
Controlling Interchain Interactions in Conjugated Polymers: The Effects of Chain Morphology on Exciton-Exciton Annihilation and Aggregation in MEH-PPV Films.
The Journal of Physical Chemistry B **104**, 237–255 (2000).

[279] R. J. Kline and M. D. McGehee,
Morphology and Charge Transport in Conjugated Polymers.
Journal of Macromolecular Science, Part C: Polymer Reviews **46**, 27–45 (2006).

[280] J. Clark, C. Silva, R. H. Friend, and F. C. Spano,
Role of Intermolecular Coupling in the Photophysics of Disordered Organic Semiconductors: Aggregate Emission in Regioregular Polythiophene.
Physical Review Letters **98**, 206406 (2007).

[281] H. Yamagata, C. M. Pochas, and F. C. Spano,
Designing J- and H-Aggregates through Wave Function Overlap Engineering: Applications to Poly(3-hexylthiophene).
The Journal of Physical Chemistry B **116**, 14494–14503 (2012).

[282] J. Yu, D. Hu, and P. F. Barbara,
Unmasking Electronic Energy Transfer of Conjugated Polymers by Suppression of O_2 Quenching.
Science **289**, 1327–1330 (2000).

[283] C. J. Collison, L. J. Rothberg, V. Treemaneekarn, and Y. Li,
Conformational Effects on the Photophysics of Conjugated Polymers: A Two Species Model for MEH-PPV Spectroscopy and Dynamics.
Macromolecules **34**, 2346–2352 (2001).

[284] D. Y. Kim, J. K. Grey, and P. F. Barbara,
A detailed single molecule spectroscopy study of the vibronic states and energy transfer pathways of the conjugated polymer MEH-PPV.
Synthetic Metals **156**, 336–345 (2006).

[285] F. A. Feist, M. F. Zickler, and T. Basché,
Origin of the Red Sites and Energy Transfer Rates in Single MEH-PPV Chains at Low Temperature.
ChemPhysChem **12**, 1499–1508 (2011).

[286] H. Lin, R. P. Hania, R. Bloem, O. Mirzov, D. Thomsson, and I. G. Scheblykin,
Single chain versus single aggregate spectroscopy of conjugated polymers. Where is the border?
Physical Chemistry Chemical Physics **12**, 11770–11777 (2010).

[287] P. Wood, I. D. W. Samuel, G. R. Webster, and P. L. Burn,
Investigating the effect of conjugation in MEH-PPV.
Synthetic Metals **119**, 571–572 (2001).

[288] A. Dogariu, D. Vacar, and A. J. Heeger,
Picosecond time-resolved spectroscopy of the excited state in a soluble derivative of poly(phenylene vinylene): Origin of the bimolecular decay.
Physical Review B **58**, 10218–10224 (1998).

[289] J. Sperling, A. Nemeth, P. Baum, F. Šanda, E. Riedle, H. Kauffmann, S. Mukamel, and F. Milota,
Exciton dynamics in a disordered conjugated polymer: Three-pulse photon-echo and transient grating experiments.
Chemical Physics **349**, 244–249 (2008).

[290] F. Panzer, H. Bässler, R. Lohwasser, M. Thelakkat, and A. Köhler,
The Impact of Polydispersity and Molecular Weight on the Order–Disorder Transition in Poly(3-hexylthiophene).
The Journal of Physical Chemistry Letters **5**, 2742–2747 (2014).

[291] C. Scharsich, R. H. Lohwasser, M. Sommer, U. Asawapirom, U. Scherf, M. Thelakkat, D. Neher, and A. Köhler,
Control of aggregate formation in poly(3-hexylthiophene) by solvent, molecular weight, and synthetic method.
Journal of Polymer Science Part B: Polymer Physics **50**, 442–453 (2012).

[292] G. Williams,
Molecular aspects of multiple dielectric relaxation processes in solid polymers. In *Electric Phenomena in Polymer Science*
Springer Berlin Heidelberg (1979).

[293] J. Klafter and A. Blumen,
Fractal behavior in trapping and reaction.
The Journal of Chemical Physics **80**, 875–877 (1984).

[294] R. G. Palmer, D. L. Stein, E. Abrahams, and P. W. Anderson,
Models of Hierarchically Constrained Dynamics for Glassy Relaxation.
Physical Review Letters **53**, 958–961 (1984).

[295] A. Blumen, G. Zumofen, and J. Klafter,
Target annihilation by random walkers.
Physical Review B **30**, 5379–5382 (1984).

[296] J. Budimir and J. L. Skinner,
Kinetic Ising model for polymer dynamics. II. Generalized transition rates and the Williams–Watts nonexponential function.
The Journal of Chemical Physics **82**, 5232–5241 (1985).

[297] J. Klafter and A. Blumen,
Models for dynamically controlled relaxation.
Chemical Physics Letters **119**, 377–382 (1985).

[298] J. Klafter and M. F. Shlesinger,
On the relationship among three theories of relaxation in disordered systems.
Proceedings of the National Academy of Sciences **83**, 848–851 (1986).

[299] B. Mollay and H. F. Kauffmann,
Direct electronic energy transfer in the presence of static site-energy disorder–dipolar coupling.
The Journal of Chemical Physics **97**, 4380–4397 (1992).

[300] P. J. Steinbach, R. Ionescu, and C. R. Matthews,
Analysis of kinetics using a hybrid maximum-entropy/nonlinear-least-squares method: application to protein folding.
Biophysical Journal **82**, 2244–2255 (2002).

[301] P. J. Steinbach,
Filtering artifacts from lifetime distributions when maximizing entropy using a bootstrapped model.
Analytical Biochemistry **427**, 102–105 (2012).

[302] C. Consani, G. Auböck, F. v. Mourik, and M. Chergui,
Ultrafast Tryptophan-to-Heme Electron Transfer in Myoglobins Revealed by UV 2D Spectroscopy.
Science **339**, 1586–1589 (2013).

[303] V. Prokhorenko,
Global analysis of multi-dimensional experimental data.
EPA Newsletter, issue June, 21–23 (2012).

[304] F. Milota, V. I. Prokhorenko, T. Mancal, H. von Berlepsch, O. Bixner, H. F. Kauffmann, and J. Hauer,
Vibronic and Vibrational Coherences in Two-Dimensional Electronic Spectra of Supramolecular J-Aggregates.
The Journal of Physical Chemistry A **117**, 6007–6014 (2013).

[305] L. J. Rothberg, M. Yan, F. Papadimitrakopoulos, M. E. Galvin, E. W. Kwock, and T. M. Miller,
Photophysics of phenylenevinylene polymers.
Synthetic Metals **80**, 41–58 (1996).

[306] R. E. Di Paolo, J. Seixas de Melo, J. Pina, H. D. Burrows, J. Morgado, and A. L. Maçanita,
Conformational Relaxation ofp-Phenylenevinylene Trimers in Solution Studied by Picosecond Time-Resolved Fluorescence.
ChemPhysChem **8**, 2657–2664 (2007).

[307] L. J. Rothberg,
Semiconducting Polymers: Chemistry, Physics and Engineering. Second edition.
Wiley (2006).

[308] H. Lin, S. R. Tabaei, D. Thomsson, O. Mirzov, P.-O. Larsson, and I. G. Scheblykin,
Fluorescence Blinking, Exciton Dynamics, and Energy Transfer Domains in Single Conjugated Polymer Chains.
Journal of the American Chemical Society **130**, 7042–7051 (2008).

[309] H. A. Mizes and E. M. Conwell,
Photoinduced charge transfer in poly(p-phenylene vinylene).
Physical Review B **50**, 11243–11246 (1994).

[310] J. W. Blatchford, S. W. Jessen, L.-B. Lin, T. L. Gustafson, D.-K. Fu, H.-L. Wang, T. M. Swager, A. G. MacDiarmid, and A. J. Epstein,
Photoluminescence in pyridine-based polymers: Role of aggregates.
Physical Review B **54**, 9180–9189 (1996).

[311] H. Lin, Y. Tian, K. Zapadka, G. Persson, D. Thomsson, O. Mirzov, P.-O. Larsson, J. Widengren, and I. G. Scheblykin,
Fate of Excitations in Conjugated Polymers: Single-Molecule Spectroscopy Reveals Nonemissive "Dark" Regions in MEH-PPV Individual Chains.
Nano Letters **9**, 4456–4461 (2009).

[312] R. Jakubiak, C. J. Collison, W. C. Wan, L. J. Rothberg, and B. R. Hsieh,
Aggregation Quenching of Luminescence in Electroluminescent Conjugated Polymers.
The Journal of Physical Chemistry A **103**, 2394–2398 (1999).

[313] C.-X. Sheng, M. Tong, S. Singh, and Z. V. Vardeny,
Experimental determination of the charge/neutral branching ratio η in the photoexcitation of π-conjugated polymers by broadband ultrafast spectroscopy.
Physical Review B **75**, 085206 (2007).

[314] G. D. Scholes, D. S. Larsen, G. R. Fleming, G. Rumbles, and P. L. Burn,
Origin of line broadening in the electronic absorption spectra of conjugated polymers: Three-pulse-echo studies of MEH-PPV in toluene.
Physical Review B **61**, 13670–13678 (2000).

[315] T. E. Dykstra, V. Kovalevskij, X. Yang, and G. D. Scholes,
Excited state dynamics of a conformationally disordered conjugated polymer: A comparison of solutions and film.
Chemical Physics **318**, 21–32 (2005).

[316] J. Kim, S. Mukamel, and G. D. Scholes,
Two-Dimensional Electronic Double-Quantum Coherence Spectroscopy.
Accounts of Chemical Research **42**, 1375–1384 (2009).

[317] S. J. Martin, D. D. C. Bradley, P. A. Lane, H. Mellor, and P. L. Burn,
Linear and nonlinear optical properties of the conjugated polymers PPV and MEH-PPV.
Physical Review B **59**, 15133–15142 (1999).

[318] P. Wang, C. J. Collison, and L. J. Rothberg,
Origins of aggregation quenching in luminescent phenylenevinylene polymers.
Journal of Photochemistry and Photobiology A: Chemistry **144**, 63–68 (2001).

[319] B. Mollay, U. Lemmer, R. Kersting, R. F. Mahrt, H. Kurz, H. F. Kauffmann, and H. Bässler,
Dynamics of singlet excitations in conjugated polymers: Poly(phenylenevinylene) and poly(phenylphenylenevinylene).
Physical Review B **50**, 10769–10779 (1994).

[320] K. Brunner, A. Tortschanoff, C. Warmuth, H. Bässler, and H. F. Kauffmann,
Site Torsional Motion and Dispersive Excitation Hopping Transfer in π-Conjugated Polymers.
The Journal of Physical Chemistry B **104**, 3781–3790 (2000).

[321] H. T. Nicolai, M. Kuik, G. a. H. Wetzelaer, B. de Boer, C. Campbell, C. Risko, J. L. Brédas, and P. W. M. Blom,
Unification of trap-limited electron transport in semiconducting polymers.
Nature Materials **11**, 882–887 (2012).

[322] A. Köhler,
Organic semiconductors: No more breaks for electrons.
Nature Materials **11**, 836–837 (2012).

[323] O. V. Mikhnenko, M. Kuik, J. Lin, N. van der Kaap, T.-Q. Nguyen, and P. W. M. Blom,
Trap-Limited Exciton Diffusion in Organic Semiconductors.
Advanced Materials **26**, 1912–1917 (2014).

[324] R. Kersting, U. Lemmer, R. F. Mahrt, K. Leo, H. Kurz, H. Bässler, and E. O. Göbel,
Femtosecond energy relaxation in π-conjugated polymers.
Physical Review Letters **70**, 3820–3823 (1993).

[325] K. S. Wong, H. Wang, and G. Lanzani,
Ultrafast excited-state planarization of the hexamethylsexithiophene oligomer studied by femtosecond time-resolved photoluminescence.
Chemical Physics Letters **288**, 59–64 (1998).

[326] S. Westenhoff, W. J. D. Beenken, R. H. Friend, N. C. Greenham, A. Yartsev, and V. Sundström,
Anomalous Energy Transfer Dynamics due to Torsional Relaxation in a Conjugated Polymer.
Physical Review Letters **97**, 166804 (2006).

Acknowledgments

Finally, I want to express my gratitude to all persons who contributed to the success of this thesis.

- Prof. Dr. Tobias Brixner for assigning me to a versatile and inspiring topic, all of our discussions, the promotion, as well as the trust and liberty in its processing, while providing excellent working conditions. Furthermore, I am grateful for the opportunity of presenting my work on several national and international conferences and research groups.
- Prof. Dr. Frank Würthner and Prof. Dr. Volker Engel for the guidance during my PhD project as additional members of my supervisory board of the Graduate School of Science and Technology. I am grateful to both for their scientific input to all my projects and the open door if help or advise was needed.
- Dr. Andreas Steinbacher for your steady helpfulness and inspiration within the laboratory, scientific discussion, or proof-reading of this thesis. In particular, I want to express my thanks to you as being a friend whom I can always count on.
- Prof. Dr. Frank Würthner, Dr. Matthias Stolte, Dr. Andreas Steinbacher, Dr. Cristina Consani, Dr. André Zitzler-Kunkel, and David Bialas for the persistent support, motivation, and discussions within the merocyanine project.
- Prof. Dr. Christoph Lambert, Dr. Sebastian Völker, Alexander Schmiedel, Dr. Marco Holzapfel, Alexander Humeniuk, Merle I. S. Röhr, and Prof. Dr. Roland Mitrić for the pleasant und successful cooperation within the squaraine project.
- Prof. Dr. Anna Köhler, Dr. Heinz Bässler, Fabian Panzer and Thomas Unger for the cooperation within the MEH-PPV project, the willigness for fruitful discussion either in Bayreuth or in Würzburg setting the basis for the synchronization of our view of the molecular dynamics of polymers.
- Prof. Dr. Patrick Nürnberger for the openness to my questions, the amazing literature overview and contagious scientific enthusiasm.
- Dr. Cristina Consani, Dr. Pramod Kumar Verma, and Dr. Jakub Dostál for a great time in Lab II/V and engagement within our projects.
- Dr. Sebastian Völker for the scientific discussions within the squaraine project, numerous activities outside of the university, and being a great friend.

- Dr. Stefan Rützel, Christian Kramer, Simon Draeger, and Sebastian Röding for engaging discussions about scientific and coding problems, and for maintaining a happy mood both inside and outside of the laboratory.
- The members of the mechanics and electronics workshop for their proactive attitude.
- The technical assistants, as well as our secretaries Andrea Gehring and Anna Rosenfeldt for their help regarding any organizational problem.
- Dr. Andreas Steinbacher, Dr. Stefan Rützel, Prof. Dr. Patrick Nuernberger, and Thomas Schubert for thoroughly proof-reading parts of this thesis.
- All current and past members of the "Lehrstuhl für Physikalische und Theoretische Chemie I" for valuable feedback and ideas, e.g., in status reports or coffee breaks, as well as for organizing numerous common activities.
- My family, especially my parents Liliana and Juan for their support not only during my PhD but throughout the last decades. My sisters Solange and Sonia and their families for being such warm-hearted persons. My brother Maxi for the fascination in science, the empathy, and being a person with whom I can talk about anything.

Affidavit

I hereby confirm that my thesis entitled

Structure-Dependent Ultrafast Relaxation Dynamics in Multichromophoric Systems

is the result of my own work. I did not receive any help or support from commercial consultants. All sources and / or materials applied are listed and specified in the thesis. Furthermore, I confirm that this thesis has not yet been submitted as part of another examination process neither in identical nor in similar form.

Würzburg, April 18, 2016

Federico Juan Koch

Eidesstattliche Erklärung

Hiermit erkläre ich an Eides statt, die Dissertation mit dem Titel

Strukturabhängigkeit ultraschneller Relaxationsdynamik in multichromophoren Systemen

eigenständig, d.h. insbesondere selbständig und ohne Hilfe eines kommerziellen Promotionsberaters, angefertigt und keine anderen als die von mir angegebenen Quellen und Hilfsmittel verwendet zu haben.
Ich erkläre außerdem, dass die Dissertation weder in gleicher noch in ähnlicher Form bereits in einem anderen Prüfungsverfahren vorgelegen hat.

Würzburg, 18. April 2016

Federico Juan Koch